Escape from Intermittent Billiards

Orestis Georgiou

School of Mathematics

August 2011

A dissertation submitted to the University of Bristol in accordance with the requirements of the degree of Doctor of Philosophy in the Faculty of Science

To my brother Orfeas...

...whom I miss infinitely.

Abstract

The purpose of this Thesis was to investigate the *intermittent* behavior exhibited by open mathematical *billiards* (2-dimensional models of 'a particle in a box') through the survival probability function $P(t)$. That is, the probability of the trapped particle not to *escape* through a pre-specified region or hole in time t. Mathematical billiards have received a lot of attention in recent years due to their ability to exhibit all kinds of dynamical behaviors (chaotic, mixed and integrable) and their corresponding experimentally realizable quantum analogues (*e.g.* quantum dots). $P(t)$ is an important statistical observable able to describe and classify the internal dynamics of the billiard.

Intermittency in billiards is introduced by the phenomenon of *stickiness* which is itself due to points or regions in phase space having zero local Lyapunov exponents (*e.g.* in the close vicinity of KAM elliptic islands or near marginally unstable periodic orbits - MUPOs). When chaotic trajectories approach such regions, they *stick* to them for long periods of time exhibiting almost regular motion. This intermittent behavior determines the main dynamical properties of the system *e.g.* transport and decay of correlations and is captured by $P(t)$ which at large times t decays as a power law $\sim \mathcal{C}/t^{\alpha}$. We find that the position of the hole offers a convenient way of quantifying these long periods allowing for, in the case of stickiness near MUPOs where $\alpha = 1$, the calculation of exact to leading order expressions of the constant $\mathcal{C}$. This quantitative result improves upon past investigations of open billiards which were only qualitative, thus allowing for the *accurate prediction*, *calibration* and *optimization* of escape distributions. The technique for calculating $P(t)$ is first developed for the *stadium* billiard and then applied to the *mushroom*

and *drivebelt* billiards. This technique can also be applied to other billiards and extended to higher dimensions.

Through the in-depth investigations of MUPOs and their stability, we discover and describe a zero-measure set of *MUPO-free* mushrooms using properties of continued fractions. This fascinating connection made with number theory unveiled a complex structure of MUPOs in the mushroom billiard, thus allowing for the prescription of finitely sticky ones, and therefore the calibration and optimization of the mushroom billiard dynamics. Furthermore, we find that transport through open intermittent billiards such as the stadium with two holes may be *asymmetric*, with the time-dependence of $P(t)$ being exponential or algebraic depending on the positions of the holes through which the particle passes. This shows that open systems can behave very differently to their closed counterparts. Finally, we derive a useful formula for calculating the density of the product of n uniform independent and identically distributed random variables. All our results are supported by numerical simulations and discussed constructively within the context of wave chaos and electronic transport.

Altogether, this Thesis offers a collection of novel investigations with connections to transport in open dynamical systems, applied probability, quantum chaotic scattering and number theory. The results presented provide new insight into the phenomenon of intermittency and suggest new directions for future investigations.

Acknowledgments

I want to express my sincere and total gratitude to my advisor, Professor Carl P. Dettmann, for his constant support, encouragement and friendship that made my studies in Bristol so enjoyable.

I am also very thankful to Professors Péter Bálint, Leonid A. Bunimovich and Jon P. Keating for believing in me and wholeheartedly offering their guidance and support towards my ambitious academic career.

I thank Professors Sebastian Müller, Roman Schubert, Martin Sieber and Nina Snaith not only for their invaluable lessons and discussions on dynamical systems and quantum chaos, but especially for providing such a stimulating environment.

Many thanks goes to my friends and fellow graduate students, in particular Sandro Bettin and Chris Joyner for their intellectual hospitality. Also, Mike Harvey, Marios Kyranides, George Stavrinos, Oguz Tepebaşili and Bénédicte Terrab with whom I have shared a flat, a house and many wonderful moments.

Special thanks go to the lovely Joanna Hutchinson who taught me that there is no success without failure, who loved, encouraged and also supported me unconditionally during this divergent period of my life.

Last, but not least, I want to thank my parents, Stelios and Myroula, who told me to look up and aim for the stars.

I would also like to acknowledge the financial support of the EPSRC who have funded my postgraduate studies in Bristol and made all of this possible.

Author's Declaration

I declare that the work in this thesis was carried out in accordance with the Regulations of the University of Bristol. The work is original except where indicated by special reference in the text and no part of the dissertation has been submitted for any other degree. Any views expressed in the dissertation are those of the author and do not necessarily represent those of the University of Bristol. The thesis has not been presented to any other university for examination either in the United Kingdom or overseas.

Orestis Georgiou

Date: August 2011

Preface

The work contained in this thesis was carried out in close collaboration with my PhD supervisor Carl. P. Dettmann.

Almost all of the results presented here have been published - refer to publication list - and are followed closely in the relevant sections and subsections. The results relating to the drivebelt billiard in chapter 8 have not been published and will be included in a future paper.

The numerical simulations of section 3.6 were performed using a code written by the author in *Mathematica v.6*, while others by a C++ code written by Dettmann.

Figures 2.13, 2.14, 2.15, 2.16, 2.17 and 2.19 were produced using MATLAB software designed by Lansel and Porter.

Contents

Part I

Prologue

Chapter 1

Introduction

How do long-time escape properties depend on the dynamics, the size and positions of holes? To a first approximation, the exponential rate of escape in chaotic systems is proportional to the size of the absorbing or escaping region and inversely proportional to the size of the accessible part of the phase space. In generic systems however, the exponential decays are usually followed by algebraic tails indicating the existence of regions exhibiting near-regular dynamics. These tails can be studied and sometimes directly related to geometrical properties of the system e.g. spatial symmetries. This in turn motivates 'optimization problems' such as where to place holes to maximize/minimize escape [1]; 'inverse problems'[1] corresponding to an open equivalent of "hearing the shape of a drum" [2]; and 'transport problems' [3] where particles can enter and exit the system through different holes, or analogously narrow tunnels connecting a network of cavities. These are the type of questions addressed in this study, and are set in the context of *open mathematical billiards*.

It is highly possible that the reader is not very familiar with dynamical systems or escape formalisms and ideas. Therefore, we step back and re-introduce the key points using an example application. Motivation for the above questions may arise from numerous physical applications ranging from as large as planetary motion to

[1] An inverse problem is a general framework that is used to convert observed measurements into information about a physical object or system.

as small as nano-sized electronic devices. In the latter case, a current (electronic *transport*) is usually induced through a bias (voltage) across a two-dimensional electron gas (quantum dot) confined in some transistor-like semiconductor structure. Hence, electrons can enter and exit the structure via a pair of gate electrodes (quantum point contacts or leads). Remarkably, even though quantum effects become increasingly important on such nano-scales, the classical dynamics (chaotic or integrable or mixed) prescribed by the geometry of the boundary of the structure may be identified to some extent just by measuring the conductance across it. In other words, the *escape* properties of open dynamical systems can be used to distinguish between regular and chaotic behavior and can thus be used to calibrate or even *optimize* the conductance of the device.

1.1 Mathematical Billiards and their Importance

Billiards [4, 5, 6] are systems in which a point particle alternates between motion in a straight line and specular reflections from the walls of its container. The sequence of reflections is described by the billiard map which completely characterizes the motion of the particle. Hence billiards have their boundaries as a natural *Poincaré section*.

Chaotic billiard theory was first introduced by Yakov G. Sinai in the 1970's [7]. The development of rigorous mathematical treatments of the billiard dynamics has henceforth established them as important paradigm models in Ergodic Theory [8], Dynamical Systems [9] and Quantum Chaos [10]. Although low in dimension they retain and exhibit all kinds of dynamical behaviors (integrable, chaotic and mixed) and hence have facilitated the in-depth understanding of the manifested mechanisms of chaos. As a result, they have been readily used as models in theoretical and experimental physics [11, 12, 13, 14].

They are widely applicable mainly because their dynamics corresponds to the (semi-)classical (short wavelength) limit of the wave equations for light, sound or quantum particles in a homogeneous cavity. Hence there exist many math-

ematically and physically motivated modifications of the usual classical billiard dynamics to include for example soft-collisions [15], few [16] and many particle systems [17], curved trajectories due to curved spaces [18] and magnetic fields [19], non-specular reflections [20, 21], time-dependent boundaries [22], and other wave phenomena such as diffraction effects [23] and the Goos-Hänchen effect [24]. Of course the list can be expanded to also include more realistic and physical effects such as attenuation, gain, noise and interference thus describing a whole new set of problems and directions of possible studies.

The development of chaotic billiard theory has proven a key point in asserting many of the fundamental assumptions made in Kinetic Theory [25] for example by providing the much needed mathematical framework for the microscopic and macroscopic properties of gases. The steep repulsive potentials of the inter-atomic and molecular interactions of gases for example can be approximated by the hard collisions exhibited in billiards. Thus, multi-particle systems have been shown to correspond to multi-dimensional semi-dispersing billiards (see Ref [8] chapter 4). Hence, rigorous results such as ergodicity and mixing have be proven. Note however that in some cases, in *soft* potentials for example, ergodicity can be broken allowing for the existence of stable periodic orbits [26, 15]. An even more interesting connection between billiards and molecules was established recently. Molecules in two dimensions were modeled by point particles joint by massless strings of fixed lengths which was shown to be equivalent to the motion of a single particle in three dimensional cylindrical billiards [27]. Similar results and connections are constantly being introduced into the literature, refining and broadening our understanding of the physical world.

Low-dimensional billiards imitating hard-ball systems have also been proven to be very important in the understanding of Statistical mechanics. Take for example the prototype model of the Lorentz gas. This consists of an extended billiard with an infinite number of convex (typically circular) scatterers. The Lorentz gas was introduced by Hendrik Lorentz as a simplified model for metallic conductance of electricity [28] where non-interacting point particles (electrons)

move in straight lines and are scattered elastically by immovable (infinitely heavy) spherical particles. The scatterers may overlap and are assumed to be randomly or periodically distributed. In the case where the scatterers are arranged periodically and the lengths of free flights between scatterers are bounded ('finite horizon'), it is proven that the displacements of particles initially uniformly distributed converges weakly to a Wiener process (Brownian motion) with variance proportional to the continuous time t as $t \to \infty$ and hence exhibits normal *diffusion* [29]. Hence this model has proven an essential mathematical playground on which some key laws of statistical physics were tested and established [30]. More recently, billiards with divided (mixed) phase space have been used as paradigm models of typical containers of ideal gases whose equilibrium distribution is not uniform [31]. This suggests that the shape of the container can indeed have a strong effect on the macroscopic properties of gases [32].

1.2 Open Dynamical systems

Typically, systems are not completely isolated from their environment but are inherently coupled with it. On a similar note, a fundamental issue when performing physical measurements (whether classical or quantum) is to ensure that the system under investigation is as little affected by the observation as possible. The above considerations motivate the study of open systems through a small hole as to leave the closed system, to good approximation, unaffected. The smaller the hole, the smaller the observational effect. Through this hole, particles or radiation may transmit information about the system's internal dynamics. Notice that theory and experiment often work in opposite directions: "theorists use closed systems to understand open ones, while experimentalists do the reverse" [33]. Open dynamical systems are reviewed in both the mathematical [34] and physical [35] literature, while a recent review of open billiards and open problems can be found in Ref [36].

The investigation of open systems (systems with holes or leakages), was first

suggested by mathematicians in the early 1980's as a means of generating transient chaos [37], retrieving information from statistical distributions [38], and deducing facts about the corresponding closed systems. The key distributions of interest classically are the escape probability density $p_e(t)$, which is given by the trajectories that leave the system at time $t > 0$, and also the *survival probability* $P(t)$, which is given by the trajectories that remain in the system up to time t. These two are simply related by $P(t) = \int_t^\infty p_e(t')\mathrm{d}t'$. Such investigations have naturally been extended to billiard systems as well. Over the years, strong links have been established between open billiards and geometrical acoustics [39, 12], quantum chaos [40, 41], controlling chaos [42, 43], atom optics [44, 45], hydrodynamical flows [46, 47, 48], astronomy [49] and cosmology [50]. Furthermore, it has become apparent over the past few years, that the subject of open billiards and their distributions provide a pathway towards a better understanding of the delicate *correspondence* between classical and quantum mechanics [51, 52]. This is emphasized in Figure 1.1 showing the close correspondence between classical and quantum propagation of a beam of classical trajectories and a quantum wave-packet through a chaotic Stadium billiard with two leads attached to it.

1.3 Billiards as a model of Quantum to Classical Correspondence

Billiards are extremely important in the microscopic quantum theoretical and experimental standing point. The connection is primarily due to their dynamics corresponding to the *semiclassical* limit (short wavelength $\lambda \ll 1$ or $\hbar \ll 1$ from the de Broglie relations) of the wave equations in a homogeneous cavity. This is often referred to as the 'geometrical optics approximation' (see Refs [54, 55]). Hence, applications of quantum billiards appear in electromagnetic and acoustic resonators [56], atomic matter waves in optical billiards (where ultracold atoms reflect from laser beams) [45], and in electronic transport through semiconduc-

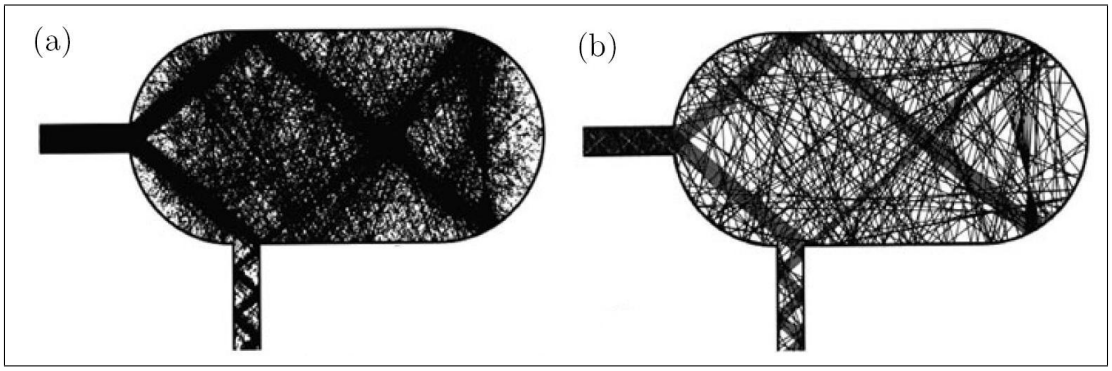

Figure 1.1: Figure reproduced from [53]. (a) The wavefunction probability density for $kd/\pi = 79.577$, where d is the width of the leads. An initial wave in a mode corresponding to $n = 51$ comes through the left lead into the cavity. The density plot shows about 95% of the largest wavefunction probability density. (b) Corresponding classical trajectories. Eleven equidistant injection positions with injection angles $\pm\theta_{51} = \pm 0.695650$ at the entrance are chosen. The injection angle (both positive and negative) into the cavity is chosen to coincide with the quantization condition in the lead for the initial wave in (a). Each trajectory is plotted until it escapes from one of the leads.

tor nano-structures (quantum dots[2]) [57]. We adopt this semiclassical approach momentarily to demonstrate and emphasize the importance of open billiards in quantum mechanics and physics in general.

Quantum billiards correspond to solving the *Helmholtz* equation [3]

$$(\nabla^2 + k^2)\psi = 0, \tag{1.1}$$

with a *Dirichlet* boundary condition $\psi|_{\partial Q} = 0$ and wave-number $k^2 = \frac{2mE}{\hbar^2}$. The discrete spectrum of eigenvalues k_n is real and defines a spectral counting (staircase) function $N(k) := \#\{k_n \leq k\} = \sum_n \Theta(k - k_n)$ which can be decomposed into a smooth $\bar{N}(k)$ and oscillating part $N_{osc}(k)$ [59]. Note that investigations of the spectral counting function go back to Lord Rayleigh more than a hundred

[2]Transistor-like structures made of semiconductors.

[3]The Helmholtz wave equation (1.1) may also describe the vibrations of a string, a membrane (drum), a mass of air in a concert hall, the heat radiation from a body in thermal equilibrium, the fluctuations of the gravitational field in cosmology, or the Schrödinger equation of an atom, a molecule or a compound nucleus [58].

years ago [60] and continue to be a topic of interest ever since. The smooth part asymptotically follows Weyl's law[4] [61]

$$\bar{N}(k) = \frac{A}{4\pi}k^2 - \frac{L}{4\pi}k + o(k), \tag{1.2}$$

as $k \to \infty$, where A and L are respectively the area and boundary length of the billiard cavity. Effectively what this means is that each quantum state occupies the same volume of the corresponding classical phase space. Notice that this also implies that the mean density of states $\bar{d}(E) = \frac{\mathrm{d}\bar{N}(E)}{\mathrm{d}E}$ is independent of the classical dynamics of the billiard. The non-smooth part $N_{osc}(k)$ however, is related in Semiclassical theory through the Gutzwiller trace formula to a Fourier series over the actions of the periodic orbits of the underlying classical system [62]. Hence, the distribution of eigenvalues (spectral statistics) and eigenfunctions of the linear wave operator depend critically on the nature of the classical dynamics. This is illustrated in Figure 1.2 where plots of the probability density wavefunctions are compared for the integrable Circle billiard and chaotic Cardiod billiard.

If the quantum billiard system is somehow opened, then the Helmholtz equation (1.1) has *resonance solutions* and k now acquires a negative imaginary part. The standard example of such systems is that of wave scattering by three or more discs on the plane. Provided that none of the discs 'shadows' the other ones, the classical scattering trajectories are organized around a *fractal trapped set* (or repeller) consisting of points remaining in the 'interaction region' at all times while the quantum resonance solutions associated with decaying *metastable* states have half-lives proportional to $1/|\mathrm{Im}k_n|$ and the modified smooth spectral counting function is conjectured to follow the so called *Fractal Weyl law* [64]. This states that the number of resonances in a critical strip such that $\mathrm{Re}k_n \leq k$ and $\mathrm{Im}k_n \geq -C < 0$, goes as $\sim k^{d_H+1}$ where d_H is the partial Hausdorff dimension of the classical trapped set. Hence, the modified mean density of states strongly depends on the classical billiard dynamics. This observation hints that open systems

[4]Hermann Weyl gave the first proof of the leading order term and conjectured the second one.

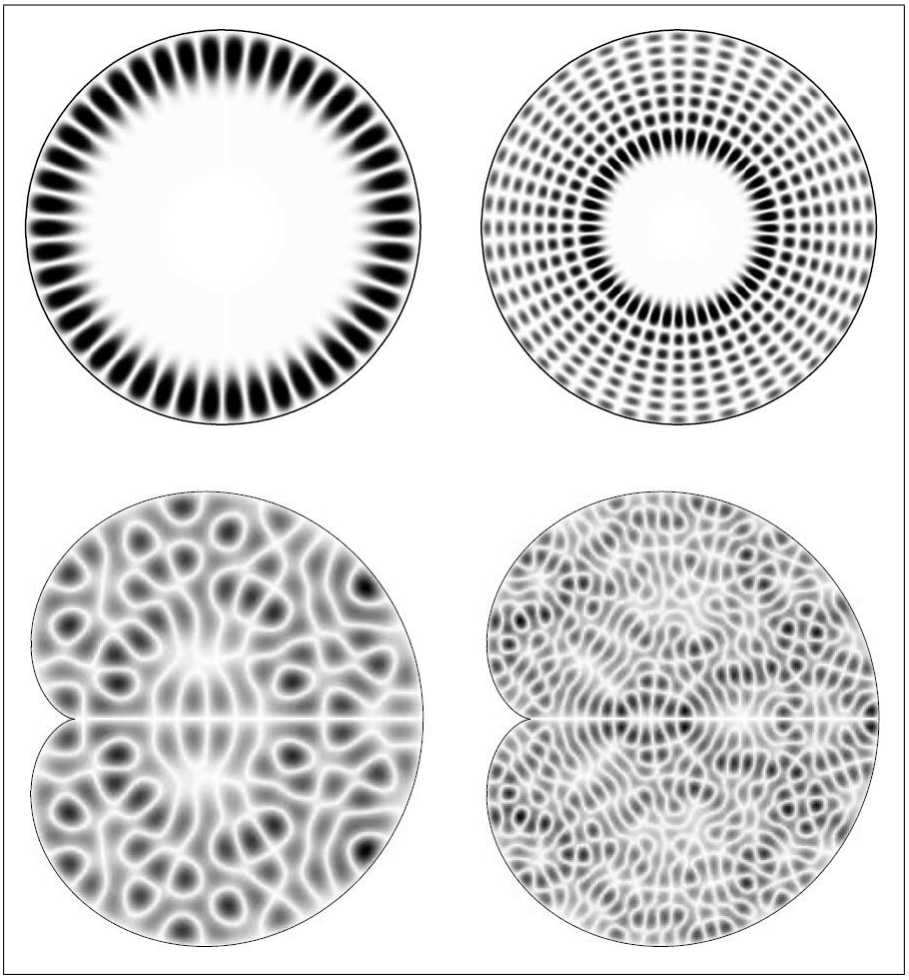

Figure 1.2: Figure reproduced from [63]. Density plot of $|\psi_n|$ for $n = 100$ (left) and $n = 400$ (right) of the integrable Circle and Cardiod billiards clearly illustrating the distinct difference in the two billiard's quantum dynamics.

and in particular open billiards may exhibit a rich variety of interesting results and do not always trivially follow from the corresponding closed billiard dynamics. See Ref [65] and references therein for a survey of quantum chaos, open quantum systems and related open problems.

From a more experimental standpoint, the study of open quantum billiards is primarily motivated through the industrial applications of quantum chaotic scattering. Prime experimental examples are the electronic transport through open ballistic micro-structures (quantum dots) [66, 57] which were guided by the original theoretical works of Jalabert, Baranger and Stone in the 1990s [67]. These experiments have become both a catalyst and a testing ground for important

developments in the field of Quantum Chaos such as the understanding of *universal conductance fluctuations* and *weak localization* [10, 68, 51].

The formalism which provides a link between the quantum transport and conductance is that of Landauer and Büttiker [69, 51]. The conductance through the gate electrodes (leads or openings as in Figure 1.1 for example) of a 2D electron gas (quantum dot 2DEG) in a high quality sample at very low temperatures is given by

$$G(E_F) = g_s \frac{e^2}{2\pi\hbar} T(E_f), \tag{1.3}$$

where E_F is the Fermi-energy[5], e is the electron charge, $g_s = 2$ accounts for spin degeneracy and $T(E_f)$ is the dimensionless conductance. Since the linearity of the wave equations implies that the whole scattering process may be described by a scattering matrix, then

$$T(E_F) = \sum_{m=1}^{N_1} \sum_{n=1}^{N_2} |t_{nm}(E_F)|^2, \tag{1.4}$$

where $N_i = W_i\sqrt{2m_eE_F}/(\pi\hbar)$ are the number of possible propagating channels/modes (hence entry/exit angles are quantized) at energy E_F through leads 1 or 2 of widths W_1 and W_2 respectively. $t_{nm}(E_F)$ are transmission amplitudes of the scattering matrix and hence $|t_{nm}(E_F)|^2$ is the transmission probability between the incoming channel m and outgoing channel n in the leads at energy E_F. Consequently, the transmission amplitudes may be expressed in terms of projections of the Green's function[6] of the scattering region onto the transverse modes in the two openings. Hence, the semiclassical Green's function may be invoked so that $T(E_F)$ becomes a sum involving contributions from pairs of classical trajectories connecting the leads. The leading contribution originates from pairs of identical trajectories often referred to as the *diagonal* contribution which can be calculated

[5]The energy of the highest occupied quantum state in a system of fermions at absolute zero temperature. Typically $E_F \approx 10$meV and $\lambda_F \approx 40$nm .

[6]The Green's function is the Laplace transform of the quantum propagator which gives the probability amplitude for a quantum particle to travel from one place to another in a given time.

using a classical sum rule [55] (which requires ergodicity) giving

$$T(E_f) = \frac{2\pi\hbar N_1 N_2}{\Sigma(E_F)} \int_0^\infty P(t)\mathrm{d}t, \tag{1.5}$$

where $\Sigma(E_F)$ denotes the phase space volume of the systems at energy E_F and $P(t)$ is the classical survival probability which for strongly ergodic systems decays exponentially $\sim e^{-t/\tau_D}$, with dwell time $\tau_D = \frac{\Sigma(E_F)}{2\pi\hbar(N_1+N_2)}$. This remarkable connection is one of the many applications which motivate our work on classical open chaotic billiards, especially ones with an asymptotic $\sim t^{-1}$ power-law decay of the survival probability.

Another important experimental realization of quantum billiards with strong industrial applications is the case of micro-resonators. Here, light is trapped by total internal reflection in some active medium (dielectric cavities) and is of great interest in applications such as laser design. The desired properties of such devices typically include a large Q-factor (small imaginary part of k) and strong directional wave functions at infinity [70].

1.4 Other Applications

Other open billiard related problems with interesting physical applications include asteroid escape from planetary neighborhoods[7] [71], in celestial mechanics, plate tectonics and hydrodynamical flows[8] [72] as well as passive advection in fluids [73]. Similarly, billiard dynamics and the more general escape formalism may also

[7]Planetary neighborhoods form a bounded region of phase space where entrance and escape are only possible by entering or exiting narrow 'bottlenecks' created by the influence of a saddle point.

[8]Mixing of geophysical flows such as the Earth's mantle through dense structures such as tectonic plates can be studied by considering how Lagrangian particle trajectories escape from or enter into different sub-regions.

have applications to heat conduction[9] [74] and Fermi acceleration[10] [75]. Moreover, because of the useful insights on controlling chaos[11] [43], applications now also include chemical reactions that occur in transition state theory [76, 77] and transport through micro-porous membranes[12] [78]. Further theoretical works involve connections with number theory [79] and may even open doors to old and important problems such as the Riemann hypothesis [80, 81].

1.5 About this Thesis

The following work, although not so mathematically rigorous is strongly motivated by the works of Bunimovich and collaborators. It mainly concentrates on 'escape' problems, in which classical particles are allowed to exit the billiard cavity from some pre-specified hole on the boundary. This arrangement makes the *survival probability* $P(t)$ the natural statistical observable which we study in some detail.

The present work on open billiards stands out from the ones mentioned above, in that we obtain *exact* to leading order asymptotic expressions in specific cases of chaotic and mixed phase space billiards, namely the stadium, the mushroom and drivebelt billiards. The ergodic component of these billiards typically contains families of *marginally unstable periodic orbits* (MUPOs). These MUPOs occupy zero volume in phase space and therefore do not affect the overall ergodicity of the closed system. However, regions surrounding these MUPOs in phase space are

[9] Thermalization of the system occurs as the result of binary collisions among locally confined gas particles on different time scales.

[10] Fermi acceleration is the phenomenon that occurs when a classical particle acquires unlimited energy upon collisions with a heavy and moving wall.

[11] Holes can be placed at desired regions in a system's phase space such that for example we may control the leakage with small perturbations. Similarly, the escape route through one of the holes may be considerably reduced by other holes. The survival probability dictates the appropriate times to attempt control of the systems.

[12] In nano-scale systems, including micro-porous media or specially designed devices, boundary walls play a significant role in determining transport properties, such as mass transport (diffusion).

locally non-hyperbolic and therefore the dynamics exhibits an *intermittent* interplay between long, approximately periodic phases and relatively shorter chaotic bursts. This phenomenon essentially causes the Poincaré recurrence times statistics to experience a cross-over from exponential decay to an asymptotic power law $\mathcal{Q}(t) \sim t^{-2}$ for large times t [82]. Moreover, since these non-hyperbolic regions surrounding the MUPOs cause orbits to *stick* to them for long periods of times, they are also *harder* to visit. This is in fact an artifact of ergodicity which demands that phase space is visited uniformly with respect to time [83]. Also note that intermittent systems are the subject of many research areas related to diffusive dynamics including fluid flows [84] and signal processing [85], therefore adding some more motivation and physical importance to our studies.

When the billiard is opened, the survival probability function $P(t)$ of a uniform distribution of particles asymptotically decays as a power law of order $\sim \mathcal{C}/t$ [86]. We find that the intermittency observed can be quantified by *strategically* placing the hole as to overlap the sticky regions surrounding the MUPOs. This allows us to effectively isolate and thus integrate the long surviving orbits, i.e. the ones responsible for the asymptotic power law decay, and obtain an exact expression to leading order of the constant $\mathcal{C}$. The method devised and the approximations used are explained and demonstrated through the paradigmatic example of the period two MUPOs also called *bouncing ball* orbits present in the stadium billiard [87]. The expression obtained for $\mathcal{C}$ is in a nice closed form and therefore allows for the accurate prediction, calibration and optimization of the asymptotic survival probability $P(t)$. This method can potentially be applied to other billiards, as well as extended to higher dimensions.

While trying to statistically model the stickiness introduced by the bouncing ball orbits in the stadium, we encountered a problem which required the calculation of the density of the product of n independent and identically distributed uniform random variables. Surprisingly, a statistical formula for such a calculation was not readily available and is therefore derived and given in Appendix B [88] along with a useful C-code which calculates the distribution (given in Appendix

C).

Another interesting result obtained during this work, has to do with 'transport', which is the scattering equivalent of the above [89]. Motivated by electronic transport in mesoscopic devices such as quantum dots and microwave billiards [51], we studied the stadium billiard with two holes placed asymmetrically with a similar set-up as the one shown in Figure 1.1 such that particles may enter and leave through either holes (leads). We find that such an arrangement of the leads utilizes the sticky regions of the phase space and causes the system to exhibit *time-dependent asymmetric transport* [79]! This means that the time-dependence of the probability of a particle remaining in the system depends on the holes through which the particle passes. This original yet simple observation masks an interesting mechanism behind it, which we first explain in detail and then argue that it holds significant future potential applications. For example it is expected to relate to dynamical trapping with applications such as filtering of long lived resonances e.g. in acoustics and wireless communications. Moreover, it allows for the possibility of extensions and applications to more general systems [90] and processes (e.g. advection and heat transfer). More importantly however, this classical, numerically confirmed, result appears to be lacking a quantum mechanical analogue in the sense that it has not been observed or predicted before. Hence we propose a simple experimental set-up for quantum dots or microwave billiards which could possibly establish some sort of correspondence between the relevant classical and quantum timescales [52].

Having studied the single family of MUPOs present in the stadium billiard, we then proceed to study the infinity of MUPOs observed in the mushroom billiard. Mushroom billiards form a class of dynamical systems with sharply divided phase space. Though sharply divided, typically their single ergodic component has an infinity of 'sticky' MUPOs populating the border between chaos and stability. Surprisingly however, although infinite in number the overall contribution to the survival probability $P(t)$ does not alter the asymptotic decay rate $\sim \mathcal{C}/t$. In fact, the escape treatment of perturbed MUPOs in the mushroom although much more

complicated is in several ways similar to that of the stadium billiard, requiring a thorough investigation of the system's mixed phase space and small angle collision rule. Eventually, we are able to successfully apply our method and techniques to obtain exact to leading order expressions for the constant $\mathcal{C}$ [91].

The inherent *number theoretic* aspect in mushroom billiards with regards to the MUPOs' existence and structural stabilities is a very interesting problem by itself. Our investigations quickly lead to a fascinating new discovery. Namely the existence of a zero measure set of MUPO-free mushrooms which we describe through properties of continued fractions expansions [91]. The set of MUPO-free mushrooms discovered and described is important as it describes the simplest two-dimensional Hamiltonian system with mixed phase space. Furthermore, through our analysis of these continued fractions expansions, we find that we are also able to fabricate mushrooms with as many MUPOs as we like and therefore are able to control the sources of intermittent behaviors.

Finally, we turn to the drivebelt billiard ('tilted stadium') which shares many properties with all the above studied billiard models. More specifically, its ergodicity is due to the defocusing mechanism and it is not uniformly hyperbolic due to the existence of a finite number of circle-type MUPOs. Therefore, this is not very exciting. It offers however a new testing ground for us to generalize our method and approximations for the asymptotic power-law decay of $P(t)$ and in particular to a different collision scenario related to the stickiness of near circle-type MUPOs.

The work contained in this thesis offers a fair amount of new results to the theory of open billiards, mainly involving the intermittent dynamics introduced by the stickiness due to marginally unstable periodic orbits. These results support the importance of finite-time statistics (as opposed to unrealistic $t \to \infty$ limits) in open dynamical systems and also ask questions about the delicate role these orbits may play in accordance with Bohr's quantum-to-classical correspondence principle [92].

The thesis is structured as follows. In chapter 2 a synoptic introduction of chaotic dynamics, escape and intermittency is given; first in the context of

chaotic maps and then in billiards. Important quantities are defined, explained and demonstrated through paradigmatic simple examples. Our main results summarized above follow in Part II and are split in six different chapters. Each of these chapters is a self-contained study of a particular system, all sharing common motivations and applications. Nevertheless they are also independent in that they serve as different 'playgrounds', ideal for studying in detail different phenomena. In chapter 3 we devise a method with which we obtain an exact to leading order expression for the survival probability function for the stadium billiard $P(t)$ at long times t. Then, in section 4 we look at the open-ended stadium and attempt a probabilistic approach based on a model suggested by Ref [83]. In chapter 5 we combine our gained knowledge about intermittency and stickiness due to bouncing ball orbits and re-examine the open stadium billiard, now with two holes instead of one, placed asymmetrically thus leading to *asymmetric transport*. In chapter 6 we turn to the fascinating world of mushroom billiards whose phase space typically includes infinitely many families of marginally unstable periodic orbits (MUPOs) and can therefore be interpreted as being *infinitely sticky*. The connection between MUPOs with number theory eventually allows us to define mushrooms which are *finitely sticky* or even completely *MUPO-free*. Finally in chapters 7 and 8, we test our devised method and obtain exact expressions for the survival probability of the mushroom and drivebelt billiards at long times t. These investigations offer hands-on examples of the application of the theory introduced in chapter 2 while also unveiling some of the beautiful mathematics of chaotic billiards. Finally in chapter 9, we conclude with a summary of our findings and a critical discussion of possible future directions.

Chapter 2

Open dynamical systems

2.1 Escape from chaotic Maps

One dimensional, non-invertible maps are the simplest systems capable of chaotic motion. Since they can exhibit a surprisingly large proportion of phenomena encountered in higher dimensional systems they often serve as convenient starting points for the study of chaotic dynamics. Moreover, they have also been used as paradigm models of open chaotic systems and continue to present us with a range of interesting new observations which we intend to comment upon in passing. In this section, we shall use one dimensional examples of chaotic maps as a basis to introduce the concepts of chaos, escape and intermittency. Then, a two dimensional map, namely the standard map, will serve as a stepping stone example towards introducing some of the dynamics of the two dimensional billiard phase space. Definitions of various dynamical quantities such as Lyapunov exponents and invariant densities as well as intuitive explanations of some useful theorems will be given through these examples. These definitions are by no means general, rigorous, or a complete introduction to open dynamical systems, but rather offer a short synopsis and serve as a brief introduction which will set the stage for the main goal of this thesis which is to quantify intermittency in specific examples of open two-dimensional billiards. Excellent and comprehensive introductions to chaos in dynamical systems, with extensive reference lists therein can be found in

Cvitanović *et al.* [93] and Ott [94]. For a more mathematical approach also see Katok and Hasselblatt [9].

2.1.1 Chaos in 1-D

2.1.1.1 A recipe for Chaos

It is instructive to start with an example. Consider the *tent map*,

$$x_{n+1} = f_T(x_n) = 1 - 2|x_n - \frac{1}{2}|, \quad \text{for } x_n \in [0,1] \tag{2.1}$$

shown in Figure 2.1. The map stretches $[0,1]$ to twice its original length and then

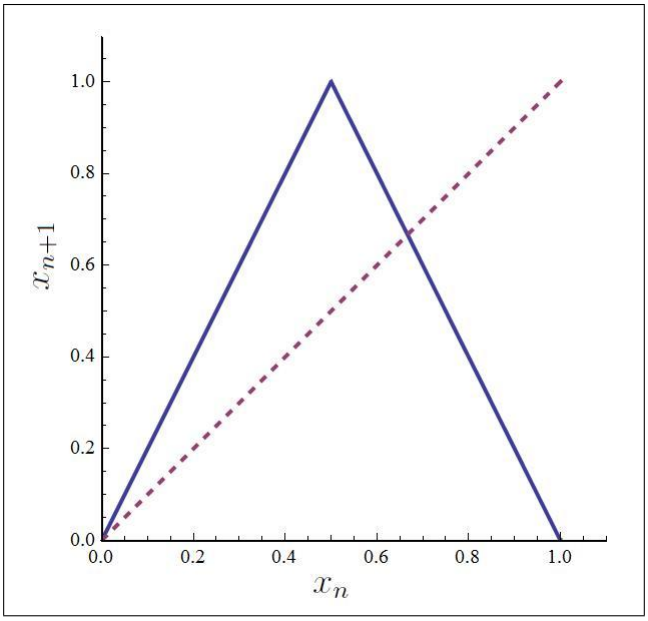

Figure 2.1: The tent map.

folds it in half back onto $[0,1]$. The stretching leads to exponential divergence of nearby trajectories by a factor of two on each iterate, while the folding keeps the orbit bounded and confined in $[0,1]$. The latter also causes the map to be non-invertible. In fact non-invertibility is a generic requirement for one dimensional maps to be chaotic. The combination of these two actions guarantees that any given open subinterval of $[0,1]$ will eventually overlap with any other given subinterval. Therefore the map is also said to be *ergodic* and also *topologically mixing*.

Another common example of a chaotic one dimensional map is the *doubling map*,

$$x_{n+1} = f_D(x_n) = 2x_n \qquad \text{modulo1}, \tag{2.2}$$

as shown in Figure 2.2. The map in this case, stretches, twists and then folds the

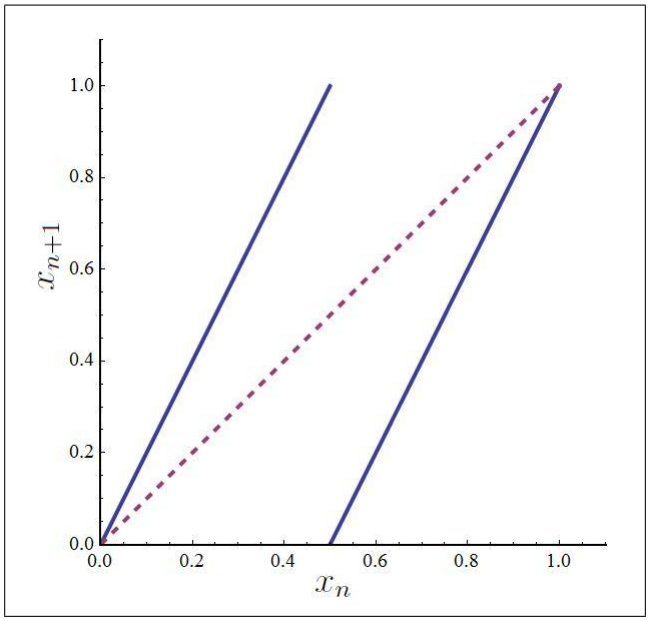

Figure 2.2: The doubling map.

unit interval back onto itself, therefore displaying the same chaotic, non-invertible dynamics as the tent map. An alternative name for the doubling map is the *bit shift map*. This name arises because, if the value of an iterate x_n is written in binary notation, such that

$$x_n = 0.a_1a_2a_3\ldots \equiv \sum_{j=1}^{\infty} 2^{-j}a_j, \tag{2.3}$$

where $a_j = 0$ or 1, then the next iterate of the map is obtained by shifting the binary point by one bit to the right, and if the bit to the left of the new binary point is a 'one', replacing it with a 'zero' such that $x_{n+1} = 0.a_2a_3a_4\ldots$ and so on. Thus, digits that are initially far to the right of the decimal point, and hence seemingly have a minimal influence on the initial value of x_n where $n \gg 1$, eventually become first and play the dominant role. This simple argument, set

in this simple one-dimensional map illustrates best the generic phenomenon of *sensitivity to initial conditions* in chaotic systems. In other words, how a small change or uncertainty in the initial condition x_0 (such as those due to rounding errors in numerical computations or observational and measuring errors) makes a large change in x_n.

Sensitivity to initial conditions is arguably the most important feature of a chaotic system. It means that its distant future and remote past become essentially *independent* of its present state and can be described only 'on average', in probabilistic terms. Therefore, on large time scales, the evolution of chaotic dynamical systems resembles that of purely random processes.

2.1.1.2 Periodic orbits and Stability

The role of periodic orbits was already fully appreciated by Poincaré [95], who noted that hidden in the apparent chaos is a rigid skeleton, a self-similar tree of *periodic orbits* of increasing lengths, and suggested that they should be the key to chaotic dynamics.

A periodic orbit corresponds to a special type of solution for a dynamical system, namely one which repeats itself in time. For a d-dimensional map

$$\mathbf{x}_{n+1} = f(\mathbf{x}_n), \qquad \mathbf{x}_i \in \mathbb{R}^d, \qquad d \geq 1, \tag{2.4}$$

a periodic orbit with period k consists of the set of k distinct ($\mathbf{x}_i \neq \mathbf{x}_j$ for $i \neq j$) points $\{\mathbf{x}_j = f^j(\mathbf{x}_0) | j = 0, 1, \ldots k-1\}$, with the k^{th} iterate of the map $f^k(\mathbf{x}_0) = \mathbf{x}_0$. Here f^j represents the composition of f with itself j times. The smallest positive value of k for which this equality holds is the period of the orbit.

Because of the simple *shift* nature of the dynamics of the doubling map (2.2), when the iterates are viewed in binary notation as in (2.3), it becomes easy to categorize the dynamics based on the initial condition. If the initial condition x_0 is irrational, then the dynamics are non-periodic meaning that they never repeat. This follows directly from the definition of irrational numbers as ones with non-repeating binary expansions. If the initial condition x_0 is rational however, its

image contains a finite number of distinct values within the unit interval and the forward orbit eventually becomes periodic, with period equal to the period of its binary expansion. More specifically, if the initial condition is a rational number with a finite binary expansion of say k bits, then after k iterations of the map, the iterates reach the fixed point at 0 and forever stay there. Similarly, if the initial condition x_0 is a rational number with a k-bit transient ($k \geq 0$) followed by an m-bit sequence ($m \geq 1$) that repeats itself infinitely, then after k iterations the iterates reach a periodic orbits of length m. This means that periods of all lengths are possible! Also, within any subinterval of $[0, 1]$, no matter how small, there is an infinite number of points whose orbits are eventually periodic, and an infinite number of points whose orbits are never periodic. Therefore, again using simple arguments in this simple setting of a one-dimensional map we have illustrated another generic and extremely important property of chaotic dynamical systems, a *dense*[1] set of periodic orbits.

It is important to note, however, that the periodic points in $[0, 1]$ form a *countably* infinite set, while the set of all points in $[0, 1]$ are *uncountable*. The former means that there exists a one-to-one correspondence with the natural numbers, while there isn't one for the later. In the same way, in higher dimensional chaotic dynamical systems almost all trajectories are aperiodic.

Nevertheless, stationary fixed points (e.g. $x_0 = 0$ in both maps considered above) and periodic orbits have turned out to be the key to unraveling the chaotic dynamics exhibited by complex systems. Here we note a few of the properties that make them so important and define some useful dynamical quantities. Firstly, periodic orbits are *topological invariants*. This means that a fixed point remains a fixed point for any continuous choice of coordinates, and similarly a periodic orbit remains periodic in any representation of the dynamics. Secondly, their stability eigenvalues (defined bellow) are *metric invariants*. This means that the stability eigenvalues of a periodic orbit remain invariant under any smooth (usually C^1) nonlinear change of coordinates.

[1] For example, every fraction with odd denominator is a periodic orbit.

The local stability of a periodic orbit can be calculated by studying the evolution around a small neighborhood of a periodic point. For a periodic orbit of period k, $f^k(x_0) = x_k = x_0$, and for one-dimensional maps this just equals

$$\begin{aligned}\Lambda_k = \frac{\mathrm{d}x_{n+k}}{\mathrm{d}x_n} &= \frac{\mathrm{d}x_{n+1}}{\mathrm{d}x_n}\frac{\mathrm{d}x_{n+2}}{\mathrm{d}x_{n+1}}\cdots\frac{\mathrm{d}x_{n+k}}{\mathrm{d}x_{n+k-1}}, \\ &= f'(x_n)f'(x_{n+1})\ldots f'(x_{n+k-1}),\end{aligned} \tag{2.5}$$

by the chain rule. If $|\Lambda_k| > 1$ the periodic orbit is said to be *unstable*. If $|\Lambda_k| < 1$ the periodic orbit is *stable*, while if $|\Lambda_k| = 1$ it is *marginal*. On non-periodic points, these considerations motivate the definition of a *local Lyapunov exponent*[2]

$$\begin{aligned}\lambda(x_0) &= \lim_{n\to\infty}\frac{1}{n}\ln\left|\prod_{i=0}^{n-1} f'(x_i)\right| \\ &= \lim_{n\to\infty}\frac{1}{n}\sum_{i=0}^{n-1}\ln\left|f'(x_i)\right|,\end{aligned} \tag{2.6}$$

characterizing the exponential separation of nearby trajectories.

Similarly, in d-dimensional systems each periodic orbit will have at most d stability eigenvalues describing the d expanding, contracting or neutral eigendirections of the flow. Consider for example the first-order, ordinary differential equation system $\frac{\mathrm{d}\mathbf{x}}{\mathrm{d}t} = \mathbf{F}(\mathbf{x})$ and an infinitesimal displacement from an initial condition $\mathbf{x}_0 \in M \subseteq \mathbb{R}^d$ in the direction of some tangent vector $\mathbf{y}_0 \in \mathbb{R}^d$ where the product $M \times \mathbb{R}^d$ is the $2d$-dimensional phase space $\mathcal{M}$ describing all possible states of the system. Then the time evolution of $\mathbf{y}$ is given by

$$\frac{\mathrm{d}\mathbf{y}}{\mathrm{d}t} = \mathbf{J}(\mathbf{x})\cdot\mathbf{y}, \tag{2.7}$$

where $\mathbf{J}(\mathbf{x})$ is the $d \times d$ Jacobian matrix of partial derivatives of $\mathbf{F}$ evaluated at the point $\mathbf{x}$. Note that equation (2.7) is only valid locally, for an infinitesimal neighborhood about $\mathbf{x}_0$. So the value of the vector $\mathbf{y}$ changes in time according to the values $\mathbf{J}$ takes on over time. Here $\mathbf{y}/|\mathbf{y}|$ gives the direction of the infinitesimal displacement from $\mathbf{x}_0$, where the bars $|\cdot|$ indicate absolute magnitude. Additionally, $|\mathbf{y}|/|\mathbf{y}_0|$ gives the factor by which the infinitesimal displacement grows

[2]This definition was proposed by A.M. Lyapunov in his Ph.D. thesis (1892).

or shrinks. Hence, assuming exponential separation of trajectories, the Lyapunov exponent is now defined as in (2.6) with respect to the initial condition $\mathbf{x}_0$ but also with respect to the initial orientation of the infinitesimal displacement $\mathbf{y}_0/|\mathbf{y}_0|$:

$$\lambda\left(\mathbf{x}_0, \frac{\mathbf{y}_0}{|\mathbf{y}_0|}\right) = \lim_{t\to\infty} \frac{1}{t} \int_0^t \ln \frac{|\mathbf{J}(\mathbf{x}_\tau)\cdot \mathbf{y}_\tau|}{|\mathbf{y}_0|} \mathrm{d}\tau. \tag{2.8}$$

The infinite time limit in (2.8) plays an important role as it indicates that the Lyapunov exponents represent time averaged quantities (meaning that any transient behavior has decayed). The existence of this limit is guaranteed by Oseledets's multiplicative ergodic theorem [96]. In addition, because of ergodicity time averages of functions are the same for almost all initial points and therefore the space average of $\mathbf{J}(\mathbf{x}_0)$ becomes a constant and Lyapunov exponents independent of $\mathbf{x}_0$. Hence, one often drops the dependence on the initial condition and such exponents are called *global Lyapunov exponents*. Finally, a point $\mathbf{x} \in M$ is called *hyperbolic* if Lyapunov exponents exist and none of them equals zero[3]. Equivalently, the dynamical system is said to be hyperbolic if almost every point $\mathbf{x} \in M$ is hyperbolic, and *uniformly hyperbolic* if all $\mathbf{x} \in M$ are hyperbolic.

Note that if the system is not ergodic, local exponents unlike the global ones are not invariant under a smooth nonlinear change of coordinates. Furthermore, we stress that in non-uniformly hyperbolic, points or regions of the phase space $\mathcal{M}$ may be locally marginally stable thus strongly affecting the local if not the global dynamics of the system. During the course of this chapter, and in fact throughout the whole of this thesis we shall be returning to this point again and again.

For the doubling map, all periodic orbits of period k have stability $\Lambda_k = 2^k$. Similarly for the tent map $|\Lambda_k| = 2^k$. In fact since $|f'(x_n)| > 1$ for all $x \in [0,1]$, then both maps are uniformly hyperbolic. Furthermore, if we partition $[0,1]$ into $N \gg 1$ equal bins, and iterate a randomly chosen initial condition (typically this will have irrational value and will hence be aperiodic) m times, then the fraction of time spent in each bin will approach $1/N$ as $m \to \infty$. This procedure defines the *equilibrium measure* $\rho(x)$, which for both tent and doubling maps is the uniform

[3]With the exception of the flow direction.

one ($\rho(x) = 1$) on $[0, 1]$.

2.1.1.3 Densities and measures

The function $\rho(x, m)$ is the density of representative points in phase space (here is just $[0, 1]$) at time step m and can be normalized $\int_0^1 \rho(x, m)\mathrm{d}x = 1$, with respect to the Lebesgue measure $\mathrm{d}x$. Also, the fact that no trajectory is created or destroyed by the action of an *area preserving map*[4] f implies conservation of representative points which can be expressed as $\int_I \rho(x_0, 0)\mathrm{d}x_0 = \int_{f^m(I)} \rho(x, m)\mathrm{d}x$, where $I \subseteq \mathcal{M}$ (here $\mathcal{M} = [0, 1]$) and $x_0 = f^{-m}(x)$. It is often easier to understand the evolution of densities in the language of operators as follows

$$\rho(x, m) = \mathcal{L}^m\rho(x) = \int_{\mathcal{M}} \mathcal{L}^m(x, x_0)\rho(x_0, 0)\mathrm{d}x_0 = \sum_{x_0 = f^{-m}(x)} \frac{\rho(x_0)}{|f^{m\prime}(x_0)|}. \tag{2.9}$$

The kernel of (2.9) $\mathcal{L}^m(x, y) = \delta(x - f^m(y))$ is known as the *Perron-Frobenius operator*[5] and can also be though of as a transfer matrix acting on partitions of the phase space for which f is linear. What it does is it assembles the density $\rho(x, m)$ at time m by going back in time to the density $\rho(x_0, 0)$ at time $m = 0$. The equilibrium or invariant density is hence defined by a density function which is left unchanged by the dynamics [6] (i.e. when $\rho(x, m) = \mathcal{L}^m\rho(x) = \rho(x)$ for all m).

Chaos in one-dimensional systems is not restricted to piecewise linear maps. A classic example is the *logistic map*

$$x_{n+1} = f_L(x_n) = 4x_n(1 - x_n), \quad \text{for } x_n \in [0, 1] \tag{2.10}$$

as shown in Figure 2.3. In fact this map is topologically conjugate to the tent map. To see this just substitute $x_n = \sin^2\left(\frac{\pi y_n}{2}\right)$ into (2.10). Therefore, since the tent map is uniformly hyperbolic, so is the logistic map. Furthermore, since $\rho(x)\mathrm{d}x = \tilde{\rho}(y)\mathrm{d}y$ due to the change of variables, then the equilibrium invariant

[4] For 1-dimensional chaotic maps (non-invertible) one considers the pre-image of the map.

[5] In d-dimensions, the denominator in the sum of (2.9) is replaced by $|\det\mathbf{J}^m(\mathbf{x}_0)|$.

[6] In general, there may be no, one, or many possible invariant densities.

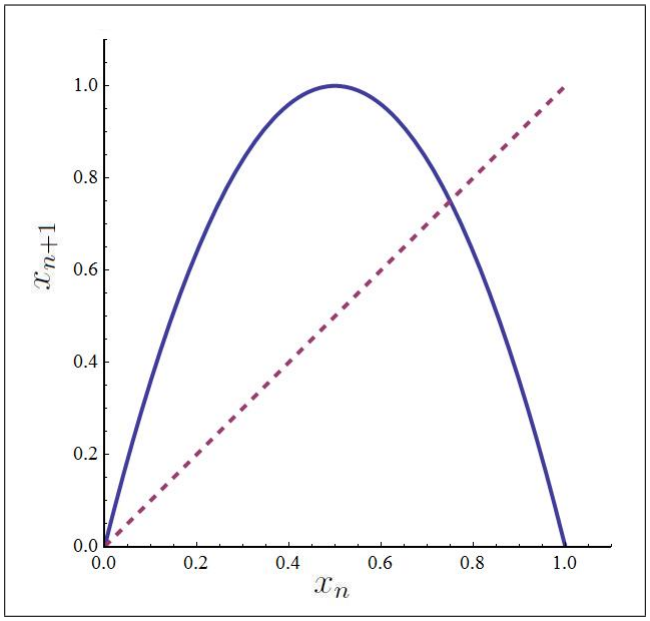

Figure 2.3: The logistic map.

measure is

$$\rho(x) = \frac{\mathrm{d}}{\mathrm{d}x}\left(\frac{2}{\pi}\arcsin\sqrt{x}\right) = \frac{1}{\pi\sqrt{x(1-x)}}. \tag{2.11}$$

2.1.2 Escape in 1-D

2.1.2.1 Fractality in Transient Chaos

Consider the *linearly perturbed* doubling map which allows for the possibility of escape from $[0,1]$ [97]

$$x_{n+1} = g(x_n) = \begin{cases} x_n/p_0, & \text{for } 0 \le x_n < \frac{1}{2}, \\ 1 + (x_n - 1)/p_1, & \text{for } \frac{1}{2} \le x_n \le 1, \end{cases} \tag{2.12}$$

where $p_0, p_1 < \frac{1}{2}$, and $p_0 + p_1 < 1$ as shown in Figure 2.4. At each iterate of the map, points between p_0 and $1 - p_1$ escape from the unit interval $[0,1]$. The points that remain in $[0,1]$ after the first application of (2.12) form two intervals of lengths p_0 and p_1 respectively (see Figure 2.4). Moreover, the points that remain inside the system after the second application of (2.12) fall into four non overlapping intervals with lengths p_0^2, p_0p_1 and p_1^2 respectively. It is clear that the

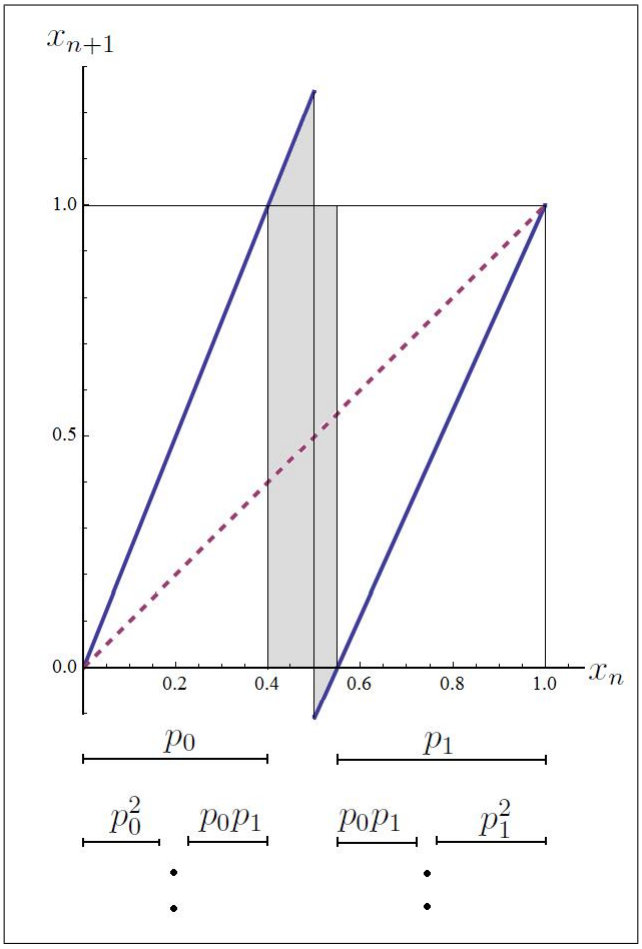

Figure 2.4: A linear expanding map with escape from the unit interval with $p_0 = 0.4$ and $p_1 = 0.45$. The first two steps in the construction of the fractal repeller are also shown.

total measure (length of the intervals) of the surviving points after one iteration is $l_1 = (p_0 + p_1)$. Similarly we can see that the measure of points which survive n iterations of (2.12) is $l_n = (p_0 + p_1)^n \to 0$ as $n \to \infty$. Therefore, the density of points in $[0, 1]$, or in other words the *Survival probability* is decaying exponentially as

$$l_n = e^{n \ln(p_0+p_1)} \equiv e^{-n\gamma}, \tag{2.13}$$

where γ is the *escape rate* given by

$$\gamma = \ln \frac{1}{p_0 + p_1} \sim 1 - (p_0 + p_1). \tag{2.14}$$

Such exponentials are the mathematical signature of strong chaotic properties as seen for example in the divergence of nearby initial conditions, in the decay of

correlations, and in the convergence to equilibrium distributions.

Iterating the above map (2.12) infinitely many times, we see that the set of initial points which never escape the unit interval forms a *fractal* Cantor set. This set is also called the *repeller*, because all other points, no matter how close they are to it, will eventually leave the unit interval. In fact, if $p_0 = p_1 = 1/3$ then the repeller is the original *middle-third* Cantor set.

This should not come as a surprise. The rigid skeleton composed of a self-similar tree of periodic orbits is what supports the repeller. Hence, if the dynamics of a system is chaotic then the repeller will inherit a fractal (non-integer) dimension[7]. Moreover, this generic self-similarity allows for an efficient calculation of dynamical quantities as done for example above for (2.13) and will be a key ingredient in our calculations in chapter 3.

2.1.2.2 Size and Location of holes

We have already seen that the natural invariant density is the uniform one for both tent and doubling maps. We have also seen that the escape rate $\gamma \sim (1-p_0-p_1)$ is proportional to the size of the escaping region which from now on will be denoted as the *hole*. These two observations are more or less expected, especially the second one. The bigger the hole, the faster the escape. How does the position of the hole affect the escape rate? To address this question consider the partition $I_n = \{I_{n,i}\}_{i=1}^{2^n}$ obtained by the pre-images of the elements of the natural Markov partition $\{[0, 0.5], [0.5, 1]\}$ of $[0, 1]$ of the symmetric tent or doubling map. Then let the ith sub-interval

$$I_{n,i} = \left[\frac{i-1}{2^n}, \frac{i}{2^n}\right], \tag{2.15}$$

be regarded as an artificial *Markov hole* through which orbits can escape through. We now have 2^n artificially opened, different dynamical systems for each map f_T

[7]The fractal dimension characterizes the local scaling properties of the dynamics (see Ref [98] for further details).

and f_D for which we can calculate and compare escape rates as functions of hole positions.

Due to our constructions of piecewise linear expanding maps and natural partition of the unit interval, the escape rate can be directly obtained by considering the $[2^n \times 2^n]$ transfer matrix[8] corresponding to the inverse application of the respective open dynamical system onto a uniform density of points shared by the 2^n sub-intervals of our partition. For example, for the tent map with a hole at $I_{3,5}$ ($i = 5$ and $n = 3$) we construct the matrix

$$T = \begin{pmatrix} \frac{1}{2} & 0 & 0 & 0 & 0 & 0 & 0 & \frac{1}{2} \\ \frac{1}{2} & 0 & 0 & 0 & 0 & 0 & 0 & \frac{1}{2} \\ 0 & \frac{1}{2} & 0 & 0 & 0 & 0 & \frac{1}{2} & 0 \\ 0 & \frac{1}{2} & 0 & 0 & 0 & 0 & \frac{1}{2} & 0 \\ 0 & 0 & 0 & 0 & 0 & 0 & 0 & 0 \\ 0 & 0 & \frac{1}{2} & 0 & 0 & \frac{1}{2} & 0 & 0 \\ 0 & 0 & 0 & \frac{1}{2} & \frac{1}{2} & 0 & 0 & 0 \\ 0 & 0 & 0 & \frac{1}{2} & \frac{1}{2} & 0 & 0 & 0 \end{pmatrix}, \tag{2.16}$$

while for the doubling map with $I_{3,2}$

$$D = \begin{pmatrix} \frac{1}{2} & 0 & 0 & 0 & \frac{1}{2} & 0 & 0 & 0 \\ 0 & 0 & 0 & 0 & 0 & 0 & 0 & 0 \\ 0 & \frac{1}{2} & 0 & 0 & 0 & \frac{1}{2} & 0 & 0 \\ 0 & \frac{1}{2} & 0 & 0 & 0 & \frac{1}{2} & 0 & 0 \\ 0 & 0 & \frac{1}{2} & 0 & 0 & 0 & \frac{1}{2} & 0 \\ 0 & 0 & \frac{1}{2} & 0 & 0 & 0 & \frac{1}{2} & 0 \\ 0 & 0 & 0 & \frac{1}{2} & 0 & 0 & 0 & \frac{1}{2} \\ 0 & 0 & 0 & \frac{1}{2} & 0 & 0 & 0 & \frac{1}{2} \end{pmatrix}. \tag{2.17}$$

Because the transfer matrices and of course the Perron-Frobenius operator $\mathcal{L}$ act multiplicatively in time, we can obtain the escape rate directly from the dominant

[8] As a consequence of the piecewise linearity of f_T and f_D this corresponds to the inverse of the Perron-Frobenius operator $\mathcal{L}^{-1}$.

eigenvalue ν_j of each transfer matrix $j = T, D$, by

$$\gamma_j = -\ln \nu_j. \tag{2.18}$$

ν_j is the measure of the surviving set at each time step. These are plotted in Figure 2.5 for the cases of $n = 4$ and 5 for holes I_n, i at $i = 1, 2, \ldots 2^n$.

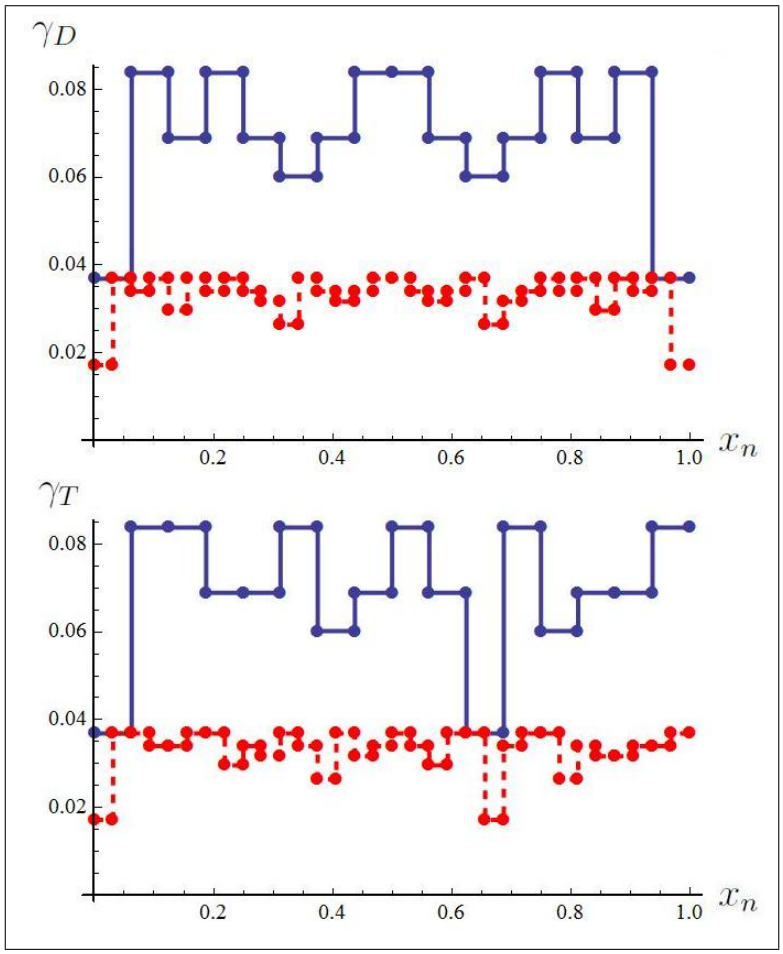

Figure 2.5: Escape rates γ_D and γ_T as functions of position for holes of size 2^{-n} for $n = 4$ (blue,solid) and $n = 5$ (red, dashed), for the doubling (top) and tent (bottom) maps with $p_0 = 2$.

We therefore see that even for strongly chaotic, uniformly hyperbolic systems such as (2.1), (2.2) and of course (2.10), the escape rate depends strongly on the position of the hole. Could it be possible that this dependence on position dominates that on the hole's size? In other words, for a uniformly chaotic system, can a smaller hole produce a faster escape than a larger one? The answer to this question is *yes* and was proven by Bunimovich and Yurchenko in Ref [1]

by considering combinatorics on words. They prove that for systems which are conjugate to the full binary shift, the faster escape occurs through the hole whose pre-images overlap less. Equivalently, escape will always be faster through the hole whose minimal periodic orbit is longer. Furthermore, they show that the escape rate γ_j has the following first order expansion as the size of the hole $\varepsilon = I_{n,i} \to 0$

$$\gamma_j = \varepsilon(1 - 2^{-p}) + o(\varepsilon) \tag{2.19}$$

where $j = T, D$, and $p \in \mathbb{N}^+$ is the period of the point where the hole is centered upon. Little-o notation implies that $f(x) = o(g(x))$ is equivalent to $\lim_{x\to\infty} f(x)/g(x) = 0$.

An important and new feature of the above results, is that they hold for all *finite* times starting with some moment of time (the largest of the two minimal periods), in comparison to the usual setup in the theory of dynamical systems where one deals with the asymptotic global or local properties at infinite times.

Given the above constructions (2.16) and (2.17), we can now also consider skewed linear expanding maps such as

$$x_{n+1} = \tilde{f_T}(x_n) = \begin{cases} p_0 x_n, & \text{for } 0 \le x_n < \frac{1}{p_0}, \\ p_1(1-x)n, & \text{for } \frac{1}{p_0} \le x_n \le 1, \end{cases} \tag{2.20}$$

and

$$x_{n+1} = \tilde{f_D}(x_n) = \begin{cases} p_0 x_n, & \text{for } 0 \le x_n < \frac{1}{p_0}, \\ p_1(x_n - 1/p_0), & \text{for } \frac{1}{p_0} \le x_n \le 1, \end{cases} \tag{2.21}$$

where $p_0 > 1$ and $p_1 = \frac{p_0}{p_0 - 1}$, with sub intervals obtained by the pre-images of the elements of the natural Markov partition $\{[0, \frac{1}{p_0}], [\frac{1}{p_0}, 1]\}$. The corresponding

inverse matrices with holes at $I_{3,3}$ now become

$$\tilde{T} = \begin{pmatrix} \frac{1}{p_0} & 0 & 0 & 0 & 0 & 0 & 0 & \frac{1}{p_1} \\ \frac{1}{p_0} & 0 & 0 & 0 & 0 & 0 & 0 & \frac{1}{p_1} \\ 0 & 0 & 0 & 0 & 0 & 0 & 0 & 0 \\ 0 & \frac{1}{p_0} & 0 & 0 & 0 & 0 & \frac{1}{p_1} & 0 \\ 0 & 0 & \frac{1}{p_0} & 0 & 0 & \frac{1}{p_1} & 0 & 0 \\ 0 & 0 & \frac{1}{p_0} & 0 & 0 & \frac{1}{p_1} & 0 & 0 \\ 0 & 0 & 0 & \frac{1}{p_0} & \frac{1}{p_1} & 0 & 0 & 0 \\ 0 & 0 & 0 & \frac{1}{p_0} & \frac{1}{p_1} & 0 & 0 & 0 \end{pmatrix}, \tag{2.22}$$

and

$$\tilde{D} = \begin{pmatrix} \frac{1}{p_0} & 0 & 0 & 0 & \frac{1}{p_1} & 0 & 0 & 0 \\ \frac{1}{p_0} & 0 & 0 & 0 & \frac{1}{p_1} & 0 & 0 & 0 \\ 0 & 0 & 0 & 0 & 0 & 0 & 0 & 0 \\ 0 & \frac{1}{p_0} & 0 & 0 & 0 & \frac{1}{p_1} & 0 & 0 \\ 0 & 0 & \frac{1}{p_0} & 0 & 0 & 0 & \frac{1}{p_1} & 0 \\ 0 & 0 & \frac{1}{p_0} & 0 & 0 & 0 & \frac{1}{p_1} & 0 \\ 0 & 0 & 0 & \frac{1}{p_0} & 0 & 0 & 0 & \frac{1}{p_1} \\ 0 & 0 & 0 & \frac{1}{p_0} & 0 & 0 & 0 & \frac{1}{p_1} \end{pmatrix}. \tag{2.23}$$

The corresponding escape rates $\tilde{\gamma_j}$ have the following expansion as the hole size $\varepsilon \to 0$

$$\tilde{\gamma_j} = \varepsilon\Big(1 - \Big(\prod_{i=0}^{p-1} |\tilde{f_j}'\left(\tilde{f_j}^i(x_0)\right)|\Big)^{-1}\Big) + o(\varepsilon), \tag{2.24}$$

for $j = T, D$, where $\tilde{f_j}'\left(\tilde{f_j}^i(x_0)\right)$ is the derivative of the function $\tilde{f}_j$ evaluated at each point $\tilde{f_j}^i(x_0)$ along the periodic orbit of period p, starting at the center of the hole x_0. It is clear that if the point x_0 is not periodic $p \to \infty$ and the product in (2.24) vanishes and $\tilde{\gamma_j} = \gamma_j = 1 - \varepsilon + o(\varepsilon)$ as in (2.14). The escape rates $\tilde{\gamma_j}$ are plotted in Figure 2.6 for the case of $n = 4$ and 5. Notice that the Markov holes now have variable sizes yet escape through smaller holes can still be faster! Similarly, completely overlapping holes of different sizes can have the same escape

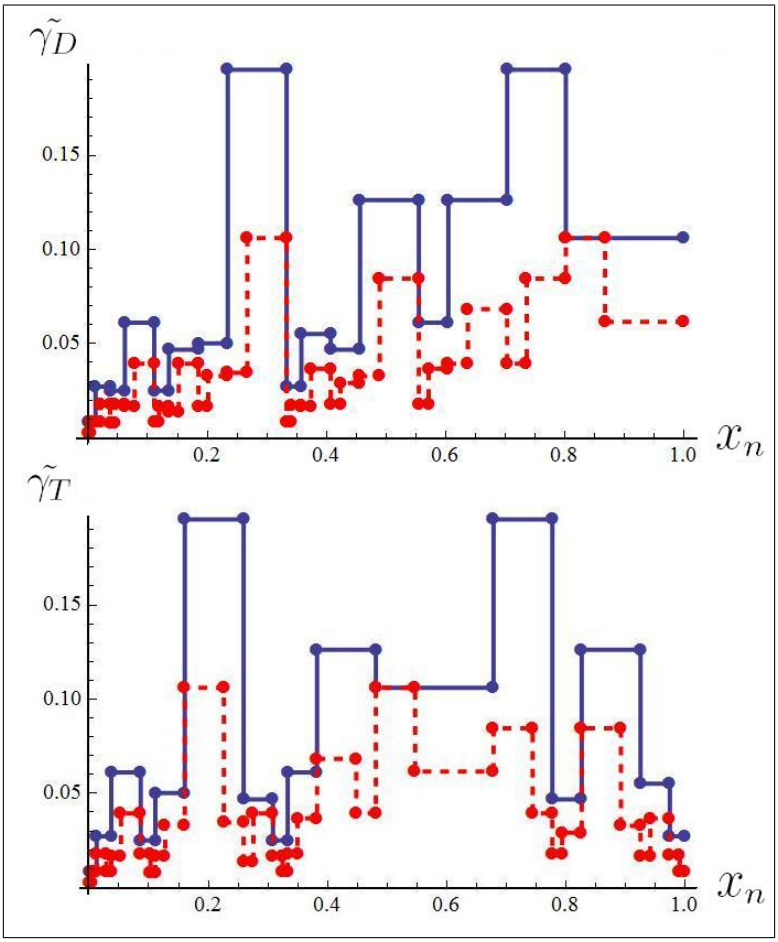

Figure 2.6: Escape rates $\tilde{\gamma_D}$ and $\tilde{\gamma_T}$ as functions of position for Markov holes of different sizes for $n = 4$ (blue,solid) and $n = 5$ (red, dashed), for the skewed doubling (top) and tent (bottom) maps with $p_0 = 3$.

rate. Hence we conclude this sub-section by noting that for dynamical systems conjugate to the full binary shift, escape will always be faster through the hole whose least unstable periodic orbit is most unstable [99].

2.1.3 Intermittency in 1-D

Not all dynamical systems decay exponentially. In fluid dynamics for example, it is often the case that long periods of regular dynamics (laminar phases) are *intermittently* interrupted by short irregular *chaotic bursts* [94]. This effect, as we shall see, is typically due to non-hyperbolic and marginally stable regions in phase space. Furthermore, the distribution of these laminar phase intervals is found

to be well described by asymptotic power law distributions. This phenomenon is called *intermittency* [100, 101], and it is a very general aspect of dynamical systems. In fact, uniform hyperbolicity as in the examples considered in the previous subsections is more the exception rather than the rule, especially when working in higher dimensional settings. Generic dynamical systems exhibit mixed phase space, where *KAM islands* of stability coexist with hyperbolic regions often called (chaotic) *seas*. Although the dynamics in hyperbolic regions is mixing exponentially fast, trajectories which come close to marginally stable regions tend to *stick* there for arbitrarily long times before being re-injected back into the 'deep' hyperbolic regions of a chaotic sea. This type of intermittent behavior is what effectively determines the main dynamical properties of the system under investigation (e.g. transport and decay of correlations).

The simplest way to illustrate intermittency is through an *intermittency transition* example in a one dimensional map. The control parameter of the map, p is increased past some critical value p_c. The dynamics before and after the transition are summarized in Figure 2.7. When $p = p_c$ the stable and unstable fixed points

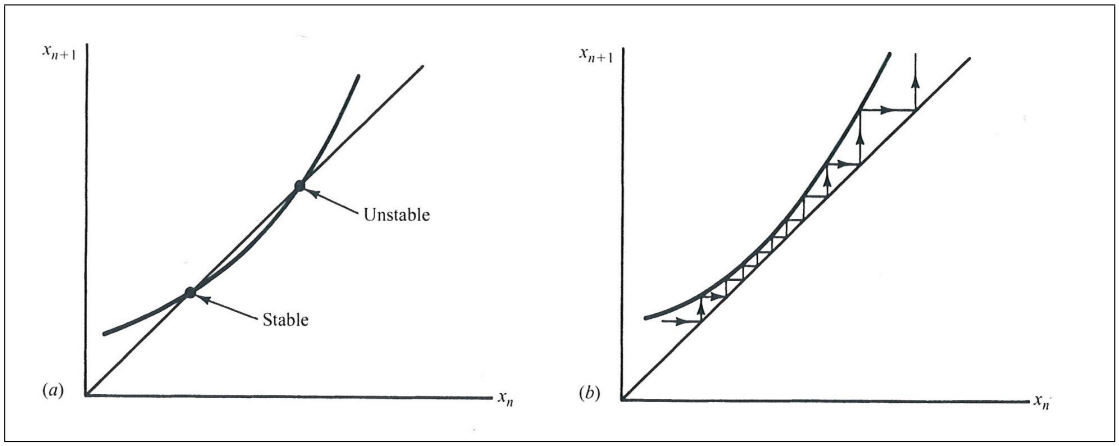

Figure 2.7: Figure reproduced from [88] (page 314). One-dimensional map for (a) $p < p_c$ and (b) $p > p_c$ where p is some control parameter of the map and p_c is some critical value at which a saddle-node bifurcation occurs. The map is only plotted on the local vicinity of the stable ($p < p_c$) orbit.

collide and annihilate each other via a saddle-node bifurcation[9]. When $p > p_c$ the orbit takes a large number of iterations to traverse the length of the narrow tunnel between the map function and the 45° line. During this time, the dynamics is said to be quasi-periodic (approximately periodic). After traversing the tunnel, the orbit is subjected to strong hyperbolic dynamics (stretching and folding) determined by the specific form of the map away from the tunnel's vicinity and is then randomly re-injected into the tunnel again. The average time between these chaotic bursts is found to be well approximated by power law distributions.

Consider the simple example of a *non-linearly perturbed* doubling map, described by

$$x_{n+1} = \breve{f}_D(x_n) = \begin{cases} x_n(1 + p(2x_n)^s), & \text{for } 0 \leq x_n < \xi, \\ 2x_n - 1, & \text{for } \frac{1}{2} \leq x_n \leq 1, \end{cases} \tag{2.25}$$

and shown in Figure 2.8 for $p = 1.2$ and $s = 1$. The map is no longer uniformly hyperbolic and exhibits intermittency for $s > 0$ due to the marginally stable fixed point at the origin. It also allows for escape from $[0, 1]$ if $p > 1$.

In general, the presence of marginally stable fixed points changes the analytic structure of dynamical zeta functions[10] [102] as well as the rules for constructing cycle expansions. The marginal orbits have to be omitted, and the cycle expansions need to include the infinity of families of longer and longer unstable orbits which accumulate close to the marginally stable one. This was first performed using a resummation procedure of stability ordered cycle expansions of the dynamical zeta function for (2.25) in [103]. An initial exponential decay of the survival probability p_n was predicted to be followed by an algebraic tail of order $\sim \frac{1}{n^{1+1/s}}$ and was then confirmed numerically as shown in Figure 2.9.

As for the invariant density $\rho(x)$, we can get a quick impression of how it

[9]This is a Type-I intermittency. Pomeau and Manneville [101] introduced three different types of intermittency, using a classification that reflects the types of local bifurcation by which a periodic orbit can lose its stability.

[10]The dynamical zeta function is a prototype formula of periodic orbit theory, the zeros of which give the asymptotic escape rate.

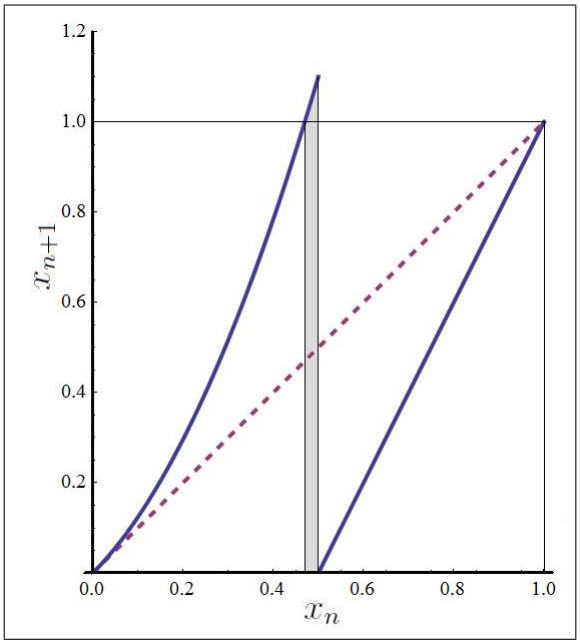

Figure 2.8: The intermittent map $\breve{f}_D$ with escape from the unit interval with $p = 1.2$ and $s = 1$.

differs from the uniform one, as we increase the perturbation strength s of the closed system $p = 1$ through a 'naive' numerical simulation shown in Figure 2.10. This is a naive approach because $\rho(x)$ is expected to have a singularity at $x = 0$ for $s > 0$ due to the marginally stable fixed point at the origin. Hence the invariant density will have a very slowly convergence to the true invariant density (if it exists). In this case however, following an argument along the lines of (2.11) we can show that $\rho(y) = \frac{\rho(x)}{f'(x)} \sim x^{-s}$.

2.1.4 Chaos, Intermittency and Escape in 2-D

Up till now we have very briefly introduced the concepts of chaos, escape and intermittency in the context of one dimensional maps. We now increase the dimension by one and see how these concepts translate into the context of more physical systems such as the very well studied *standard map* [104].

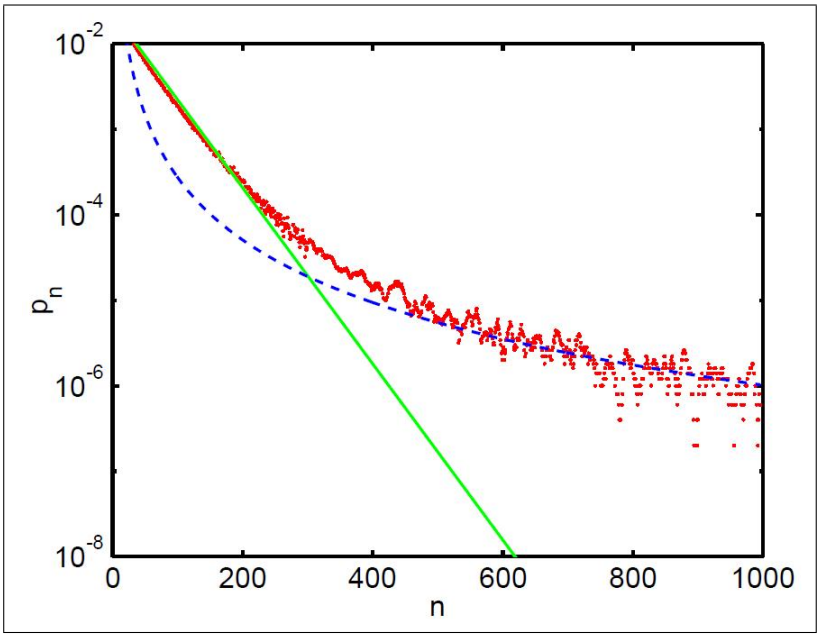

Figure 2.9: Figure reproduced from [95]. Distribution of escape times obtained from simulation (shaky red curve) and the pre exponential (full green line) and the asymptotic power law (dashed blue line) obtained from re-summation.

2.1.4.1 The standard map

The standard map (also called Chirikov - Taylor map) is a two dimensional area-preserving map with variables q and p, often considered as the position and momentum coordinates of the time dependent Hamiltonian:

$$H(q,p,t) = \frac{p^2}{2} + K\delta_1(t)\cos q, \tag{2.26}$$

where $\delta_1(t)$ is a periodic delta function with period one in time t, and both x and p are taken modulo 2π. The dynamics of this Hamiltonian systems is given by a sequence of free propagations on the torus $[2\pi] \times [2\pi]$, interleaved with periodic kicks of strength $|K\cos q|$. By integrating Hamilton's equations

$$-\frac{\partial H}{\partial q} = \dot{p} = K\sin(q)\delta_1(t), \qquad \frac{\partial H}{\partial p} = \dot{q} = p, \tag{2.27}$$

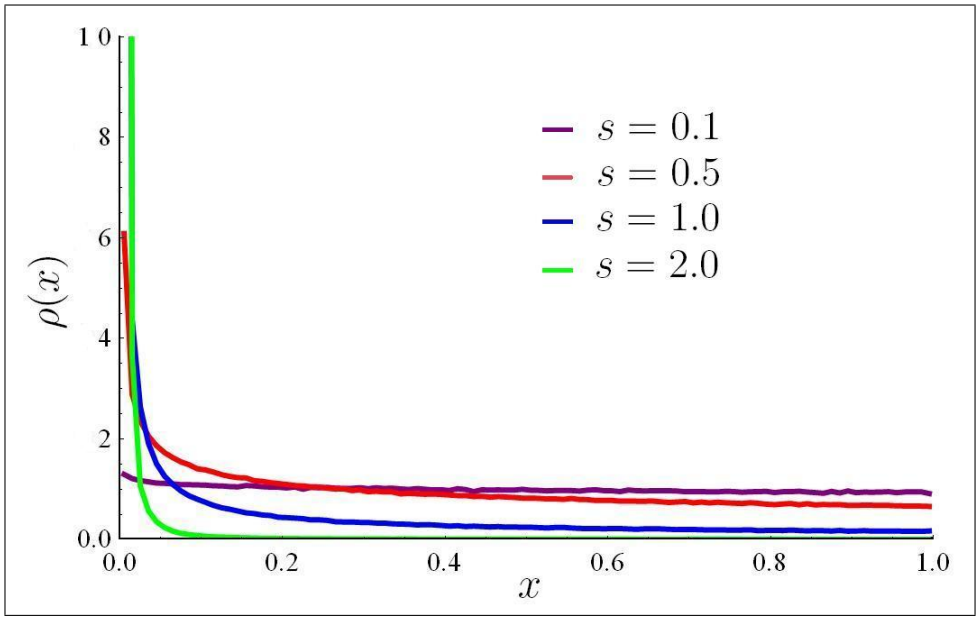

Figure 2.10: Invariant density $\rho(x)$ for the closed ($p = 1$) map (2.25), for different perturbation strengths s.

we obtain a sequence of 'snap-shots' of the state of the system's dynamics. These are described by the equations:

$$\begin{aligned} p_{n+1} &= p_n + K \sin q_n, \\ q_{n+1} &= q_n + p_{n+1}, \end{aligned} \tag{2.28}$$

which effectively define a *Poincaré map* of the system which in turn produces the 2 dimensional *phase space* $\mathcal{M}$, where all possible states $(q, p) \in \mathcal{M}$ of (2.26) can be represented. The panels in Figure 2.11 show the phase space of 50 randomly chosen initial conditions iterated and followed for 10^4 time steps by (2.28) for different values of the kicking strength K.

For $K = 0$ the map is linear and clearly only periodic and quasi-periodic orbits are possible. Periodic orbits appear in the top left panel of Figure 2.11 as dots, and quasi-periodic orbits as dashed lines which appear as closed lines. Which type of orbit is observed depends on whether the initial condition q_0 is a rational multiple of 2π in a similar way as for the doubling and tent maps considered in the previous subsections.

The non-linearity of the map increases with kicking strength K. This causes

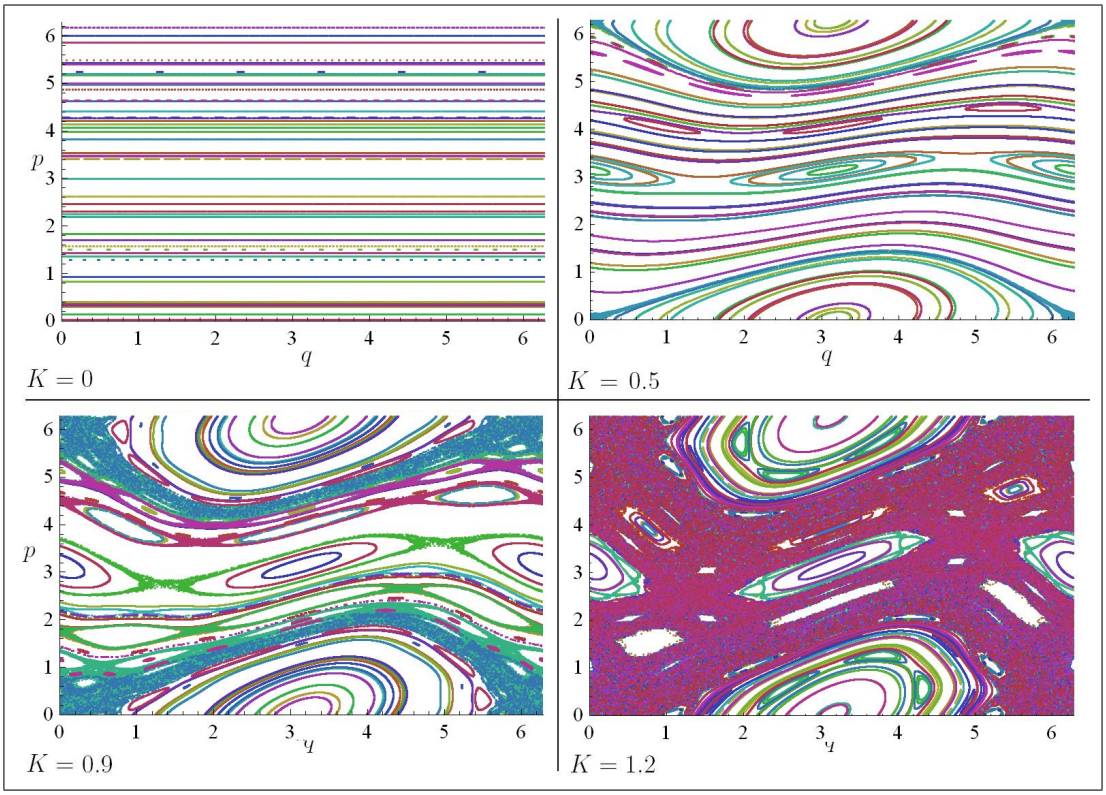

Figure 2.11: Phase space picture of the standard map showing 50 randomly chosen initial conditions iterated and followed 10^4 times for different values of $K = \{0, 0.5, 0.9, 1.2\}$. Each trajectory is shown in a different color.

periodic orbits to bifurcate and become unstable, allowing for the possibility to observe *chaotic dynamics* due to the existence of *horseshoes* [105] (stretching and folding mechanism of chaos) for appropriate initial conditions. We note that stable (elliptic) points are circulated by quasi-periodic trajectories forming the so called *KAM islands of stability*. Phase space is thus shared between periodic, quasi-periodic and chaotic trajectories with the last two occupying a positive measure of the phase space $\mathcal{M}$. Therefore the standard map with $K > 0$ is said to have a *mixed phase space*. As K is increased, more and more KAM elliptic islands of stability are 'absorbed' by the expanding chaotic sea. For $K > K_c \approx 0.984375$ the golden KAM curve is destroyed [106] and p becomes unbounded allowing chaotic initial conditions to attain all possible values in $[0, 2\pi]$ as shown in Figure 2.12 for a single chaotic initial condition for K just above and bellow K_c.

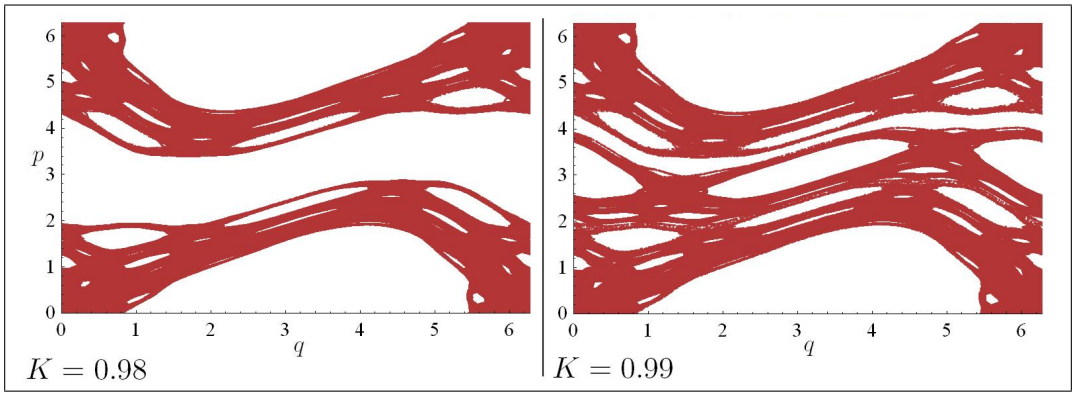

Figure 2.12: A single chaotic initial condition iterated 10^9 times for $K = 0.98 < K_c$ (*Left*) and $K = 0.99 > K_c$ (*Right*).

2.1.4.2 A universal paradigm of chaotic maps

A very important feature of the standard map, although not immediately apparent from the figures above, is that even for larger values of K, there are an infinite number of diminishingly small KAM islands forming a *hierarchical* fractal structure around each other. As a result, chaotic orbits approaching one of these islands become trapped and are forced to behave in an almost periodic fashion for long periods of time thus causing the overall dynamics of the system to be *intermittent*! This intermittency is usually quantified through the power law decay of the Poincaré recurrence distribution. A further important point to be made is that the hierarchical structure surrounding elliptic fixed points 'embedded' in chaotic components of the phase space $\mathcal{E} \subset \mathcal{M}$ is in fact generic as various dynamical systems can be locally reduced to it via some nonlinear change of coordinates. This property, when contrasted with our remarks about the topological invariance of periodic orbits in section 2.1.1. makes the standard map a *universal* paradigm model of generic area-preserving maps, which in turn also confirms and emphasizes the generality and importance of intermittency in dynamical systems.

2.1.4.3 Poincaré recurrence: A measure of Intermittency

We now define the *Poincaré recurrence time distribution* for the standard map. Consider a region $I \subset \mathcal{E}$ of positive normalized measure $\mu(I) = \int_I \mathrm{d}\mu / \int_{\mathcal{E}} \mathrm{d}\mu$, well inside the chaotic component of the phase space $\mathcal{E} \subset \mathcal{M}$ and compute the trajectory of a randomly chosen initial condition $(q_0, p_0) \in I$ produced by iterating (2.28) m times. The initial condition will soon exit I and according to the Poincaré recurrence theorem [97], will return to it infinitely many times as $m \to \infty$. This produces a sequence of recurrence times $\{t_1, t_2 \ldots, t_{N(m)}\} \in \mathbb{N}^N$ corresponding to the time spent outside of I between each exit and entry, where $N(m) \leq m/2$ is monotonically increasing with m. The Poincaré recurrence time distribution $\mathcal{R}(t)$ is the distribution of this sequence and was originally proposed by Chirikov and Shepelyansky [107] as a useful statistic of the entire dynamics of (2.28).

Following our discussions for one-dimensional maps, if a system is strongly chaotic the dynamics resembles that of a random process and the probability p of a trajectory to enter I is thus $p \approx \mu(I)$. Therefore, the probability of entering I after t (t is assumed to be large) iterations is approximately given by the binomial distribution

$$\mathcal{R}(t) = p(1-p)^{t-1} = \frac{p}{1-p} e^{t \ln(1-p)}, \tag{2.29}$$

which for a small recurrence region I ($p \ll 1$) is known to be well approximated by the Poisson distribution

$$\mathcal{R}(t) \approx p e^{-pt}. \tag{2.30}$$

This in turn gives Kac's famous Lemma [108] for the expectation value of t

$$\mathbb{E}(t) = \lim_{N \to \infty} \frac{1}{N} \sum_{i=1}^{N} t_i = \sum_{t=1}^{\infty} t\mathcal{R}(t) = \frac{1}{p} \approx \frac{1}{\mu(I)}, \tag{2.31}$$

which also implies that the probability of finding a trajectory in I is equal to $1/\mathbb{E}(t)$. However, as discussed in section 2.1.2, the stability of periodic orbits intersecting I causes deviations from the distribution of $\mathcal{R}(t)$ (2.30).

The standard map and therefore other generic dynamical systems are not strongly chaotic systems but rather intermittent ones. We therefore intuitively expect that 'sticky' trajectories which approach KAM islands will in general have longer return times t_i due to a large number of *consecutive* time periods spent near regions of stability. Thus $\mathcal{R}(t) \sim t^{-\alpha}$, where $\alpha > 2$ due to (2.31) [109].

It is often numerically more convenient to calculate the distribution of recurrence times greater than some τ. This is called the recurrence time statistics (RTS) and is given by

$$\mathcal{Q}(\tau) = \sum_{t=\tau}^{\infty} \mathcal{R}(t) = \lim_{N\to\infty} \frac{N_\tau}{N}, \tag{2.32}$$

due to ergodicity, where N_τ is the number of recurrences with time $t \geq \tau$. This implies that $\mathcal{Q}(\tau) \sim \tau^{-\alpha+1}$. However, a numerical calculation of α for the standard map, is as before (see Figure 2.10) 'naively' inaccurate due to the sensitive dependence on initial conditions, the uncertainty (due to round-off errors) in the value of K, computational rounding errors and also the fact that the t_is are unbounded. Overall this causes $\mathcal{Q}(t)$ and $\mathcal{R}(t)$ to exhibit 'wild' oscillations. Not all is doomed however. Recent work by Cristadoro and Ketzmerick [110] based on a stochastic Markov tree model and also some convincing numerical simulations by Altmann [11] [111] provide supporting evidence of a universal exponent of $\alpha \approx 2.57$ for mixed phase space systems with a hierarchical structure. Furthermore, the power-law exponent α is found to be independent of the choice of the recurrence region I and of the initial density $\rho(x)$ provided that $I \subset \mathcal{E}$ [35].

Similarly with the one-dimensional case described in section 2.1.3 for map (2.25), the power-law behavior observed numerically in the standard map (2.28) due to stickiness and non-uniform hyperbolicity is apparent in both recurrence time and survival probability $P(t)$ distributions. The latter describes the probability of a randomly chosen chaotic initial condition $x_0 \in \mathcal{E}$ not to have escaped through some preselected region in phase space called the hole $h \subset \mathcal{E}$, where

[11] This was achieved by considering many different realizations of a noise-perturbed standard map.

$\mu(h) \ll 1$ up to some time t. This scenario is typical in transient chaos problems. The asymptotic power law decay of the survival probability function $P(t)$ is thus of order $\sim t^{-\alpha+2}$ (see also the Appendix of Ref [112]). Similarly in scattering problems, where one considers an initial distribution concentrated on the hole, the exponent of $P(t)$ is of order $\sim t^{-\alpha+1}$. This connection was originally studied by Pikovsky [89]. One should note that when dealing with continuous time (i.e. the dynamics of the flow) rather than with discrete map iterations, all of the above quantities are defined in terms of integrals and infinitesimal time steps.

Résumé

Through the study of one and two dimensional maps, mathematicians have managed to isolate and study many of the fundamental dynamical properties of chaos in physical systems. These have formed the building blocks of a growing and successful theory of Dynamical systems which we have attempted to summarize in this short introductory subsection. The key points and ideas presented were those of *chaos*, *intermittency* and *escape*. Optimization problems such as where to place the hole were discussed in parallel with the important role played by periodic orbits and their stabilities. Also, *universality* in generic dynamical systems was discussed through the paradigm model of the standard map which also facilitated for the demonstration and explanation of the phase space. Finally, recurrence time and survival probability distributions were argued to offer 'good' statistical observables which are tractable both numerically and analytically. Overall, this brief introduction has hopefully set the stage for the beautiful mathematical theory of open billiards which we discuss next.

2.2 Escape from Billiards

In this section, we shall give some basic definitions and constructions in order to introduce the beautiful dynamics generated by billiards. We shall briefly categorize classical billiard dynamics into three groups and also give simple intuitive

and graphical[12] explanations of how these come about. A nice introduction to the subject of (closed) billiards can be found in Ref [5] with more mathematical details on chaotic billiards in Ref [6]. Finally we introduce open billiards and the different escape rates and patterns observed and compare with the dynamics of the corresponding closed systems. For a more detailed review of open billiards and open problems see Ref [36].

2.2.1 Billiard Dynamics: Some basic definitions

2.2.1.1 The billiard flow and the billiard map

We shall only consider billiards on finite domains. Therefore we let $Q \subset \mathbb{R}^2$ denote an open but *bounded* domain with piecewise C^2 oriented boundary ∂Q. The billiard's dynamics is generated by a point-like particle (of unit mass) moving along straight lines inside Q and experiencing specular reflections (angle of incidence equals angle of reflection) off the billiard boundary ∂Q. At each time instant, the state of the system is determined by the particle's position $q \in Q$ and momentum $p \in S^1$ (it is common to consider the motion with unit speed such that $|p| = 1$). We let $n(q)$ be the unit normal vector to ∂Q at point $q \in \partial Q$ pointing to the interior of the billiard. At the instant that the particle reaches ∂Q, its direction changes such that $p' = p - 2(p, n(q))n(q)$, where $(\cdot, \cdot)$ is the inner product and p' is the particle's new velocity unit vector. The phase space $\mathcal{M}$ of the *billiard flow* $\Psi^t : \mathcal{M} \to \mathcal{M}$ is given by the quotient of $Q \times S^1$ by the identification $(q, p) = (q, p')$. This means that a billiard is a Hamiltonian system with a four dimensional phase space[13] $\mathbf{x} = (q_1, q_2, p_1, p_2)$, with potential $V(q) = 0$ for $q \in Q$ and $V(q) = \infty$ for $q \in \partial Q$.

Billiards have their boundaries as a natural Poincaré surface of section. Therefore a natural projection of $\mathcal{M}$ onto its boundary is $M = \{(q, p) : q \in \partial Q, |p| = 1, (p, n(q)) \geq 0\}$, which in turn defines the *billiard map* $\Phi : M \to M$. The nat-

[12] Figures 2.13, 2.14, 2.15, 2.16, 2.17 and 2.19 were produced using [113].

[13] The phase space is three dimensional if $|p| = 1$.

ural choice of coordinate system on M is the arc length parameter $s \in [0, |\partial Q|)$ and the angle θ between p and the normal vector $n(q)$, where $-\frac{\pi}{2} < \theta < \frac{\pi}{2}$ and $(n(q), p) = \cos\theta$. This is also the customary way of defining the billiard map using the so called *Birkhoff coordinates* $(s, \sin\theta)$ which are area preserving by Liouville's theorem, thus reducing the four dimensional phase space of the planar billiard Hamiltonian flow to a two dimensional one. A uniform (Liouville) measure projected onto the billiard boundary has the form $\mathrm{d}\mu = (2|\partial Q|)^{-1} \cos\theta \mathrm{d}\theta \mathrm{d}s$ and defines a smooth invariant probability measure. Hence, the measure of a set $D \subset M$ is defined by $\mu(D) = \int_D \mathrm{d}\mu / \int_M \mathrm{d}\mu$. Note that the billiard flow and map are not defined if q is a singular point of the boundary ∂Q (e.g. corners or tangencies), while the measure of the set of orbits that hit such singularities must equal zero. Further details including the subtle differences between the billiard flow and billiard map can be found in [6].

2.2.1.2 Stability of billiards

As described for one and d-dimensional systems in the previous section (see equation (2.7)), a linear stability analysis of the local $d = 2$ billiard dynamics leads to a [22] Jacobian matrix $\mathbf{J}(\mathbf{x})$ describing the stability at each point $\mathbf{x} = (q_1, q_2, p_1, p_2)$ of phase space $\mathcal{M}$. By considering the variation along the kth free flight segment of the flow one obtains the stability matrix

$$\mathbf{J}_T(\mathbf{x}_k) = \begin{pmatrix} 1 & t_k \\ 0 & 1 \end{pmatrix}, \tag{2.33}$$

where t_k is the flight length between the k and $k-1$ collision. Similarly, the stability matrix associated with the reflection process at the boundary is

$$\mathbf{J}_R(\mathbf{x}_k) = -\begin{pmatrix} 1 & 0 \\ r_k & 1 \end{pmatrix}, \tag{2.34}$$

where $r_k = \frac{2}{\rho_k \cos\theta_k}$, ρ_k is the radius of curvature (positive for collisions with concave objects) at the kth collision $q_k \in \partial Q$ and θ_k the angle of incidence. Notice that if the collision occurs on a flat boundary, then $r_k = 0$ and $-\mathbf{J}_R(\mathbf{x}_k)$ is just

the identity matrix. By using the multiplicative property of the Jacobian, the full matrix[14] for $p \in \mathbb{N}^+$ consecutive collisions of the initial condition $\mathbf{x}_0$ is given by

$$\mathbf{J}_p(\mathbf{x}_0) = \prod_{k=p}^{1} \mathbf{J}_T(\mathbf{x}_k)\mathbf{J}_R(\mathbf{x}_k), \tag{2.35}$$

where the product is runs from $k = p$ to $k = 1$ such that the matrix operations are performed in the correct order. $\mathbf{J}_p(\mathbf{x}_0)$ describes how a beam of trajectories is defocused by $\mathbf{J}_T$ along the free flights and is defocused/refocused at reflections by $\mathbf{J}_R$. Notice that because the billiard dynamics preserves phase space volumes, $\det\mathbf{J}_p(\mathbf{x}_0) = 1$. The stability eigenvalues of $\mathbf{J}_p(\mathbf{x}_0)$ depend only on the trace of $\mathbf{J}_p(\mathbf{x}_0)$ and are given by:

$$\Lambda_{1,2} = \frac{1}{2}\left(\mathrm{tr}\mathbf{J}_p(\mathbf{x}_0) \pm \sqrt{(\mathrm{tr}\mathbf{J}_p(\mathbf{x}_0) - 2)(\mathrm{tr}\mathbf{J}_p(\mathbf{x}_0) + 2)}\right). \tag{2.36}$$

It can be shown that if Λ is an eigenvalue of $\mathbf{J}_p$, so are $1/\Lambda$, Λ^* and $1/\Lambda^*$. This follows from the symplectic invariance of the billiard map. If $\Lambda \neq 1$ and real then the orbit is *hyperbolic*. If $\Lambda = 1$ the orbit is *parabolic*. Finally, if Λ_i is complex, then $\Lambda_{1,2}$ are conjugate pairs with $|\Lambda_i| = 1$ and the corresponding orbit is called *elliptic*.

The above constructions suffice for calculating the *local* stability of periodic orbits as in (2.5) but also for calculating Lyapunov exponents[15] as in (2.8) and can also be generalized to higher dimensional billiards.

Of course, there exists a variety of statistical properties which can be calculated and measure the *chaoticity* of a dynamical system. These include ergodicity, decay of correlations, mixing rates, central limit theorems for time averages of phase functions (see Ref [114]) and finally the Kolmogorov-Sinai (KS) entropy which measures the unpredictability of the system (see Ref [97]). However all of the above statistics and techniques are mathematically very involved and are often restricted to small classes of dynamical systems such as hyperbolic.

[14] This is also known as the Monodromy matrix.

[15] Lyapunov exponents are one of the most commonly used statistical quantities which describes the *chaoticity* (hyperbolicity) of dynamical systems.

As discussed in the introduction and preceding sections, more practical measures of the chaoticity of a system are the Poincaré recurrence statistics $\mathcal{Q}(t)$ and the survival probability function $P(t)$ for systems with holes. Power law decays in these distributions are a quick and easy indicator of the presence of non-hyperbolicity and thus intermittency. The problem of analytically quantifying this intermittency in two dimensional billiards, is the main goal of this thesis which we are slowly but steadily building up to.

2.2.2 Billiard Dynamics: Overview

2.2.2.1 Regular Billiards:

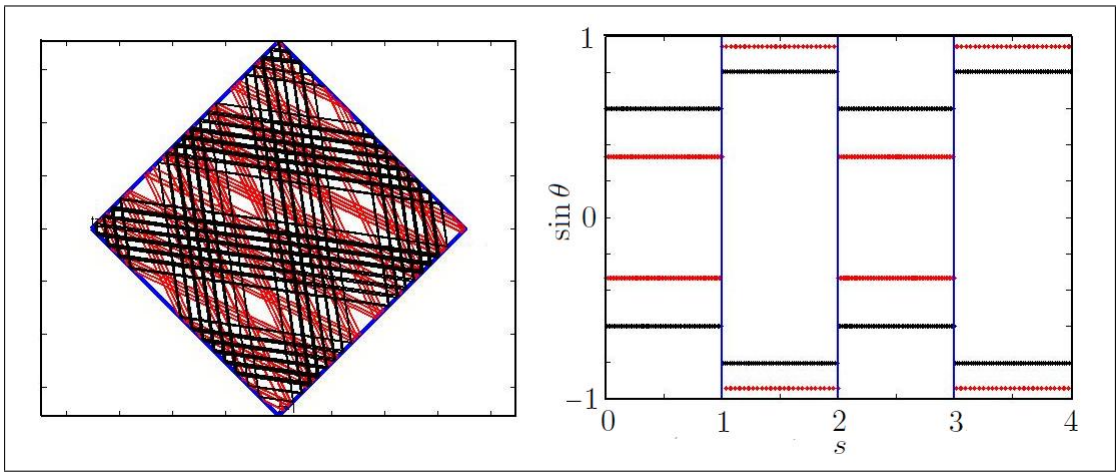

Figure 2.13: *Left:* Coordinate space of square billiard with two trajectories in different colors. *Right:* Corresponding orbits in phase space.

The square and circle billiards are arguably the most popular (and simplest) paradigm models of regular billiard dynamics. In the case of a square, the particle's trajectory can be directly identified with free motion on $\mathbb{R}^2$ by an *unfolding* process and the system is integrable[16]. Unfolding is often used for collisions with flat boundaries. A standard result is that if the angle of incidence with the boundary

[16] A Hamiltonian system is said to be 'integrable' if one can find a change of coordinates to an action-angle coordinate frame where the phase space dynamics is described by motion on circles, one circle for each degree of freedom.

θ is a rational multiple of π then the orbit is periodic and if not then it is *dense*. In the same sense as for the doubling and tent maps, initial conditions with rational conditions with rational slope form a countably infinite set while the set of all points in M are uncountable. Therefore the phase space M of the square billiard is completely foliated with invariant curves (see Figure 2.13). This is also true for the rectangular billiard, though deviations from generic (Poisson[17]) statistics arise when considering the spectral statistics of the corresponding quantum billiard [116].

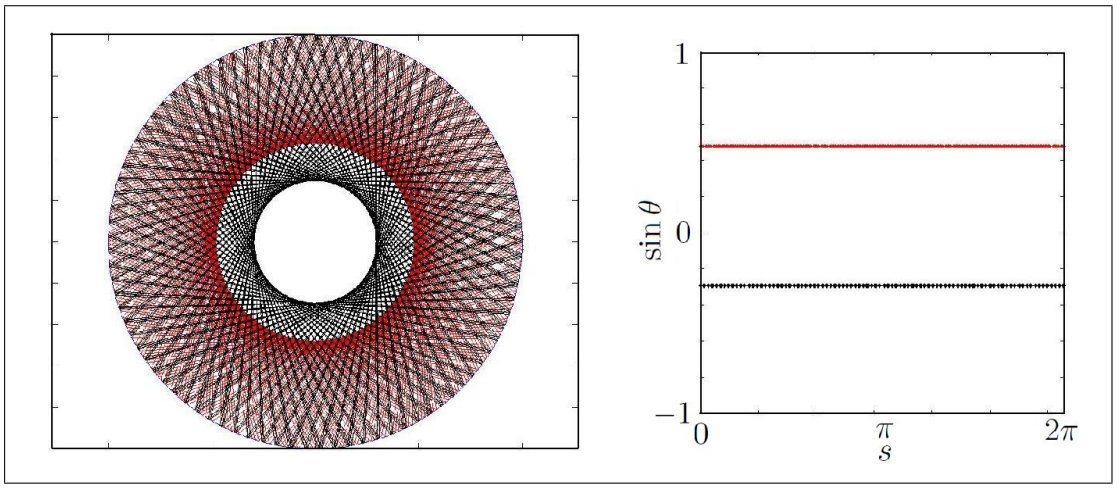

Figure 2.14: *Left:* Coordinate space of circle billiard with two trajectories in different colors. *Right:* Corresponding orbits in phase space.

The circular billiard behaves very similarly with the square though exhibits some interesting new properties. Obviously the angular momentum is a constant of motion (the angle of reflection remains unchanged). Hence the billiard is integrable. Again, incident angles which are rational multiples of π form periodic orbits and irrational ones are dense (see Figure 2.14). Here also is the phase space foliated by similar invariant curves. In fact each invariant curve in phase space corresponds to a confocal circle of radius $\sin\theta$ which is also called a *caustic* (which means "burning"[18] in Greek). An important feature of the periodic orbits

[17]It has been conjectured that generically, in the semiclassical limit, quantum spectral statistics on the scale of the mean level separation are Poissonian in classically integrable systems [115].

[18]If the particle's trajectory were the path of a laser ray and the billiard boundary was a

of the circle (and square) is the fact that they are not isolated in M. They form a continuous family of periodic orbits produced by rotation (for circle) or translation (for square) with respect to the billiard. All of these orbits have stability eigenvalues $\Lambda_{1,2} = 1$ and are therefore marginally stable (parabolic). This implies that the distance between two neighboring trajectories grows *linearly*.

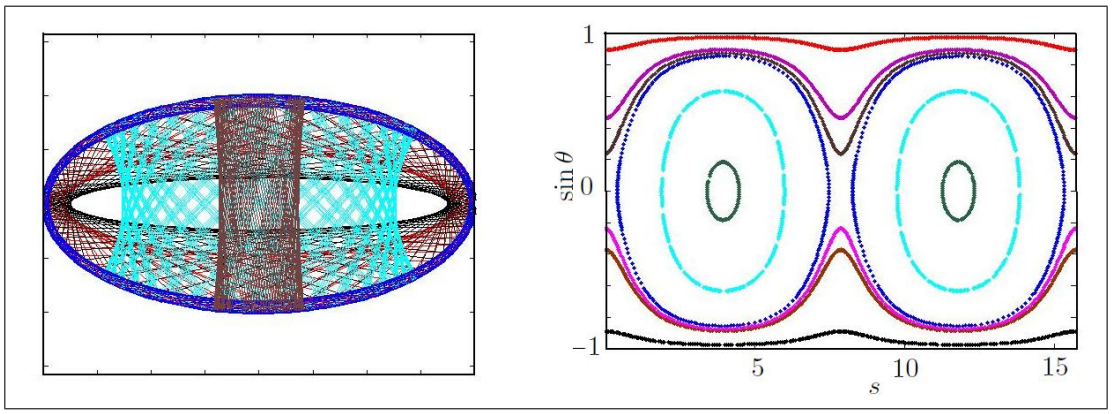

Figure 2.15: *Left:* Coordinate space of ellipse billiard with four trajectories in different colors. *Right:* Corresponding orbits in phase space.

A generalization of the circle is the ellipse where quite interesting new orbits are observed. The dynamics in the ellipse is integrable no matter what the value of its eccentricity. The corresponding constant of motion can be interpreted as the product of the angular momenta about the two foci of the ellipse. In coordinate space this conserved quantity corresponds to caustics in the form of confocal conics (hyperbolas or ellipses). Figure 2.15 shows some of the contour-like invariant curves of the constant of motion. It is clear that there are two types of orbits: the rotational ones and the librational ones. The former form elliptic caustics and never pass through the two foci while the latter form hyperbolic caustics and always pass through the two foci. Much like the circle and other integrable billiards, periodic orbits in the ellipse are not isolated and form continuous families. However, there are two periodic orbits, namely the diametrical ones which are isolated and dominate the topology of the phase space. The one along the major

perfect mirror, then it would feel 'very hot' on this caustic.

axes is unstable while the other one is not. Note however that this single unstable periodic orbit is isolated and thus only locally hyperbolic.

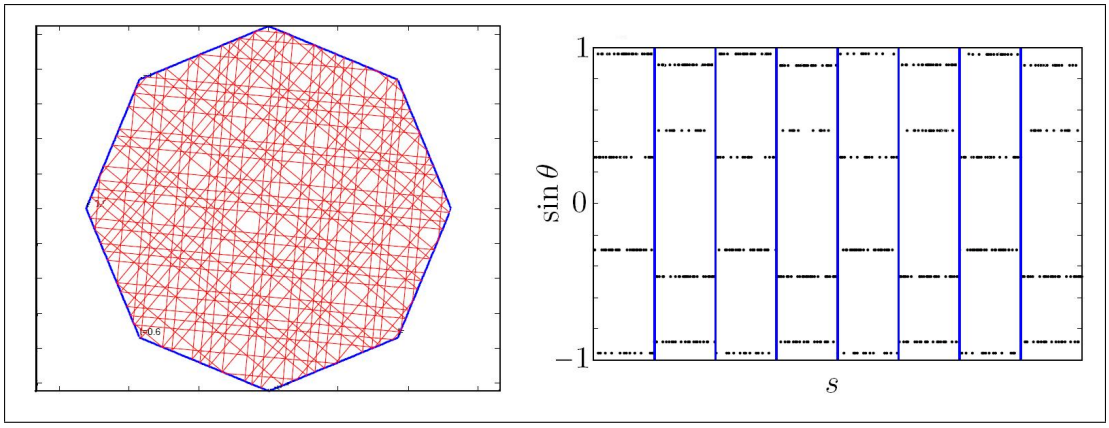

Figure 2.16: *Left:* Coordinate space of an octagon billiard with a single trajectory which can explore 8 different incident angles. *Right:* Corresponding orbit in phase space.

One would naively expect that the unfolding method can be 'easily' applied to all polygonal billiards [117]. Although this is possible in some specific cases of rational polygons [19] and gives rise to the concepts of *translational surfaces* and *directional flows* [118], not much is known for irrational polygons [119], except that Lyapunov exponents are always zero. Hence, in this sense the dynamics is completely regular. Trajectories in rational polygons explore only a finite number of incident angles (see Figure 2.16) and the dynamics is topologically equivalent to the motion on a torus of some genus g. If $g = 1$ then the billiard is integrable. The set of integrable billiards is rather small and only includes bounded billiards defined on confocal conics [120], the ellipse (and circle), the rectangle and the triangles with angles $(\pi/3, \pi/3, \pi/3)$, $(\pi/3, \pi/2, \pi/6)$ and $(\pi/2, \pi/4, \pi/4)$. If there is overlapping in the unfolding procedure of rational polygons then the equivalent topological surface is a torus of higher genus ($g \geq 2$) and the system is called pseudo-integrable. In such cases, the distance between two neighboring trajectories grows at least linearly [121] with time due to singularities (edges or corners) which split a beam of trajectories into two separate parts [122]. Numerical simu-

[19] Polygons with angles which are rational multiples of π.

lations in a number of different pseudo-integrable billiards have showed that the decay of correlations is always faster than linear [123].

2.2.2.2 Chaotic Billiards:

There are two mechanisms of chaos in billiards: that of *Dispersing* and that of *Defocusing*. This in turn motivates the sub-categorization of billiards into dispersing, focusing and even absolutely defocusing [124] ones.

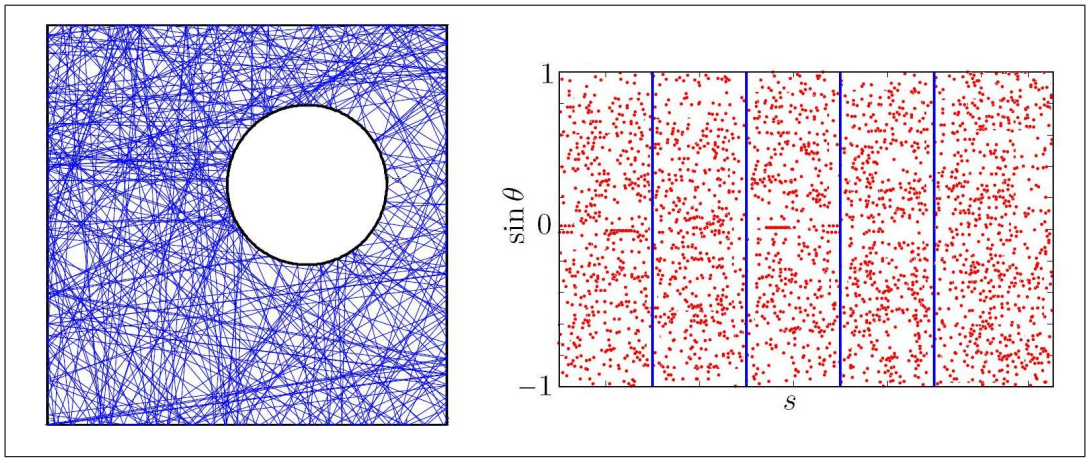

Figure 2.17: *Left:* Coordinate space of a Sinai billiard with a single chaotic trajectory which explores the whole of the phase space uniformly. *Right:* Corresponding orbit in phase space.

Dispersing[20] billiards are billiard tables with scattering boundary components. A typical example in two dimensions is a convex object (scatterer) such as a disc in a square box of side l[21]. These billiards were the first class of billiards for which hyperbolicity and ergodicity was established in 1970 (see [7]). The reason for the hyperbolicity is that nearby trajectories will diverge (exponentially) upon a reflection off a scatterer. This can be directly seen by computing the eigenvalues of $\mathbf{J}(\mathbf{x}_0)$ for the shortest periodic orbit. In Figure 2.17 we can see how a single orbit explores the phase space *uniformly* in time in a Sinai billiard with a circular scatterer of radius $r < l/2$ in a square with sides l. Orbits which are tangent

[20] Often referred to as Sinai billiards or Sinai tables especially in Physics literature.

[21] By identifying opposite parallel sides we obtain what is also known as the periodic Lorentz gas which is therefore defined on an infinite domain.

to the scatterer form what is called *grazing* collisions and are singularities of the billiard flow and require close and detailed investigations (see Ref [125] section 4). If $r \in (l/2, l/\sqrt{2})$ the dynamics is reduced to that of a *diamond* shaped billiard (see Figure 2.18). If $r = l/2$ however, cusps (zero angle corners) are formed, which allow for an unbounded number of collisions as an orbit approaches them. Such a singularity accentuates the subtle differences between billiard flow and billiard map[22] (see Ref [126] for more details). Note that within the cusp each free flight between consecutive collisions decays quadratically.

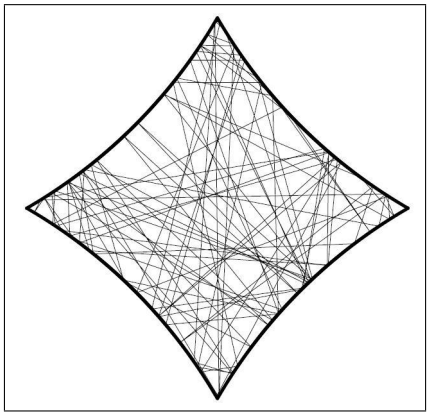

Figure 2.18: Coordinate space of a diamond billiard with a single chaotic trajectory.

Now consider two disk-like particles of radius r in a two dimensional box (a square), which experience elastic collisions with each other. By changing to center of mass coordinates, this system can be reduced to a single point particle in a square billiard containing a stationary disc scatterer of radius $2r$. Due to this interpretation dispersing billiards are important models in rigorous statistical mechanics, for which strong statistical properties like exponential decay of correlations or the central limit theorem can be proven. In addition, the corresponding quantum billiards are expected to be characterized by the statistics of random matrix eigenvalue ensembles. For systems invariant under time reversal (e.g. with no external magnetic field), the energy-level statistics of a number of chaotic systems

[22]The number of collisions is also unbounded during grazing collision along convex boundaries (whispering-gallery orbits).

have been shown to be in good agreement with the predictions of the Gaussian orthogonal ensemble (GOE) of random matrices, and it has been suggested that this phenomenon is generic for all chaotic systems with this kind of symmetry [10].

After a reflection off a focusing boundary component, where $\rho_k < 0$ two nearby trajectories will converge. Thus, establishing hyperbolicity in billiards with focusing boundary components is much more delicate. In fact, while dispersing billiards are always hyperbolic, billiards with focusing boundary components can have elliptic periodic orbits, a mixed phase space, or they can be completely integrable (e.g. the ellipse). Lazutkin famously proved in 1973 [127, 128] that for any strictly convex billiard with 'smooth' enough boundary[23] there exist caustics near the boundary (corresponding to invariant curves in phase space), which prevent global ergodicity and hyperbolicity. Shortly after, in 1974 it was shown by Bunimovich [129, 130] that convex hyperbolic and ergodic billiards exist and only require one continuous derivative except at a small set of singular points. These constructions are called *Bunimovich stadia*.

The mechanism behind the hyperbolicity in focusing billiards is in fact a generalization of the dispersing mechanism. The key idea is that after a reflection off a focusing part of the boundary an initially parallel beam of rays will converge and eventually pass through a conjugate point. Once they pass through this conjugate point the trajectories will start to move apart (and disperse!). If the free path after the conjugate point is sufficiently large, then this expansion can compensate for the initial contraction. Thus the overall expansion (divergence) prevails over contraction (convergence) of wavefronts and hyperbolicity is established.

The simplest example of a hyperbolic and ergodic focusing billiard is a surprisingly simple deformation of the circle called the *stadium* billiard. It consists of two semi-circles, which are connected by straight lines and thus looks like a stadium. In Figure 2.19 we can see how a single orbit can explore the phase space uniformly in time in the stadium billiard. We shall return to the stadium in chapter 3 and describe many of its properties in greater detail. For now it suffices to say that the

[23] The smoothness required was 533 continuous derivatives!

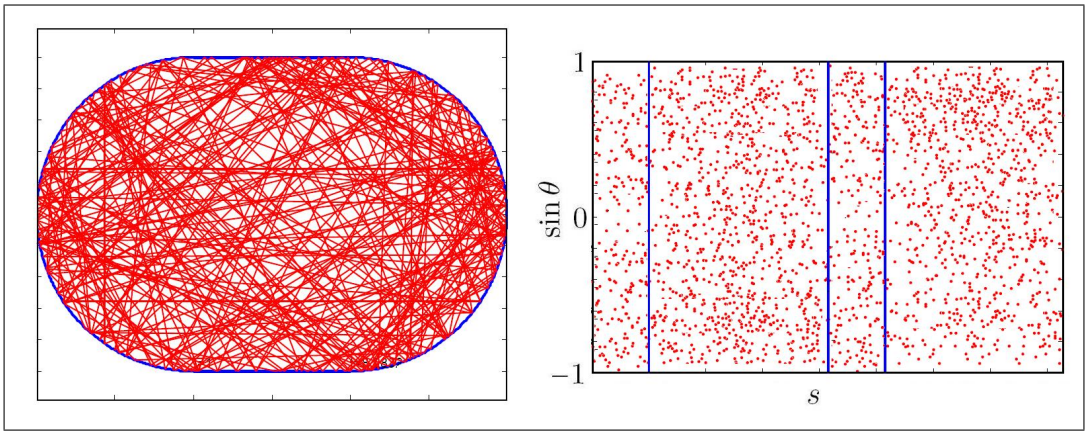

Figure 2.19: *Left:* Coordinate space of the stadium billiard with a single chaotic trajectory which explores the whole of the phase space uniformly. *Right:* Corresponding orbit in phase space.

stadium's phase space is densely filled by infinitely many periodic orbits (typical of chaotic systems) all of which are unstable (hyperbolic). All except one that is. There exists a single continuous family of period two orbits between the stadium's parallel walls which are in fact locally stable and hence termed *marginally unstable*. This means that $\Lambda_{1,2} = 1$ though a small perturbation in their incidence angle will after a series of an unbounded number of approximately periodic collisions with the flat boundaries will eventually explore the stadium's phase space uniformly. These orbits are called *bouncing ball* orbits and can also be found in dispersing billiards (e.g. Sinai billiards[24]) whenever there exist orbits of possibly unbounded 'free' motion (orbits with no collisions with the convex scatterers). These orbits occupy zero measure in phase space and therefore do not affect the overall ergodicity of the system. However as we shall see later (chapter 3), the intermittency introduced by them can affect other important statistical observables including the survival probability $P(t)$ can also lead to interesting new phenomena such as *asymmetric transport* in scattering problems (chapter 5).

[24]Sinai billiards allowing for trajectories of unbounded free motion are also called *infinite horizon Sinai* billiards.

2.2.2.3 Mixed Billiards:

So far, we have encountered billiards with stable periodic orbits, unstable periodic orbits, marginally unstable periodic orbits, non-periodic orbits covering smooth invariant curves and orbits filling areas chaotically. In the 'generic' case, that is for typical billiards Q, just like for the standard map (2.28) all of these different kinds of orbits co-exist and hence compose a mixed phase space with some fractal hierarchy of elliptic islands according to Kolmogorov-Arnold-Moser (KAM) theory [131]. In this respect, all the above examples are **not** generic billiards.

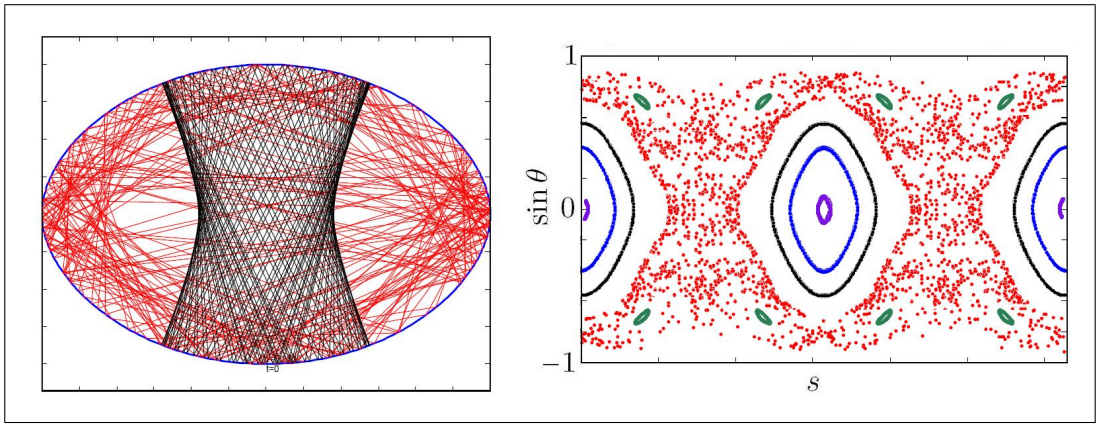

Figure 2.20: *Left:* Coordinate space of a oval billiard (with $a = 1$ and $\delta = 0.6$) with two trajectories, one is stable and one is chaotic. *Right:* Phase space plot of five different trajectories plotted in different colors.

There is no prescription as to how to construct billiards which posses a mixed phase space. However a nice example can be obtained by smooth deformations of the circle billiard according to the following parametrization in cartesian coordinates:

$$\begin{aligned} x(t) &= a\left(\left(1+\frac{\delta}{2}\right)\sin t + \frac{\delta}{6}\sin 3t\right), \\ y(t) &= a\left(\left(-1+\frac{\delta}{2}\right)\cos t - \frac{\delta}{6}\cos 3t\right), \end{aligned} \tag{2.37}$$

with $t \in [0, 2\pi)$ and $\delta \in (0, 1)$, such that the perimeter is given by $2\pi a$. The limits $\delta = 0$ and $\delta = 1$ of this *oval* billiard (see Figure 2.20) correspond to the circle and *lemon* billiards respectively [132]. Unlike in the ellipse, all (infinitely many)

periodic orbits are isolated while the phase space structure of invariant curves surrounding the stable fixed points and chaos the unstable ones repeats recursively down to infinitely fine scales just as in the standard map. Furthermore, as δ is increased these islands bifurcate, shrink and eventually disappear in an intricate way while the chaotic region along the separatrix expands along the dominant unstable (for all $\delta > 0$) period two diametrical orbit (see Ref [133] for more details).

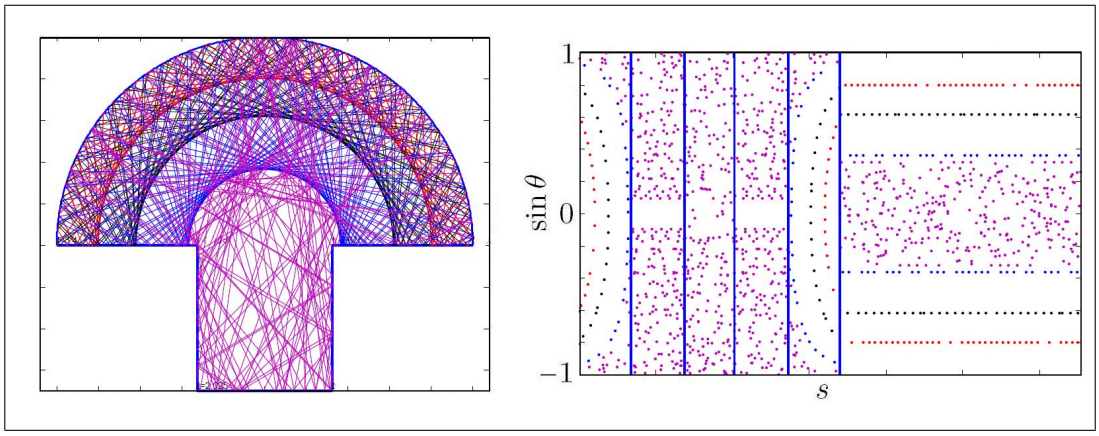

Figure 2.21: *Left:* Coordinate space of a mushroom billiard (with circular hat of radius $R = 1$ and stem width $r = 0.45$) with 4 trajectories, three stable and one chaotic. *Right:* Corresponding phase space plot of these trajectories plotted in different colors.

The oval billiard and other similar mixed phase space billiards are not easily treated rigorously. An exception is offered by another deformation of the circle giving a prototype mixed phase space billiard which does not suffer from such a disadvantage, namely the *mushroom* billiard. This was introduced in 2001 by Bunimovich and consists of a convex semi-elliptical (including semi-circular) 'hat' attached to a 'stem' such that their intersection is smaller than the diameter of the hat. We shall return to the mushroom in chapter 3 and describe many of its properties in greater detail. For now it suffices to say that the mushroom's mixed phase space is sharply divided, meaning that there is no hierarchical structure of KAM islands, but rather a single chaotic ergodic component and a single regular island (see 2.21) [91].

Both examples have intermittent dynamics. The source being the border between regular and chaotic dynamics. This is clear in the oval billiard as its phase space resembles that of the standard map. In the case of the mushroom however, non-hyperbolic points, typically supported by an infinite number of marginally unstable periodic orbits will be studied thoroughly in chapters 6 and 7.

2.2.3 Open Billiards: A dynamical window

Billiards are opened by allowing trajectories to leave, *leak* out, or escape through some pre-specified region of the phase space. This region can correspond to a hole in coordinate space, motivated by scattering problems or in momentum space, for example in micro-resonators where light is trapped by total internal reflection and escapes if the incidence angles are smaller than the critical one. Alternatively, motivated from room acoustics, escape could occur with some probability depending on the billiard boundary.

The initial distribution is usually given by the equilibrium measure of the billiard map or flow accordingly. If considering a transport type problem with injection of particles through the hole then the initial measure is restricted on the hole.

As discussed in the introduction, open billiards can be thought of as 'optimization problems' concerned with questions such as where to place holes to maximize/minimize escape [1]; 'inverse problems' corresponding to an open equivalent of "hearing the shape of a drum" [2]; or even 'transport problems' [3] where particles can enter and exit the system through different holes, or similarly holes (narrow tunnels) connecting a network of cavities. The survival probability $P(t)$ is in all these cases the relevant statistical observable from which we may obtain useful information. In this sense, open billiards and open systems in general can be thought of as *non-destructive windows* into the corresponding closed systems classical or even quantum dynamics [33].

2.2.3.1 Regular Open Billiards:

In billiards exhibiting regular dynamics as described above, the survival probability at long times is expected to decay according to some power-law $\sim \mathcal{C}/t^{\sigma}$ [134] where $\mathcal{C}$ is some constant and $\sigma > 0$. This power-law decay follows from the following argument. Consider the square billiard. Although the decay along each invariant curve is exponential[25] with a decay rate proportional to the tangential (with respect to the boundary ∂Q) component of the momentum $p_{\parallel} = \cos\theta$, the overall survival probability decays algebraically after integration

$$P(t) \sim \int_{-\pi/2}^{\pi/2} e^{-t\cos\theta} \mathrm{d}\theta \sim t^{-1}, \tag{2.38}$$

as $t \to \infty$.

Similarly for the integrable circle billiard $P(t) \sim t^{-1}$. Furthermore, for a hole of angle size $2\pi h$ in the circle billiard, the leading order coefficient of $P(t)$ was obtained exactly [80]; in particular it was shown that the statement

$$\lim_{h\to 0}\lim_{t\to\infty} h^{\delta-1/2}(tP(t)) - \frac{1}{\pi h} = 0, \tag{2.39}$$

for all $\delta > 0$ is equivalent to the Riemann Hypothesis [26]. It also appears that if both limits are taken simultaneously so that ht is a constant, the survival probability reaches a limiting function.

There is not much work on open polygonal billiards. In [136] it was found numerically that $P(t)$ decayed as $\sim \mathcal{C}/t$ in an irrational polygonal billiard where at least one periodic orbit was present, and vanished at some finite time for a rational polygonal billiard containing no periodic orbits. Finally, due to the quadratic separation of nearby trajectories in pseudo-integrable polygonal billiards, one would expect a decay of order $\sim t^{-2}$.

[25] If we fix momentum the total phase space is identical to that of the coordinate space which is ergodic and escape is as in the (2.19).

[26] The Riemann hypothesis is a very well known open problem in number theory and is the statement that all the complex zeros of the Riemann zeta function, the analytic continuation of $\zeta(s) = \sum_{n=1}^{\infty} n^{-s}$ in the complex plane, lie on the line $Re(s) = 1/2$, and is related to the distribution of prime numbers [135]

2.2.3.2 Strongly Chaotic Open Billiards:

From the examples of chaotic billiards given above, only the diamond billiard with $r \in (l/2, l/\sqrt{2})$ is uniformly hyperbolic. Hence it displays what is often referred to especially in the Physics literature [62] as *strong chaos*. In such systems a typical initial condition will explore the entire phase space exponentially fast and hence will also escape exponentially fast. The escape rate is proportional to the hole's length h and is given by [109]

$$\gamma = \lim_{t\to\infty} -\frac{\ln P(t)}{t} = \frac{h}{\langle\tau\rangle|\partial Q|}, \tag{2.40}$$

where $\langle\tau\rangle = \frac{\pi|Q|}{|\partial Q|}$ is the mean free path for two dimensional billiards.

Such exponential decays have been used to model many real physical applications especially in the context of acoustics. The standard acoustical problem of sound decaying in a room, due to a small absorption at the walls follows the classical and universal Sabine's law of reverberation. γ in such a situation is the average absorption coefficient weighted appropriately with the variety of absorbing surfaces inside the three dimensional room whose small wavelength dynamics is well approximated by that of billiards. In fact, Sabine's result relies implicitly on the ergodic properties of geometrical billiard-like trajectories. A paradigm of an ergodic auditorium is the stadium billiard and is studied in Ref [39].

Following the discussions about where to place the hole in strongly chaotic maps one is lead to try and expand γ in powers of the hole size h. This was performed in Ref [33] and the next-to-leading terms were expressed as sums of correlation functions which depend on hole position and particularly on the stability of the hole-overlapping periodic orbits.

2.2.3.3 Weakly Chaotic Open Billiards:

Hamiltonian systems with a mixed phase space are often referred to as systems exhibiting *weak chaos*. In such systems the exponential decay law (2.40) has been numerically [137, 86] and analytically [103] shown to experience a *cross-over* for

longer times towards an asymptotic power-law behavior

$$P(t) \approx \begin{cases} \text{irregular}, & \text{for } t < t^* \\ a\gamma e^{-\gamma t}, & \text{for } t^* < t < t_\sigma, \\ \gamma\left(ae^{-\gamma t} + b(\gamma t)^{-\sigma}\right), & \text{for } t > t_\sigma, \end{cases} \tag{2.41}$$

where $ae^{-\gamma t_\sigma} \gg b(\gamma t_\sigma)^{-\sigma}$. This formula was proposed in Ref [35] (eq. (25)) and is interpreted as the effective splitting of the *chaotic saddle*[27] into hyperbolic and non-hyperbolic components. This in turn requires the definition of various effective time scales as follows. t^* is the short-time memory, within which fluctuations due to short-time periodic orbits appear in $P(t)$. After this time the recurrence times lose correlations and can be approximated by a random Poisson process as seen in (2.30) and hence $P(t)$ should follow a purely exponential decay. t_σ is the minimum time a typical chaotic trajectory takes to approach the non-hyperbolic region before escaping through the hole causing $P(t)$ to acquire an algebraic tail of order $\sim t^{-\sigma}$, $\sigma > 0$. We shall return to this formula later in this thesis and re-examine its accuracy.

According to the conjecture of Ref [110] and numerical simulations of [111] for the standard map (2.28), then the survival probability for generic billiards should also decay as (2.41) with a universal power law exponent $\sigma \approx 0.57$. This rather slow decay is associated with stickiness observed near the hierarchical island structure.

As hinted in the previous subsection, although the stadium billiard is a chaotic system with positive Lyapunov exponents almost everywhere [130], the zero-measure family of marginally unstable periodic orbits between the parallel straight segments called 'bouncing ball' orbits renders the billiard weakly chaotic. These bouncing ball orbits have been shown to lead to an intermittent, quasi-regular behavior which effectively causes the closed stadium to display some weaker chaotic properties such as an algebraic decay of correlations [138]. Quantum mechani-

[27] A chaotic saddle is a compact invariant set consisting of all orbits that never escape either in forward or backward time.

cally they cause scarring [139], the system is not quantum uniquely ergodic [140] while an $\hbar$ dependent 'island of stability' appears to surround them in phase space [141]. Furthermore deviations from random matrix theory (RMT) predictions are observed (especially in the Δ_3-statistics[28]) if not treated appropriately (see Refs [142, 143]). In the open stadium, $P(t)$ is therefore found to experience a cross-over from exponential to power-law decay of order $\sim \mathcal{C}/t$ [83]. A similar decay is also observed in infinite horizon Sinai billiards i.e. when $r < l/2$ [144]. The exponent $-\sigma = -1$ is in fact expected in the stadium, sinai, and all other integrable billiards because of the presence of marginally stable periodic orbits causing small perturbations to grow only linearly in time (see[111] section 4.2 and equation (2.38)). What is even more interesting than the above examples of weakly chaotic open billiards is the case of the mushroom billiard. There, the ergodic component of the phase space typically has infinitely many marginally unstable periodic orbits; yet the power law decay of $P(t)$ persists and is of the same order ($\sim t^{-1}$) nonetheless.

Résumé

In this section, we have defined the billiard dynamics, and described how their stability may be analyzed. Examples of regular, chaotic and mixed billiards were discussed with a specific emphasis on the intermittency in their dynamics. The closed billiard dynamics is captured by exponentials and power-laws of the survival probability function in the presence of one or more holes. The exponential escape rate γ depends primarily on hole size (see (2.40)) but also on position through periodic orbits. In weakly chaotic systems, intermittency causes a crossover in $P(t)$ from exponential to some power-law with exponent, for generic area preserving maps (including the billiard map Φ) with a hierarchical phase space structure, universally at $\sigma \approx 0.57$, while for systems with marginally unstable periodic orbits $\sigma = 1$. All this information feeds into the generalized formula (2.41) which characterizes the various decays at different timescales. Because generic low dimensional

[28]The spectral rigidity statistics Δ_3 was fist introduced by Madan Lal Mehta and is defined as the mean square deviation of the best local linear fit to the cumulative spectral density.

Hamiltonian systems display weak chaos, it is thus highly desirable to be able to say as much as possible about all the unknown variables appearing in (2.41). In the following five chapters we attempt to quantify the intermittency of billiards with marginally unstable periodic orbits by calculating the power-law coefficient for the specific examples of the stadium, mushroom and drivebelt billiards.

Part II

Main Results

Chapter 3

Escape from the Stadium

Having introduced the concepts of chaos, escape and intermittency both in the context of maps and billiards through a variety of examples and in some generality, one is now tempted to apply the theory on specific new problems. In this chapter we consider the open stadium billiard, consisting of two semicircles joined by parallel straight sides with one hole situated somewhere on one of the sides. Due to the hyperbolic nature of the stadium billiard, the initial decay of trajectories, due to loss through the hole, appears exponential. However, some trajectories (bouncing ball orbits) persist and survive for long times and therefore form the main contribution to the survival probability function $P(t) \sim \mathcal{C}/t$ at long times. This simple model will facilitate for our investigations and using both numerical and analytical methods we will obtain an explicit expression for the constant $\mathcal{C}$. In contrast with Ref.[80] however, we do not assume or require that the hole is vanishingly small and in contrast to Ref.[83], we do not use a probabilistic description of the billiard dynamics. These results have been published in Ref [87] and therefore this chapter follows the published article closely. The numerical simulations presented in this section have been performed using a code written in *Mathematica v.6* (not included in the thesis).

We start with a brief description of the stadium's main properties through a review of the stadium's literature. Then we give the main ideas and we also set up the problem and define all the variables and sets required. We then consider

the two main sets of initial conditions which contribute to the survival probability at long times and introduce and explain in detail the approximation method used to obtain the constant $\mathcal{C}$. Finally, we present our numerical results from computer simulations and compare with the analytical ones. A conclusion and discussion follows where future work is also discussed.

3.1 Introduction to the stadium

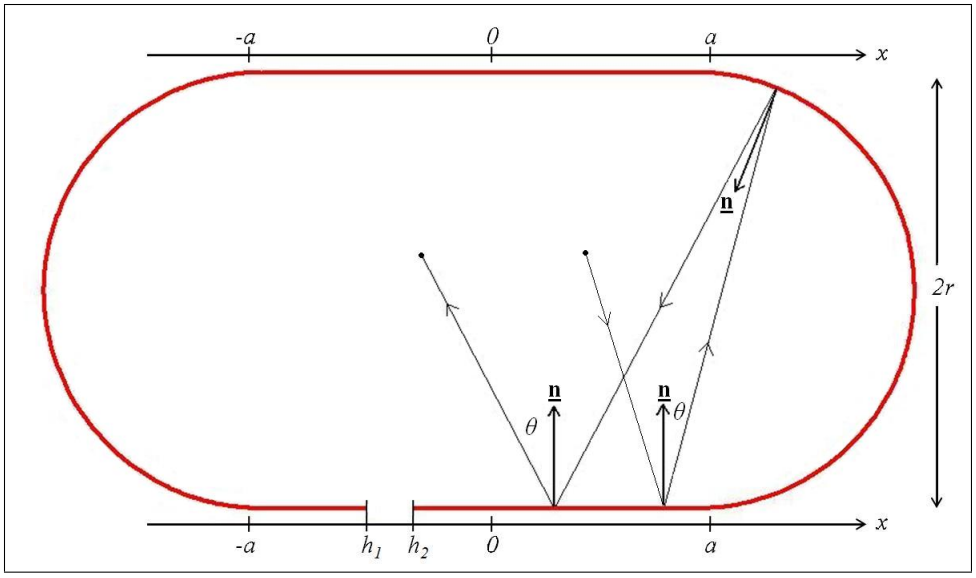

Figure 3.1: The Set-Up of the stadium billiard.

The stadium billiard (see Figure 5.1 below) is a seemingly simple dynamical system, and was first introduced by Leonid Bunimovich in 1974 [129]. It was later proven by him to be ergodic, to be mixing, to have the Kolmogorov property [130], and in 1996 by Chernov and Haskell to have the Bernoulli property [145]. It has been described as a system with "fully developed chaos" [146]. Its entropy has been numerically estimated in [147] and theoretically in [148]. The stadium billiard is a special case of a chaotic billiard. Being constructed from two fully integrable billiard segments, the circle and the rectangle, it is remarkable that the system remains completely chaotic no matter how short its parallel segments are. It is also a limiting case of the larger set of Hamiltonian systems, which Bunimovich

refers to as "mushrooms" [149] with sharply divided phase-space areas, regular and chaotic. The stadium is the fully chaotic limit of the simple mushroom billiard, while the circle is the fully regular limit. If the parallel segments are of length $2a$ say, where $a > 0$, then the global Lyapunov exponents (see (2.8)) $\lambda(a) \to 0$ in both limiting cases of $a \to 0$ and $a \to \infty$. Also, it is well known that the defocusing mechanism, which is one of the two sources of chaos in billiards [150] (the other being the dispersing mechanism), characteristic of all Bunimovich type billiards, requires $a > 0$ in order for any wave-front to defocus and therefore exhibit hyperbolicity. Wojtkowski in 1986 [151] clarified much of the mechanism behind this hyperbolic behavior.

The very existence of the parallel segments of the boundary is also the source of the intermittent behavior found in the stadium billiard. They allow for the existence of a set of marginally unstable periodic orbits (MUPOs) of zero measure but indeed of great importance. They are the main reason why the stadium is not uniformly hyperbolic. Also, though it is classically and quantum mechanically ergodic, it does not have the property of unique ergodicity [152, 140]. This means that not *all* eigenfunctions are uniformly distributed and therefore this causes scarring [139]. This is due to the existence of the so called "bouncing ball" orbits, sometimes also called "sticky orbits". Semi-classically, they have caused much trouble in the treatment of the system as explained in great detail by Tanner [141] since they affect the stability of periodic orbits close to them but do not contribute to individual eigenvalues in the spectrum of the stadium.

Lai-Sang Young's infinite Markov extension construction called a *Young tower* in 1998 [153, 154] triggered a series of rigorous mathematical proofs concerning the long time statistical properties of the stadium billiard. In 2004 Markarian [155] proved that asymptotically the billiard map in the stadium has polynomial decay of correlations of order $(\log n)^2 n^{-1}$ (here n is the number of iterations of the billiard map). This method was then simplified and generalized by Chernov and Zhang in 2005 [138] to include for example the drive-belt stadium where the straight segments are no longer parallel. Bálint and Gouëzel [156] in 2006, used this

method to prove that the Birkhoff sums of a sufficiently smooth generic observable with zero mean in the stadium, satisfy a non-standard limit theorem where its convergence to a Gaussian distribution requires a $\sqrt{n \log n}$ normalization. In 2008, Chernov and Zhang sharpen their previous estimate by removing the $\log n$ factor [157] and Bálint and Melbourne show that these relations hold for observables smooth in the flow direction as well (this excludes position and velocity)[126]. These results for the rate of decay of correlations can, at least heuristically, be transferred into the context of the open stadium to address problems such as escape rates and survival probabilities.

Therefore, even though the stadium billiard has been observed to exhibits strong chaotic properties for short times such as approximate exponential decays of $P(t)$ and decays of correlations of initial conditions both numerically and experimentally, it has also been shown to experience a *cross-over* at longer times, towards an asymptotic power-law behavior [104, 137, 86]. Hence, the stadium billiard is an example of a transient chaotic system which exhibits intermittency. In fact, it has recently been suspected that the very long regular flights present in the expanded stadium are the reason why numerically, at least, the moments of displacement diverge from the Gaussian [158]. It is arguably an ideal model for studying the influence of almost regular dynamics near marginally stable boundaries both theoretically [141] and numerically [159]. Armstead, Hunt and Ott [83] have carried out a detailed investigation into the asymptotic stadium dynamics and have shown that $P(t) \sim \frac{\mathcal{C}}{t}$ for long times but do not calculate the constant $\mathcal{C}$.

3.2 The main ideas and Set-up of the problem

Consider an open stadium as shown in Figure 5.1. A classical non-interacting particle of unit mass and unit speed experiences elastic collisions on ∂Q, the boundary of the billiard table. The length of the parallel sides is $2a$, while the radius of the circular segment is r. A hole of size ϵ is punched onto one of the straight segments of ∂Q with x coordinates $x \in (h_1, h_2)$, $h_2 = h_1 + \epsilon$. x is the position coordinate

which we only need to take values along the straight segments, $x \in [-a, a]$. We define the inward pointing normal vector $\hat{\underline{\mathbf{n}}}$ which defines the angle θ made by the reflected particle and $\hat{\underline{\mathbf{n}}}$. The angle $\theta \in (-\pi/2, \pi/2)$ and is positive in the clockwise sense from $\hat{\underline{\mathbf{n}}}$. As discussed in the previous chapter, the billiard flow conserves the phase volume and the corresponding invariant equilibrium measure is $\mathrm{d}\mu = (2|\partial Q|)^{-1} \cos\theta \mathrm{d}\theta \mathrm{d}x$, where $2|\partial Q| = \int_{-\pi/2}^{\pi/2} \cos\theta \mathrm{d}\theta \int_{\partial Q} \mathrm{d}r = 2\big(4a + 2\pi r\big)$ is the canonical probability measure preserved by the billiard map on the billiard boundary. $\mathrm{d}\mu$ is also the distribution of initial conditions. We shall not be defining a parametrization of the position coordinate along the circular segments of the billiard as it is not needed for the following analysis. Finally, if the particle hits the hole, it will escape; as previously noted we are interested in the long time behavior of the survival probability.

As discussed in the introduction above, the stadium is hyperbolic as a result of the defocusing mechanism. However it is not uniformly hyperbolic, as there exist a small set of parabolic, non-isolated periodic orbits [160] called bouncing ball orbits which is of zero measure. We have already seen how orbits in the chaotic region of the phase space which are close to these MUPOs show almost regular behavior for finite but unbounded periods of time. As a result, the decay through the hole appears exponential for short times, followed by an algebraic tail [161]. A theory for explaining the intermediate time transition from exponential to power-law decay is that of intermittency and was first introduced in 1979 by Manneville and Pomeau in their study of the Lorenz system [100, 101]. Usually, intermittency signifies a small, finite time Lyapunov exponent for unstable periodic orbits approaching regular regions in phase space [162]. Trajectories almost tangent to the circular arcs ("whispering gallery orbits, or rolling orbits") are intermittent with respect to the collision map, but not with respect to the flow. This is because they are of bounded total path length and sufficiently unstable [141, 126]. Near bouncing ball orbits on the contrary are not of bounded total path length therefore exclusively determining the asymptotic tail [86, 83] of the survival probability $P(t)$. These orbits are characterized by small angles θ (near vertical) that

remain small for relatively long periods of time. Chernov and Markarian describe them in their book [6] as orbits with a large number of '*nonessential collisions*'. Semi-classically, it has been suggested that an '*island of stability*' surrounds this marginally stable family. Its boundary depends explicitly on $\hbar$ and the measure of this island shrinks to zero (compared with the total volume) in the semiclassical limit $\hbar \to 0$ [141].

Having noted, following [86, 83], that the set of orbits surviving for long times is contained in the near bouncing ball orbits, with small angles θ and position on the straight segments, we now categorize these orbits into two simple families: orbits initially moving towards the hole, and orbits initially moving away from the hole. We would like to identify the set of orbits from these two families which do not escape until a given time t. An important result by Lee, that dates back to 1988 [163], states that the angle of a near bouncing ball orbit in the stadium remains small even after a reflection with a semicircular segment. In fact, as will be explained soon, small angles can change by at most a factor of 3 after being reflected off the curved billiard boundary. Therefore, given a sufficiently large time constraint t, surviving orbits are restricted to angles unable to 'jump over' the hole, even after a reflection on the circular part of the billiard boundary. In this way we identify the surviving orbits as members of time dependent, monotonically shrinking subsets of the two families of orbits described above. The measure of these subsets tends to zero as $t \to \infty$. These two subsets are considered in detail and are thus used to calculate, to leading order the stadium's survival probability function $P(t)$ (see equation (3.33) below).

3.3 Case I: Moving towards the hole

We start by considering trajectories initially on the right of the hole with $x \in (h_2, a)$ moving towards it. These trajectories will prove to be only a part of the survival probability function for long times. However, they are essential in order to construct a complete and accurate expression for the asymptotic limit of the full

survival probability function. To ensure that such trajectories will escape when they reach the hole's vicinity, they must satisfy the following condition:

$$|\theta| < \arctan\Big(\frac{\epsilon}{4r}\Big), \tag{3.1}$$

hence they will definitely not jump over the hole. The set of initial conditions (x, θ) for trajectories which will escape in exactly time t satisfies:

$$t\sin|\theta| - \delta 4r\tan|\theta| \leq x - h_2 \leq a - h_2, \tag{3.2}$$

where $0 < \delta < 1$. For long times $\delta 4r\tan|\theta|$, which is the horizontal distance from the edge of the hole to where the particle exits the billiard, will shrink to zero ($\sim 1/t$) as the set of surviving trajectories is limited to near vertical angles. Hence we drop this nonsignificant term in what follows. Notice that we will be using physical time t for our calculations but the equations are set up as if considering a map between $p \in \mathbb{N}$ collisions, with $t = \frac{2rp}{\cos\theta}$. This way, we do not need to define equations for the billiard map, which in any case would just be described by the usual reflection map. From equations (3.11) and (3.2) we can deduce that the angles must satisfy:

$$|\theta| < \min\Big\{\arctan\Big(\frac{\epsilon}{4r}\Big), \arcsin\Big(\frac{a-h_2}{t}\Big) + \mathcal{O}(1/t^2)\Big\}. \tag{3.3}$$

The second term in (3.3) is the dominant one for long times. This leads to the following integral for the conserved measure of the billiard map:

$$I_r = \frac{2}{2|\partial Q|}\int_0^{\arcsin\left(\frac{a-h_2}{t}\right)+\mathcal{O}(1/t^2)} \Big(\int_{h_2+t\sin\theta+\mathcal{O}(1/t)}^{a} \cos\theta \mathrm{d}x\Big)\mathrm{d}\theta, \tag{3.4}$$

where the subscript r stands for *right*. We are integrating over the set of initial conditions, on the right of the hole, which will not escape until time t. Hence we are considering escape times greater than or equal to t. We have also dropped the modulus sign from θ and multiplied the whole expression by a factor of 2, due to the vertical symmetry of the problem. This simplifies to

$$I_r = \frac{\big(a-h_2\big)^2}{2|\partial Q|t} + \mathcal{O}(1/t^2). \tag{3.5}$$

This result is valid for trajectories satisfying:

$$\arcsin\left(\tfrac{a-h_2}{t}\right) + \mathcal{O}(1/t^2) < \arctan\left(\tfrac{\epsilon}{4r}\right),$$

that is

$$t \gtrsim \frac{8ar}{\epsilon}, \tag{3.6}$$

since the supremum of $a - h_2$ is $2a$. We continue with this calculation by adding the analogous contribution I_l from the small angle trajectories starting on the *left* of the hole with $x \in (-a, h_1)$ moving towards it. This operation can easily be calculated from equation (3.5) by simply sending $h_1 \mapsto -h_2$ and $h_2 \mapsto -h_1$.

$$I_l = \frac{\left(a + h_1\right)^2}{2|\partial Q|t} + \mathcal{O}(1/t^2).$$

Adding the two integrals gives the measure of all initial conditions moving towards the hole that survive until time t:

$$I_{r+l} = \frac{\left(a + h_1\right)^2}{2|\partial Q|t} + \frac{\left(a - h_2\right)^2}{2|\partial Q|t} + \mathcal{O}(1/t^2). \tag{3.7}$$

Hence, part of the canonical survival probability function due to the nonessential orbits initially approaching the hole from either side, for long times satisfying condition (3.6) is:

$$P_1(t) = \frac{\left(a + h_1\right)^2 + \left(a - h_2\right)^2}{2(4a + 2\pi r)t} + \mathcal{O}(1/t^2). \tag{3.8}$$

This expression is essentially a sum of contributions from two families of bouncing ball orbits, each proportional to the square of the available length.

3.4 Case II: Moving away from the hole

Numerical simulations confirm that $P_1(t)$ in equation (3.8) is indeed not the full expression for the long time survival probability function of the open stadium billiard. We now consider orbits initially moving away from the hole, so that they experience a reflection process when they collide with the right semicircular end. We only consider the right semicircular end, as we shall later use the symmetry of the stadium to see what happens at the left one. If the initial angles are small,

then the final angles (after being reflected at the wings of the stadium) will remain small and therefore survive for long times and account for the remaining set of orbits and built up the long time survival probability. Here we investigate and identify exactly the initial conditions which survive for long times t.

Throughout this and the following section we will be using (x_i, θ_i), where $x_i = x_1 - 2rn\theta_i$, as the coordinates of our initial conditions which lie on the right of the hole, $x_i \in (h_2, a)$, and move away from it. Due to the stadium's symmetry, we only need consider the case $\theta_i > 0$. We will use (x_1, θ_1) to indicate the position and angle of a trajectory right after its final collision on a flat segment, while still moving away from the hole. Therefore, the next collision of such trajectories will be on the right semi-circular segment of the billiard. This helps to distinguish between the initial conditions and their transformed final values. Notice that $\theta_i = |\theta_1|$.

We begin by formulating the time to escape

$$T(x_i, \theta_i) = \frac{2rn}{\cos\theta_i} + \frac{2rm}{\cos\theta_f} + D_f, \tag{3.9}$$

where n and m are the respective numbers of non essential collisions before and after the reflection process on the right semicircular end, and are defined as:

$$n = \left(\frac{a-x_i}{2r\tan|\theta_i|} - \delta_i\right)$$
$$m = \left(\frac{a-h_2}{2r\tan|\theta_f|} - \delta_f\right),$$

with $0 < \delta_{i,f} < 1$, and $f = 3, 4$. We chose these indices for f (3 and 4) to indicate the number of collisions comprising the reflection process as the incidence angles change two or three times respectively. D_f is the time taken for the reflection process at the semicircular end, and is bounded by:

$$4r < D_3 < 2r\left(\frac{1}{\cos\theta_i} + \frac{1}{\cos\theta_3}\right)$$
$$6r < D_4 < 2r\left(1 + \frac{1}{\cos\theta_i} + \frac{1}{\cos\theta_4}\right).$$

The number of reflections on the curved boundary alternates between two scenarios, as shown in Figure 3.2, the case with one collision on the semicircle and

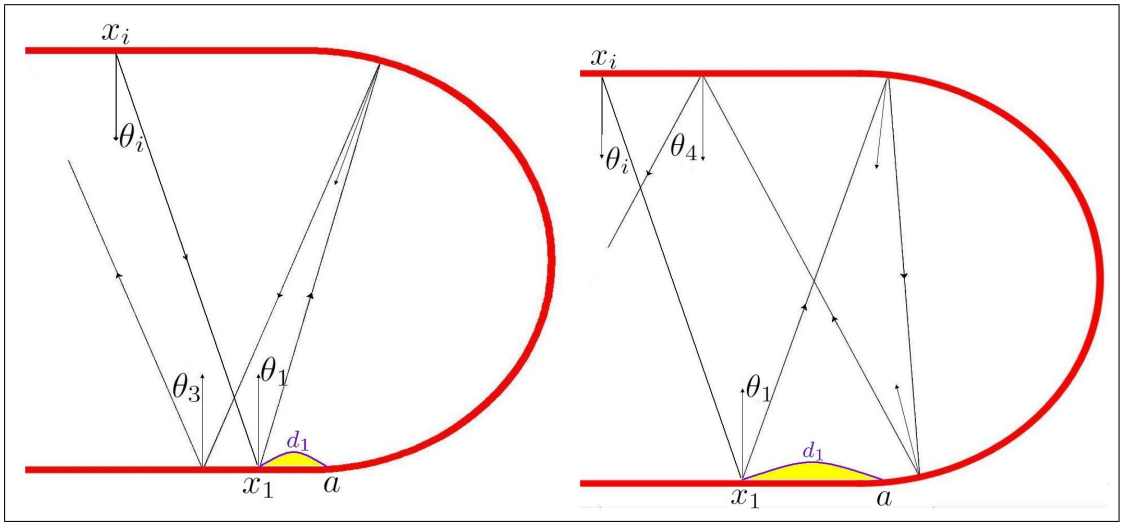

Figure 3.2: The two possible scenarios of reflection from the semicircles, where $d_1 = a - x_1 = a - x_i - 2rn\theta_i > 0$.

the case with two collisions depending on the initial conditions of the trajectory x_i and θ_i. Specifically, θ_f can be found and defined by the use of small angle approximations as:

$$\theta_3 = \frac{2d_1}{r} - 3\theta_i < 0, \tag{3.10}$$

$$\theta_4 = \frac{4d_1}{r} - 5\theta_i > 0 \tag{3.11}$$

(see Refs [83, 163]), where $d_1 = a - x_1 = a - x_i - 2rn\theta_i > 0$, is the horizontal distance between $x = x_1$ and $x = a$ as indicated in Figure 3.2. Using the above information, equation (3.9) can be expressed in the following way:

$$T(x_i, \theta_i) = \frac{a - x_i}{|\theta_i|} + \frac{a - h_2}{|\theta_f|} + \Delta_f, \tag{3.12}$$

where $\Delta_f = D_f - 2r(\frac{\delta_i}{\cos\theta_i} + \frac{\delta_f}{\cos\theta_f})$.

Before we continue, it is essential to find the boundaries of validity for the functions of θ_f. These will define the geometry of the two scenarios. We ask the question: When do we see one and when two collisions at the semicircular ends? This is answered by considering a number of inequalities. The first and most obvious one is $\theta_1 \geq \frac{d_1}{2r}$ which requires the next collision to be on the circular segment. We also note that $\theta_1 = \frac{3d_1}{4r}$ is the transition line between θ_3 and θ_4 and

is the case where the reflected particle will hit exactly the point $x = a$, where the circular segment meets the straight segment. Finally, if we are also to satisfy condition (3.1) we must form two more inequalities:

equation (3.10) gives

$$\theta_i < \frac{2d_1}{3r} + \frac{\arctan\left(\frac{\epsilon}{4r}\right)}{3}, \tag{3.13}$$

and equation (3.11) gives

$$\theta_i < \frac{4d_1}{5r} - \frac{\arctan\left(\frac{\epsilon}{4r}\right)}{5}. \tag{3.14}$$

These inequalities enclose a small area in the $x_i - \theta_1$ plane, the plane of initial conditions. Notice that d_1 is a function of x_i but also depends on n, the number of nonessential collisions before the nonlinear (now linearized) reflection process (3.10, 3.11), which if not equal to zero introduces an extra θ_1 dependence. This means that inequalities (3.13) and (3.14) have to be solved for θ_1 for every $n = 0, 1, 2, 3 \ldots$. This is done and shown in Figure 3.3, up to and including $n = 2$, where z is taken to be equal to $\arctan(\epsilon/4r)$. These boundaries of validity define the set of orbits which escape after being reflected at the right semicircular segment of the billiard. It is not immediately clear from Figure 3.3, but the peaks of these spikes are of the same height $\theta_1 = 3z$. However, we note that the set of orbits that survive up to time t, where t is large, is not identical with the set defined by these inequalities.

To motivate what is to follow we have a look momentarily to Figure 3.4 below, which on its left panel shows a numerical simulation which identifies the set of initial conditions (x_i, θ_i) which survive until time $t = 50$. Notice that the peaks of the spikes grow in height as we move from right to left, moving away from the end of the flat segment at $x = a$, and therefore in a sense increasing the count of pre-reflection collisions n.

To find the survival probability function, $P_2(t)$, of these trajectories we must now consider $T(x_i, \theta_i)$ as the parameter t. Hence we can rearrange equation (3.12) according to (3.10) and (3.11), to form two expressions which depend not only on

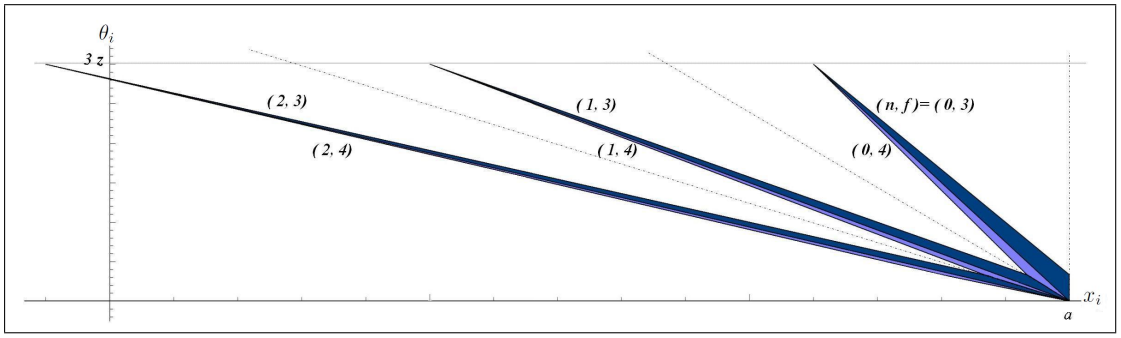

Figure 3.3: The set of initial conditions initially on the right of the hole, which collide and reflect on the right semicircular segment of the stadium and do not jump over the hole are defined by the boundaries of validity. These are shown here for $n = 0, 1, 2$. The dotted diagonal lines are given by $\theta_i = (a - x_i)/2r(n + 1)$ and separate the plane into the relative areas of n. The top triangle of each spike (dark blue) is for $f = 3$ (one collision on semicircle) while the bottom (light blue) is for $f = 4$ (two collisions on semicircle). They are separated by the straight lines given by $\theta_i = 3(a - x_i)/2r(3n + 2)$. The remaining two sets of lines which define the spikes are given by the solutions of equations (3.13) and (3.14). Notice that all spikes have the same maximum height of $3z = 3\arctan(\epsilon/4r)$.

x_i, θ_i and n, but also on the time t:

$$f_3(x_i, \theta_i, t) \equiv (a - x_i)\Big(\frac{2d_1}{r} - 3\theta_i\Big) - (a - h_2)\theta_i + (\Delta_3 - t)\Big(\frac{2d_1}{r} - 3\theta_i\Big)\theta_i = 0 \tag{3.15}$$

$$f_4(x_i, \theta_i, t) \equiv (a - x_i)\Big(\frac{4d_1}{r} - 5\theta_i\Big) + (a - h_2)\theta_i + (\Delta_4 - t)\Big(\frac{4d_1}{r} - 5\theta_i\Big)\theta_i = 0 \tag{3.16}$$

The above expressions are conic sections as they are quadratic in both x_i and θ_i and describe hyperbolas in the plane of initial conditions. This is not immediately obvious because of the factors x_i and θ_i which are hidden in the d_1 term. The two hyperbolas, (3.15) and (3.16), approach each other as an effect of increasing the time t and tilt and shift discontinuously when increasing n. We notice that if we impose these hyperbolas onto the boundaries of validity we found earlier (see Figure 3.3), we are essentially imposing a time constraint on the set of initial conditions which will survive up to time t. Their effect will be for smaller n to

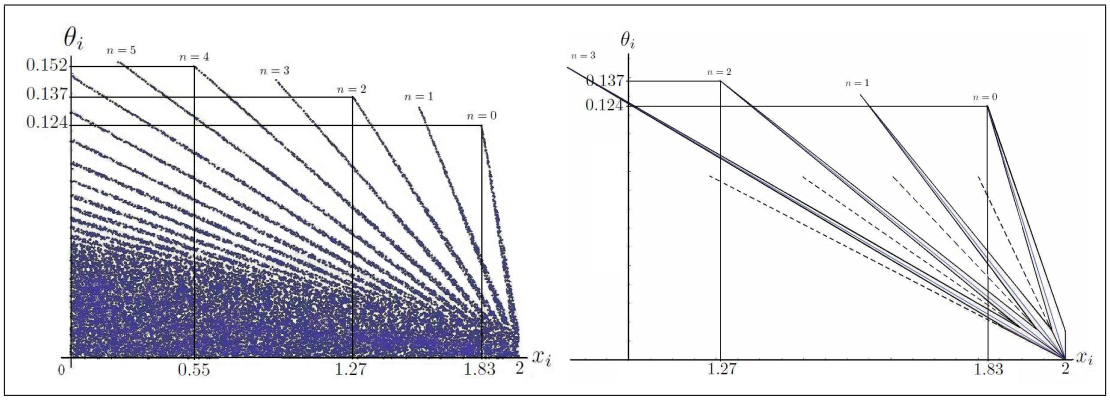

Figure 3.4: *Left*: Numerical simulation identifying the set of initial conditions initially moving away from the hole that survive until time $t = 50$. *Right*: Area enclosed by the hyperbolas for times $t = 50$, for $n = 0, 1, 2$ and 3. The line running through the middle of each spike and the diagonal lines separating them are as described in Figure 3.3. Notice that unlike Figure 3.3, the height of each spike is different. This is because the spikes are formed by segments of the time dependent hyperbolae defined in equations (3.15) and (3.16). This is further explained in the text. The parameters used for both left and right figures are: $a = 2, r = 1, \epsilon = 0.2, h_1 = -\epsilon, h_2 = 0$. The agreement of the two figures indicates that $t = 50$ is sufficiently large.

erode the area enclosed by the inequalities, therefore sharpening them, and for larger n to thicken them from either side, effectively shaping them into a series of spikes, allowing for larger and larger values of θ_i as we increase n from left to right.

This effect can be seen on the right panel of Figure 3.4, where the boundaries of validity for $n = 0, 1, 2$ and 3 are eroded by the hyperbolas which are time dependent, causing each spike to grow taller as we move away from the edge of the straight segment of the billiard. It can be easily seen that the pictures in Figure 3.4 are almost identical to a very small error, confirming that we are measuring the correct set of initial conditions and therefore the orbits they describe. The thickening effect is a consequence of the survival probability function's set up. Trajectories which fall just outside of the area enclosed by the boundaries of validity but for large enough n, are trapped between the two hyperbolas, will not eventually escape through the hole, *i.e.* they will jump over it, but they will still survive until the given time t.

We notice that for finite t, n is also finite. The key of the relation between t and n lies in the conic section equations (3.15)-(3.16). Solving them for n we discover that for $n = \frac{-3r+2t-2\Delta_3}{4r}$ and $n = \frac{-5r+4t-4\Delta_4}{8r}$ respectively, the conic sections are no longer hyperbolas but turn into negative parabolas. Hence, we can define the maximum number of pre-reflection collisions for finite but large time t as:

$$N_{max}(t) = \left\lfloor \min\left\{ \frac{-3\mathrm{r} + 2\mathrm{t} - 2\Delta_3}{4\mathrm{r}}, \frac{-5\mathrm{r} + 4\mathrm{t} - 4\Delta_4}{8\mathrm{r}} \right\} \right\rfloor = \left\lfloor \frac{-5\mathrm{r} + 4\mathrm{t} - 4\Delta_4}{8\mathrm{r}} \right\rfloor, \tag{3.17}$$

where the lower square brackets $\lfloor h \rfloor$ are defined as the integer part of h (also known as the floor function). Actually, as we shall find out in the next section, this term (N_{max}) is never reached in practice (see N_3 in equation (3.22) below).

It seems that we have the area of interest well defined and bounded. We thus need to integrate over the area of each spike and then sum them all up to N_{max} for any given t. Multiplying the result by a factor of 2 (vertical symmetry), would eventually give the measure of the long surviving orbits initially on the right of the hole moving away from it.

Integrating hyperbolas and then summing their enclosed areas is a lengthy and unpleasant process. This calculation has been done numerically and an accurate result has been obtained successfully and is presented in section 3.6. However, this calculation can only be carried out numerically, as an analytical result is in our opinion impossible to obtain. Therefore we shall present a simpler approximation method for $P_2(t)$, which is analytically tractable, but still accurate to leading order in $1/t$.

3.5 A method for approximating hyperbolas

In this section we will take equations (3.15) and (3.16) and argue that for large enough times t, the sections of the hyperbolas that are of interest can be simply and accurately described by straight lines. We can visually confirm this from Figure 3.4; however, further investigations have shown that the distance between the foci of each hyperbola converges to zero faster than the lengths of the integration limits

(on $\theta_i = (a - x_i)/2rn$ and $\theta_i = (a - x_i)/2r(n+1)$) as $t \to \infty$. In fact, for any n we find that the corresponding rates are $\sim t^{-1.5}$ and $\sim t^{-1}$. This in turn shows that the error made by approximating hyperbolas by straight lines, after integrating and summing over n, is still negligible with respect to the leading term (t^{-2} rather than t^{-1}). This approximation method will later be verified by further numerical simulations where we calculate the error between the approximate solution and the numerical integration result.

In this section we will use $\tau = t - \Delta$ without any subscript to avoid unnecessary confusion given that for long times, Δ will completely vanish from our results. We consider the same initial conditions as in the previous section. For the first step of the approximation method, we must find the coordinates where equations (3.15) and (3.16) meet with $\theta_i = \frac{3(a-x_i)}{2(1+n)r}$. We also need to find the coordinates where equation (3.16) meets with $\theta_i = \frac{a-x_i}{2(1+n)r}$ and finally equation (3.15) with $\theta_i = \frac{a-x_i}{2nr}$. These three points along with $(a, 0)$ define the four corners of a quadrilateral in phase space shown in Figure 3.5. Here are their coordinates:

$$
\begin{aligned}
A &= \Big(a + \frac{6(a-h_2)(2+3n)r}{(4+6n)r - 3\tau}, \frac{9(a-h_2)}{3\tau - (4+6n)r}\Big),\\
B &= \Big(a + \frac{2(a-h_2)nr}{3(2nr-\tau)}, \frac{(a-h_2)}{3(\tau - 2nr)}\Big),\\
C &= \Big(a + \frac{2(a-h_2)(1+n)r}{3(2(1+n)r-\tau)}, \frac{(a-h_2)}{3(\tau - 2(1+n)r)}\Big).
\end{aligned}
$$

The next step is to form four equations, one for each side of the quadrilateral by using these coordinates for $n \geq 0$. Afterwards, elementary integration methods in x_i are used to produce explicit functions for the area of each spike with τ and n as the only parameters:

$$
Area_1 = \frac{(a-h_2)^2 r}{(2nr-\tau)\big(2(1+n)r - \tau\big)}. \tag{3.18}
$$

Before we insert equation (3.18) into a sum, we must figure out the upper limit of n for which this expression is valid. We do this by finding the smallest integer value of n for which the x_i coordinate of point A is smaller than h_2 and

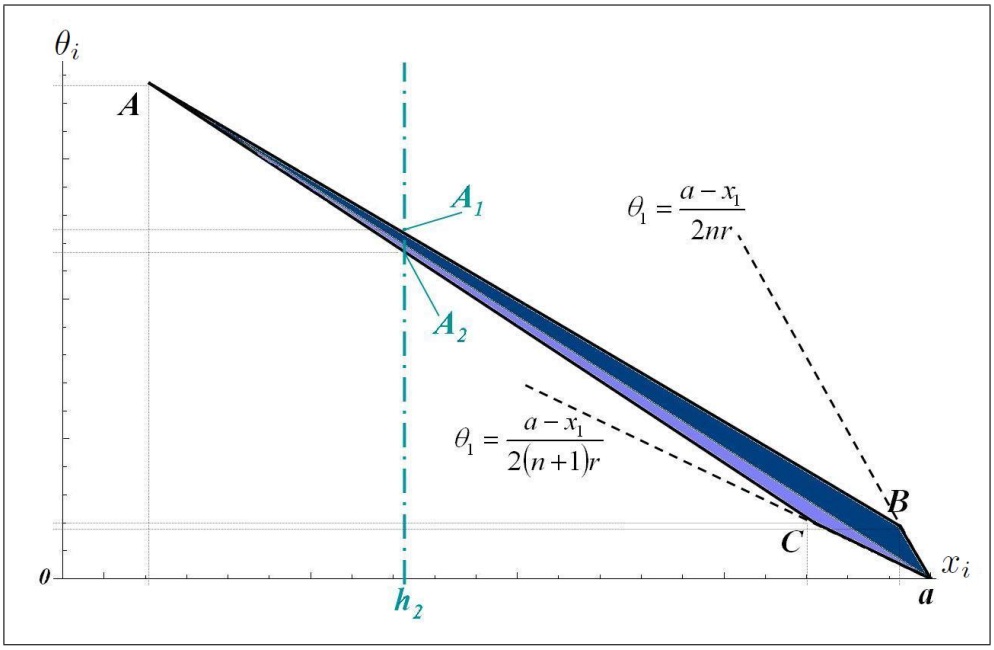

Figure 3.5: The corners which make up the polygons which approximate the hyperbolas, for any n, are defined by the coordinates of points A, B, C and the corresponding coordinate of the endpoint of the straight segment (in this case $(a, 0)$). The x_i and θ_i coordinates of these corners are clearly marked by the dotted lines. The color coding is similar to that of Figure 3.3. The green/dashed vertical line indicates the hypothetic position of the closest edge of the hole (in this case $x_i = h_2$) which acts and changes the shape of the spike by defining two new corners A_1 and A_2 instead of A.

call it N_1. This is because, for increasing values of n, all the corners (A, B, C) shift to the left causing the spike to tilt and stretch but when $n \geq N_1$ point A is no longer a valid coordinate. A closer look at the situation reveals that point A will split in to two points, A_1 and A_2 say, both situated on the line $x_i = h_2$. For $n > N_1$, the quadrilateral is replaced by a pentagon as the spike's peak (point A) overshot the vicinity of the hole's location. This process is best described diagrammatically in Figure 3.5 where the four corners A, B, C and $(a, 0)$ are replaced by A_1, A_2, B, C and $(a, 0)$ which are then fed back to the integration method to produce a new expression describing the area of the truncated spike. The same will happen to all corners, and different combinations of them will be necessary to produce the corresponding area functions. In other words, as the x_i coordinates of corners A, C and B, in this order, overshoots the hole's location at

$x_i = h_2$, as we increase n, a new area function ($Area_j$, $j = 1 - 4$) via integration, with a new expiration number (summation limit) via equation solving in n, will be required. This process produces three more area functions, and therefore four summations, each with different limits:

$$
\begin{aligned}
&Area_2 = \\
&-\Bigg((a-h_2)^2\Big[1152n^4r^4 + (-224r^3 + 313r^2\tau - 114r\tau^2 + 9\tau^3)\tau + 192n^3r^3(14r - 9\tau) \\
&+ 4n^2r^2(512r^2 + 225\tau^2 - 762r\tau) + 4nr(128r^3 + 270r\tau^2 - 45\tau^3 - 400r^2\tau)\Big]\Bigg) \\
&\div \Bigg(r\Big(16(1+n)(2+3n)r - 3(5+8n)\tau\Big)(2nr - \tau)\Big(2(1+n)r - \tau\Big) \\
&\times \Big[-9\tau + 4n\Big((4+6n)r - 3\tau\Big)\Big]\Bigg), \qquad (3.19)
\end{aligned}
$$

$$
Area_3 = \frac{(a-h_2)^2\Big(32nr^2 + 16n^2r^2 - (14r + 3\tau)\tau\Big)}{4r(1+n)(\tau - 2nr)\Big[-9\tau + 4n\Big((4+6n)r - 3\tau\Big)\Big]}, \qquad (3.20)
$$

$$
Area_4 = \frac{(a-h_2)^2}{4(n+n^2)r}. \qquad (3.21)
$$

Having all the *puzzle* pieces at hand, we form an expression for the invariant measure of all the long surviving initial conditions moving away from the hole from the right. The sum over the areas of quadrilaterals ($Area_1$) added to the sum of pentagons ($Area_2$) and another sum of quadrilaterals ($Area_3$) and finally the infinite sum of triangles, $Area_4$, gives:

$$
Area_{Right} = \sum_{n=0}^{N_1} Area_1 + \sum_{n=N_1}^{N_2} Area_2 + \sum_{n=N_2}^{N_3} Area_3 + \sum_{n=N_3}^{\infty} Area_4, \qquad (3.22)
$$

where

$$
N_1 = \Big\lfloor \frac{3t - 3\Delta - 16r}{24r} \Big\rfloor, \qquad N_2 = \Big\lfloor \frac{3t - 3\Delta - 8r}{8r} \Big\rfloor, \qquad \text{and} \quad \mathrm{N_3} = \Big\lfloor \frac{\mathrm{3t} - 3\Delta}{\mathrm{8r}} \Big\rfloor.
$$

All these sums, except the second one, where simplified as follows by *Mathematica v.6*, by allowing the summation limits to acquire their non-integer values. This is allowed since the upper limit $N_l \sim t$ ($l = 1, 2, 3$), and therefore losing or gaining a

term from the end of each summation effectively makes no difference whatsoever for long times. We get

$$\sum_{n=0}^{N_1} Area_1 = \frac{(a-h_2)^2(8r+3\tau)}{2\tau(9\tau-8r)}, \tag{3.23}$$

$$\sum_{n=N_2}^{N_3} Area_3 = \frac{32(a-h_2)^2 r\big(192r^2+56r\tau+3\tau^2\big)}{(8r+3\tau)(-8r-\tau)\big(64r^2-9\tau^2-72r\tau\big)}, \tag{3.24}$$

$$\sum_{n=N_3}^{\infty} Area_4 = \frac{(a-h_2)^2}{4rN_3}. \tag{3.25}$$

The simplification of the second sum (that of $Area_2$) requires a more lengthy and tricky process, as it can not be simplified explicitly by any conventional means. This is so, not only because $Area_2$ has the most complicated of the four expressions, but also because its sum covers the largest range over n ($N_2 - N_1 \sim t/4$). Therefore, for large t, n is never small. By using a substitution of the form $u = 1/t$, assuming u to be small for large t and then substituting $n = s/u$, where s is of $\mathcal{O}(1)$, before expanding $Area_2$ into a power series effectively incorporates the effect of large n into the leading order term of the series. We get:

$$Area_2 = \sum_{k=0}^{\infty} \alpha_k u^k = -\frac{\Big((a-h_2)^2(1-16sr+32s^2r^2)\Big)u^2}{32\Big(s^2r(-1+2sr)^2\Big)} + \mathcal{O}(u^3), \tag{3.26}$$

We reverse the substitution, and simplify the sum to obtain:

$$\sum_{n=N_1}^{N_2} Area_2 = (a-h_2)^2\left(\frac{12ru\big(\Psi^{(0)}(z_1)-\Psi^{(0)}(z_2)+\Psi^{(0)}(z_3)-\Psi^{(0)}(z_4)\big)}{32r} + \frac{-\Psi^{(1)}(z_1)-\Psi^{(1)}(z_2)+\Psi^{(1)}(z_3)+\Psi^{(1)}(z_4)}{32r}\right). \tag{3.27}$$

where

$$\begin{aligned} z_1 &= \frac{8r-9/u-3\Delta}{24r}, \\ z_2 &= \frac{8r+3/u-3\Delta}{24r}, \\ z_3 &= \frac{3(1/u-\Delta)}{8r}, \\ z_4 &= -\frac{1/u+3\Delta}{8r}, \end{aligned}$$

and $\Psi^{(k)}$'s are polygamma functions. The polygamma function of order k is defined as the $(k+1)$th derivative of the logarithm of the gamma function:

$$\Psi^{(k)}(z) = \frac{\mathrm{d}^{(k+1)}}{\mathrm{d}z^{(k+1)}} \ln \Gamma(z).$$

Fortunately the polygamma functions are of the form $z = \frac{a}{bu} + c$, where a, b and c are constants, and can be expanded as a Taylor series to leading order as follows:

$$\Psi^{(0)}(\frac{a}{bu} + c) = \ln(a/b) - \ln u + \mathcal{O}(u),$$
$$\Psi^{(k\geq 1)}(\frac{a}{bu} + c) = (-1)^{(k-1)}(k-1)!\Big(\frac{bu}{a}\Big)^k + \mathcal{O}(u^{k+1}).$$

Substituting these expressions into equation (3.27) will simplify the expression dramatically, finally leaving us with the desired result. We substitute $t = 1/u$ back in to get:

$$\sum_{n=N_1}^{N_2} Area_2 = \frac{(a-h_2)^2(9\ln 3 - 4)}{12t} + \mathcal{O}(1/t^2). \tag{3.28}$$

In light of equations (3.23),(3.24),(3.25) and (3.28), we can now simplify (3.22) to leading order to get:

$$Area_{Right} = \frac{(a-h_2)^2(3\ln 3 + 2)}{4t} + \mathcal{O}(1/t^2). \tag{3.29}$$

To find an expression for $Area_{Left}$ we must use the same approach used in section 3.3 to calculate I_l. This gives:

$$Area_{Total} = 2(Area_{Right} + Area_{Left}),$$
$$Area_{Total} = \frac{(3\ln 3 + 2)\Big((a+h_1)^2 + (a-h_2)^2\Big)}{2t} + \mathcal{O}(1/t^2). \tag{3.30}$$

Dividing by $2|\partial Q|$, we obtain an approximate result for the long time survival probability of all initial conditions initially moving away from the hole:

$$P_2(t) = \frac{(3\ln 3 + 2)\Big((a+h_1)^2 + (a-h_2)^2\Big)}{4(4a + 2\pi r)t} + \mathcal{O}(1/t^2). \tag{3.31}$$

As done for $P_1(t)$, the above result is valid for

$$t > \frac{32ar}{\epsilon}. \tag{3.32}$$

The factor 32 arises from the condition that $|\theta_f| < \arctan\frac{\epsilon}{4r}$ (*i.e* reflected orbit does not jump over the hole) similarly as in (3.1). Since $|\theta_f| \in (1/3, 3)\theta_i$ if $|\theta_i| \ll 1$, then $|\theta_i| < \arctan\frac{\epsilon}{12r}$. Assuming that the hole is situated at the very edge of the straight $h_1 = -a$, the maximum time such a trajectory takes is $\frac{2a-\epsilon}{\sin\theta_f} + \frac{2a-\epsilon}{\sin\theta_i} \approx \frac{32ar}{\epsilon}$.

3.6 Main Result and Numerical Simulation

It remains to add the probability measure of the two types of trajectories to obtain the asymptotic limit of the survival probability function:

$$P_s(t) = P_1(t) + P_2(t),$$

where the subscript s stands for the *straight* lines we have approximated the hyperbolas with. This gives:

$$P_s(t) = \frac{(3\ln 3 + 4)\Big((a+h_1)^2 + (a-h_2)^2\Big)}{4(4a + 2\pi r)t} + \mathcal{O}(1/t^2), \tag{3.33}$$

which is valid only for trajectories satisfying (3.32), i.e. sufficiently large t.

In the left panel of Figure 3.6 below, we compare P_s (equation (3.33)) with P_d which is obtained by a *direct* numerical simulation using *Mathematica v6.*, consisting of 1.5 million initial conditions distributed according to the invariant measure of the billiard map. We see that P_s gives a good prediction of the numerical survival probability for long times P_d. We have tested this result with other values of the parameters: a, r, h_1, h_2 as well. What is even more important however is that equation (3.33) is found to be an asymptotic formula. This is shown in the right panel of Figure 3.6, where we have plotted the $(P_s - P_h)$ at regular intervals of time, and fitted it to an inverse time curve $\mathcal{D}/t^2$, where $\mathcal{D}$ is some constant. Here, P_h is the result obtained by numerically summing over the areas of each spike (see Figure 3.4), found by the integrated difference of $\theta_3(x_i, t, n)$ and $\theta_4(x_i, t, n)$ which define the *hyperbolas* in the $x_i\theta_i$ plane. We find that the $(P_s - P_h)$ fits perfectly into $\mathcal{D}/t^2$, where $\mathcal{D}$ needs to be calculated by a numerical fit. Thus we confirm that the approximation chosen in section 3.5 was justifiable from the asymptotic

convergence to the integral P_h. $\mathcal{D}$ is simply the coefficient of the second order term in:

$$P(t) = \frac{(3\ln 3 + 4)\Big((a+h_1)^2 + (a-h_2)^2\Big)}{4(4a+2\pi r)t} + \frac{\mathcal{D}}{t^2} + o(1/t^2). \tag{3.34}$$

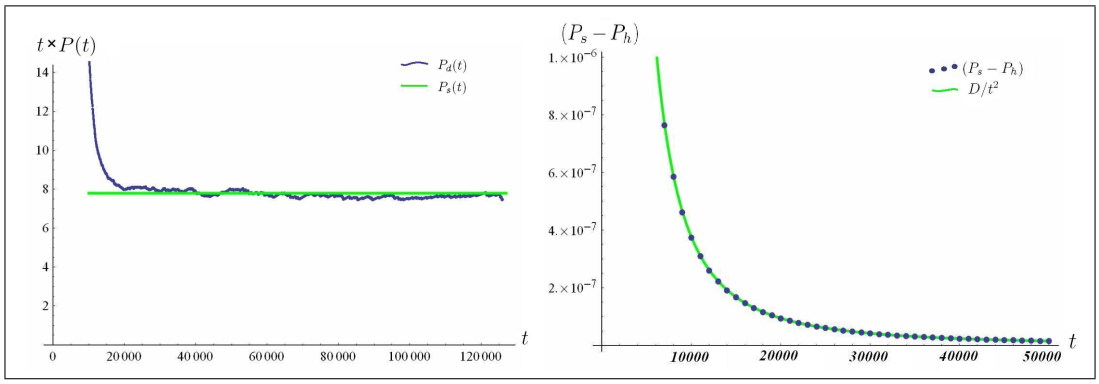

Figure 3.6: *Left:* Plot comparing the survival probability P_s (light green/horizontal line) found by equation (3.33), with the numerical survival probability P_d (dark blue/curve), found by direct numerical simulation, both multiplied by the time t. *Right:* The difference between equation P_s and P_h which is found by numerically integrating hyperbolas and summing the relative areas under the spikes created, decays as $\mathcal{D}/t^2$. $\mathcal{D}$ is the coefficient of the second order term in equation (3.34). Parameters used: $a = 10, r = 1, \epsilon = 0.1, h_1 = -0.05$.

3.7 Conclusion, Discussion and some more Results

In this section, we have investigated the open stadium billiard and managed to derive, using phase space methods, an expression consisting of the two main contributions (see equations (3.8) and (3.31)) to the long time asymptotic tail of the survival probability function of the stadium billiard. Both expressions are to leading order in t. The second one (equation (3.31)) is an approximate result which converges to the true result as $\sim t^{-2}$ which means the errors are $\mathcal{O}(1/t^2)$ and hence do not appear in the closed form of equation (3.33). The expression has

been confirmed through numerical simulation (see Figure 3.6 *Left*). In total, we confirm that the survival probability of the stadium for long times goes as $\frac{\mathcal{C}}{t}$, and we find that the constant $\mathcal{C}$ depends quadratically on the lengths of the parallel segments of the billiard on either side of the hole and hence the size of the hole as well as its position on one of the straight segments of the boundary (see equation (3.33)).

We emphasize here that the above calculation was possible because the stadium's classical phase space is split by the hole into separate regions occupied by 'fully-chaotic' and 'sticky' orbits, which are responsible for the exponential and algebraic decays respectively. As an orbit approaches the sticky region in phase space, which surrounds the bouncing ball orbits, it will inevitably escape through the hole quickly after it obtains an incidence angle $|\theta| < \arctan\left(\frac{\epsilon}{4r}\right)$. This is a key point that we will return to when considering escape through two holes placed asymmetrically. We also remark here that due to this splitting of the phase space, there is no justification for an intermediate purely exponential decay, as proposed generically for intermittent systems by Altmann *et al.* [35] (see also (2.41)), but rather a coexistence of exponential and algebraic decay given by:

$$P(t) = \begin{cases} \text{irregular}, & \text{for } t < \hat{t} \\ e^{-\gamma t} + \frac{\mathcal{C}}{t}, & \text{for } t > \hat{t}, \end{cases} \tag{3.35}$$

where we have neglected terms of order t^{-2} and $\hat{t} \leq \frac{32ar}{\epsilon}$ (see also (3.32)). The 'irregular' short-time behavior is a result of geometry dependent short orbits which become less important if the hole is small. We note that the coefficient of the exponential term above is 1 since for small holes and times greater than $\approx 1/\lambda$, where λ is the largest Lyapunov exponent, mixing causes the system to forget its initial state and therefore the probability decays as a Poisson process.

In the context of stadia, there is a variety of possible shapes for which one can observe similar properties. It is possible to construct different ergodic stadia by using circular arcs of lengths less than πr or by using elliptical arcs [164]. In both cases we expect ergodicity and an initial strong decay of the survival probability

followed by an asymptotic power law decay at longer times, provided that the parallel straight sides are still present, and that the dynamics remain defocusing [165]. Hence, the method used here to obtain (3.33) should be applicable to stadia of similar geometries. We address the case of a chaotic elliptical stadium with many holes in Appendix A.

At this point, we would like to comment on the $\ln 3$ term, which first appeared in equation (3.28). Similar terms where found in the work of both Bálint and Gouëzel [156] and Armstead's *et al.* [83] as well as several other papers relating to the stadium's bouncing ball orbits and its long time dynamics. It appears, that the $\ln 3$ term is a direct consequence of the geometry of our stadium billiard. More specifically, the circular curvature of the boundary near the straight segments, leads to a reflected final angle $|\theta_f| \in (|\theta_i|/3, 3|\theta_i|)$, if θ_i is small enough; this follows from equations (3.10) and (3.11) above and is further confirmed in Appendix A where we consider a chaotic elliptic stadium. The survival probability is then given by

$$P(t, L, c, h^-, h^+) = \frac{1}{2(4L + \mathcal{E})t} \left[\left(\frac{\left(\frac{4}{c^2} - 1\right) \ln\left(\frac{4}{c^2} - 1\right)}{2\left(\frac{2}{c^2} - 1\right)\frac{1}{c^2}} + 2 \right) \left((L + h^-)^2 + (L - h^+)^2 \right) \right], \tag{3.36}$$

where the new variables correspond to the old ones through $(a, h_1, h_2) \to (L, h^-, h^+)$, $c \geq 1$ is the ratio of semi-major to semi-minor axes, $\mathcal{E}$ is given by (A.15) and we have neglected terms of order $\sim t^{-2}$ (see also equation (A.16)). Notice how the $\ln 3$ term has changed according to the curvature of the semi-elliptic stadium wings.

Motivated by Bunimovich's recent paper [1] already discussed in the context of chaotic maps (see section 2.1.2), there are many interesting remarks which one may derive from formula's like (3.33) and (3.35) almost for free. One of them is that when $c = \sqrt{4 - 2\sqrt{2}}$, then the collision process at the elliptical arcs stretches near bouncing ball orbits so that at each semi-ellipse only a factor of $\cosh^{-1}\sqrt{2}$ of them survive up to time t. In fact $P(t, c)$ is maximized when $c = \sqrt{4 - 2\sqrt{2}}$. We may thus define the function

$$\mathcal{F}(c) = \frac{\left(\frac{4}{c^2} - 1\right) \ln\left(\frac{4}{c^2} - 1\right)}{2\left(\frac{2}{c^2} - 1\right)\frac{1}{c^2}}, \tag{3.37}$$

such that $\mathcal{F}(c) \in \left(\frac{3\ln 3}{2}, 2\cosh^{-1}(\sqrt{2})\right)$ is a factor describing how near bouncing ball orbits are stretched by a reflection on the semi-elliptical arcs of the billiard.

Other questions that one might be interested in are concerned with the effect the position of the hole has on the survival probability. We find that $P(t, L, c, h^-, h^+)$ is maximized when the hole is placed at one of the ends of the straight segments, that is when $h^- = -L$ or $h^+ = L$ hence eliminating the cropping effect of $\mathcal{F}(c)$ at one of the ends of the billiard discussed above. Similarly, $P(t, L, c, h^-, h^+)$ attains its lowest value when the hole is placed in the middle of the straight segment. Hence one can calibrate $P(t, L, c, h^-, h^+)$ by changing the curvature of the elliptical arcs, or by shifting the hole along the straight segments rather than simply changing the size of the hole.

We can also consider the case of having two holes of the same size $\epsilon > 0$, on any of the straight segments of the billiard. The holes are situated at $x \in (h_1^-, h_1^+)$ and $x \in (h_2^-, h_2^+)$, such that $h_i^+ = h_i^- + \epsilon$ $(i = 1, 2)$, and $h_1^+ \leq h_2^-$. Then, the long time survival probability is

$$P(t, L, c, h_1^-, h_1^-, \epsilon) = \frac{1}{2(4L + \mathcal{E})t}\left[(\mathcal{F}(c) + 2)\left((L + h_1^-)^2 + (L - h_2^+)^2\right) + 2(h_2^- - h_1^+)^2\right], \tag{3.38}$$

where we have neglected terms of order $\sim t^{-2}$.

In this case, one finds that $P(t, L, c, h_1^-, h_1^-, \epsilon)$ is maximum when the holes are situated at either ends of the straight segments, that is $h_1^- = -L$ and $h_2^+ = L$. The minimum value of $P(t, L, c, h_1^-, h_1^-, \epsilon)$ is now attained when $h_1^- = \tilde{h}_1^- = -\frac{4\epsilon + L(\mathcal{F}(c)+2)}{\mathcal{F}(c)+6}$ and $h_2^- = \tilde{h}_2^- = -(\tilde{h}_1^- + \epsilon) = -\tilde{h}_1^+$. The result is symmetric as expected. It is quite interesting to note that one central hole of twice this size (2ϵ), produces the same value of $P_s(t)$ as having two holes, each of size ϵ, situated at $h_1^- = \tilde{\tilde{h}}_1^- = \frac{(\mathcal{F}(c)-2)\epsilon - 2L(\mathcal{F}(c)+2)}{\mathcal{F}(c)+6}$ and $h_2^- = \tilde{\tilde{h}}_2^- = -\tilde{\tilde{h}}_1^+$.

The above result can be further generalized to n number of holes where the sum of their lengths is fixed, but each individual hole may be of different size, i.e.

$\sum_{i=1}^{n}(h_i^+ - h_i^-) = \sum_{i=1}^{n}\epsilon_i = \Delta$, for $i = 0, 1, 2 \ldots n$. We find

$$P(t, L, c, h_1^-, \ldots, h_n^-, \epsilon_1, \ldots, \epsilon_n) = \frac{1}{2(4L+\mathcal{E})t}\Big[\big(\mathcal{F}(c)+2\big)\Big((L+h_1^-)^2 + (L-h_n^+)^2\Big) + 2\sum_{i=1}^{n-1}(h_{i+1}^- - h_i^+)^2\Big] + \mathcal{O}\left(\frac{1}{t^2}\right). \tag{3.39}$$

Further relations for the maximum and minimum value for $P(t, L, c, h_1^-, \ldots, h_n^-, \epsilon_1, \ldots, \epsilon_n)$ can be derived easily using simple differentiation, as done for the cases of one and two holes above.

We expect that such results might be of use to experimentalists in the fields of ultra-cold atoms confined in a spatial structure formed by beams of light and similarly in the study of quantum dots shaped as the stadium billiard.

In the next chapter we consider the open stadium with holes on the circular segments. Such an example is expected to behave very similarly to the case described in the present paper as is numerically shown in [159]. This is because the trajectories which dominate and survive for long times will also be characterized by small (near vertical) angles. Their collisions will mainly be with the straight segments of the billiard, but also on very short segments of the semicircular arcs. What is obviously different in such a situation is that the number of collisions with the semicircular arcs is not restricted to only one, as was the case here. This fact will complicate the dynamics substantially. Therefore, we opt for a probabilistic approach, as suggested by in Armstead's *et al.* [83], rather than an analytic one.

Chapter 4

The open-ended Stadium

In the previous chapter we investigated the open stadium billiard with one or more holes on its straight segments. We showed that the survival probability function $P(t)$ experiences a cross-over at longer times, from exponential to a power-law behavior $\mathcal{C}/t$ and devised of a method by which one can calculate $\mathcal{C}$ to leading order by only knowing the small angle collision rule where the curved and straight segments of the billiard boundary connect *smoothly* (see equations (3.33) and (3.35)).

In this much shorter chapter, we investigate the *open-ended* stadium billiard through a probabilistic approach motivated from Ref [83]. The open-ended stadium is formed by removing part of its wings therefore exposing the inside of the billiard from either side while keeping small yet important circular segments. The survival probability of this system is expected to behave similarly to the case described in the previous chapter with the survival probability $P(t) \sim \mathcal{C}/t$. This because the long surviving trajectories are again characterized by small (near vertical) angles. We model the small angle collision rule (3.10) and (3.11) as an independent identically distributed random variable (i.i.d.r.v.) and attempt to calculate the probability density function of n such collision events. We thus derive a result for the product of n uniformly i.i.d.r.v's though fail to implement it successfully for our purpose of calculating $P(t)$ at large times t for the open-ended stadium billiard. Reasons for this are given at the end of the chapter. The numer-

ical simulations presented in this and remain chapters have been performed using a code written by Dettmann in C++ and is briefly described in Ref [81] (page 9).

4.1 Open-ended setup of the billiard

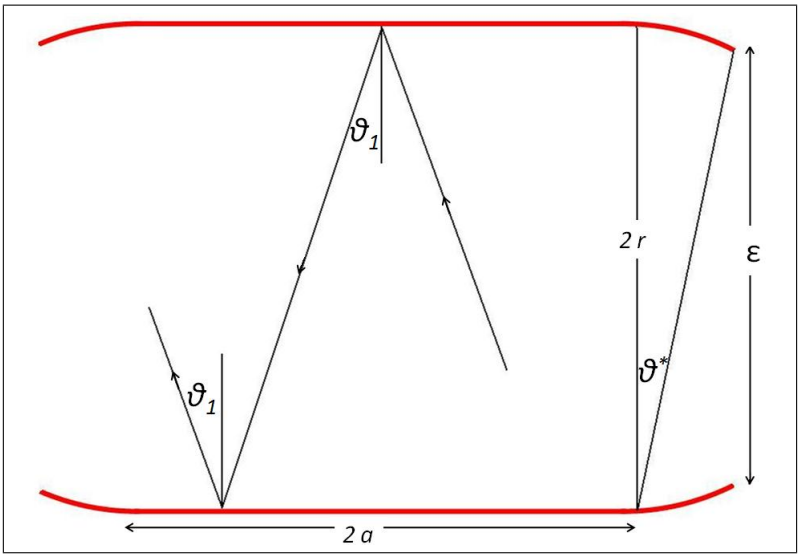

Figure 4.1: The open-ended stadium billiard is obtained by partly removing opposite ends so that two opposite holes are of opening height ε.

Consider the open-ended stadium as shown in Figure 4.1. The length of the straight segments is $2a$ and the radius of the circular arcs is r. The billiard has been trimmed at the ends so that two opposite holes are of opening height ε. A more convenient quantity to work with is $\theta^* = \frac{\sqrt{r^2-\frac{\varepsilon^2}{4}}}{r-\frac{\varepsilon}{2}}$ which approximately describes the minimum angle of escape. We will consider orbits defined by their initial position coordinates $x_1 \in (-a, a)$, $y_1 = \pm r$ and their initial direction $\theta_1 \in (-\frac{\pi}{2}, \frac{\pi}{2})$ such that it is positive if it points to the right of the inward boundary normal.

4.2 Numerical motivation

A numerical simulation identifying the set of initial conditions $(x_1, -r, \theta_1)$ which survive up to $t = 1000$ is shown in Figure 4.2. An immediate similarity with the orbits in Figure 3.4 is observed, though each spike seems to be composed by

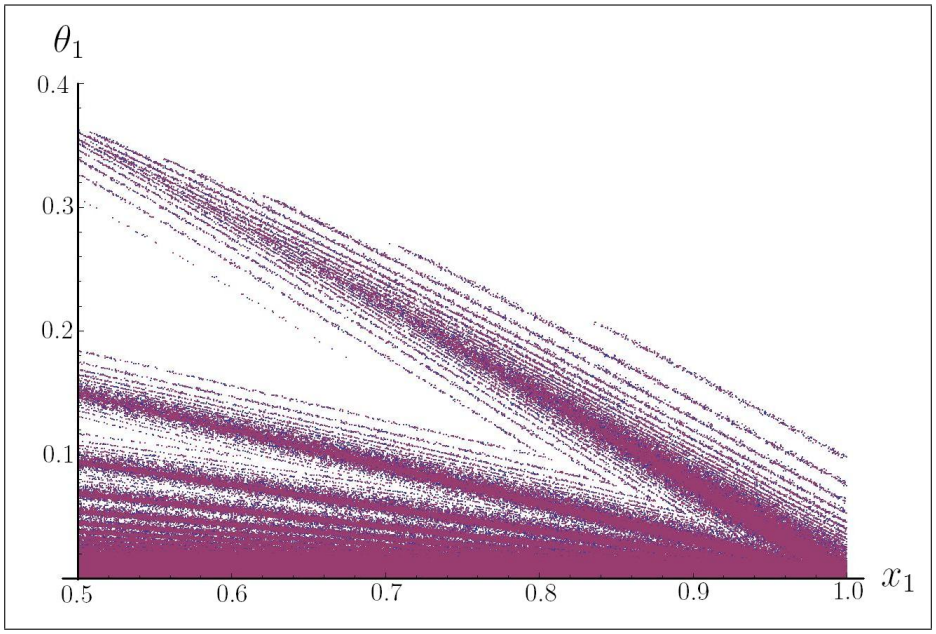

Figure 4.2: Numerical simulation showing of the set of initial conditions (x_1, y_1, θ_1) such that $x_1 \in (a/2, a)$, $y_1 = -r$, and $\theta_1 \in (0, 0.4)$ which survive for up to $t = 1000$. The values used here are $a = 1, r = 1$ and $\varepsilon \approx 1.936$ (see also Figure 4.1).

many other self similar spikes. This *spike within spike* structure is attributed to the number of *runs*, an initial condition will make along the length of the billiard $2a$, or equivalently the number of nonlinear collision processes k an initial condition will experience before escaping. Note that in the previous chapter $k \leq 1$. This observation makes an analytic approach unfavorable if not unrealistic and suggests a different approach.

4.3 A probabilistic approach

Given the numerical discoveries concerning the dynamics of the open-ended stadium billiard one might choose to attempt a probabilistic approach. Armstead *et al.* [83] in fact suggest such a probabilistic model for orbits with small angles but only implement it numerically. They first note that every reflection process off a semi-circular wall changes the angle of incidence for the next string of reflections along the straight segment of the billiard by at most a factor of 3 (this was also

seen in (3.10) and (3.11)). They also note that each reflection process denoted by n, differs by a time of $2a/\theta_n$. Therefore, a small change $\delta\theta$ in the angle of incidence θ_n produced by the reflection process at the semi-circular ends can bring about a change of $(2a/\theta_n^2)\delta\theta$ for the time needed for the orbit to traverse the length $2a$ of the billiard, which for $\theta_1 \ll 1$ can be large even for fractional changes $\delta\theta/\theta_n$. Hence, Armstead *et al.* suggest that the linearized map $M(x_n, \theta_n) = \frac{\theta_{n+1}}{\theta_n} \in [\frac{1}{3}, 3]$ (see also eq (A.2)) can be well approximated by a map $f(\theta_n) = \frac{\theta_{n+1}}{\theta_n} \in [\frac{1}{3}, 3]$ which is independent of initial position x_1. Furthermore, by assuming that subsequent reflections are independent events we may attempt to model this function $f(\theta_n)$ as a random variable X_n uniformly distributed on $[1/3, 3]$. Hence we have that for example $\theta_3 = f(\theta_2)\theta_2 = f(f(\theta_1)\theta_1)f(\theta_1)\theta_1$ and hence $\frac{\theta_3}{\theta_1} \approx \mathbb{E}(X_1 X_2)$. Similarly

$$\frac{\theta_n}{\theta_1} \approx \mathbb{E}\left(\prod_{j=1}^{n} X_j\right), \tag{4.1}$$

where $\mathbb{E}(X)$ denotes the expectation value of X.

4.4 Product of n Uniform random variables

To obtain the probability density function of a product of two continuous random variables is explained for example by Rohatgi [166]:

Theorem 1. *Let X be a random variable of the continuous type with PDF $f(x)$ which is defined and positive on the interval (a, b), where $0 < a < b < \infty$. Similarly, let Y be a random variable of the continuous type with PDF $g(y)$ which is defined and positive on the interval (c, d), where $0 < c < d < \infty$. The PDF of $V = XY$ is:*

$$h(v) = \begin{cases} \int_a^{v/c} g(\frac{v}{x}) f(x) \frac{1}{x} \mathrm{d}x, & ac < v < ad, \\ \int_{v/d}^{v/c} g(\frac{v}{x}) f(x) \frac{1}{x} \mathrm{d}x, & ad < v < bc, \\ \int_{v/d}^{b} g(\frac{v}{x}) f(x) \frac{1}{x} \mathrm{d}x, & bc < v < bd, \end{cases}$$

when $ad < bc$,

$$h(v) = \begin{cases} \int_a^{v/c} g(\frac{v}{x}) f(x) \frac{1}{x} \mathrm{d}x, & ac < v < ad, \\ \\ \int_{v/d}^{b} g(\frac{v}{x}) f(x) \frac{1}{x} \mathrm{d}x, & bc < v < bd, \end{cases}$$

when $ad = bc$, *and*

$$h(v) = \begin{cases} \int_a^{v/c} g(\frac{v}{x}) f(x) \frac{1}{x} \mathrm{d}x, & ac < v < bc, \\ \\ \int_{v/d}^{v/c} g(\frac{v}{x}) f(x) \frac{1}{x} \mathrm{d}x, & bc < v < ad, \\ \\ \int_{v/d}^{b} g(\frac{v}{x}) f(x) \frac{1}{x} \mathrm{d}x, & ad < v < bd, \end{cases}$$

when $ad > bc$.

The product of 2, identically distributed, uniform random variables can be calculated by taking $a = c$ and $b = d$ and using **Theorem 1.** The product of 3, identically distributed, uniform random variables can be calculated by using the theorem twice, and so on. In our paper Ref [88] which is also included in Appendix B we obtain a formula for calculating the probability density function of the product of n independently and identically distributed uniform $[a, b]$ random variables and present the method of its derivation. Here we restate the final result:

Theorem 2. *Let* X_i *be independent random variables with PDF* $f_{X_i}(x) = \frac{1}{b-a}$ *on the interval* $x \in [a, b]$ *and* 0 *otherwise, where* $0 \leq a < b < \infty$ *and* $i = 1, 2, \ldots n$, $n \geq 2$. *Then the PDF of* $X = \prod_{i=1}^{n} X_i$ *is given by the piecewise smooth function:*

$$f_X(x) = \begin{cases} f_X^k(x), & a^{n-k+1} b^{k-1} \leq x \leq a^{n-k} b^k, \\ & k = 1, 2, \ldots n, \\ \\ 0, & \text{otherwise}, \end{cases} , \tag{4.2}$$

where

$$f_X^k(x) = \sum_{j=0}^{n-k} \frac{(-1)^j}{(b-a)^n (n-1)!} \binom{n}{j} \Big(\ln \frac{b^{n-j} a^j}{x} \Big)^{n-1}. \tag{4.3}$$

In the case of the open-ended stadium $a = 1/3$ and $b = 3$. Hence **Theorem 2.** reads:

$$f_X^k(x) = \sum_{j=0}^{n-k} \frac{(\frac{3}{8})^n(-1)^j}{(n-1)!}\binom{n}{j}\Big(\ln\frac{3^{n-2j}}{x}\Big)^{n-1}. \tag{4.4}$$

for $k = 1, 2, \ldots n$, and each function $f_X^k(x)$ is supported on $3^{(2k-n-2)} < x < 3^{(2k-n)}$.

4.5 The end of the Road

The result above is expected to be of use to many applications involving Uniform random variables. However, it seems to have lead us to a "dead end" as we are not able to obtain the PDF of the survival times as a function of time. Our result lacks any information about N, the number of reflections needed for the initial angle θ_1 to grow larger than θ^*. To see this consider the time to escape T which is a function of the initial conditions x_1, θ_1 given by

$$T(x_1, \theta_1) = \frac{a - x_1}{\theta_1} + \frac{2a}{\theta_2} + \frac{2a}{\theta_3} + \frac{2a}{\theta_4} + \ldots + \frac{2a}{\theta_N}, \tag{4.5}$$

such that $\theta_{N-1} < \theta^* < \theta_N$. Given our assumptions above, we have that

$$T(x_1, \theta_1) = \frac{a - x_1}{\theta_1} + 2a\sum_{n=2}^{N}\frac{1}{\theta_n} \approx \frac{a - x_1}{\theta 1} + \frac{2a}{\theta_1}\sum_{n=2}^{N}\Big(\prod_{j=1}^{n-1} X_j\Big)^{-1}. \tag{4.6}$$

However we are able to test our result next to the Central Limit Theorem (CLT) numerically. From Equation (4.1) we have $\frac{\theta_n}{\theta_1} = \prod_{i=1}^{n} X_i$, where X_i are independent random variables with PDF $f_{X_i}(x) = \frac{3}{8}$ on the interval $x \in (\frac{1}{3}, 3)$ and 0 otherwise. Hence, given an orbit's angle θ_1 and θ^* we may calculate its distribution as a function of the number of reflections n. A code for calculating the cumulative distribution function (CDF) of (4.3) is included in Appendix *C*. Similarly we may apply the CLT and compare. This is done by expressing the product of X_i's, as the exponential of the sums of the logarithm of the X_i's. By the CLT:

$$\prod_{i=1}^{n} X_i = \exp(n\mu + \xi\sqrt{n}\sigma), \tag{4.7}$$

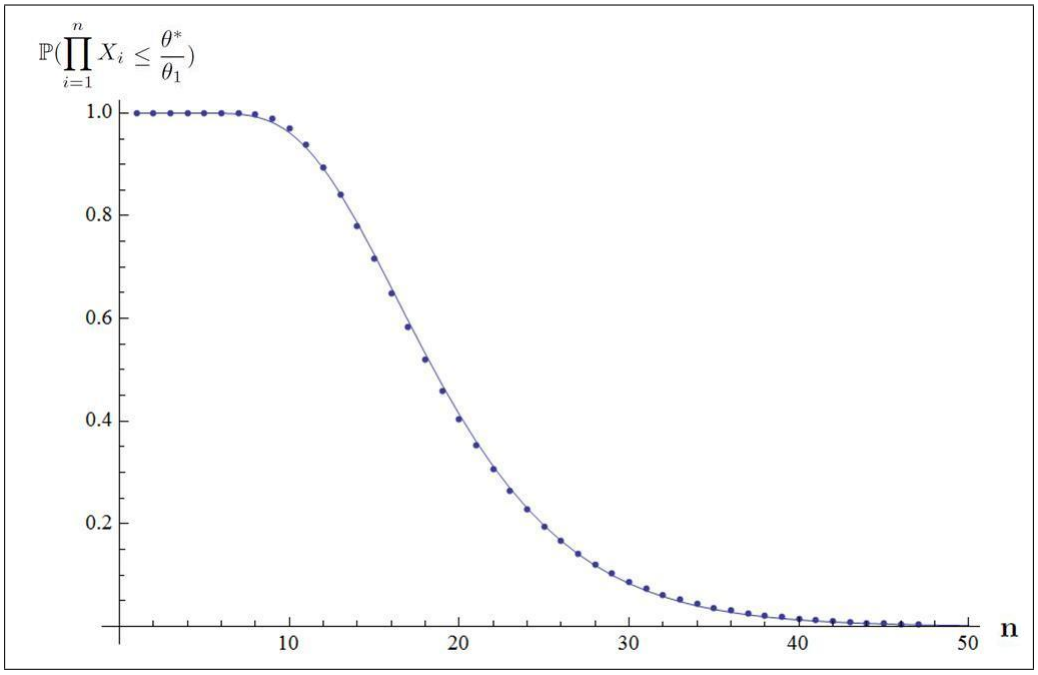

Figure 4.3: Numerical calculation of the survival probability for $\frac{\theta^*}{\theta_1} = 1000$ using equation (4.4) (dots), and the CLT result (4.8) (full line).

where

$$\mu = \mathbb{E}\big((\ln X_i)\big) = 0.373265, \sigma = \sqrt{\mathbb{E}\big((\ln X_i)^2\big) - \big(\mathbb{E}((\ln X_i))\big)^2} = 0.566649,$$

and ξ is a random variable distributed Normally with mean zero and standard deviation one. Thus:

$$\mathbb{P}(\prod_{i=1}^{n} X_i \leq \frac{\theta^*}{\theta_1}) = \mathbb{P}(\xi \leq \frac{\ln \frac{\theta^*}{\theta_1} - n\mu}{\sqrt{n}\sigma}) = \frac{1}{2}\mathrm{erfc}[\frac{\ln \frac{\theta^*}{\theta_1} - n\mu}{\sqrt{2n}\sigma}]. \tag{4.8}$$

The two results are found to be in excellent agreement as shown in Figure 4.3.

Chapter 5

Time-dependent asymmetric transport

The survival probability of the open stadium billiard with one hole on its boundary is well known to decay asymptotically as a power law due to the stickiness introduced by the bouncing ball orbits. This is expected to persist even if the hole is placed on the curved segment of the billiard and was addressed without much success in the previous chapter.

In this chapter we investigate the *transmission* and *reflection* survival probabilities for the case of *two* holes placed *asymmetrically*. Classically, these distributions are shown to lose their algebraic decay tails depending on the choice of injecting hole therefore exhibiting asymmetric transport. The mechanism behind this is explained while exact expressions are given and confirmed numerically. We propose a model for experimental observation of this effect using semiconductor nano-structures and comment on the relevant quantum time-scales. The results of this chapter have been published in Ref [79] and therefore this chapter follows the published article closely.

5.1 Introduction

The set up we consider in this chapter is motivated from the study of Quantum open billiards. Quantum open billiards were experimentally realized first in flat microwave resonators in the early 90's [167, 168] and later in semiconductor nanostructures such as quantum dots [66, 51]. Experiments perturbing these systems with small magnetic fields exhibit principal quantum interference effects like weak localization, Altshuler-Aronov-Spivak oscillations and conductance fluctuations, all of which semiclassical theory has arguably succeeded to explain using properties of the underlying classical dynamics [51, 67]. Similarly, in microwave resonators, due to their clean, impurity-free geometry and the tunable coupling strength to the various decay channels, predicted phenomena such as resonance trapping have been experimentally observed [169].

Here we investigate the classical transport of a popular example for the above and other experiments, the stadium billiard with two holes on its boundary placed asymmetrically (see Figure 5.1). Looking at the phase space of this open system, we find that the predominantly chaotic character of the corresponding closed system is non-trivially affected by the positioning of the holes. In particular we find that the transmission and reflection probabilities, when particles are injected from one of the two holes, are qualitatively different at long times depending on the choice of the injecting hole therefore displaying time-dependent asymmetric transport. We give detailed analytical expressions for these distributions and confirm them numerically. Although investigations through random matrix theory (RMT)[170] regarding the variety of symmetric or asymmetric openings in chaotic systems have been performed [171], to the best of our knowledge there has been no analogous analytic prediction or experimental observation of such an asymmetry in the transport. Hence we conclude with a discussion of a possible experimental model with regards to the relevant quantum time scales.

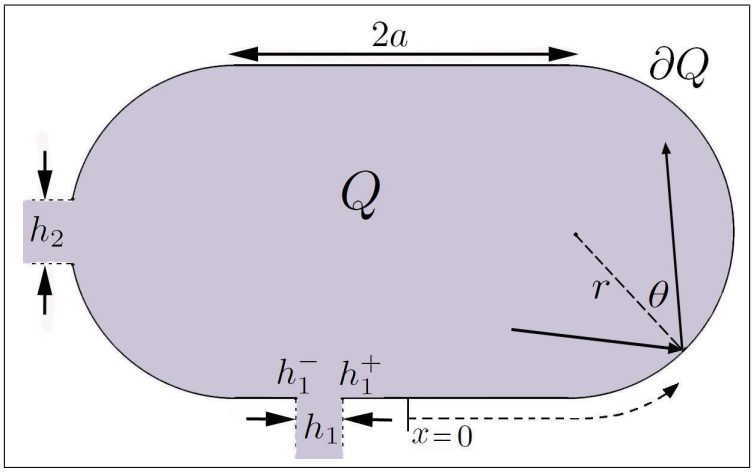

Figure 5.1: Stadium billiard with two holes H_1 and H_2. The billiard map is parameterized using arc length $0 \leq x < 4a + 2\pi r$ and velocity parallel to the boundary $v \sin\theta$ with $\theta \in (-\frac{\pi}{2}, \frac{\pi}{2})$. The hole on the straight segment is such that $-a < h_1^- < h_1^+ < a$.

5.2 Transport and Escape from two holes

Consider the case of the stadium with two holes as shown in Figure 5.1. In Figure 5.2 we plot in the top panel a picture of the phase space, showing in different colors, the different sets of initial conditions which eventually exit through each hole. The bottom panel shows the time scales of escape as noted in the caption. We notice that the phase space is again separated, as described above, and that the sticky, long-surviving orbits escape only through the hole on the straight segment H_1. Restricting the initial density of particles to one of the holes defines the transport problem and establishes the schematic setup of quantum dots and microwave cavities, where particles/waves are injected through one of the holes and allowed to escape through either, thus creating a direct link with experiment. Looking at the spatial distribution of the final (escape) coordinates (x_f, θ_f) (see Figure 5.3) we also notice that long surviving orbits entering and subsequently exiting through H_1, unlike in the other possible entry/exit combinations, accumulate on the edges of the hole $x_f = h_1^{\pm} \mp \delta$, $(\delta \ll 1)$ and have small angles θ_f. Note that $(x_f, \theta_f) \to (h_1^{\pm}, 0^{\pm})$ as the time of escape $t_f \to \infty$. This further confirms the splitting of the phase space, but also that the classical *spatial* distribution of

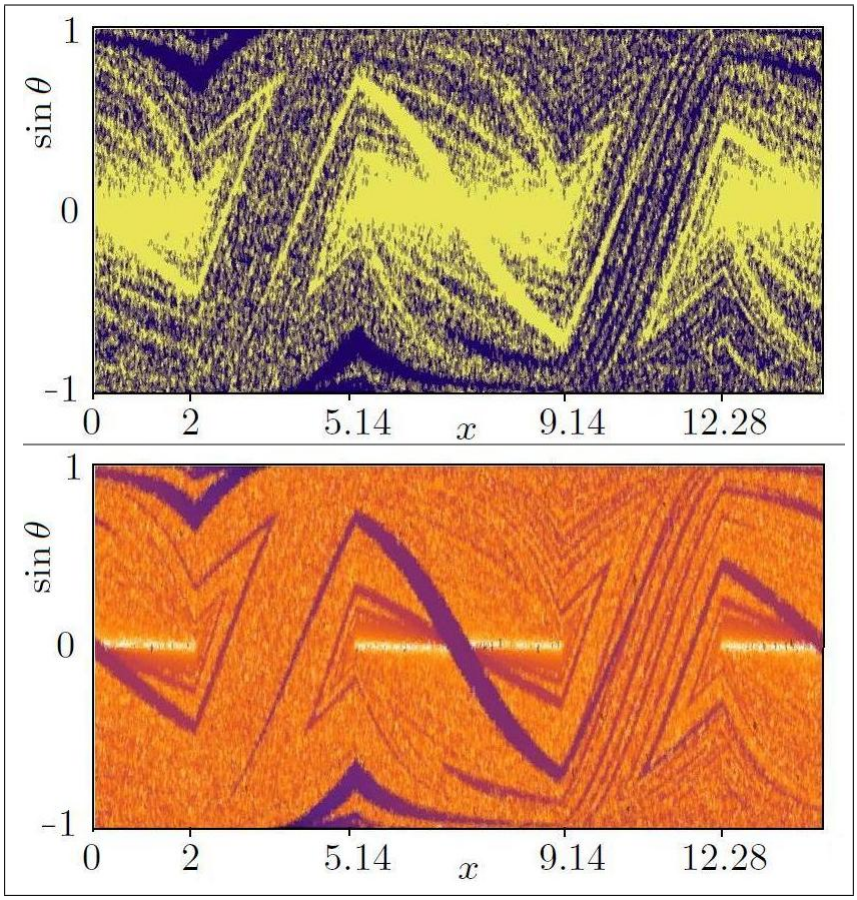

Figure 5.2: Phase space of open stadium with 2 holes. *Top*: Initial conditions which will escape through hole H_1 are shown in light yellow while those escaping through hole H_2 in dark blue. *Bottom*: Color grading of initial conditions going from purple (dark), to orange, to white corresponding to short, medium and long escape times. ($a = 2$, $r = 1$, $h_i = 0.5$, $h_1^+ = 0.25$).

exiting particles has a well defined time-dependent character, which only exists in the situation described and plotted in Figure 5.3.

In order to quantify our above observations, we define transmission and reflection survival probabilities by $P_i^j(t)$ and $P_i^i(t)$ respectively $(i, j = 1, 2)$, such that

$$P_i^j(t) = P(x_1 \dots x_{\mathcal{N}} \notin H \big| x_0 \in H_i, x_f \in H_j), \tag{5.1}$$

where $H = H_1 \cup H_2$, $\mathcal{N}(x_0, t)$ is the number of collisions with the boundary up to time t and x_n denotes the position of the particle at the nth collision. For example, $P_1^2(t)$ is the probability that a particle injected from hole H_1 will survive until time t given that it will escape through hole H_2. It follows from our construction that

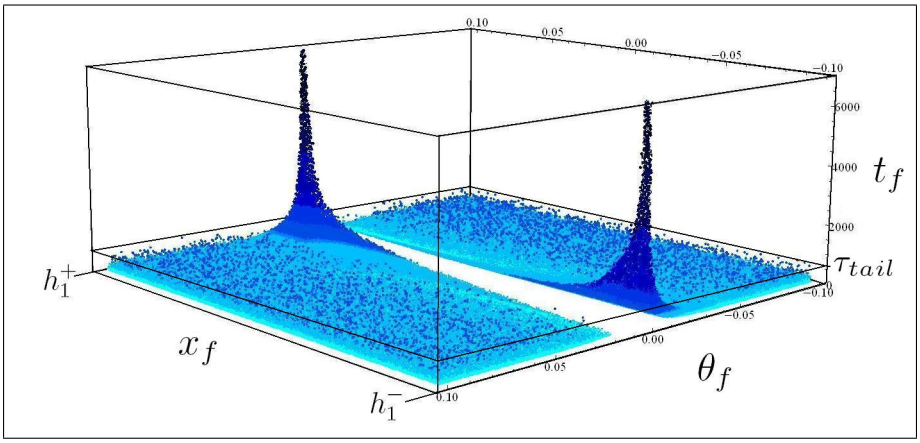

Figure 5.3: 3D plot of the final (escape) coordinates and time of escape (x_f, θ_f, t_f) for the case of entry and exit through H_1. The color scheme runs from light to dark blue linearly with increasing exit times t_f. Only in this case are the 2 dark spikes observed. ($a = 2$, $r = 1$, $h_i = 0.2$, $h_1^+ = 0.1$). $\tau_{tail} \approx 631.85$ is explained in Figure 5.4.

$P_1^1(t)$ has an algebraic decay tail while the other three possible distributions do not and thus decay purely exponentially with an escape rate given by

$$\gamma = \frac{h_1 + h_2}{\langle \tau \rangle |\partial Q|}. \tag{5.2}$$

The algebraic tail of $P_1^1(t)$ is due to particles injected near the edges of hole H_1, with small incident angles θ but which do not immediately reflect back into H_1. This extra constraint is described by

$$|\theta| > \arctan \left| \frac{h_1^{\pm} - x_0}{4r} \right|, \tag{5.3}$$

($\pm$ depending on the sign of θ) and gives $P_1^1(t)$ an algebraic tail $\mathcal{O}(t^{-2})$, as expected in integrable scattering problems. As in the one hole escape problem, the phase space is split and fully-chaotic orbits cannot enter the sticky region and therefore do not contribute to the algebraic tail of $P_1^1(t)$. Furthermore, the imposed 'preference' of long surviving particles to escape through H_1 as indicated by Figures 5.2 and 5.3, is what denies $P_1^2(t)$ an algebraic tail. In the reverse situation of particles injected through H_2, the splitting of the phase space due to the position of H_1, renders the sticky region surrounding the bouncing ball modes inaccessible. Thus both $P_2^1(t)$ and $P_2^2(t)$ do not have algebraic tails. This would

not have been be the case if both H_1 and H_2 were placed on a straight[1] or curved segment of the boundary.

In summary the total survival probability $P_i(t)$, where the subscript i indicates the injecting hole, is given by:

$$P_1(t) = e^{-\gamma t} + \frac{D}{t^2} = \wp_1^1 \overbrace{\left(e^{-\gamma t} + \frac{D}{\wp_1^1 t^2}\right)}^{P_1^1(t)} + \wp_1^2 \overbrace{e^{-\gamma t}}^{P_1^2(t)}, \tag{5.4}$$

$$P_2(t) = e^{-\gamma t} = \wp_2^2 \overbrace{e^{-\gamma t}}^{P_2^2(t)} + \wp_2^1 \overbrace{e^{-\gamma t}}^{P_2^1(t)}, \tag{5.5}$$

for $t > \hat{t}$, where the $\wp_i^j$ are time independent coefficients controlling the $t \to \infty$ reflection and transmission probabilities. Notice that $\wp_i^1 + \wp_i^2 = 1$ due to flux conservation, and $\wp_1^2 = \wp_2^1$ due to time-reversal symmetry. D is given by a similar calculation to that of section 3.5:

$$D = \frac{r(3\ln 3 + 4)\Big((a + h_1^-)^2 + (a - h_1^+)^2\Big)}{2h_1 v^2} + \mathcal{O}\left(\frac{1}{t}\right). \tag{5.6}$$

with parameters as defined in Figure 5.1.

In Figure 5.4, we plot the four conditional distributions $P_i^j(t)$ as functions of time t, and find an excellent agreement with the analytical results summarized in equations (5.4)-(5.5). This is the simplest possible example where a classically fully chaotic billiard exhibits time-dependent asymmetric transport when opened. This phenomenon we expect to be shared by many other well studied chaotic or mixed open billiards which display intermittency due to the presence of marginally unstable periodic orbits such as the drivebelt [138] and mushroom [149, 91] billiards. We note that the variety of options with regards to hole positions and sizes and system parameters offers ways of calibrating and controlling these classical distributions as to achieve faster or slower escape. This point of view relates closely to that of Ref[1] discussed in section 2.1.2. Also, the exact results obtained here encourage the possibility of experimental observation of the quantum ana-

[1]We exclude here the case where both holes are on straight segments and one or both are right at the edge.

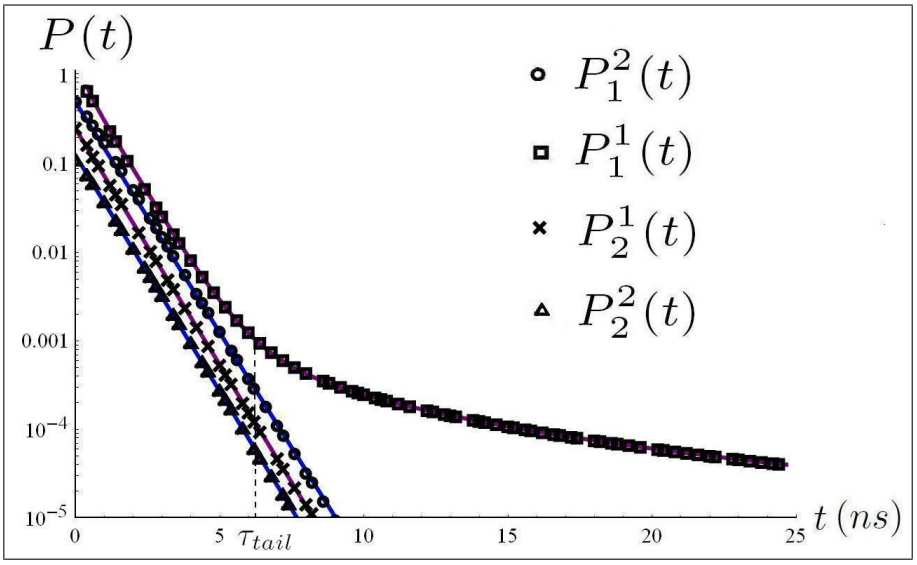

Figure 5.4: Slightly offset plots comparing numerical simulations (see key) with the analytic expressions (5.4) and (5.5) (solid curves) as functions of time t in ns. The simulations consist of 10^9 particles with stadium parameters given by: $a = 2\ \mu m$, $r = 1\ \mu m$, $h_i = 0.2\ \mu m$ and $h_1^- = 0$. $\tau_{tail} \approx 6.315\ ns$ is the large solution of $e^{-\gamma t} = \frac{D}{\wp_1^1 t^2}$, where $\wp_1^1 \approx 0.5594$ was calculated numerically.

logue of asymmetric transport in cavities with classically chaotic closed dynamics, which we discuss next.

5.3 Correspondence in Quantum Dots

At low temperatures ($\sim$ 15mK), electronic transport through the gate electrodes (openings) of a 2D electron gas (quantum dot) in a high quality sample is ballistic [66, 51] with quantized entry angles as described in (1.4). For typical semiconductor nano-structure parameters, the time scale τ_{tail} at which the above observed algebraic tail becomes visible (see Figures 5.3 and 5.4) is of the order of a nanosecond (assuming an electron speed $v \approx 10^5\ ms^{-1}$). This is slightly larger than the predicted Ehrenfest time $\tau_E = \lambda^{-1} \ln(1/\hbar)$ for chaotic systems [52] (the time scale at which quantum interference effects become apparent $\approx 0.3\ ns$), and thus at first instance suggests that direct observation of a quantum difference in transmission and reflection survival probabilities is unlikely in existing devices. However, since

the nature of chaos lies in orbital instability, the Ehrenfest time varies with the fluctuations of the Lyapunov exponent, which are further intensified by leaks in the system [172]. In the case studied here however, the effect of hole H_1 is crucial since for the sticky, near-bouncing ball subset of the phase space, the finite-time local Lyapunov exponent is zero [173], therefore leading to a much longer validity and persistence of the classical description. In fact, this region could be thought of as an h_1-dependent fictitious island of stability in which loss of quantum-to-classical correspondence is much slower, resembling that in mixed systems, such that $\tau_E \propto \hbar^{-1/\beta}$ [174], where β is a scaling parameter characteristic of the system's local phase space structure. Furthermore, we find that by varying the size and hole positions of the dot (while remaining in the ballistic regime) it is possible to calibrate and reduce τ_{tail} by a whole order of magnitude. A good way to do this is by elongating the stadium slightly such that $a/r \approx 5$ and by placing H_1 at the very edge of the straight segment.

Suppose we apply a time-dependent voltage $V(t)$ across the gates of the stadium heterostructure such that the incoming current $I_i^{in}(t)$ through hole H_i is proportional to $V(t)$. Then the charge exiting through each hole will follow the driving current with a lag-time τ which is distributed according to (5.4) or (5.5) appropriately. This can be modeled by

$$I_j(t) = (-1)^{i+j+1}\wp_i^j \int_0^\infty I_i^{in}(t-\tau)\frac{\mathrm{d}P_i^j(\tau)}{\mathrm{d}\tau}\mathrm{d}\tau, \tag{5.7}$$

where i and j indicate the injecting and exiting hole respectively. The observed, net current through the system is thus given by $I_i^{net}(t) = I_i^{in}(t) + I_1(t) + I_2(t)$. Because the probability density $\frac{\mathrm{d}P_1^1(\tau)}{\mathrm{d}\tau}$ is slightly skewed to the right, relative to the other densities, the two observables $I_1^{net}(t)$ and $I_2^{net}(t)$ will differ by

$$\wp_1^1 \int_0^\infty \frac{\mathrm{d}I^{in}(t-\tau)}{\mathrm{d}\tau}\left(P_1^1(\tau) - P_2^2(\tau)\right)\mathrm{d}\tau. \tag{5.8}$$

For experimental observation we propose using a square wave signal $V(t) = V_0\left(1 + sign(\sin\omega t)\right)$ such that $\omega > \pi/\tau_{tail}$ as to accentuate the power-law contribution of $P_1^1(t)$. Quantum interference effects such as universal conductance

fluctuations may be statistically removed since the skewness of $\frac{\mathrm{d}P_1^1(\tau)}{\mathrm{d}\tau}$ is to leading order geometry dependent through the constant D in (5.6). In experiments of course, one should make sure that the excess density of charged particles within the dot is always low enough as to avoid a build up of an internal electric field which would effectively destroy the fictitious island of stability (sticky region) enclosing the bouncing ball orbits. For microwave billiards this is not an issue.

5.4 Conclusions and Discussion

To conclude, we have investigated the classical dynamics of the chaotic stadium billiard with two holes placed asymmetrically. We have found that the transmission and reflection survival distributions can have algebraic and exponential decays observed in the same classically ergodic geometry depending on the choice of injecting hole. We have identified the reason for this being the hole's asymmetric positioning on the straight segment of the billiard, which essentially splits the classical phase space of the system, rendering the sticky region surrounding the bouncing ball orbits inaccessible to chaotic orbits. As a result, the transmission and reflection survival distributions are qualitatively different. Moreover, when injecting from the hole on the curved segment both transmission and reflection distributions decay with a pure exponential. We expect that this observation along with the analytic expressions obtained and confirmed numerically can be appreciated by the (quantum) chaos community. We further propose that observation of this classical result in semiconductor nano-structures (quantum dots) or microwave cavities can improve our understanding of classical to quantum correspondence in transport problems in relation with the different quantum time scales introduced by the classical phenomenon of stickiness. Finally, we expect that the asymmetric transport scenario exhibited here as well as the mechanism described may apply in a similar way to more general open dynamical systems with mixed phase space [90], permitting dynamical trapping of trajectories by suitably placed holes. This shows that long studied systems such as the stadium billiard continue

to provide us with interesting new phenomena to study.

Chapter 6

Mushrooms: Stickiness revisited

In this chapter we investigate the stickiness exhibited by mushroom billiards, a class of dynamical systems with sharply divided phase space. For typical values of the control parameter of the system ρ, an infinite number of marginally unstable periodic orbits (MUPOs) exist making the system sticky in the sense that unstable orbits approach regular regions in phase space and thus exhibit quasi-regular behavior for long periods of time. As will be defined in due course, ρ is the ratio between stem opening and hat radius, effectively controlling the size of ergodic and integrable components in phase space. The problem of finding these MUPOs is expressed as the well known problem of finding optimal rational approximations of a real number, subject to some system-specific constraints. By introducing a generalized mushroom and using properties of continued fractions, we describe for the first time a zero measure set of control parameter values $\rho \in (0, 1)$ for which all MUPOs are destroyed and therefore the system is less sticky, leading to a different power law exponent for the Poincaré recurrence time distribution statistics. The results of this chapter have been published in Ref [91] and therefore this chapter follows the published article closely.

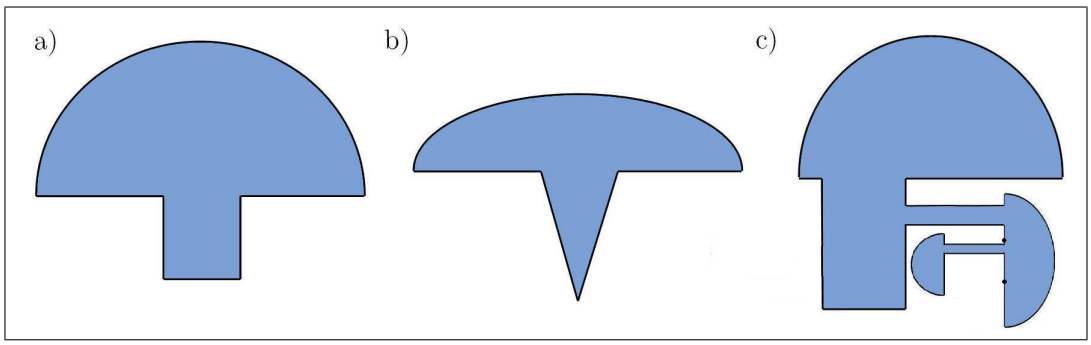

Figure 6.1: a) Simple mushroom, b) Elliptic mushroom with triangular stem, c) 'Honey mushroom' with 4 integrable islands and 2 ergodic (chaotic) components.

6.1 Introduction to Mushrooms

The mushroom billiard is constructed by a convex semi-elliptical (including semi-circular) 'hat' attached to a 'stem' such that their intersection is smaller than the diameter of the hat. Examples are shown in Figure 6.1. It is special in that under certain conditions [149, 175], it forms a class of dynamical systems with sharply divided phase space which are easy to visualize and analyze. For example, the phase space of the mushroom shown in Figure 6.1 a) is composed of a single completely regular (integrable) invariant component and a single connected chaotic and ergodic component (see Figure 6.2b), in contrast with other generic mixed systems such as the standard map (2.28) [104], where KAM hierarchical islands form a dense family in the neighborhood of each other. Interestingly, mushrooms can also be designed to have an arbitrary number of integrable and chaotic ergodic components (see Figure 6.1 c))[149]. Therefore, mushroom billiards are paradigmatic models for studying the phase space dynamics near the boundary of integrable islands but can also be used to study the so called 'LAB' effect [124], where even for systems with interacting particles the stationary distribution can be nonuniform [16]. One must note however that small perturbations (imperfections) to the mushroom's boundary can cause the emergence of KAM islands or even complete chaos [176] (see also Ref [175] for rigorous arguments).

Because of their unusually simple divided classical phase space, mushroom bil-

liards are of increasing interest to the quantum chaos community. As a result, this has facilitated the numerical verification [177] of Percival's conjecture which states that in the semiclassical limit, eigenmodes localize to one or another invariant region of phase space (regular or chaotic), with occurrence in proportion to the respective phase space volumes [178]; recently this has been applied to generalist the boundary term in Weyl's law [179]. Similarly, the mechanism of dynamical tunneling between classically isolated phase space regions has also been investigated in the context of mushrooms [180] and has been observed in microwave mushrooms [181].

Although the classical phase space of mushroom billiards is sharply divided, generic 'simple' mushrooms (Figure 6.1 a)) exhibit long power-law tails of order $\sim t^{-2}$ in the Poincaré recurrence time statistics [182]. These tails have been attributed to the presence of one-parameter families of marginally unstable periodic orbits (MUPOs, see definition in the next section), 'embedded' in the ergodic component of the phase space [182]. The flow close to these orbits, is strongly reminiscent of that close to KAM islands [82] and therefore causes the system to display the phenomenon of 'stickiness', where chaotic orbits stick close to regions of stability for long periods of time causing the emergence of power-law tails (more details in the next section). In fact, the stickiness of chaotic trajectories was shown (using continued fractions representations) to occur through an infinite number of MUPOs concentrating near the border with the regular island [112] (also see [111] for further discussions). Although the quantum analogue of stickiness is not well understood, MUPOs seem to play an important role both in the density of states of microwave billiards [112] and the directionality of dielectric micro-cavities [183, 184].

It is worth mentioning that non-sticky mushrooms have been previously constructed using elliptical hats and non-rectangular stems [175, 32] but have not been studied experimentally yet. Their non-stickiness arises from the fact that each focus of the semi-elliptical hat provides a sharp boundary between rotational and librational orbits, and may be used as the end point of the entrance to the

foot. However, in such a case, some care is needed with the stem's length and it's base width, to ensure sufficient defocusing. In addition to this, the size of the opening of the stem must also ensure a bounded number of maximum possible collisions in the hat [32]. Further details concerning the defocusing mechanism and hyperbolicity in billiards are given in Ref [151].

In this and following chapters we only focus on classes of mushrooms with circular hats, in which stickiness to leading order is due to the presence of MUPOs. In the first part of our investigation we follow the more detailed Ref [111] as well as [112] and express the problem of finding MUPOs as the well known problem of finding optimal rational approximations of a number (see section 6.2). This interesting connection made with number theory allows us to introduce and characterize a zero measure set of control parameter values, using continued fractions, for which all MUPOs are completely removed (see section 6.3). This set, not previously discussed in the literature, corresponds to mushrooms with a less sticky hat, the implications of which are yet to be studied classically or quantum mechanically and are likely to be relevant to applications mentioned above. We obtain upper bounds for MUPO-free and finitely sticky irrational mushrooms and also give an explicit example of a MUPO-free mushroom billiard (see section 6.3.3). Finally we conclude with a short discussion regarding the implications of this chapter's results on quantum and higher dimensional mushrooms (see section 6.4).

6.2 Stickiness in Closed Mushrooms

MUPOs being of zero measure do not affect the overall ergodicity of the system. Yet as we have previously seen in the case of the stadium billiard, they govern long time statistical properties of the system, such as the Poincaré recurrence times statistics $\mathcal{Q}(t) \sim t^{-2}$ [182] which is intimately related [89] with the long time survival probability $P(t) \sim t^{-1}$ [82]of the corresponding open system, as well as the rate of mixing (the rate of the decay of correlations) $\mathcal{C}(t) \sim t^{-1}$ [157]. Fur-

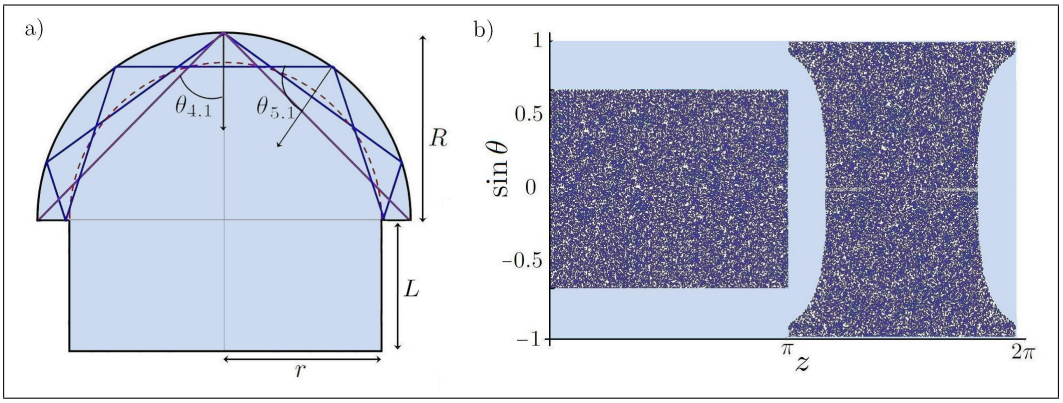

Figure 6.2: *Left*: Any orbit intersecting the dashed red semicircle of radius r is not stable while any orbit not intersecting it is. MUPOs are the periodic orbits which intersect the semicircle while not entering the mushroom's stem. The MUPOs $(s, j) = (4, 1)$ and $(s, j) = (5, 1)$ for $r = 0.83$ are shown. *Right*: Phase space plot of the ergodic component for a simple mushroom using Birkhoff coordinates $(z, \sin\theta)$, with $\frac{r}{R} = 0.65$ and $L = 0.5$. Here, $z \in [0, \pi R + 2(R + L))$ is the arc length parametrization along the billiard's boundary, increasing from zero from the right-most point of the mushroom, in an anticlockwise fashion. $\theta \in \left(-\frac{\pi}{2}, \frac{\pi}{2}\right)$ is the angle of incidence at each collision.

thermore, the exponents of these power-laws appear to be a universal fingerprint of nonuniform hyperbolicity and stickiness, at least for one and two dimensional Hamiltonian systems with sharply divided phase space [82]. The MUPOs in the mushroom's hat and in the annular billiard were extensively studied by Altmann in his PhD thesis [111] and more briefly in Refs [182, 82, 112] and occur in many billiards with circular arcs.

As discussed in the introduction, a generic, simple mushroom billiard's phase space consists of a single integrable and a single ergodic component with an infinite number of MUPOs populating close to the boundary of the ergodic component. These MUPOs are best understood when introduced geometrically. The dashed red semicircle of radius r in Figure 6.2a) corresponds to the border between the ergodic and regular component of the mushroom's phase space (see Figure 6.2b). Any orbit intersecting this semicircle will sooner or later fall into the mushroom's stem and is therefore unstable and lies in the ergodic component of the phase space. Any non-periodic orbit not intersecting the dashed semicircle does not 'see' the

stem and thus exhibits regular motion remaining forever in the mushroom's hat. MUPOs, as shown in Figure 6.2a), are periodic orbits which do intersect it and therefore are not stable though always remain in the mushroom's hat. A compact way of describing them was given in Ref [182]

$$\alpha_{s,j} = \cos\frac{j\pi}{s} \leq \frac{r}{R} < \frac{\cos\frac{j\pi}{s}}{\cos\frac{\pi}{\lambda s}} = \beta_{s,j}, \tag{6.1}$$

where

$$s \geq 3, \qquad 1 \leq j \leq \begin{cases} \frac{s}{2} - 1, & \text{if } s \text{ is even,} \\ \frac{s-1}{2}, & \text{if } s \text{ is odd,} \end{cases} \qquad \lambda = \begin{cases} 1, & \text{if } s \text{ is even,} \\ 2, & \text{if } s \text{ is odd.} \end{cases} \tag{6.2}$$

In equation 6.1), r and R are as defined in Figure 6.2. The coprime integers s and j describe periodic orbits of the circle billiard with angles of incidence $\theta_{s,j} = \frac{\pi}{2} - \frac{j\pi}{s}$. More specifically, s is the period and j the rotation number of the orbit. $R\alpha_{s,j}$ is the shortest distance from the periodic orbit (s, j) to the origin. $R\beta_{s,j}$ is half the longest straight line passing through the origin which intersects the unfolded (along the hat's base) periodic orbit (s, j) at equal distances on either side. Hence, (6.1) guarantees that (s, j) is a MUPO and can be oriented in such a way as not to enter the stem while still intersecting the dashed semicircle. Let $\mathcal{S}_\rho$ denote the set of periodic orbits which are marginally unstable for a given $\rho = \frac{r}{R}$.

A small perturbation η with respect to the incidence angle $\theta_{s,j}$ of a MUPO will cause the orbit to precess in the opposite direction, following the corresponding orbit in a semicircle billiard and will eventually 'fall' into mushroom's stem causing it to feel the strong chaotic effect of the defocusing mechanism. However, since the precessing angular velocity is proportional to the perturbation strength η which may be arbitrarily small, the orbit will behave in a quasi-periodic fashion and entry into the stem may take an unbounded amount of time. Hence the term 'stickiness', meaning that orbits in the immediate vicinity of MUPOs stick close to the regular component of phase space for long periods of time. Note however that although these periodic orbits are dynamically marginally unstable, they are not structurally robust against parameter perturbations of ρ.

The intervals $(\alpha_{s,j}, \beta_{s,j})$ are shrinking quadratically with increasing s. We see this by rearranging (6.1) into:

$$\frac{j}{s} \geq \frac{1}{\pi} \arccos \rho > \frac{1}{\pi} \arccos \left(\frac{\cos \frac{j\pi}{s}}{\cos \frac{\pi}{\lambda s}} \right), \tag{6.3}$$

expanding for large s

$$\frac{j}{s} \geq \vartheta^* > \frac{j}{s} - \left(\frac{\pi \cot \frac{j\pi}{s}}{2} \right) \frac{1}{\lambda^2 s^2} + \mathcal{O}\left(\frac{1}{s^4} \right), \tag{6.4}$$

where we have set $\vartheta^* = \frac{1}{\pi} \arccos \rho$ and rearranging once more to get

$$0 \leq \frac{j}{s} - \vartheta^* < \left(\frac{\pi \cot \frac{j\pi}{s}}{2\lambda^2} \right) \frac{1}{s^2}, \tag{6.5}$$

where we have neglected the positive terms of order $\sim s^{-4}$, thus possibly losing some of the MUPOs; we give explicit bounds on this term in the next section. In this way the problem of finding the elements of $\mathcal{S}_\rho$ is expressed as the well known number theoretic problem of finding rational approximations $\frac{j}{s}$ of $\vartheta^* \in (0, \frac{1}{2})$ [112]. However in this case we have a couple of complications: the approximations are one-sided and the tolerance depends both on the numerical value of $\frac{j}{s}$ and the parity of s through λ in (6.2).

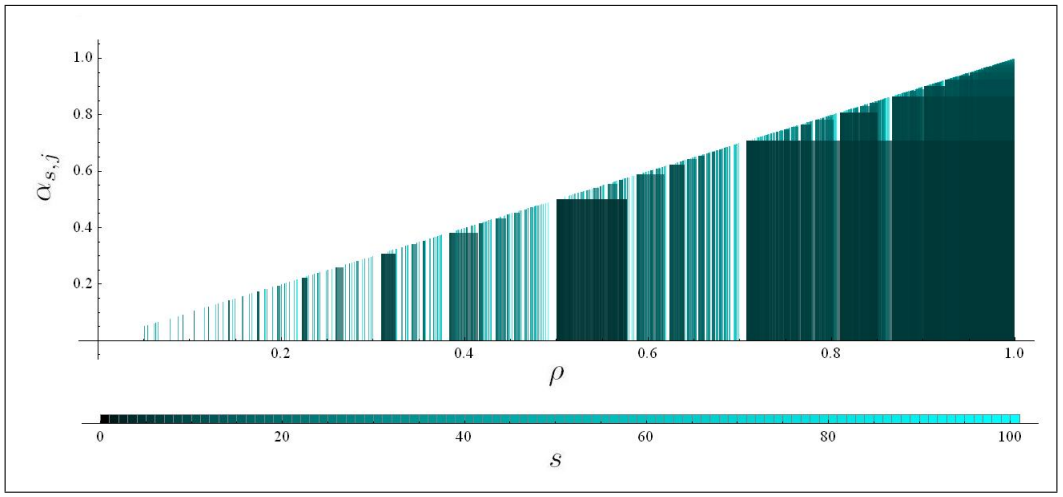

Figure 6.3: For each (s, j) pair ($s \leq 100$) we plot the rectangle $[\alpha_{s,j}, \beta_{s,j}] \times [0, \alpha_{s,j}]$ with color gradient depending on s. These cover the unit interval modulo a set of zero measure but full Hausdorff dimension.

The interesting connection made here allows one to apply well known results from number theory to the present dynamical system and infer useful dynamical properties about it. Altmann *et al.* [112] showed using continued fractions representations that for almost all (a set of measure one) $\rho \in (0, 1)$ there exist infinitely many MUPOs (for more details see Ref [111]). Hence, orbits in a generic mushroom exhibit stickiness causing the Poincaré recurrence times distribution to decay as $\sim t^{-2}$. The density of MUPOs can be graphically seen in Figure 6.3 where the intervals $(\alpha_{s,j}, \beta_{s,j})$ for $s \leq 100$ are plotted and seem to cover more and more of the unit interval in an overlapping fashion (for a similar representation see [182]).

In the following section we remove the parity dependent λ in the context of a more general mushroom model. This in turn allows us to use properties of continued fractions more effectively to derive a sufficient condition so that (6.1) has no solutions and hence destroy all MUPOs in the hat of the mushroom.

6.3 MUPO-free mushrooms

6.3.1 Generalized Mushroom

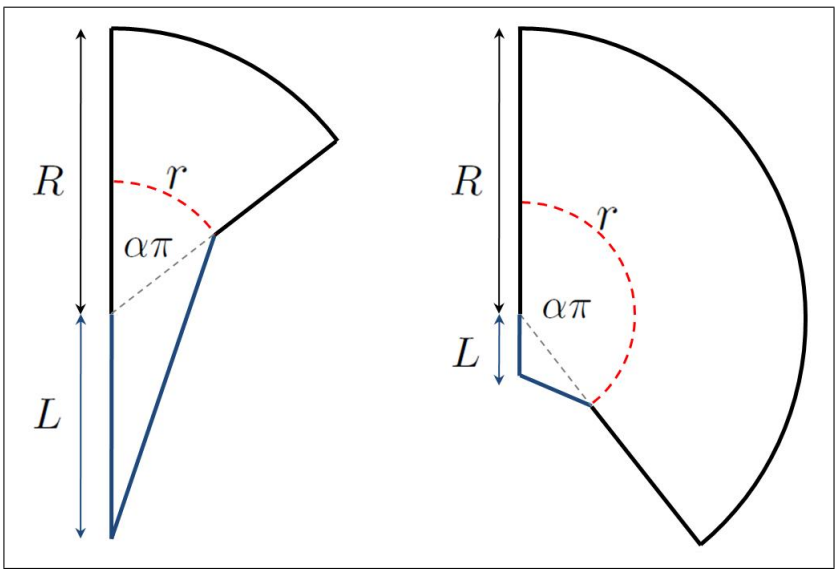

Figure 6.4: Generalized mushroom billiards with variable hat sizes and triangular stems.

We have seen that MUPOs in the mushroom billiard, are directly related to number theory through (6.5). In this subsection we propose a generalization of the mushroom billiard within the class of billiards proposed in [185] (see also [175]), which will allow us to efficiently use properties of continued fractions without having to worry about the parity of MUPOs. The main result here will be to prove the existence of a zero measure set of $\rho = \frac{r}{R}$ values for which the mushroom's hat is MUPO-free. Furthermore, we shall obtain a sufficient condition which explicitly describes a subset of this set.

Consider the 'elementary cell' obtained by slicing the mushroom along its vertical axis of symmetry. Then the period of the corresponding (s, j) orbit is $s\lambda/2$. Similarly, since we are currently only interested in collisions with the curved segment of the billiard, we introduce the parameter $\alpha \in (0, 1)$ which allows the mushroom to have circular hats of variable size. This billiard, shown in Figure 6.4 was shown to have a sharply divided phase space in [175] as long as $L > 0$. The boundary between the two components is given by the dashed arc of radius $r \in (0, R)$. Notice that because the stem is triangular, there are no bouncing ball orbits present.

Periodic orbits in the hat of the proposed mushroom will now have incidence angles with the curved boundary given by $|\theta_{q,p}| = \frac{\pi}{2} - \frac{\alpha p\pi}{q}$ for some coprime p and q, and equation (6.1) becomes

$$\cos\frac{\alpha p\pi}{q} \leq \frac{r}{R} < \frac{\cos\frac{\alpha p\pi}{q}}{\cos\frac{\alpha\pi}{q}}, \tag{6.6}$$

Notice that there is no longer a parity dependent λ. Similarly to (6.5), this becomes

$$0 \leq \frac{p}{q} - \frac{\vartheta^*}{\alpha} < \frac{\alpha\pi\cot\frac{\alpha p\pi}{q}}{2q^2} + \frac{R_2(q)}{q^2}, \tag{6.7}$$

where $\vartheta^* = \frac{1}{\pi}\arccos\rho$, and $R_2(q)$ is the remainder term obtained from the Taylor expansion for large q. In the following we bound the argument of the cotangent by $\pi\vartheta^*$ and also bound R_2, so that for $q \geq Q$ we have

$$0 \leq \frac{p}{q} - \frac{\vartheta^*}{\alpha} < \frac{\alpha\pi\cot\frac{\alpha p\pi}{q}}{2q^2} + \frac{R_2(q)}{q^2} < \left[\overbrace{\left(\frac{\alpha\pi\rho}{2\sqrt{1-\rho^2}}\right) + \hat{R}_2(q, Q)}^{K(q,Q)}\right]\frac{1}{q^2}, \tag{6.8}$$

where $R_2(q)$ is bounded by

$$\hat{R}_2(q,Q) = \frac{\alpha^2\pi^2}{\cos^2\left(\frac{\alpha\pi}{Q}\right)q^2}\Bigg[\left(\tan^2\left(\frac{\alpha\pi}{Q}\right)+\frac{4}{3}\right)\frac{\rho}{\sqrt{1-\rho^2}}+\frac{\rho^3}{2(1-\rho^2)^{\frac{3}{2}}} + \left(1+\frac{\alpha^2\pi^2}{\cos(\frac{\alpha\pi}{Q})^2Q^2}\right)\frac{\rho^3}{2\cos(\frac{\alpha\pi}{Q})^2\left(1-\rho^2(1+\frac{\alpha^2\pi^2}{\cos(\frac{\alpha\pi}{Q})^2q^2})^2\right)^{\frac{3}{2}}}\Bigg], \tag{6.9}$$

as obtained in Appendix *D* Here, Q is a fixed number up to which (6.8) must be checked numerically. It must be greater than $\max\left(\alpha\pi, \frac{\alpha\pi}{\cos 1}\sqrt{\frac{\rho}{1-\rho}}\right)$, following from Appendix *D*.

6.3.2 MUPO-free Condition

We now turn to some number theory and introduce some basic concepts. It is well known that the best rational approximations of a real number ξ are obtained through its continued fraction representation [11]

$$\xi = a_0 + \frac{1}{a_1 + \frac{1}{a_2+\ldots}} = [a_0; a_1, a_2, \ldots], \tag{6.10}$$

where the quantities $a_0, a_1, a_2, \ldots$ are called 'partial quotients' and are usually taken to be positive integers. Irrational numbers have an infinite continued fraction representation while rationals have finite. The n^{th} truncation of a continued fraction representation gives the n^{th} 'convergent' $\frac{A_n}{B_n}$ of ξ. Hence irrational numbers have an infinite number of convergents while rationals finite. Convergents are 'best approximations' to ξ, meaning that there is no other fraction with denominator smaller than B_n which approximates ξ better. Furthermore, we have that $A_{k+1} = a_{k+1}A_k + A_{k-1}$ and $B_{k+1} = a_{k+1}B_k + B_{k-1}$ for $0 \leq k \leq n-1$ such that $A_{-1} = 1, A_0 = a_0, B_{-1} = 0$ and $B_0 = 1$.

For the mushroom, we would like to find values of $\frac{\vartheta^*}{\alpha} = [a_0; a_1, a_2, \ldots]$ for which

$$0 \leq \frac{p}{q} - \frac{\vartheta^*}{\alpha} < \frac{K(Q,Q)}{q^2}, \tag{6.11}$$

has no solutions since this would also imply no solutions to (6.6). Solutions to (6.11), if any, are only given by the convergents of $\frac{\vartheta^*}{\alpha}$ if $0 < K(Q,Q) \leq \frac{1}{2}$ [186].

Obviously, if $\frac{\vartheta^*}{\alpha}$ is rational then there is only a finite number of solutions to (6.11) and the corresponding mushroom is 'finitely' sticky. However if $\frac{\vartheta^*}{\alpha}$ is irrational the answer is not so simple. We focus on the convergents $\frac{p}{q} = \frac{A_n}{B_n}$ of $\frac{\vartheta^*}{\alpha}$ and express it in terms of them such that

$$\frac{\vartheta^*}{\alpha} = \frac{\zeta_{n+1}A_n + A_{n-1}}{\zeta_{n+1}B_n + B_{n-1}}, \tag{6.12}$$

where $\zeta_n = [a_n; a_{n+1}, a_{n+2}, \ldots]$ is the n^{th} 'complete quotient' of $\frac{\vartheta^*}{\alpha}$. Hence

$$\frac{A_n}{B_n} - \frac{\vartheta^*}{\alpha} = \frac{A_nB_{n-1} - A_{n-1}B_n}{\left(\zeta_{n+1} + \frac{B_{n-1}}{B_n}\right)B_n^2} = \frac{(-1)^{n-1}}{\left(\zeta_{n+1} + \frac{B_{n-1}}{B_n}\right)B_n^2}. \tag{6.13}$$

It is easy to see that if n is even, then $\frac{A_n}{B_n} - \frac{\vartheta^*}{\alpha} < 0$. Therefore, equation (6.11) will not have any solutions if

$$K(Q,Q) < \frac{1}{\zeta_{n+1} + \frac{B_{n-1}}{B_n}}, \tag{6.14}$$

for all odd n. Since $a_{n+1} < \zeta_{n+1} < a_{n+1} + 1$ and $\frac{B_{n-1}}{B_n} < 1$, it follows that

$$K(Q,Q) < \frac{1}{\wp + 2}, \tag{6.15}$$

where $\wp = max(a_{2n})$, is a sufficient condition for (6.11) and therefore (6.6) not to have any solutions. The condition is never satisfied if a_{2n} is unbounded.

The set of numbers with bounded even partial quotients as derived above has zero measure [186] and has Hausdorff dimension one as $\wp$ is unbounded as $\rho \to 0$ ($\vartheta \to 1/2$) [187]. As shown in Ref [112], a generic mushroom will be "infinitely sticky" in the sense that it has infinitely many MUPOs (for more details see Ref [111]). However, we have shown here that there are infinitely many values of $\frac{\vartheta^*}{\alpha}$, and therefore ρ, for which MUPOs in the hat are finite or completely removed.

Since the smallest possible value of $\wp$ is one, for the original mushroom with $\alpha = \frac{1}{2}$, if $\rho < \left(\left(\frac{3\pi\alpha}{2}\right)^2 + 1\right)^{-\frac{1}{2}} \approx 0.390683$, (6.15) gives a sufficient condition for (6.11) not to have any solutions and therefore describes a mushroom with no MUPOs in its hat. Nevertheless, a MUPO-free mushroom is still expected to exhibit stickiness through orbits which are just inside the ergodic component of the phase space and therefore just intersecting the dashed semicircle of radius r of Figure 6.2a). What

this means is that points with zero local Lyapunov exponents are more sparsely distributed as they are no longer supported by periodic orbits. How this lack of MUPOs affects the power-law decays of different statistical observables is a natural question which we attempt to answer in the context of an 'open' mushroom in the chapter 7.

6.3.3 MUPO-free Example

For larger values, $\frac{1}{2} < K(Q,Q) \leq 1$, solutions to (6.11), if any, are given by the convergents $\frac{A_n}{B_n}$ and also by the so called 'intermediate' convergents of the form $\frac{cA_{n+1}+An}{cB_{n+1}+B_n}$ [186], where c is an integer such that $1 \leq c < a_{n+2}$. The increased 'easiness' in finding good approximations and therefore solutions to (6.11) is immediately and graphically apparent from the increased frequency of overlaps and density for larger values of ρ in Figure 6.3. There are however values of ϑ^* with $K(Q,Q) > \frac{1}{2}$ satisfying (6.14) such that the corresponding mushrooms will have no MUPOs. An example of such a mushroom is $\rho = \cos\left(\frac{5+\sqrt{2}}{23}\pi\right) \approx 0.64013$ which has $K(q,95) < 0.6549$ and $2\vartheta^* = [0;1,1,3,\{1,4\}]$ (where we have numerically checked the absence of MUPOs up to $q = 95$). Here, the odd convergents of $2\vartheta^*$ satisfy $0 < \frac{A_n}{B_n} - \frac{\vartheta^*}{\alpha} = \frac{K_n}{B_n^2}$ where $K_n = \left(\zeta_{n+1} + \frac{B_{n-1}}{B_n}\right)^{-1}$ for odd $n \geq 3$, where $\zeta_{n+1} = [1;4,\{1,4\}] = \frac{1}{2}(1+\sqrt{2})$. Using (6.11) it is an easy exercise to show that for all odd $n > 3$

$$\begin{aligned} B_n &= \frac{1}{4}\left(\alpha_- \lambda_+^{\frac{n}{2}} - \alpha_+ \lambda_-^{\frac{n}{2}}\right), \\ B_{n-1} &= \frac{1}{8}\left(\beta_- \lambda_+^{\frac{n}{2}} + \beta_+ \lambda_-^{\frac{n}{2}}\right), \end{aligned} \tag{6.16}$$

where $\lambda_\pm = 3 \pm 2\sqrt{2}$, $\alpha_\pm = 12 \pm 7\sqrt{2}$ and $\beta_\pm = \pm 26 + 19\sqrt{2}$ are all positive numbers. Hence $\frac{B_{n-1}}{B_n} = \frac{1}{2}\left(\frac{\beta_- + \beta_+\left(\frac{\lambda_-}{\lambda_+}\right)^{\frac{n}{2}}}{\alpha_- - \alpha_+\left(\frac{\lambda_-}{\lambda_+}\right)^{\frac{n}{2}}}\right)$ is strictly decreasing with n and therefore K_n is bounded by

$$K(q,95) < K_5 \leq K_n < \frac{1}{\sqrt{2}}, \tag{6.17}$$

for all odd $n \geq 5$, where $K_5 \approx 0.706$. Similarly for the intermediate convergents of $2\vartheta^*$ we have that

$$\frac{cA_{n+1}+A_n}{cB_{n+1}+B_n} - 2\vartheta^* = \frac{cA_{n+1}+A_n}{cB_{n+1}+B_n} - \frac{\zeta_{n+2}A_{n+1}+A_n}{\zeta_{n+2}B_{n+1}+B_n}, \tag{6.18}$$

which for odd $n \geq 5$ simplifies to

$$\frac{2+2\sqrt{2}-c}{(cB_{n+1}+B_n)\left(B_{n+1}(2+2\sqrt{2})+B_n\right)} \equiv \frac{\bar{K}_n(c)}{(cB_{n+1}+B_n)^2}, \tag{6.19}$$

since $\zeta_{n+2} = [4;1,\{4,1\}] = 2+2\sqrt{2}$. Hence, using (6.16) and a similar argument as above $\bar{K}_n(c) = \frac{4+4c-c^2}{4\sqrt{2}} - \frac{(2+5\sqrt{2})(c-2-2\sqrt{2})^2}{8(5-\sqrt{2})}\left(\frac{\lambda_-}{\lambda_+}\right)^{\frac{n}{2}}$ is bounded by

$$K(q,95) < \bar{K}_5(1) \leq \bar{K}_n(c) < \frac{4+4c-c^2}{4\sqrt{2}}, \tag{6.20}$$

for $c = 1,2,3$ and odd $n \geq 5$ where $\bar{K}_5(1) \approx 1.237$. Therefore, $\rho = \cos\left(\frac{5+\sqrt{2}}{23}\pi\right)$ describes a mushroom with no MUPOs in its hat.

6.3.4 Supremum of MUPO-free Values

From the example above we can now use similar arguments to establish that MUPO-free values of ρ exist up to $\frac{1}{\sqrt{2}}$. In other words $\sup\big(\rho \in (0,1) : \mathcal{S}_\rho = \emptyset\big) = \frac{1}{\sqrt{2}}$. To see this, let $\hat{K}(Q,Q)$ denote the value of $K(Q,Q)$ at $\rho = \frac{1}{\sqrt{2}}$. Then from equations (6.7) and (6.8) $K(Q,Q) < \hat{K}(Q,Q) = \frac{\pi}{4} + \frac{7\pi^2}{12Q^2} + \mathcal{O}(Q^{-4})$ for $0 < \rho < \frac{1}{\sqrt{2}}$. Now consider for $m \in \mathbb{Z}^+$ large

$$2\vartheta^* = [0;1,\{1,m\}] = \frac{m+2+\sqrt{m^2+4m}}{4m-4} = \frac{1}{2} + \frac{1}{4m} + \mathcal{O}\left(\frac{1}{m^2}\right), \tag{6.21}$$

so that $\rho = \cos\pi\vartheta^* = \frac{1}{\sqrt{2}} - \frac{\pi}{8\sqrt{2}m} + \mathcal{O}(m^{-2})$. We first look at the odd convergents of $2\vartheta^*$ as in (6.13)

$$0 < \frac{A_n}{B_n} - 2\vartheta^* \equiv \frac{K_n}{B_n^2}, \tag{6.22}$$

where $K_n = \left(\zeta_{n+1} + \frac{Bn-1}{B_n}\right)^{-1}$ and $\zeta_{n+1} = [1;m,\{1,m\}] = \frac{1}{2} + \sqrt{\frac{1}{4}+\frac{1}{m}}$. Via a similar manipulation as in (6.16) we obtain that for odd $n \geq 3$

$$\frac{B_{n-1}}{B_n} = \frac{(2-\lambda_-) + (\lambda_+ - 2)\left(\frac{\lambda_-}{\lambda_+}\right)^{\frac{n-1}{2}}}{(1+2m-\lambda_-) - (1+2x-\lambda_+)\left(\frac{\lambda_-}{\lambda_+}\right)^{\frac{n-1}{2}}}, \tag{6.23}$$

where $\lambda_\pm = \frac{1}{2}\big(2+m\pm\sqrt{4m^2+m^3}\big)$. Thus $K_n \geq K_1 = \frac{2m}{3m+\sqrt{m(4+m)}} = \frac{1}{2} - \frac{1}{4m} + \mathcal{O}(m^{-2})$ converges exponentially to $\frac{m}{\sqrt{m(4+m)}} = 1 - \frac{2}{m} + \frac{6}{m^2} + \mathcal{O}(m^{-3})$ with n and therefore $K_n > \hat{K}(q, B_n) \approx \frac{\pi}{4}$ for large enough m and n. Similarly, when looking at the intermediate convergents of $2\vartheta^*$ as in (6.17) and (6.18) such that

$$\bar{K}_n(c) = \frac{(\zeta_{n+2}-c)\Big(c+\frac{B_n}{B_{n+1}}\Big)}{\Big(\zeta_{n+2}+\frac{B_n}{B_{n+1}}\Big)}, \tag{6.24}$$

where $c = 1, 2, \ldots (m-1)$, $\zeta_{n+2} = [m; 1, \{m, 1\}] = \frac{m}{2} + \sqrt{\frac{m^2}{4}+m}$ and $\frac{B_n}{B_{n+1}}$ can be obtained from (6.22), we find that $\bar{K}_n(1) \leq \bar{K}_n(c)$ and $\bar{K}_{n+1}(c) < \bar{K}_n(c)$. Hence, since $\bar{K}_n(1)$ converges exponentially to $\frac{1-2m}{m^2-m\sqrt{m(4+m)}-1} = 1 - \frac{2}{m^2} + \mathcal{O}(m^{-3})$ with n, then $\bar{K}_n(c) \geq \bar{K}_n(1) > \frac{1-2m}{m^2-m\sqrt{m(4+m)}-1} > \hat{K}(q, cB_{n+1}+B_n) \approx \frac{\pi}{4}$ for large enough m and n, thus verifying our claim above for the supremum of MUPO-free mushrooms.

6.3.5 Supremum of Finitely Sticky Irrational Values

If $\frac{\vartheta^*}{\alpha} \in \mathbb{Q}$, then the corresponding mushroom has a finite number of MUPOs and is thus 'finitely' sticky. This is because rational numbers have a finite continued fraction representation and there is no other way to approximate a rational $\frac{\vartheta^*}{\alpha}$ by rationals $\frac{p}{q}$ that is faster than q^{-2} [186]. There are however infinitely many $\frac{\vartheta^*}{\alpha} \notin \mathbb{Q}$ which are also finitely sticky [111]. Furthermore, the set of finitely sticky mushrooms is of measure zero and dimension one; just like the MUPO-free set. Such mushrooms may be constructed by simply adding periodic tails of small even partial quotients to the continued fraction expansion of $\frac{\vartheta^*}{\alpha}$. Therefore, we find that $\sup\big(\rho : \#\mathcal{S}_\rho < \infty, \alpha = 1/2, \frac{1}{\pi}\arccos\rho \notin \mathbb{Q}\big) = \frac{4}{\sqrt{16+\pi^2}} \approx 0.7864$. To see this take the leading order term of $K(Q,Q)$ as $Q \to \infty$ and equate it to one, so that $\frac{\alpha\pi\rho}{2\sqrt{1-\rho^2}} = 1$. Now since $\rho = \cos\pi\vartheta^*$, then $2\vartheta^* = \frac{2}{\pi}\arccos\frac{4}{\sqrt{16+\pi^2}} = [0; 2, 2, 1, 3, 1, 1, 1, \ldots] < [0; 2, 2, 1, 3, 1, 2, 1, \{1, m\}] = 2\tilde{\vartheta}^*$. It follows that the corresponding $\tilde{K}(Q,Q) < 1$ in the limit $Q \to \infty$. Now since we may augment the tail of the continued fraction expansion of $2\vartheta^*$ as done above by the transformations $a_\nu \to a_\nu + 1$ and $\zeta_{\nu+2} \to [1; m, \{1, m\}]$ for any even ν, then $K_n \equiv B_n^2\left(\frac{A_n}{B_n} - 2\tilde{\vartheta}^*\right)$

will converge exponentially to some function $f(m) = 1 - \frac{k}{m} + R_1(m)$ with n for some constant k and $R_1(m) = \frac{f''(\xi)}{2m^2}$ for some $0 < \xi < m$. Therefore, as $\nu \to \infty$, $(\tilde{\vartheta}^* - \vartheta^*) \to 0^+$ and $\tilde{K}(Q, Q) \to 1$. However we may always choose m and n big enough such that $K_n > \tilde{K}(B_n, B_n)$. A similar statement can be made for the intermediate convergents of $2\tilde{\vartheta}^*$. Therefore, for values of $\rho > \frac{4}{\sqrt{16-\alpha^2\pi^2}}$, $K(Q, Q) > 1$ and therefore all convergents of $\frac{\vartheta^*}{\alpha} \notin \mathbb{Q}$ are solutions of (6.11) [11] hence describing mushrooms with infinitely many MUPOs.

6.4 Conclusions and Discussion

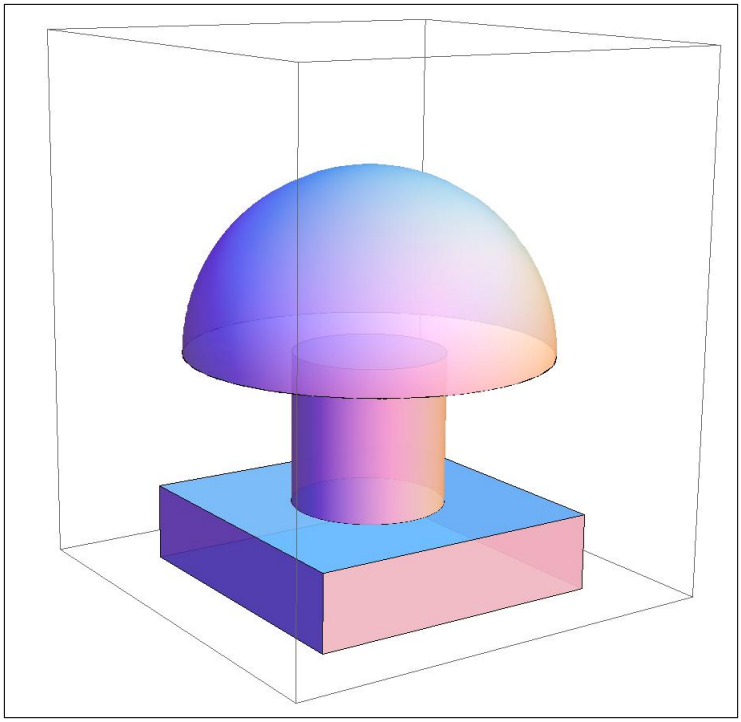

Figure 6.5: A three-dimensional mushroom billiard.

A major result of this chapter is the introduction of a zero-measure set which describes MUPO-free mushrooms (see section 6.3) which to the best of our knowledge possess the simplest mixed phase space in two dimensions. The interesting connection between mushrooms and number theory (see equation (6.5)) first appearing in [112, 111] cannot be directly exploited due to a sensitive parity depen-

dence of the periodic orbits of the mushroom. We have overcome this complication by considering a generalized mushroom with a variable sized hat and triangular stem (see Figure 6.4). This allowed us to efficiently use properties of continued fractions and characterize a subset of the infinitely many MUPO-free mushrooms. We thus obtained upper bounds for MUPO-free and finitely sticky irrational mushrooms and also gave an explicit example of a MUPO-free mushroom billiard (see section 3.4.3.3). Furthermore, unlike the non-sticky elliptical mushrooms mentioned in the introduction, we expect that the MUPO-free mushroom exhibits a reduced amount of stickiness (larger scaling exponent since $\mathcal{C} = 0$). This is attributed to the difficulty in 'finding' the foot of the mushroom by chaotic orbits which are just inside the dashed circular arc of radius r. We shall test this claim numerically in the next chapter where we examine the open mushroom.

The results of section 6.3, should also hold in the case of a three dimensional mushroom billiard with a hemispherical hat of radius R, a cylindrical stem of radius r and height $h > 0$ and a cuboidal pedestal of base length $l \geq 2r$ to break angular momentum conservation[1] (see Figure 6.5). Orbits inside a three-dimensional spherical billiard always lie in the same two-dimensional plane containing the center of the corresponding sphere. Hence, due of the axial symmetry of the hat and stem opening, the conditions for the existence of MUPOs are exactly the same in higher dimensions as in equations (6.1)-(6.2). The remaining (zero-measure) MUPOs in such a system are of the bouncing ball type and are found both in stem and pedestal. We conjecture that the corresponding mushroom has a sharply divided phase space with a MUPO-free hat[2].

Finally, one would expect to see the classical dynamical features of the less sticky mushroom introduced in section 6.3 appear in the analogous quantum mushroom in accordance with Bohr's correspondence principle. Some possible direc-

[1]Other ways of achieving this are possible, however care is needed in order to guarantee ergodicity in the stem.

[2]L.A. Bunimovich and G. Del Magno have also considered this model, but have not yet proved ergodicity of the chaotic component (L.A.Bunimovich, private communication).

tions for investigating such effects are the localization of wave-functions (scars) [177], dynamical quantum tunneling rates from regular to chaotic regions of phase space [180] as well as experimentally in the emission directionality of mushroom microlasers [183]. In the next chapter we investigate the stickiness due to MUPOs in the hat and stem of the mushroom in the context of escape through a small hole placed on the stem of the mushroom.

Chapter 7

Escape from Mushrooms

In the previous chapter we investigated the dynamics of the mushroom billiard and specifically focused on the chaotic region of phase space, close to the regular island. We saw how MUPOs come into existence, how they affect the dynamics of orbits in their immediate vicinity but also how they can be removed. In this chapter we consider the open mushroom (billiard with a hole) in order to quantify the stickiness exhibited due to MUPOs. We obtain exact leading order expressions for the algebraic decay of the survival probability function $P(t) \sim \mathcal{C}/t$ for mushrooms with triangular and rectangular stems. Numerical simulations are then performed which confirm our predictions for sticky, less sticky and MUPO-free mushrooms. The results of this chapter have also been published in Ref [91] and therefore this chapter follows the published article closely.

7.1 Introduction to Open Mushrooms

In the second part of our mushroom investigation, we attempt to quantify the stickiness exhibited due to MUPOs in the mushroom by placing holes through which particles may escape. We consider linear perturbations of MUPOs and obtain exact leading order expressions for the asymptotic algebraic decay of $P(t) \sim \mathcal{C}/t$. This is done for two separate cases, firstly for MUPOs in the semi-circular hat of the mushroom (section 7.2) and then for bouncing ball type MUPOs in the

case of a rectangular stem (section 7.3). The explicit form of these expressions depends on the geometrical parameters of the billiard and in turn allows us not only to predict but also to calibrate the survival probability function. Furthermore, in connection with the results of section 6.3 we reach to the conclusion that a MUPO-free mushroom will have $\mathcal{C} = 0$ therefore displaying a power law decay of order $\sim t^{-2}$ or faster. Finally, the results are confirmed numerically (section 7.4) and then discussed briefly (7.5).

Assuming that the hole is placed well inside the ergodic component of its phase space, $P(t)$ is expected to be composed of a constant term, corresponding to the initial conditions (ICs) trapped forever in the mushroom's hat and a time-dependent term corresponding to ergodic ICs. Typical chaotic orbits will decay exponentially as before, while sticky orbits will decay with a power-law of order $\sim t^{-1}$ [82]. All these behaviors coexist and are formulated below:

$$P(t) \approx \mathcal{A} + \mathcal{B}\left(e^{-\bar{\gamma}t} + \frac{\mathcal{C}}{t}\right), \tag{7.1}$$

where we have neglected terms of order t^{-2}. In equation (7.1) $\mathcal{A}$ is the measure of the integrable island given by:

$$\mathcal{A} = 4(2|\partial Q|)^{-1}\left[R\sqrt{1-\rho^2} - \rho R \arccos\rho + \frac{\pi}{2}R(1-\rho)\right], \tag{7.2}$$

and $\mathcal{B}$ is its complement ($\mathcal{B} = 1 - \mathcal{A}$). The exponential escape rate is given by:

$$\bar{\gamma} \approx \frac{\sum_{i=1}^{k}\epsilon_i}{\langle\bar{\tau}\rangle\mathcal{B}|\partial Q|}, \tag{7.3}$$

while the mean free path in the ergodic component is [188]:

$$\langle\bar{\tau}\rangle = \frac{c_\nu}{c_\mu} = \frac{\pi\left(|Q_s| + R^2\arcsin\rho + \rho R^2\sqrt{1-\rho^2}\right)}{\mathcal{B}|\partial Q|}, \tag{7.4}$$

where $|Q_s|$ is the area of the mushroom's stem while c_ν and c_μ are the invariant probability measures of the ergodic component for the billiard flow and map respectively.

Algebraic decays, of the form $\frac{\mathcal{C}}{t}$ in (7.1), originate from the stickiness exhibited, and in particular due to the presence of MUPOs as discussed in the previous

sections. It is a geometrical description of the constant $\mathcal{C}$ that we seek here similar to the ones obtained in chapter 3. In the following two subsections we attempt this, first for the MUPOs living the mushroom's hat and then for near-bouncing ball orbits present in mushrooms with rectangular stems.

7.2 Sticky Hat

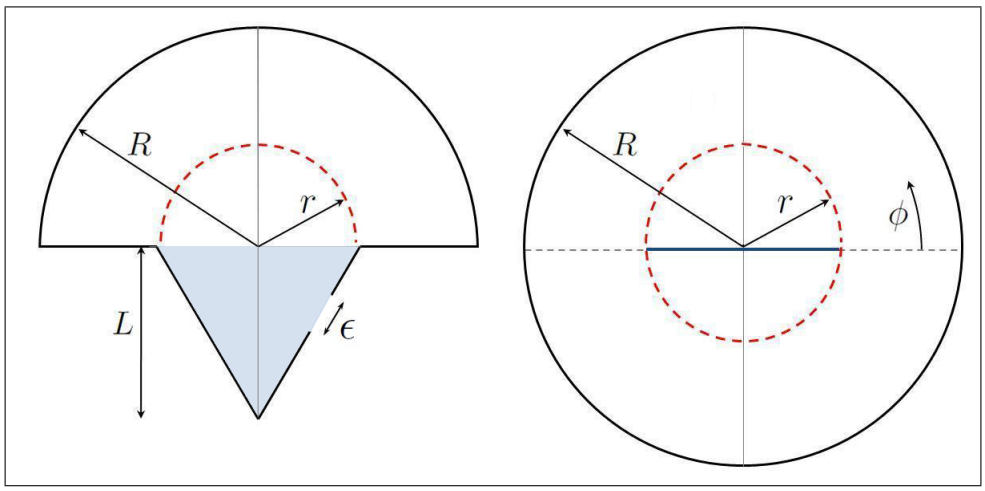

Figure 7.1: *Left*: Mushroom with triangular stem. *Right*: Image reconstruction trick at the base of the mushrooms hat. Orbits entering the lower semicircle through the thick blue horizontal line of length $2r$ are assumed to escape through the hole ϵ soon thereafter.

We consider a mushroom with a central triangular stem and circular hat as shown in Figure 7.1, hence removing any bouncing ball orbits between parallel walls. The asymptotic algebraic decay $\frac{\mathcal{C}}{t}$ should be equal to the measure (relative volume occupied in phase space) of the set of quasi-periodic ICs which do not enter the stem until a time t. Such an assumption is justified by to the apparent 'reluctance' [83] displayed by orbits to (re-)enter a 'sticky' mode. This reluctance to (re-)enter as well as to leave sticky modes is demanded by ergodicity, which requires trajectories to fill the phase space uniformly. When the mushroom is opened, the exponential decay of (7.1) prevents most of these orbits from (re-)entering the sticky modes surrounding MUPOs.

We use the *image reconstruction trick* [149] and neglect collisions with the base

of the mushroom's hat. Hence the dynamics in the hat remains unchanged while a horizontal slit of length $2r$ centered at the origin corresponds to the stem's opening. We parameterize the now circular boundary by the angle ϕ, where $\phi \in (0, 2\pi)$ increases anticlockwise as shown in the right panel of Figure 7.1. Now, each IC $(\phi, \theta_{s,j})$ is a MUPO if the collision coordinate ϕ satisfies:

$$\phi \in \bigcup_{k=0}^{\lambda s-1} \left(\phi_1(\theta_{s,j}, k), \phi_2(\theta_{s,j}, k)\right), \tag{7.5}$$

with

$$\phi_1(\theta_{s,j}, k) = \theta_{s,j} + \frac{\pi}{\lambda} + \arccos\left(\rho^{-1} \sin\theta_{s,j}\right) + (k-1)\frac{2\pi}{\lambda s}, \tag{7.6}$$

$$\phi_2(\theta_{s,j}, k) = \theta_{s,j} + \frac{\pi}{\lambda} - \arccos\left(\rho^{-1} \sin\theta_{s,j}\right) + k\frac{2\pi}{\lambda s}, \tag{7.7}$$

where $\rho = \frac{r}{R}$ and the angles ϕ_i are taken modulo 2π. Each MUPO then defines a dashed, horizontal line in the $\phi - \theta$ plane (the phase space), and each dashed line has length $\phi_2 - \phi_1 = \frac{2\pi}{\lambda s} - 2\arccos\left(\rho^{-1}\sin\theta_{s,j}\right)$. Notice that ϕ_1 and ϕ_2 are not defined if $\sin\theta > \rho$.

To help visualize how the long surviving ICs near the above described MUPOs populate the phase space, we turn to some computer simulations. Initial conditions near the integrable island's boundary are chosen randomly so that $\phi \in (0, 2\pi)$ and $\theta \in (0, \arcsin\frac{r}{R})$. The ones that survive for at least N collisions with the boundary are shown in the top left panel of Figure 7.2 for parameters $N = 200$ and $\rho = 0.815$. We notice that for the selected value of ρ, the most dominant MUPO is the square with $(s, j) = (4, 1)$ (see also Figure 7.2b)). In Figure 7.2c) one can identify the pentagon orbit $(s, j) = (5, 1)$ which like all odd s-orbits has twice its period ($\lambda s = 10$) of surviving intervals along the horizontal line $\theta_{5,1}$. Further magnification into the phase space reveals the $(s, j) = (66, 13)$ orbit (see also Figure 7.2d)) and then an accumulation of higher order orbits closer to the island's boundary at $\arcsin\rho$. The next MUPO is $(s, j) = (920, 181)$.

We introduce a small perturbation $\eta \ll 1$ in the angle $\theta_{s,j}$ of each MUPO and

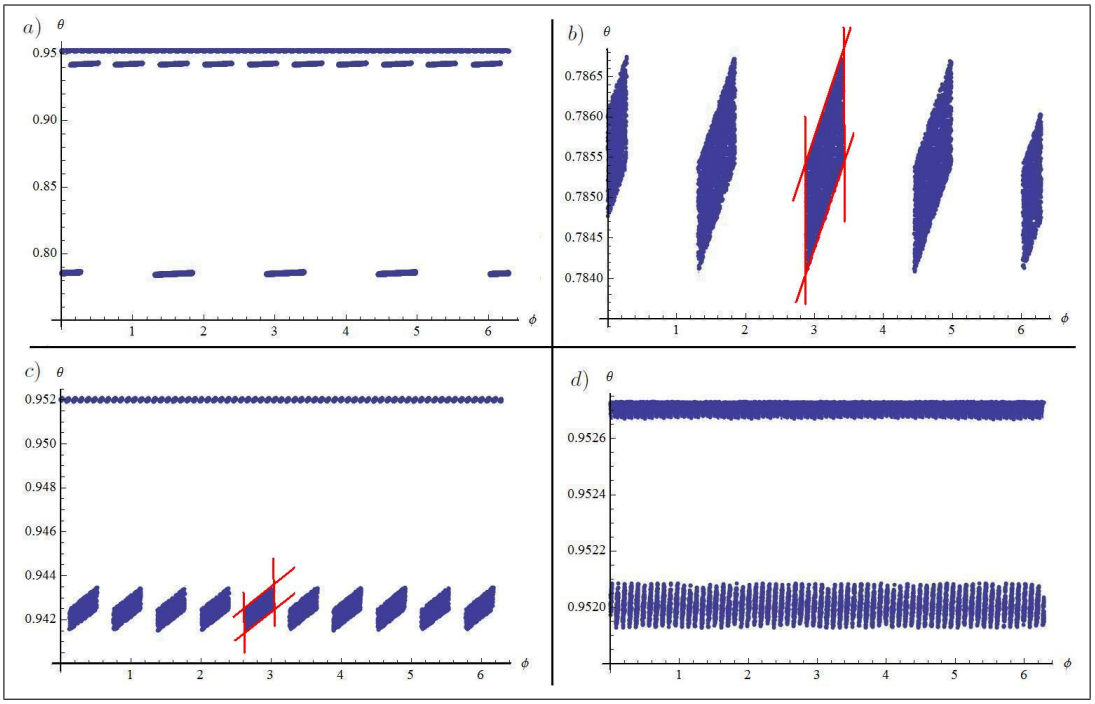

Figure 7.2: Phase space plots of initial conditions that do not escape from the hat for at least $N = 200$ collisions with the boundary at $\rho = 0.815$. Plots *b*) *c*) and *d*) are magnifications of *a*), showing in more detail the MUPOs (4,1), (5,1), (66,13) and their surrounding sticky orbits. MUPOs accumulate close to the boundary of the integrable island at $\theta = \arcsin\rho$ (see also Figure 6.2b)). The red lines in *b*) and *c*) are the analytic prediction given by (7.5)-(7.7) and can be used to integrate the enclosed areas.)

expand (7.6)-(7.7) to leading order:

$$\phi_1(\theta_{s,j}+\eta,k) = \phi_1(\theta_{s,j},k) + \left(1 - \frac{\cos\theta_{s,j}}{\sqrt{\rho^2-\sin^2\theta_{s,j}}}\right)\eta + \mathcal{O}(\eta^2), \tag{7.8}$$

$$\phi_2(\theta_{s,j}+\eta,k) = \phi_2(\theta_{s,j},k) + \left(1 + \frac{\cos\theta_{s,j}}{\sqrt{\rho^2-\sin^2\theta_{s,j}}}\right)\eta + \mathcal{O}(\eta^2). \tag{7.9}$$

We also impose a time constraint such that the perturbed MUPO will survive up to time t by requiring that

$$\phi \geq \phi_1(\theta_{s,j}+\eta,k) + 2\eta N, \tag{7.10}$$

$$\phi \leq \phi_2(\theta_{s,j}+\eta,k) + 2\eta N. \tag{7.11}$$

where $N = \lceil \frac{t}{2R\cos(\theta_{s,j}+\eta)} \rceil$ is the number of collisions in time t. Expanding (7.10)-(7.11) to leading order together with (7.8)-(7.9) defines in total 4 lines which form

a quadrilateral in phase space with area $\Delta_{s,j}$ which can be integrated with respect to the invariant measure $(2|\partial Q|\mathcal{B})^{-1}\mathrm{d}\phi\ \mathrm{d}\sin\theta$ to give:

$$\Delta_{s,j} = \frac{8R\cos^2\theta_{s,j}\left(\pi - s\lambda\arccos\left(\rho\sin\theta_{s,j}\right)\right)^2}{2s^2\lambda^2|\partial Q|\mathcal{B}t} + \mathcal{O}\left(\frac{1}{t^2}\right), \tag{7.12}$$

to leading order in t. There are $2\lambda s$ such quadrilaterals due to θ-symmetry, however only half of the total area for each MUPO lies in $\phi \in (0,\pi)$, which corresponds to the actual mushroom's hat. As for the ICs on the straight segments of the hat, since the billiard map is measure preserving, only $2\lambda j$ quadrilaterals are mapped onto them. Hence overall we obtain:

$$\frac{\mathcal{C}}{t} = \sum_{(s,j)\in\mathcal{S}_\rho} \lambda(s+2j)(\Delta_{s,j} - \delta_{s,j}), \tag{7.13}$$

where $\mathcal{S}_\rho$ was defined in section 6.2 and

$$\delta_{s,j} = \begin{cases} \Delta_{s,j}/2, & \text{if } \cos\frac{j\pi}{s} = \rho, \\ 0, & \text{otherwise.} \end{cases} \tag{7.14}$$

accounts for the possibility that a MUPO is situated exactly on the border of the chaotic region and therefore can only be perturbed from one side. The sum in (7.13) converges since the elements of $\mathcal{S}_\rho$, if any, are distributed with a bounded density with respect to $\ln s$. Also, notice that $\mathcal{C}$ does not depend on the size or position of the hole on the stem.

If there are no MUPOs in the mushrooms hat ($\mathcal{S}_\rho = \emptyset$) and stem, then $\mathcal{C} = 0$. In such a case, as discussed at the end of section 6.3, a MUPO-free mushroom would still exhibit stickiness, realized by some faster power law exponent. The stickiness is due to orbits which only slightly intersect the dashed semicircle of radius r and therefore satisfy $\rho - \varepsilon \leq \sin\theta < \rho$, where $0 < \varepsilon \ll 1$. The measure of this set is obviously proportional to ε, of which $\sigma \propto \arccos\frac{\rho-\varepsilon}{\rho} = \sqrt{2\varepsilon/\rho} + \mathcal{O}(\varepsilon^{3/2})$ will enter the mushroom's stem at each forward iteration of the billiard map. Since the motion of these ICs is quasi-periodic, their typical lifetime before entering the mushroom's stem is $\sim \sigma^{-1}$ and therefore $\sim \varepsilon^{-1/2}$. For this reason we expect the power law exponent of the stickiness in a MUPO-free mushroom to be equal to

2 and that equation (3.79) should then read $P(t) = \mathcal{A} + \mathcal{B}\left(e^{-\bar{\gamma}t} + \frac{\mathcal{D}}{t^2}\right)$. Such an algebraic tail is related to other important statistical observables which quantify stickiness such as Poincaré recurrence times (see Appendix of Ref[82]) and decay of correlations (see [111] pp24). Numerical simulations of the survival probability function for different ρ values are performed and discussed in section 7.4.

7.3 Sticky Stem

In the previous section we derived an expression to leading order for the asymptotic behavior of $P(t)$ (see equations (7.1)-(7.4) and (7.12)-(7.14)) for a mushroom with a triangular stem. Here we investigate the stickiness introduced by the bouncing ball orbits present in mushrooms with rectangular stems of length L and a hole of size ϵ on one of the two parallel segments as shown in Figure 7.3. A method for calculating the contribution of these orbits to $P(t)$ was devised and explained in detail in [87]. Here, we follow this method and obtain an exact expression to leading order for the survival probability of the mushroom billiard. In doing so we discover an interesting discontinuous dependence of $P(t)$ on $\rho = \frac{r}{R}$ and also show that in the limit $\rho \to 1$ the expression for $P(t)$ reduces to (3.33) obtained for the stadium billiard in chapter 3.

We first split the billiard's boundary ∂Q into four, non-overlapping, connected segments: $\partial Q_s^b, \partial Q_s^w, \partial Q_h^b$ and ∂Q_h^c, referring to the stem's base, the stem's parallel walls, the hat's base and the hat's curved segment respectively. We parameterize the right parallel wall of ∂Q_s^w by $s \in (0, L)$ such that the interval (h^-, h^+) defines the hole of size ϵ as shown in Figure 7.3. We notice that ICs (x, θ) with $0 < x < h^-$ and $0 < \theta < \arctan \frac{\epsilon}{4\rho R}$ cannot jump over the hole and therefore do not interact with the mushroom's hat. Such orbits behave in a completely regular manner and therefore can be integrated directly to give

$$\frac{2}{2|\partial Q|\mathcal{B}}\Big(\int_0^{\arcsin\left(h^-/t\right)}\int_{t\sin\theta}^{h^-}\cos\theta \mathrm{d}s\mathrm{d}\theta + \int_0^{\arcsin\left(2h^-/t\right)}\int_{t\sin\theta}^{2h^-}\cos\theta \mathrm{d}s\mathrm{d}\theta\Big) = \frac{(2h^-)^2 + (h^-)^2}{2|\partial Q|\mathcal{B}t}, \tag{7.15}$$

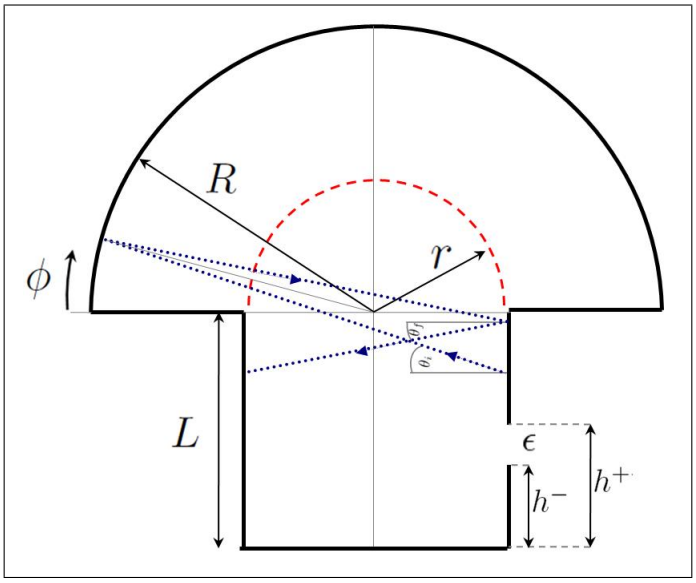

Figure 7.3: Mushroom with rectangular stem and a hole of size ϵ on one of its parallel walls. A near-bouncing ball orbit experiencing a nonlinear collision process in the mushroom's hat is shown.

where we have neglected terms of order $\sim t^{-2}$ and multiplied by 2 due to the horizontal symmetry of the billiard. Similarly, ICs with $h^+ < x < L$ and $0 > \theta > -\arctan\frac{\epsilon}{4\rho R}$ give

$$\frac{2}{2|\partial Q|\mathcal{B}}\int_0^{\arcsin\left((L-h^+)/t\right)}\int_{t\sin\theta}^{L-h^+}\cos\theta \mathrm{d}s\mathrm{d}\theta = \frac{(L-h^+)^2}{2|\partial Q|\mathcal{B}t}. \tag{7.16}$$

ICs from ∂Q_s^b have contributions of order $\sim t^{-2}$ to $P(t)$ and therefore are ignored.

As expected, the survival probability at long times is proportional to the square of the available length on either side of the hole. For the remainder of this section we consider ICs (x_i, θ_i) such that $h^+ < x_i < L$ and $0 < \theta_i \ll 1$, and investigate how they contribute to $P(t)$. We let n denote the number of collisions a particle experiences from straight to straight segment before entering the hat of the mushroom, and define $d_1 = L - (x_i + 2rn\tan\theta_i) > 0$ as the distance from the edge of the straight to the point of the last straight wall collision. We can see that $n = \left\lfloor \frac{L-x_i}{2r\tan\theta_i} \right\rfloor$, where $\lfloor\cdot\rfloor$ $\lceil\cdot\rceil$ are the floor and ceiling functions respectively. Note that $0 < d_1 < 2r\tan\theta_i$. Once a particle enters the hat of the mushroom it is advantageous to switch to coordinates suitable for the circle billiard map given

by $(\phi, \psi) \to (\phi + \pi - 2\psi, \psi)$ such that ϕ is the angular collision coordinate and increases from zero in an anticlockwise fashion as shown in Figure 7.3, while $\psi \in (-\frac{\pi}{2}, \frac{\pi}{2})$ is the angle of reflection. Note that ϕ is different from what was used in section 7.2 Also, ψ is used instead of θ here to distinguish between collisions on the curved segment of the billiard boundary (∂Q_h^c) and collisions elsewhere. Once in the hat, we neglect collisions with the vertical base ∂Q_h^b, by using the image reconstruction trick as before. We find that the particle entering the hat will first collide with ∂Q_h^c at

$$\phi = -\frac{d_1}{R} + (1 + \rho)\,\theta_i > 0, \tag{7.17}$$

and its angle will be

$$\psi = -\frac{d_1}{R} + \rho\theta_i. \tag{7.18}$$

Let θ_f be the final angle obtained when the orbit re-enters the stem of the mushroom after experiencing a reflection process (a series of $k \in \mathbb{Z}^+$ collisions with ∂Q_h^c) in the hat. We thus find that

$$\theta_f = \frac{2kd_1}{R} - (2k\rho + 1)\,\theta_i. \tag{7.19}$$

By carefully investigating the reflection process we find that k is actually restricted to only three possible scenarios such that k can either be equal to 1, $\lceil \frac{R}{r} \rceil$ or $\lceil \frac{R}{r} \rceil + 1$, depending on the ICs (x_i, θ_i), which agree with the so called 'magic numbers' from Ref [185]. This can be seen if one looks at the least number of iterations of the circle billiard map before the orbit described by (7.17) and (7.18) intersects the horizontal slit hole:

$$k = inf\left\{ j \in \mathbb{Z}^+ : \left| \frac{\psi}{(2j-1)\,\psi + \phi} \right| < \rho \right\}. \tag{7.20}$$

In equation (7.21) below we have substituted the possible values of k into (7.19) and also calculated the values of θ_i for which each collision scenario corresponds

to:

$$\theta_f = \begin{cases} \frac{2d_1}{R} - (2\rho+1)\,\theta_i < 0, & \frac{(2\rho+1)d_1}{2\rho(\rho+1)R} < \theta_i, & k=1 \text{ collision} \\ \frac{2\zeta d_1}{R} - (2\zeta\rho+1)\,\theta_i > 0, & \frac{d_1}{2\rho R} < \theta_i < \frac{(2\zeta\rho-1)d_1}{2\zeta\rho^2 R}, & k=\zeta \text{ collisions} \\ \frac{2(\zeta+1)d_1}{R} - (2\,(\zeta+1)\,\rho+1)\,\theta_i > 0, & \frac{(2\zeta\rho-1)d_1}{2\zeta\rho^2 R} < \theta_i < \frac{(2\rho+1)d_1}{2\rho(\rho+1)R}, & k=(\zeta+1) \text{ collisions} \end{cases} \tag{7.21}$$

where we have set $\zeta = \left\lceil \frac{R}{r} \right\rceil$. Note that d_1 is a function of both x_i and θ_i. The first inequality on θ_i ($k=1$ collision) seems to suggest that θ_i is unbounded, however this is not the case. This can be seen in an example situation plotted in Figure 7.4 where we have made the substitution $\omega = \frac{d_1}{2R\theta_i} \in (0,\rho)$. Notice that if ρ^{-1} is

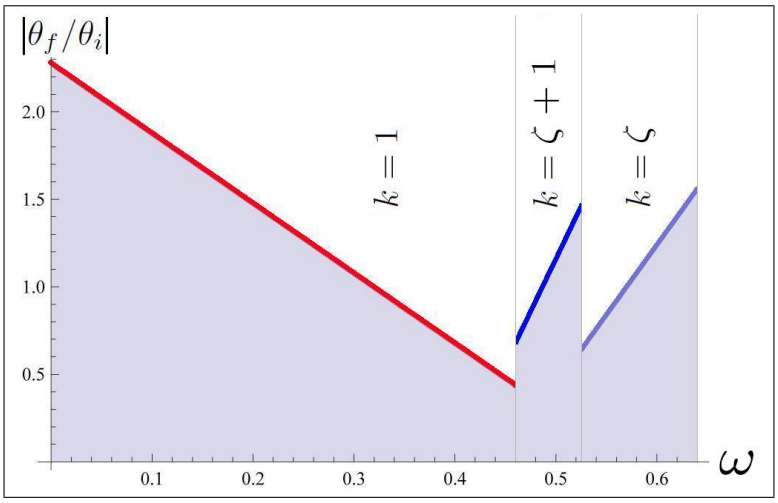

Figure 7.4: Reflection process in the mushroom's hat described in (7.19) using the substitution $\omega = \frac{d_1}{2R\theta_i} \in (0,\rho)$ with $\rho = \cos\frac{(5+\sqrt{2})\pi}{23}$ and $d_1 = 0.01$. The Red, Blue and light Blue lines correspond to $k = 1, \zeta+1$ and ζ reflection process respectively as inscribed in the figure.

an integer, then the ζ-collision processes in (7.21) is no longer attainable and we only have two possible collision scenarios. It is interesting to note that if $\rho = 1$, equation (7.21) reduces to equations (3.10) and (3.11).

We now formulate the time of escape for ICs (x_i, θ_i):

$$t(x_i,\theta_i,k) \approx \frac{L-x_i}{\theta_i} + \frac{L-h^+}{|\theta_f|} + 2R\,(\rho+k+1)\,, \tag{7.22}$$

where we have taken small angle approximations, and substitute the values of θ_f and k for each collision scenario to get three equations for the time to escape. Each one of these equations describes conic sections since they are quadratic in both x_i and θ_i variables. Rearranging to make θ_i the subject, we obtain three hyperbolae in the $x_i - \theta_i$ plane, describing the ICs that escape exactly at large times t. It is important to know the domain of each hyperbola. This can be obtained by substituting for the d_1 variables into the inequalities of (7.21), and then rearranging for θ_i. These inequalities are given below for the corresponding collision scenarios:

$$\begin{aligned}
&k = \zeta \text{ collisions }, && \frac{L - x_i}{2\rho(1+n)R} < \theta_i < \frac{(2\zeta\rho - 1)(L - x_i)}{2\rho\zeta\rho R(1+2n) - 2\rho n R}, \\
&k = (\zeta + 1) \text{ collisions }, && \frac{(2\zeta\rho - 1)(L - x_i)}{2\rho\zeta\rho R(1+2n) - 2\rho n R} < \theta_i < \frac{(2\rho + 1)(L - x_i)}{2\rho R(\rho + 2n\rho + 1 + n)}, \\
&k = 1 \text{ collision }, && \frac{(2\rho + 1)(L - x_i)}{2\rho R(\rho + 2n\rho + 1 + n)} < \theta_i.
\end{aligned} \tag{7.23}$$

For $n = 0, 1, \ldots$ and for t large, we plot the three hyperbolae from (7.22) subject to (7.23) and the three straight lines from (7.21) onto the $x_i - \theta_i$ plane (see Figure 7.5). These define an area in phase space which corresponds to the ICs that survive at least until time t for fixed n. The various colors indicate the type of reflection process k the ICs experience in consistence with the ones in Figure 7.4. To obtain the contribution to $P(t)$ of these long surviving ICs, we must integrate each non-overlapping area and sum them all up. Note that the invariant measure will be assumed to be $\mathrm{d}\mu = (2|\partial Q|\mathcal{B})^{-1}\mathrm{d}\theta_i \mathrm{d}x_i$ here since θ_i is small and thus $\mathrm{d}\sin\theta_i \approx \mathrm{d}\theta_i$.

The corners of each enclosed area $A - G$, as shown in Figure 7.5, for each value of n are given in Appendix E. As we already expect, there are various issues which one needs to consider in order to obtain correct asymptotic expressions for the areas. Firstly, one needs to approximate all the hyperbolae by straight lines. This is done by joining the corners $A - G$ and thus forming an irregular polygon. For example, the hyperbola between A and F, which comes from $t(x_i, \theta_i, 1)$, is approximated by a straight line joining A and F. Similarly, for the hyperbola

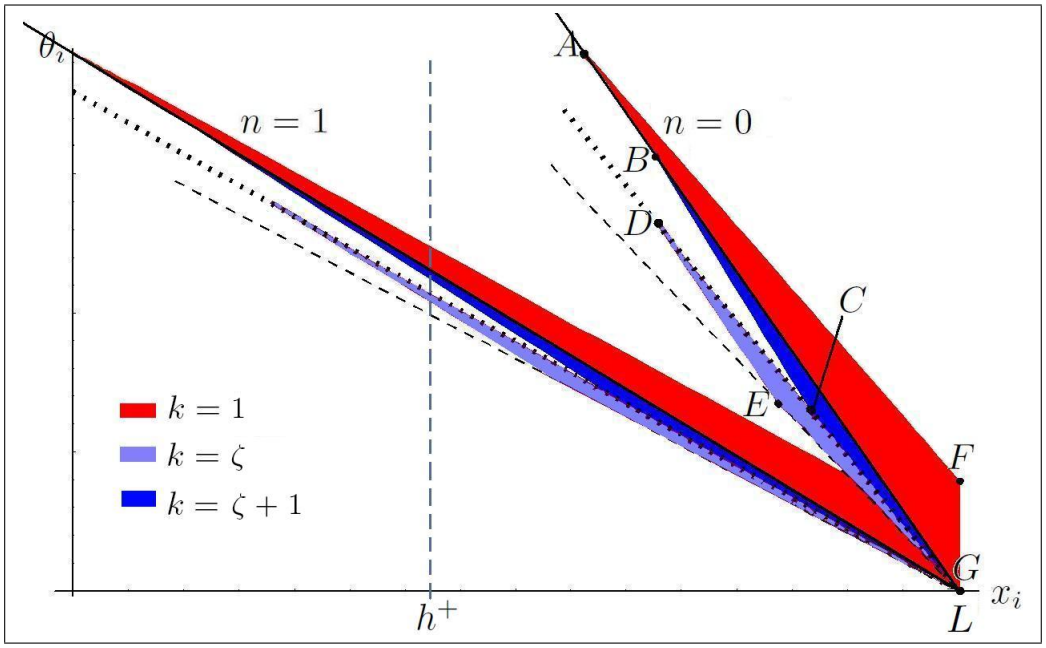

Figure 7.5: Area enclosed by equations (7.22) subject to (7.23) and equations (7.21) in the $x_i - \theta_i$ phase space for $n = 0$ and 1, using $\rho = 0.6$, $L = 1$ and $t = 50$. The colors used are in consistence with the ones in Figure 7.4. The dotted, dashed and solid black straight lines come from the inequalities in equation (7.21). The corners $A - G$ are defined in Appendix E and are each highlighted by a black dot for $n = 0$. The dashed vertical line at $x_i = h^+$ shows how the hole truncates the area of interest. The area defined for all n, corresponds to the ICs that survive at least until time $t = 50$.

joining B and C, which comes from $t(x_i, \theta_i, \zeta)$, and for the hyperbola joining D and E which comes from $t(x_i, \theta_i, \zeta + 1)$. The remaining edges are already straight lines and thus need no approximating. As argued at the beginning of section 3.5, the error in these approximations is $\mathcal{O}(t^{-2})$ and hence meets our required asymptotic accuracy.

Another issue to be dealt with is the position of the hole which restricts the irregular polygons in $x_i \in (h^+, L)$. This forces a deformation by truncating each polygon from the left each time one of its corners surpasses the hole's position as seen for example in Figure 7.5. This is due to the tilting effect caused as n is increased. Following the analysis of section 3.5, we expect 7 different sums since there are 6 corners $(A - F)$, each of which will intersect the hole at h^+ at different values of n. We thus solve for n and find that the leftmost corner

$A_{x_i} = h^+$ when $n = n_A = \left\lfloor \frac{\frac{t}{R}(1+2\rho)-2-20\rho-12\rho^2-4\rho^3}{4\rho+12\rho^2+8\rho^3} \right\rfloor$. Similar expressions have been obtained for all other corners $(B-F)$ and are given in Appendix F. Interestingly,

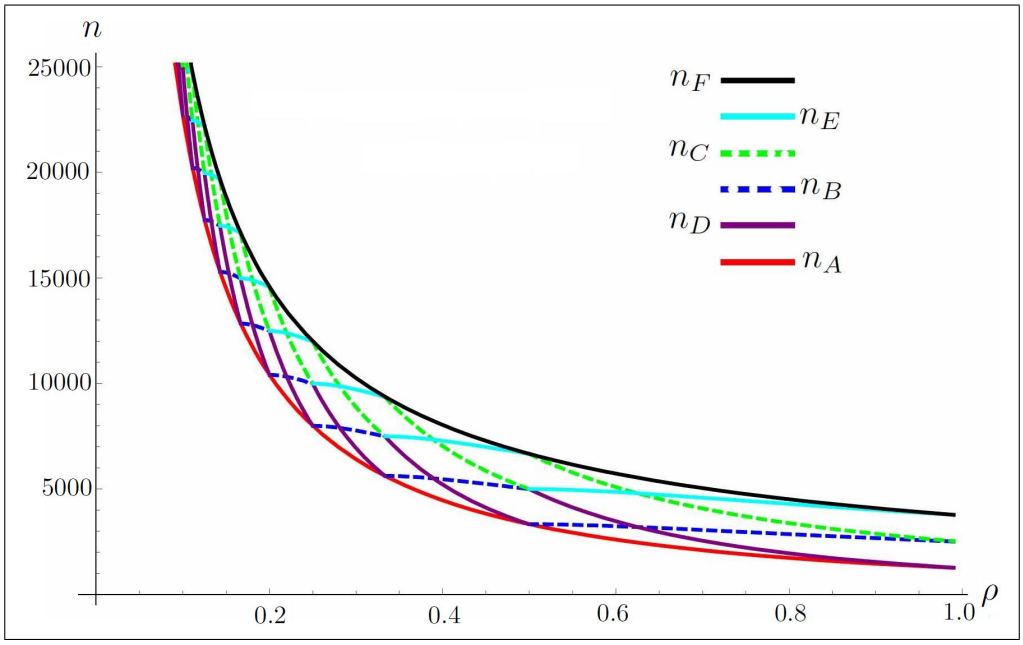

Figure 7.6: $n_A - n_F$ are defined in the text above and given in Appendix F. The figure shows how they vary discontinuously as a function of $\rho = \frac{r}{R} \in (0,1)$ for $t = 10^4$.

we find that the order in which the corners $A-F$ coincide with the hole's position depends on the system's control parameter $\rho = \frac{r}{R}$. Their order alternates between $n_A < n_B \leq n_D < n_E \leq n_C < n_F$ and $n_A < n_D \leq n_B < n_C \leq n_E < n_F$ for $\rho \in (0,1)$, which is shown in Figure 7.6. This is due to the discontinuity introduced by the ceiling function in ζ for $n_B - n_E$, hence the lower and upper bounds of the 7 sums will depend on the above order, and so will their arguments. Altogether we write:

$$\sum_{n=0}^{n_A} \hat{P}_1 + \sum_{n=n_A+1}^{n_B} \hat{P}_2 + \sum_{n=n_B+1}^{n_D} \hat{P}_3 + \sum_{n=n_D+1}^{n_E} \hat{P}_4 + \sum_{n=n_E+1}^{n_C} \hat{P}_5 + \sum_{n=n_C+1}^{n_F} \hat{P}_6 + \sum_{n=n_F+1}^{\infty} \hat{P}_7, \tag{7.24}$$

$$\sum_{n=0}^{n_A} \tilde{P}_1 + \sum_{n=n_A+1}^{n_D} \tilde{P}_2 + \sum_{n=n_D+1}^{n_B} \tilde{P}_3 + \sum_{n=n_B+1}^{n_C} \tilde{P}_4 + \sum_{n=n_C+1}^{n_E} \tilde{P}_5 + \sum_{n=n_E+1}^{n_F} \tilde{P}_6 + \sum_{n=n_F+1}^{\infty} \tilde{P}_7, \tag{7.25}$$

where $\hat{\cdot}$ and $\tilde{\cdot}$ are used to distinguish between the two orderings described above. $\hat{P}_i$ and $\tilde{P}_i$, $i = 1, \ldots 7$, are the respective areas of the polygons which we are

summing over. Note that $\hat{P}_1 = \tilde{P}_1$ and $\hat{P}_7 = \tilde{P}_7$. The process of finding all the $\hat{P}_i$ and $\tilde{P}_i$ is long but fairly elementary.

We now obtain leading order expressions for each sum in t. First we substitute $t = \frac{1}{u}$, and then $n = \frac{v}{u}$ into the $\hat{P}_i$ and the $\tilde{P}_i$, such that u is small and $v = \mathcal{O}(1)$. We Taylor expand $\hat{P}_i$ and $\tilde{P}_i$ into series up to order u^2 and then reverse the substitution by setting $v = nu$, thus effectively incorporating the large n into the leading order term of each series expansion. Now each sum can be simplified into expressions involving polygamma functions of order 0 and 1 which can be expanded to leading order (see section 3.5). With these approximations at hand, we obtain expressions for the sums in (7.24) and (7.25). We only present here the first of the approximated sums and include the rest in Appendix G:

$$\sum_{n=0}^{n_A} \hat{P}_1 = \sum_{n=0}^{n_A} \tilde{P}_1 = \frac{(h^+ - L)^2}{2(2\rho+1)t}, \tag{7.26}$$

where we have neglected terms of order $\sim t^{-2}$. Altogether (7.24) and (7.25) take the form:

$$\frac{(L-h^+)^2}{4\zeta(1+\zeta)\rho t}\left[\frac{\varepsilon_1\rho + \varepsilon_2\rho^2 + \varepsilon_3\rho^3 + \varepsilon_4\rho^4}{(2\rho+1)(2\zeta\rho-1)^2} + \ln\left((2\rho+1)^{\jmath_1}(2\zeta\rho-1)^{\jmath_2}\right)\right], \tag{7.27}$$

where the coefficients ε_i $(i = 1\ldots4)$ and $\jmath_j$ $(j = 1, 2)$ are given in Appendix H for both orderings $\hat{}$ and $\tilde{}$. It remains to multiply (7.27) by 2 due to the horizontal symmetry of the mushroom, and normalize by $2|\partial Q|\mathcal{B}$ to obtain a probability. The sum of expressions (7.15)-(7.16) and (7.27) depending on the value of ζ, therefore gives the asymptotic contribution of the long surviving near-bouncing ball orbits $\frac{\mathcal{C}}{t}$ to the mushroom's survival probability $P(t)$.

Interestingly yet reassuringly, in the limit of $\rho \to 1$, $\zeta = 2$ and the complicated expression for (7.27) reduces to $\frac{(L-h^+)^2(3\ln 3+2)}{4t}$ (see equation (3.33)), which is exactly what one would expect since in this limit, the mushroom billiard is reduced to the half-stadium billiard [87]. In the opposite limit where $\rho \to 0$, $\zeta \to \infty$ the mushroom's stem shrinks and expression (7.27) has asymptotic expansions of

$$\frac{1}{t}\left(\frac{7}{2}(L-h^+)^2 - 2(1+\zeta)(L-h^+)^2\rho + 3\zeta(L-h^+)^2\rho^2\right) + \mathcal{O}(r^3) \tag{7.28}$$

and

$$\frac{1}{t}\left(-\frac{5}{2}(L-h^+)^2+4(1+\zeta)(L-h^+)^2\rho-4(2\zeta-3)(L-h^+)^2\rho^2\right)+\mathcal{O}(r^3), \quad (7.29)$$

for the two orderings $\hat{\cdot}$ and $\tilde{\cdot}$ respectively, indicating that the discontinuous dependence on ζ persists, hence this limit is in some sense ill-defined.

7.4 Numerical Simulations

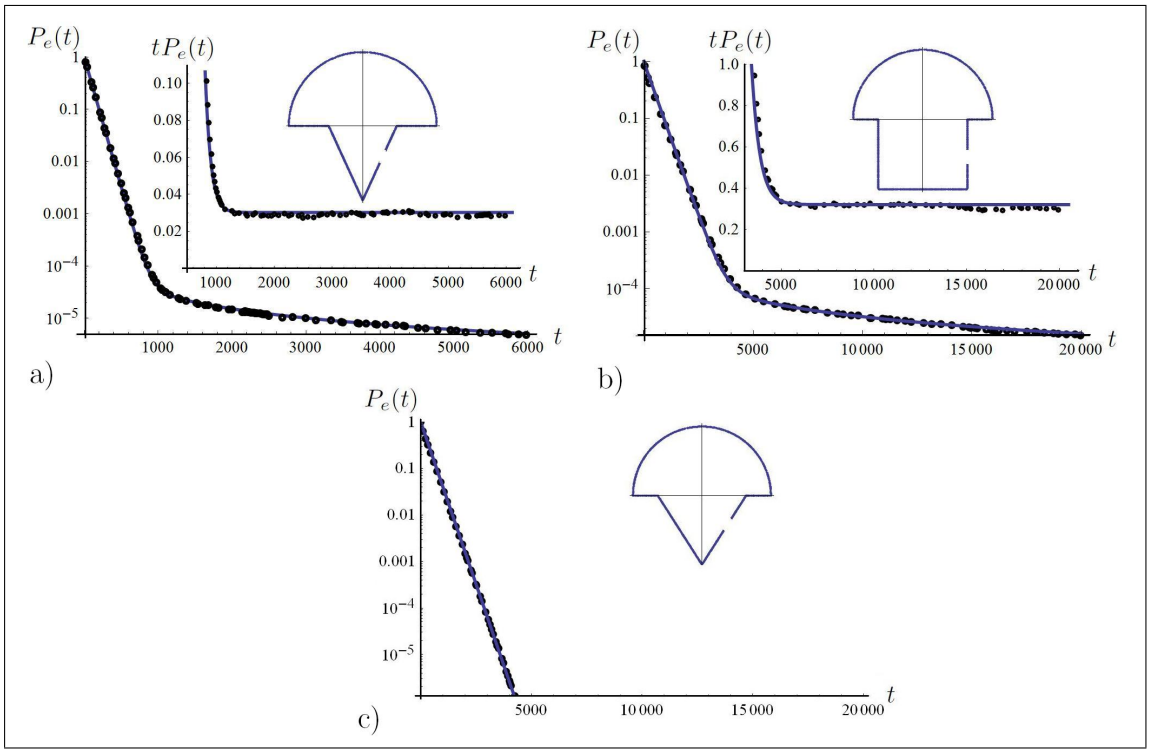

Figure 7.7: Numerical simulations of $P_e(t)$ defined in (7.30) are plotted on a logarithmic scale using 10^8 chaotic ICs as a function of t. The parameters (r, R, L, ϵ) used for the triangular stem *(a)* are $(\cos 0.3484\pi, 1, 1, 0.048)$ such that $\mathcal{S}_\rho = \{(20, 7), (66, 23), (376, 131)\}$, while for the rectangular stem *(b)* $(\cos\left(\frac{5+\sqrt{2}}{23}\pi\right), 1, 1, 0.02)$, with $h^+ = 0.3$ such that the mushroom's hat has no MUPOs. The MUPO-free mushroom *(c)* has parameters $(\cos\left(\frac{5+\sqrt{2}}{23}\pi\right), 1, 1, 0.02)$ and appears not to have a power-law tail. The blue curves are the analytic predictions while the numerical data correspond to the empty circles. The insets are plots of $tP_e(t)$ showing the agreement with the analytic expressions for the constant $\mathcal{C}$.

Having obtained exact leading order analytic expressions for all the parameters appearing in (7.1) we now numerically test their validity by plotting the conditional probability $P_e(t)$ that a particle survives up to time t given that the particle is chosen uniformly from the ergodic component of the billiard flow (see Figure 7.7).

$$P_e(t) = (P(t) - \mathcal{A})/\mathcal{B} = e^{-\bar{\gamma}t} + \frac{\mathcal{C}}{t} + \mathcal{O}\left(\frac{1}{t^2}\right). \tag{7.30}$$

The plots are purposely chosen (from many more) to portray and verify the results obtained in the previous subsection. Three different mushrooms are simulated: one

with a finite number of MUPOs present only in the hat *(a)*), one with bouncing ball orbits in the stem and a MUPO-free hat *(b)*), and one with no MUPOs at all *(c)*). The empty black circles in the plots correspond to the numerical data while the blue curves give the analytic predictions of (7.30). Different hole sizes and total perimeters give different exponential escape rates $\bar{\gamma}$ and in turn cross-over times to a power law decay. Notice the huge contribution to $\mathcal{C}$ from the bouncing ball orbits. Although each simulation consists of $\sim 10^8$ chaotic ICs, we were unable to detect any power law decay in the MUPO-free mushroom *(c)*) and hence any clues of stickiness.

7.5 Conclusions and Discussion

In this chapter, we have attempted to quantify the stickiness due to MUPOs observed in the mushroom billiard by placing a hole in its ergodic component and looking at the survival probability function $P(t)$ at long times (see equation (7.1)). Our analytic predictions are in good agreement with the numerical simulations performed and therefore confirm that $P(t) \sim \frac{\mathcal{C}}{t}$ for long enough times. Also, their good agreement with the constants $\mathcal{C}$ derived in sections 7.2 and 7.3 for MUPOs present in the hat and in the stem respectively, implies that these MUPOs are indeed the primary causes of the power-law decay $\mathcal{O}(t^{-1})$. This observation in turn applies to the Poincaré recurrence times distribution $\mathcal{Q}(t)$ and the rate of mixing of the ergodic component [157].

The explicit expressions obtained here for $\mathcal{C}$, allow one not only to predict but also to calibrate the asymptotic behavior of $P(t)$. Also, we have shown that these distributions as well as the overall existence of MUPOs in the hat are sensitive to the system's control parameter $\rho = \frac{r}{R}$, whilst only the near-bouncing ball orbits' contribution to $P(t)$ depends on the hole's position and size. The reason for this is that the hole intersects the sticky region generated in phase space by the period-2 bouncing ball orbits. This creates a fictitious, time dependent 'island of stability' in the mushroom's ergodic component. Although orbits in it

are unstable, they only experience up to one non-linear collision process before escaping, thus allowing us to approximate their occupancy in phase space with polygonal 'spikes' which we could then integrate over. In the case of the MUPOs in the mushroom's hat, we could easily bound the long surviving orbits by assuming that they will escape exponentially fast once in the stem.

Furthermore, as discussed in chapter 6, we expect that the MUPO-free mushroom (see section 6.3) exhibits a reduced amount of stickiness (larger scaling exponent since $\mathcal{C} = 0$). This is attributed to the difficulty in 'finding' the foot of the mushroom by chaotic orbits which are just inside the dashed circular arc of radius r. However, despite our extensive numerical simulations performed we have been unable to detect any power law decay of $P(t)$ thus far.

Finally, it is expected that the methods used here can be further generalized and applied to other mushrooms with elliptical hats for instance, or even to other billiards such as the annular and drivebelt billiards where circle-type MUPOs act as scaffolding for sticky orbits to cling onto. We also hope that the exact results obtained for the classical survival probability function $P(t)$ in sections 7.2 and 7.3 will be of benefit to future semiclassical treatments of quantum mushrooms.

Chapter 8

The Drive-Belt stadium

In the previous two chapters we investigated the mushroom billiard. An interesting paradigm of a mixed phase space billiard, which reduces to the chaotic stadium and integrable circle billiards in the limits $\rho \to 1$ and $\rho \to 0$ respectively. For typical control parameter values $\rho \in (0, 1)$, an infinity of MUPOs populate the ergodic component of its phase space. We investigated their structural stability using continued fraction expansions and managed to describe a zero measure set of control parameter values ρ for which there are no MUPOs. The resulting open MUPO-free mushroom has been shown to exhibit a reduced amount of stickiness, realized through an asymptotic decay of $P(t) \sim t^{-2}$. Mushrooms with finitely many MUPOs can also be constructed through the manipulation of the continued fraction expansion of $\frac{2 \arccos \rho}{\pi}$ (see section 6.3) and their asymptotic contribution to $P(t)$ can be calculated exactly to leading order (see equation (7.13)). Furthermore, the small angle collision rule of near bouncing ball orbits entering the mushroom's hat from a rectangular shaped stem has allowed us to use the method first devised for the stadium in section 3.5 and obtain exact results for the asymptotic survival probability of the open mushroom billiard (see equation (7.27)).

All of the above results give a very good understanding of the structure of the intermittent dynamics exhibited by the mushroom billiard. We now turn to a different deformation of the stadium, namely the *drivebelt* billiard. This smooth, non-dispersing, ergodic billiard has no bouncing ball type MUPOs however still

exhibits intermittency through a finite number of circle-type MUPOs. The number of these marginally unstable families of periodic orbits is controlled by the size of the larger of the drivebelt's two circular arcs. The drivebelt's phase space is investigated and an equivalent of the small angle collision rule is derived. We find that our method for calculating the asymptotic survival probability can be generalized and applied to this family of billiards as well. We end with a short discussion on the results and implications of this chapter's results.

8.1 Introduction

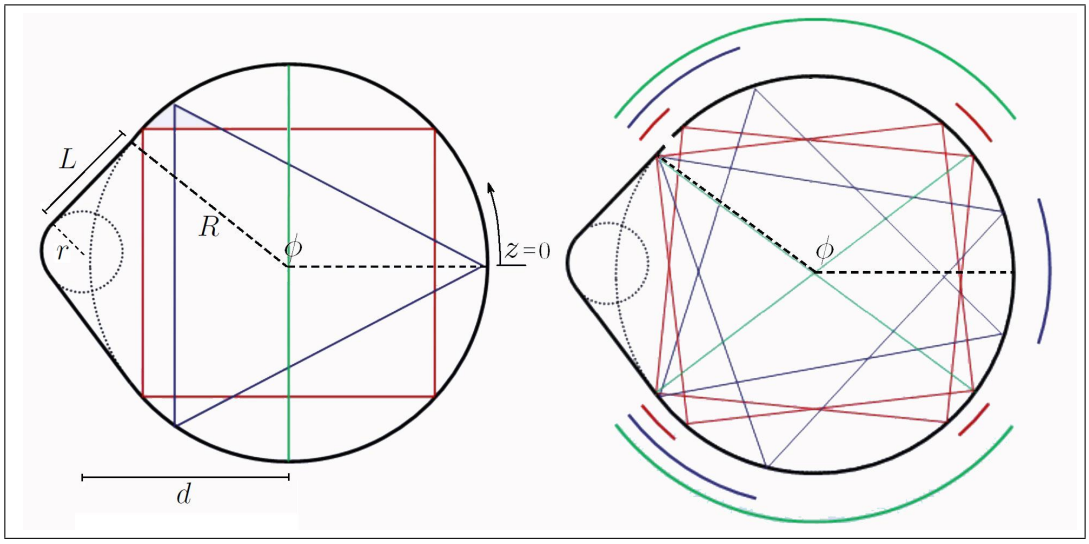

Figure 8.1: The drivebelt billiard is defined by the ratio of the small and big radii $\frac{r}{R} \in (0,1)$ and the arc of the larger of the two circular arcs $\phi \in (\pi/2, \pi)$ which in turns defines which MUPOs exist in the drivebelt's phase space. *Left:* Drivebelt with $\frac{r}{R} = 0.3$ and $\phi = 2.5$. The period two diametrical MUPO, the period three triangle MUPO and the period four square MUPO are shown. *Right:* These MUPOs can be oriented within a certain range depending on the value of ϕ.

The billiard to be studied in this section is defined by two arcs of circles, one with the radius of r, the other with R, with centers placed at a distance d. The arcs are connected by their common outer tangent of length L (see Figure 8.1) such that the boundary is C^1 smooth. This construction, also known as a 'titled'

stadium, or a 'squash' was originally proposed by Bunimovich (unpublished), investigated numerically in [45], and later rediscovered in [138] and [157], where it was first called a 'drivebelt' billiard and it's polynomial mixing rates were studied in detail.

The billiard is hyperbolic, ergodic, and Bernoulli [130] and remains chaotic no matter how short L is, but turns into the integrable circle when $L \to 0$. The mechanism of chaos present is the defocusing one (same as for the stadium billiard) where a parallel beam of rays becomes convergent and then divergent after focusing. Therefore expansion in phase space is guaranteed almost everywhere [151]. Recently, Bálint *et al.* study a two-parameter set of two-dimensional billiards with one of the limiting cases being the drivebelt and conjecture that they obtain ergodic non-dispersing billiards which are close to their drivebelt limit [189]. Birkhoff coordinates (z, θ) are defined such that $z \in (0, |\partial Q|)$ increases from zero anticlockwise from the rightmost point of the billiard as shown in Figure 8.1 and $\theta \in (-\frac{\pi}{2}, \frac{\pi}{2})$ is the angle of incidence.

8.2 Multiple Intermittency

The drivebelt billiard is of interests to our investigations for two reasons. Firstly, it is a non-uniformly hyperbolic system due to the existence of circle-type MUPOs in the larger of the two arcs. Therefore we expect the open drivebelt's survival probability to decay as $P(t) \sim \mathcal{C}/t$. The number of MUPOs grows approximately as $\frac{3}{2}\pi \ln \frac{\pi}{2(\pi-\phi)}$, hence the term 'multiple intermittency'. This is because a MUPO of period s will exist only if it satisfies $\frac{2\pi}{s} > 2(\pi - \phi)$. Note that for every s there exists a multiplicity of at most $\lfloor \frac{s}{2} \rfloor$ MUPOs. The mountain-plot in Figure 8.2 shows how MUPOs come into existence as ϕ is increased from $\frac{\pi}{2}$ to π. Also in Figure 8.2 we can see how the families of MUPO define a range along which they can be oriented inside the larger circular arc. The example case shown in the right panel of Figure 8.1 is also highlighted in Figure 8.2. We define the set containing all MUPOs for a given ϕ by $\mathcal{S}_\phi := \left\{(s,j) \middle| \frac{2\pi}{s} > 2(\pi-\phi), s \geq 2, 1 \leq j \leq \lfloor \frac{s-1}{2} \rfloor \right\}$,

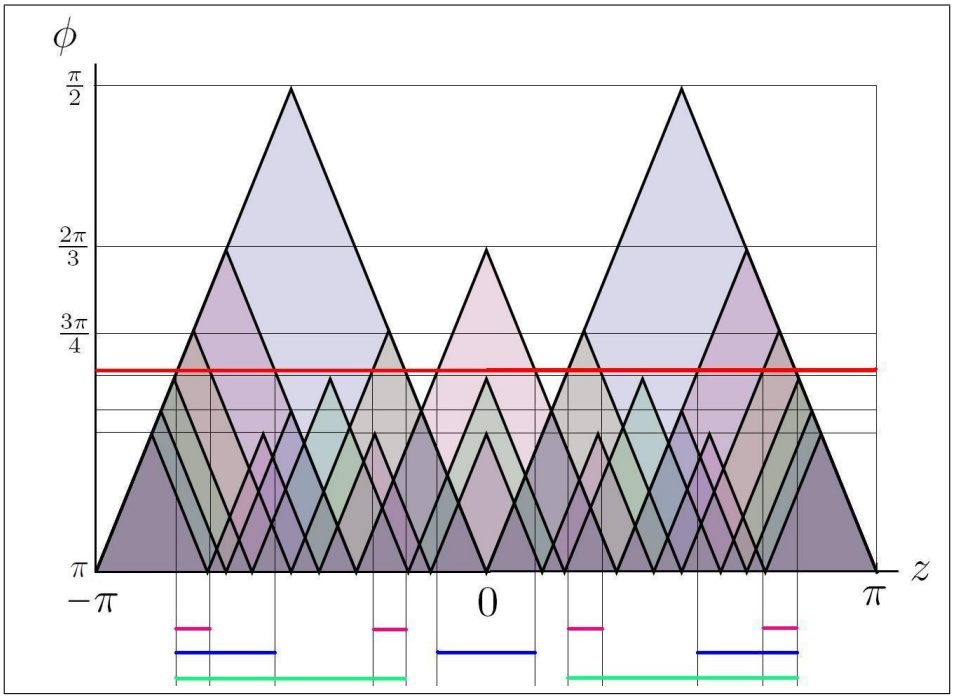

Figure 8.2: As $\phi \in (\pi/2, \pi)$ is increased, more and more MUPOs come into existence. Only the first 7 MUPOs are shown here. The range they cover also increases linearly and is shown on the horizontal axes. The range covered by MUPOs for the example case of $\phi = 2.5$ used in all drivebelt related figures and numerical simulations is explicitly shown (also see right panel of Figure 8.1).

where s and j are coprime integers describing the period and rotation number as in the previous sections.

Secondly, it is interesting to see whether our methods can be applied to produce exact asymptotic results for $P(t)$. A necessary ingredient in our previous investigations was to obtain a small angle collision rule (see equations (3.10)-(3.11) and (7.21)), which described how a nonlinear collision process affects a slightly perturbed MUPO. In the case of the stadium we considered near bouncing ball orbits with a symbolic dynamics collisions sequence given by $S \dots SC^f S \dots S$ until escape, where S and C correspond to collisions on straight and curved boundary segments respectively and $f = 1$, or 2 corresponding to the two possible collision scenarios. For a mushroom with a rectangular stem we considered orbits with a similar symbolic dynamics collision sequence, though f could now attain three val-

ues $f = 1, \lceil \frac{R}{r} \rceil$, and $\lceil \frac{R}{r} \rceil + 1$ corresponding to the three possible collision scenarios (see Figure 7.4). What is the corresponding collision sequence and collision rule in the drivebelt?

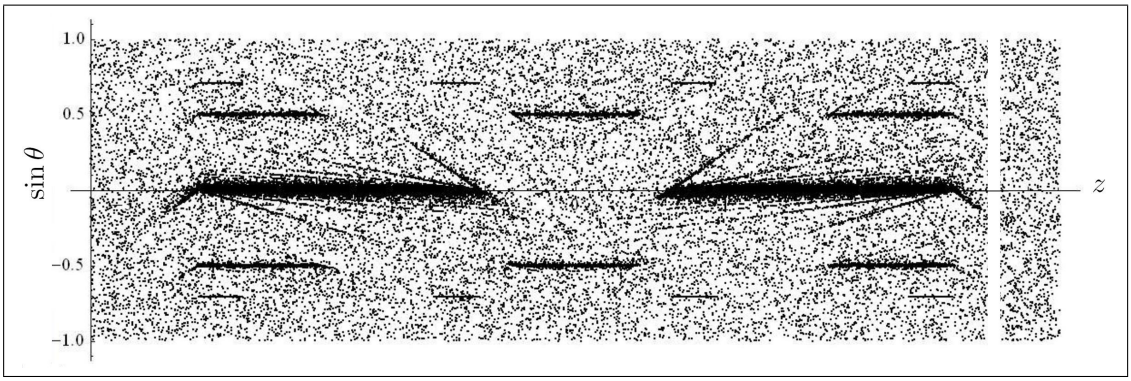

Figure 8.3: Phase space plot of drivebelt billiard showing 10^5 randomly chosen initial conditions which survive up to time $t = 1000$ with drivebelt parameters $\phi = 2.5$, $R = 1$, $r = 0.3$ and a hole of size $\epsilon = 0.1$ positioned at $z \in (2.8, 2.9)$.

We begin our investigations with some numerical simulations of a drivebelt billiard with $R = 1$, $r = 0.3$ and $\phi = 2.5$. Notice that $\mathcal{S}_\phi = \{(2,1),(3,1),(4,1)\}$. Figure 8.3 shows all the initial conditions (ICs) (initially distributed on the billiard boundary according to the equilibrium density) which do not escape after time $t = 1000$ through a small hole of size $\epsilon = 0.1$ placed well inside the ergodic component of the phase space and away from any sticky regions at $z \in (2.8, 2.9)$. The hole can be clearly identified as the thin blanc vertical strip on the right of the figure. We notice that long surviving initial conditions seem to populate the sticky regions surrounding the locations of the MUPOs. We also notice that these ICs are supported on a spike-like fractal-looking pattern formed by the removal of the unstable manifold of the hole up to $t = 1000$.

Figure 8.4 shows all the initial conditions which do not escape after time $t = 2000$ through a small hole of size $\epsilon = 0.1$ intentionally placed at $z \in (2.3, 2.4)$ as to overlap part of all four MUPO ranges. Note that the number of initial conditions plotted in Figures 8.3 and 8.4 are the same. Also notice that the hole repeats itself in all sticky regions. The density of long surviving orbits in regions

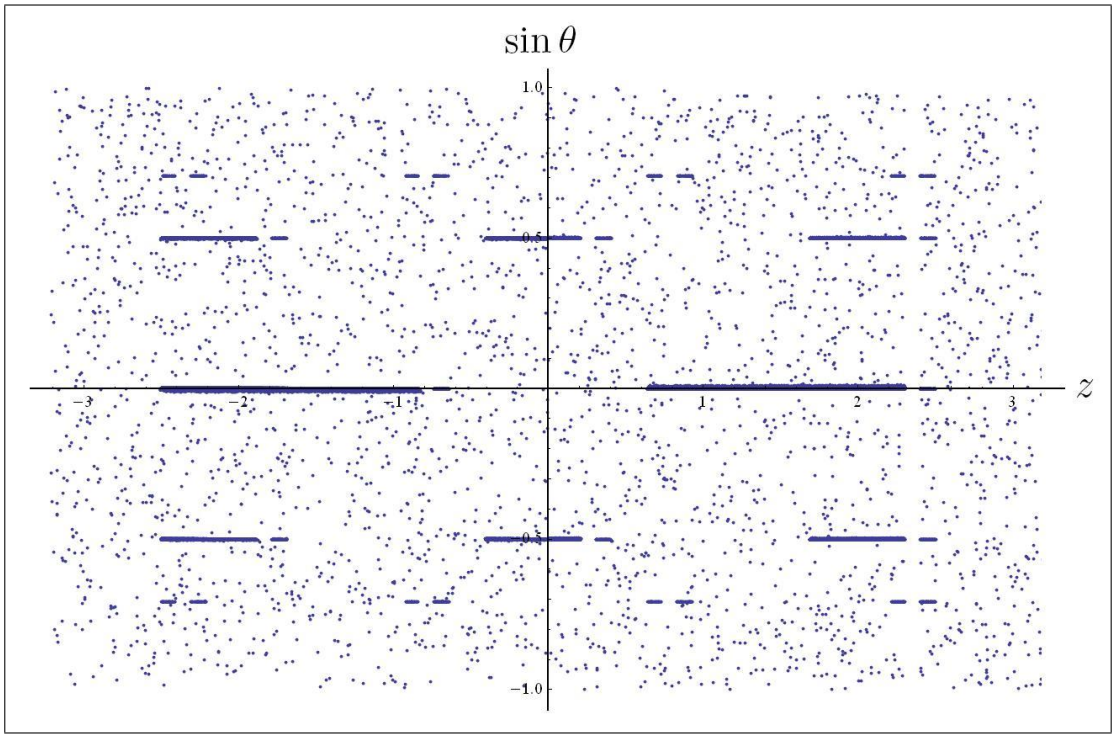

Figure 8.4: Phase space plot of drivebelt billiard showing 10^5 randomly chosen initial conditions which survive up to time $t = 2000$ with drivebelt parameters $\phi = 2.5$, $R = 1$, $r = 0.3$ and a hole of size $\epsilon = 0.1$ positioned at $z \in (2.3, 2.4)$.

away from MUPOs appears to have decreased while the spike like structure has shrank dramatically. We therefore zoom in and take a closer look (see Figure 8.5). This encouraging figure shows that the long surviving obits are supported on familiar structures (as in Figure 3.4 for the stadium) and suggests that our methods should be applicable if modified appropriately.

8.3 Asymptotic Survival Probability

Assuming that for large enough times the long surviving initial conditions are dense only in the close vicinity of MUPOs, then a hole which overlaps part of all MUPO ranges will separate the long surviving IC into two simple families: orbits initially precessing towards the hole, and orbits initially precessing away from the hole. We clarify this last point. A small perturbation $\eta_i \ll 1$ in the angle of incidence $\theta_{s,j}$ of a MUPO will cause the orbit to precess in a quasi-periodic fashion

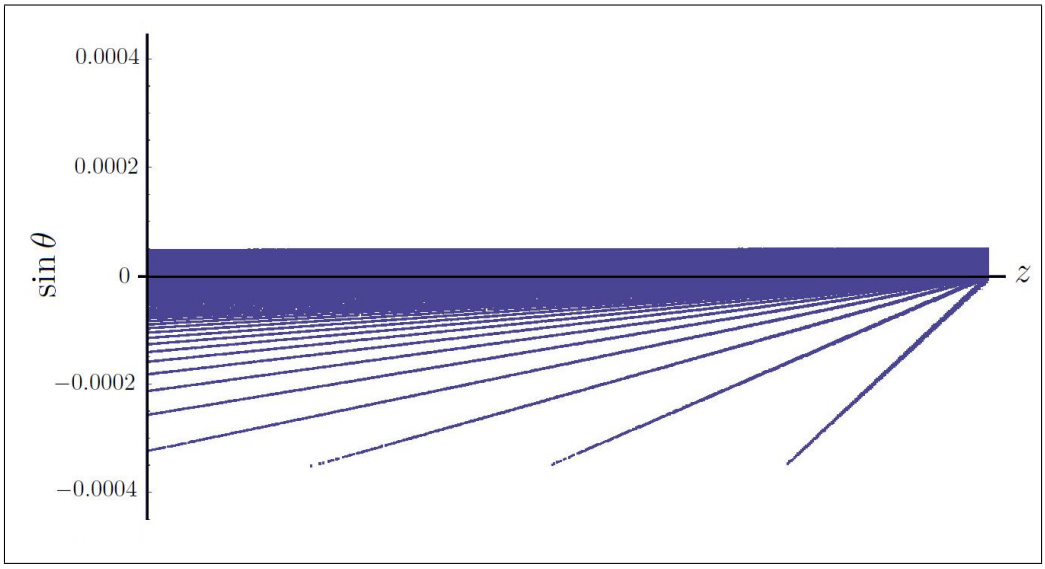

Figure 8.5: Magnification of phase space plot in Figure 8.4 at $z \in (2.45, 2.5)$ and $\sin\theta \in (-0.0004, 0.0004)$ showing how the long surviving $t > 2000$ initial conditions populate the area near the period two diametrical MUPO.

(as was the case in the mushroom's hat). If the orbit is precessing towards the hole and η_i is small enough then the orbit may survive for an unbounded amount of time and hence will contribute to the asymptotic power-law $\sim t^{-1}$ tail of $P(t)$. In fact such orbits correspond to the ICs with $\theta > 0$ shown in Figure 8.5 and are bounded linearly from above. If the orbit is precessing away from the hole and the η_i is small enough, the orbit will experience a nonlinear collision processes which reverses the orbit's precession direction and is of the type $C \ldots CSC^{s-1}(S)C \ldots C$ until escape. Note that the s in the superscript corresponds to the period of the nearest MUPO. Also the S in brackets, as we shall see only occurs when the first straight segment collision does not reverse the precessing orbit's direction. Finally, the orbit is precessing towards the hole with a final angle of incidence which is not far from $\theta_{s,j}$ and may again have unbounded survival time. Such ICs constitute the spike-like structure observed for $\theta < 0$ in Figure 8.5.

8.3.1 Moving towards the hole

The arguments that follow are in most cases very similar with those of chapter 3 and are therefore only given in brief for the sake of completeness. Let a small hole of size ϵ be situated at $z \in (h^-, h^+) \subset (0, \phi)$, where $h^+ = h^- + \epsilon$, such that it overlaps all MUPO ranges, like the one shown in the right panel of Figure 8.1 for example. We only need to consider ICs (ϕ_i, θ_i) such that $\phi_i \in (0, \phi - h^+)$ is the angular distance of the IC from the nearest edge of the hole and $\theta_i = \theta_{s,j} + \eta_i = \frac{\pi}{2} - \frac{j\pi}{s} + \eta_i$ is the angle of incidence such that the perturbation $\eta_i \ll 1$ causes the orbit to precess towards the hole. Note that the precessing angular velocity is proportional to the perturbation strength η_i. The condition that

$$|\eta_i| < \frac{\epsilon}{2s}, \tag{8.1}$$

guarantees that the IC does not 'jump over' the hole. Hence such an orbit will escape in time t given by

$$\begin{aligned} t(\phi_i, \theta_i) &= \left\lceil \frac{\phi_i}{2\eta_i s} \right\rceil s2R\cos\theta_i \\ &= \frac{R\phi_i \cos\theta_{s,j}}{\eta_i} + \mathcal{O}(1). \end{aligned} \tag{8.2}$$

From the above information we can obtain a lower bound on the relevant time scales for which our results are valid

$$|\eta_i| < \min\left\{ \frac{\epsilon}{2s}, \frac{R\phi_i \cos\theta_{s,j}}{t} \right\}, \tag{8.3}$$

and hence $t > \frac{2sR\phi_i \cos\theta_{s,j}}{\epsilon}$, or even better

$$t > \frac{4\pi R}{\epsilon}, \tag{8.4}$$

since $\sup(\phi_i) = 2\pi/s$.

We can now integrate the area described by the above inequalities with respect to the equilibrium measure $(2|\partial Q|)^{-1}\mathrm{d}z\mathrm{d}\sin\theta = (2|\partial Q|)^{-1}(\cos\theta_{s,j} - \eta_i \sin\theta_{s,j})\mathrm{d}\phi_i\mathrm{d}\eta_i$

as follows:

$$\begin{aligned}\mathcal{I}_1 &= \frac{1}{2|\partial Q|}\int_0^{\frac{\phi_i R\cos\theta_{s,j}}{t}}\int_{\frac{t\eta_i}{R\cos\theta_{s,j}}}^{\phi_1}(\cos\theta_{s,j}-\eta_i\sin\theta_{s,j})\mathrm{d}\phi_i\mathrm{d}\eta_i \\ &= \frac{R^2\phi_1^2(3t-R\phi_1\sin\theta_{s,j})\cos^2\theta_{s,j}}{(2|\partial Q|)6t^2} \\ &= \frac{R^2\phi_1^2\cos^2\theta_{s,j}}{4|\partial Q|t}+\mathcal{O}\left(\frac{1}{t^2}\right),\end{aligned} \tag{8.5}$$

where $\phi_1(s)$ is the angular distance available within the range of the MUPO on the corresponding side of the hole. Similarly we obtain the asymptotic contribution from ICs moving towards the hole but from the other side of the hole

$$\mathcal{I}_2 = \frac{R^2\phi_2^2\cos^2\theta_{s,j}}{4|\partial Q|t}+\mathcal{O}\left(\frac{1}{t^2}\right), \tag{8.6}$$

and the total contribution to the survival probability is

$$P_1(t) = \sum_{(s,j)\in\mathcal{S}_\phi} p(\mathcal{I}_1+\mathcal{I}_2)+\mathcal{O}\left(\frac{1}{t^2}\right), \tag{8.7}$$

where the $p = 1$ if $s = 2$ and $p = 2$ otherwise as to account for the vertical symmetry of the total phase space as seen in Figures 8.3 and 8.4.

8.3.2 Moving away from the hole

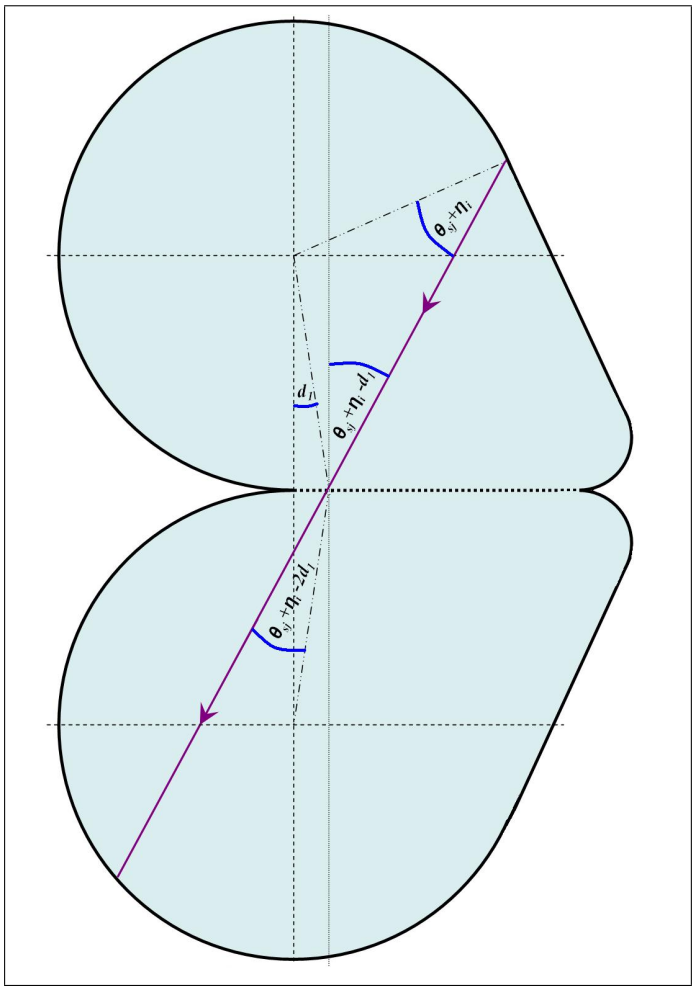

Figure 8.6: A near-periodic orbit (*i.e* a slightly perturbed in angle periodic orbit) with initial angle of incidence $\theta_i = \theta_{sj} + \eta_i$ is 'unfolded' when it collides on a flat segment. The final angle in this case is $\theta_f = \theta_i - 2d_1$. It is possible for the a second flat segment collision to occur after $s-1$ collisions on the lower circular arc. The total collision process is described in equation (8.9) and Figure 8.7.

We now consider ICs (ϕ_i, θ_i) such that the perturbation $\eta_i \ll 1$ causes the orbit to initially precess away from the hole. Here, we define ϕ_i to be the angular distance from the IC to the edge of the circular arc at $z = \phi$. The precessing orbit will first collide with the straight segment after $sn \in \mathbb{N}^+$ collisions. In fact the collision will occur at $z = \phi + d_1$ where $d_1 = 2|\eta_i|sn - \phi_i + \mathcal{O}(\eta_i^2) \geq 0$. Since the collision occurs on a straight segment of the billiard's boundary, we

may 'unfold' the billiard using the *image reconstruction trick* [149] (see Figure 8.6). The resulting angle of incidence with the curved segment is to leading order $\theta_f = \theta_i - 2d_1 = \theta_{s,j} + \eta_f$. Hence, we conclude that the nonlinear collision process described above causes an orbit initially perturbed by η_i to have a final incidence angle θ_f which is η_f away from the original MUPO angle $\theta_{s,j}$ such that $\frac{\eta_f}{\eta_i} = 1 - \frac{2d_1}{\eta_i}$.

If we fix $\theta_i = \theta_{s,j} + \eta_i$ then we expect the collision's type to be $2\eta_s$-periodic in ϕ_i. Hence, there should be at least one more collision scenario. Turns out that this occurs when the orbit follows a $C \dots CSC^{s-1}SC \dots C$ type collision. This means that a second collision with the straight is needed to reverse the precessing direction of the near-periodic orbit. More explicitly this occurs when

$$\phi_i(4s-1) < 2\eta_i s(4ns - 1 - n). \tag{8.8}$$

The appropriate scaling which linearizes $\frac{\eta_f}{\eta_i}$ is given by $\lambda = \frac{d_1}{2\eta_i s}$. The required periodicity in collisions gives an equivalent expression for the small angle collision rule which we name the *small perturbation collision rule*:

$$\left|\frac{\eta_f}{\eta_i}\right| = \begin{cases} 16s^2\lambda - s(4 - 8\lambda) + 1, & 0 \le \lambda < \frac{1}{4s-1}, \quad f = 2 \\ 4\lambda s - 1, & \frac{1}{4s-1} \le \lambda < 1, \quad f = 1. \end{cases} \tag{8.9}$$

This is plotted in Figure 8.7 for the period two diametrical orbit. We notice

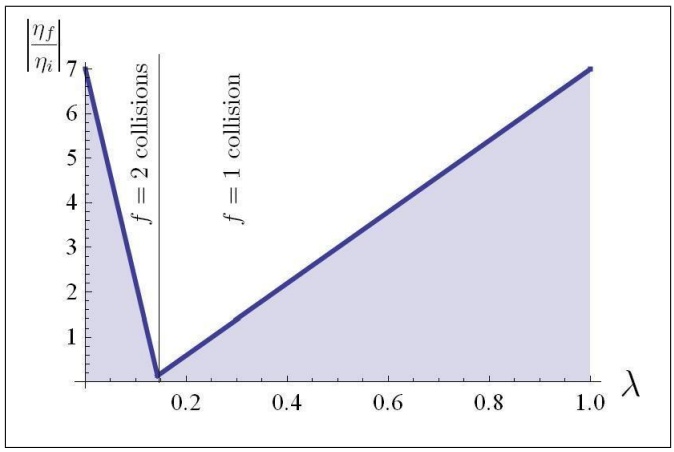

Figure 8.7: The dependence of $\left|\frac{\eta_f}{\eta_i}\right|$ on λ for the period two diametrical MUPO ($s = 2$), where $\eta_i \ll 1$ and $\lambda = \frac{d_1}{2\eta_i s}$ as described in equation (8.9).

that the nonlinear collision increases the return precessing velocity of the IC with a higher probability. Also, it seems that the $f = 2$ collision scenario is much less probable than $f = 1$.

We now formulate the time to escape:

$$\begin{aligned} t(\phi_i, \theta_i) &= \left\lceil \frac{\phi_i}{2\eta_i s} \right\rceil s2R\cos\theta_i + \left\lceil \frac{\phi_1}{2|\eta_f|s} \right\rceil s2R\cos\theta_f + \delta \\ &\approx \frac{R\phi_i \cos\theta_{s,j}}{\eta_i} + \frac{R\phi_1 \cos\theta_{s,j}}{\eta_f}, \end{aligned} \tag{8.10}$$

where $\delta = s2R\cos\theta_{s,j} + \mathcal{O}(\eta_i)$ and we have assumed that both η_i and η_f are small. We then rearrange to obtain:

$$0 = R\eta_f\phi_i \cos\theta_{s,j} + R\eta_i\phi_1 \cos\theta_{s,j} - t\eta_i\eta_f, \tag{8.11}$$

which is a conic since it is quadratic in both ϕ_i and η_i due to (8.10). Substituting η_f into (8.11) and projecting onto the $\phi_i - \eta_i$ plane we obtain two hyperbolas for each value of n. Each pair of hyperbolas encloses an area which stretches and tilts in a non-overlapping fashion as n is increased. Figure 8.8 shows how this approximation reproduces the area occupied by the long surviving orbits in the vicinity of the diametrical period two MUPO.

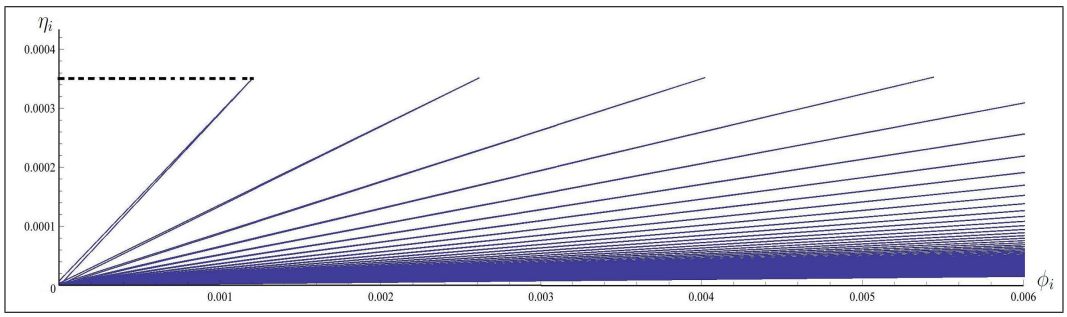

Figure 8.8: The first 100 spikes produced by the hyperbolas of equation (8.11) for the same parameter values as in Figure 8.5.

As performed previously in sections 3.5 and 7.3, we may approximate the hyperbolas by straight lines thus allowing us to integrate and sum over the areas

to obtain $P_2(t)$ to leading order. The result is:

$$P_2(t) = \sum_{(s,j)\in\mathcal{S}_\phi} p\frac{R^2(\phi_1^2+\phi_2^2)\cos^2\theta_{s,j}(2s(2s-1)+(4s-1)\ln(4s-1))}{2|\partial Q|4s(2s-1)t} + \mathcal{O}\left(\frac{1}{t^2}\right), \tag{8.12}$$

where p was defined in the previous subsection. Note that this equation is valid for times $t \geq \frac{16s^2(\phi-\pi/s)}{\epsilon}$ derived as in (3.32).

8.3.3 Exact results and Numerical tests

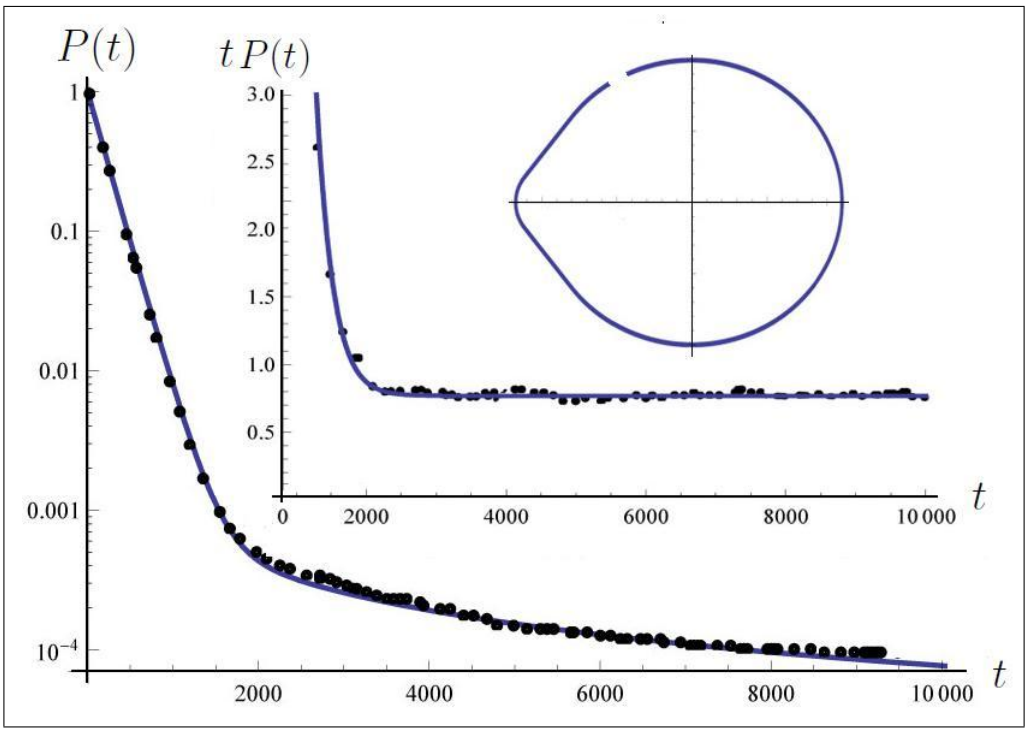

Figure 8.9: Log-linear plot of the Survival probability $P(t)$ as a function of time t for the open drivebelt with $\phi = 2.5$, $R = 1$, $r = 0.3$ and a hole of size $\epsilon = 0.1$ positioned at $z \in (2.3, 2.4)$ as can be seen in the inset. The blue curve is given by the analytic prediction of equation (8.13) while the empty black circles are from a numerical simulation consisting of 10^8 initial conditions. The inset is a plot of $tP(t)$ showing the agreement with the analytic expressions for the constant $\mathcal{C}$.

We have calculated the asymptotic survival probability for the drivebelt billiard

to be

$$P(t) = P_1(t) + P_2(t)$$
$$= \sum_{(s,j)\in\mathcal{S}_\phi} p\frac{R^2(\phi_1^2+\phi_2^2)\cos^2\theta_{s,j}(4s(2s-1)+(4s-1)\ln(4s-1))}{2|\partial Q|4s(2s-1)t} + \mathcal{O}\left(\frac{1}{t^2}\right), \tag{8.13}$$

and now confirm our analytical results with some numerical simulations. These are shown in Figure 8.9 which demonstrates how the initial exponential decay of $P(t)$ is overtaken by the power-law $\sim \mathcal{C}/t$ at longer times. Our analytical predictions of equation (8.13) are in good agreement with our numerical simulations. Other simulations with different ϕ and ϵ have also been performed but are not included here.

8.4 Conclusions and Discussion

The study of the drivebelt billiard in this section successfully completes our analysis of the long time behavior of intermittent chaotic billiards. We have generalized our approximation method and applied it to the somewhat different collision scenario exhibited in the drivebelt billiard and obtained exact results for $P(t)$ which agree with our numerical simulations. This implies that our technique can be applied to a variety of smooth billiards constructed of conic components. Furthermore, we expect that the drivebelt billiard, also exhibits *asymmetric transport* as described in section 3.3. if the holes are placed appropriately.

Because of the multiple intermittency exhibited by its dynamics, the drivebelt offers an interesting model to study $P(t)$ in the case that the hole is not placed as to overlap all the sticky regions of phase space. In such a case, just like for the open-ended stadium of chapter 5, sticky orbits may experience more than one nonlinear collision process at the straight-curved joints. Although this was found to complicate matters in the open-ended stadium, here new multi-escape roots may appear which may possibly simplify the problem or at least offer some new insight. For instance, a sticky orbit may exit and then enter into a different sticky

mode with some 'transfer' probability. Similarly, one may consider how a number of holes can affect escape through one another and discover further analogues and connections with phenomena such as asymmetric transport. Such considerations are very relevant in the field of controlling chaos since the escape route through one of the holes may be considerably reduced by other holes [43].

Part III

Epilogue

Chapter 9

Summary and Outlook

We began with the question *"How do long-time escape properties depend on the dynamics, the size and positions of holes?"*. After reviewing some established old and new results in the context of maps and mathematical billiards we isolated an interesting class of two dimensional (planar) chaotic billiards, namely intermittent ones, whose dynamics exhibit stickiness due to the existence of marginally unstable periodic orbits (MUPOs). This stickiness is realized in power-law decays of the Poincaré recurrence time statistics $\mathcal{Q}(t) \sim t^{-2}$ and the survival probability $P(t) \sim \mathcal{C}/t$ given a small hole through which particles may escape. More importantly however, we found that in some cases $\mathcal{C}$ could be described to leading order in $t \gg 1$ in terms of the geometrical dimensions of the system, the size and position of the hole, hence providing partial answers to the above question. These answers fall under three different settings; *'optimization problems'* such as where to place holes to maximize/minimize escape [1]; *'inverse problems'* corresponding to an open equivalent of "hearing the shape of a drum" [2]; and *'transport problems'* [3] where particles can enter and exit the system through different holes.

In chapter 3 we devised an approximation method with which we obtained an exact to leading order expression for $\mathcal{C}$ for the *stadium* billiard [87]. The method was applied to the more interesting and complicated *mushroom* billiard in chapter 7 [91] and generalized for a curved-to-straight-to-curved type collision process in the *drivebelt* billiard in chapter 8. All our results are by no means rigorous,

though are indeed tested through extensive numerical simulations. The expressions obtained for $\mathcal{C}$ are in a nice closed form and therefore allow for the accurate prediction, calibration and optimization of the asymptotic survival probability $P(t)$. The approximation method used, is restricted to holes which overlap all sticky regions (due to MUPOs) of the ergodic component of the billiard's phase space. This provides a first restriction to the applicability of our results but also a first obstacle which needs to be overcome in future investigations discussed below.

Parallel investigations in these billiards have produced a number of interesting results. Firstly, a probabilistic approach to the open-ended stadium in chapter 4 lead to the derivation of a useful formula for calculating the product of n independent and identically distributed uniform random variables [88]. Secondly, in chapter 5 the acquired knowledge about intermittency and stickiness due to bouncing ball orbits lead to the discovery and characterization of asymmetric transport in the stadium billiard with two holes placed asymmetrically [79]. Finally, in chapter 6 the connection between MUPOs in the mushroom billiard and number theory allowed us to define mushrooms which are finitely sticky or even completely MUPO-free [91]. The novelty and importance of all these investigations was discussed separately at the end of each relevant chapter.

What can we learn from the sum of calculations in previous chapters? The work contained in this thesis offers a fair amount of new results to the theory of open billiards, with main focus the intermittent dynamics introduced by the stickiness due to MUPOs. These results support the importance of finite-time statistics (as opposed to unrealistic $t \to \infty$ limits) in open dynamical systems and also ask questions about the delicate role these orbits may play in accordance with Bohr's quantum-to-classical correspondence principle [92] further accentuated by semiclassical theory and trace formulae [62]. In other words, the sum of our classical results on $P(t)$, as well as the existence and structural stability of MUPOs is hoped to shed new light on the otherwise not so well understood quantum analogue of stickiness (e.g. scarring), thus offering important ramifications in the context of quantum chaos and experimental applications such as electronic

transport through open ballistic micro-structures (quantum dots).

It was discussed in the introduction that open quantum systems are of crucial experimental relevance. Resonances, sometimes called quasi-bound states, are poles of the scattering matrix, corresponding to complex wave-numbers with negative imaginary part and correspond to exponentially decaying with time wave-functions; sometimes even faster than the average classical dwell time inside the system. This correspondence is achieved via the Green function for open systems expressed as a sum over resonances compared with its semiclassical approximation [53]. Strongly chaotic open systems are well understood, where it is found that the semiclassical contribution of orbits with large lengths is highly oscillatory but can be averaged out over energy, *i.e.* by sampling data at different energies, thus leaving the dominant semiclassical description up to the shorter ones (as in weak scarring theories). The quantum description in generic (mixed) open systems however, is currently not so well understood. The main reason for this is that the resonance wave-functions are not orthogonal to each other (due to non-Hermitian operators) hence leading to a scarcity of analytical tools.

Hence, a semiclassical investigation of long-lived resonances in model open billiards such as the ones studied here seems like an 'honest' approach. In such systems, standard descriptions such as fractal Weyl laws and random wave models are expected to hold subject to some corrections. These corrections are attributed, often depending on the authors, to the slower (algebraic) loss of quantum-to-classical correspondence (Ehrenfest time) or the slower (polynomial) rates of mixing in the sticky subsets of phase space and hence the asymptotic power-law escape probabilities. Are these two equivalent, and if so how do they scale? The proposed billiard models hold the advantage of a large range of classical results which include an explicit classical description of the MUPOs locations, their coupling to the escape regions (holes) and exact finite-time results of the classical survival probability $P(t)$. Overall, this should facilitate for the appropriate discrimination of the non-homogeneous, multi-fractal phase space into sticky and non-sticky regions thus potentially allowing for an independent treatment of the corresponding

semiclassical contributions.

There are a number of classical directions in which this work could also be extended to. For example, one may consider a generalization of the results of chapter 6 to elliptical mushrooms. Here, similar results are expected, involving an explicit description of the invariant of motion associated with the rotational[1] periodic orbits in the ellipse. A system specific Diophantine approximation is expected to be relevant, describing some superset of badly approximable numbers. This however is a naturally difficult generalization of the simple mushroom as it involves elliptic integrals.

As described in section 8.4, the multiple intermittency exhibited by the drive-belt offers an interesting model to study escape distributions in the case that the hole does not overlap all sticky regions of the phase space. In such a case, just like for the open-ended stadium of chapter 5, sticky orbits may experience more than one nonlinear collision process at the straight-curved joints. Although this was found to complicate matters in the open-ended stadium, here new multi-escape roots may appear which may possibly simplify the problem or at least offer some new insight. For instance, a sticky orbit may exit and then enter into a different sticky mode (with different quasi-period) with some 'transfer' probability, hence producing some interesting nonstandard power-law decay distributions while also exhibiting asymmetric transport.

Finally, our results may have direct connections with more realistic physical applications such as wireless communications. The transmission range necessary to keep a network of nodes (antennas) connected is an important parameter in optimization and design of ad hoc multi-hop radio networks [190]. Their connectivity and capacity analysis has usually focused on asymptotic results in the number of nodes in the network more recently deriving results from percolation theory [191]. However, most of these studies although currently extremely relevant and market oriented, rarely include information about the geometry of the network's confinements. Hence, the study of these networks in a probabilistic

[1] Librational MUPOs do not exist in elliptical mushrooms with centered stems.

framework while introducing techniques and results from classical billiard dynamics is arguably very promising. As a starting point one may look at the connectivity of nodes along a thin waveguide composed of conic boundaries. Similar and related constructions have been considered, for example in track billiards [192], transport through semi-dispersing polygonal channels [78] and disordered quasi-one-dimensional nano-wires [193], though none of them address questions relating connectivity.

The proposed research directions deriving from this thesis mainly involve the study of quantum chaos and open dynamical systems with main goal to establish and propose new connections between classical escape properties and semiclassical approaches. This builds upon the current research contained in this thesis while also incorporating results from a variety of sources, all together ambitiously and eagerly aiming for a better understanding of the 'bigger picture'.

Appendices

Appendix A

Elliptical stadium billiard

The long time statistical properties of the chaotic stadium billiard are dominated by a family of marginally unstable periodic orbits called "bouncing ball orbits". Here, we investigate the open stadium billiard with a hole on one of its parallel segments and semi-elliptical arcs (instead of semi-circular ones), and consider how near bouncing ball orbits affect the long time survival probability $P(t)$ of a uniform distribution of non-interacting particles. We obtain an explicit expression for the leading order term of $P(t)$ and then investigate how the position and number of holes may affect $P(t)$. These classical results are helpful for comparison with the quantum chaotic analogues of such systems and of interest to experimentalists involved with escape-rates of ultra-cold atoms for example or with Quantum dots.

We have previously shown that the long time survival probability of the Bunimovich stadium billiard consisting of a small hole with coordinates $x \in (h^-, h^+)$, placed on one of the two parallel straight segments of length $2L$ is:

$$P(t, L, r, h^-, h^+) = \frac{1}{2(4L + 2\pi r)t}\left[\left(\frac{3\ln 3}{2} + 2\right)\left((L + h^-)^2 + (L - h^+)^2\right)\right] + \mathcal{O}\left(\frac{1}{t^2}\right), \tag{A.1}$$

where r is the radius of the semi-circular arcs (also see eq (3.33)).

In the present text we generalize this result to the case of the chaotic elliptical stadium. Markarian *et al.* [164, 194] showed that the elliptical stadium constructed by joining two half-ellipses, with half axes $a > b$ and two straight segments of equal

length $2L$ has a positive Lyapunov exponent almost everywhere if $a < b\sqrt{4-2\sqrt{2}}$ and $L > 2\left(\frac{a}{b}\right)^2\sqrt{\left(\frac{a}{b}\right)^2-1}$. The elliptical stadium is shown in figure 1. below.

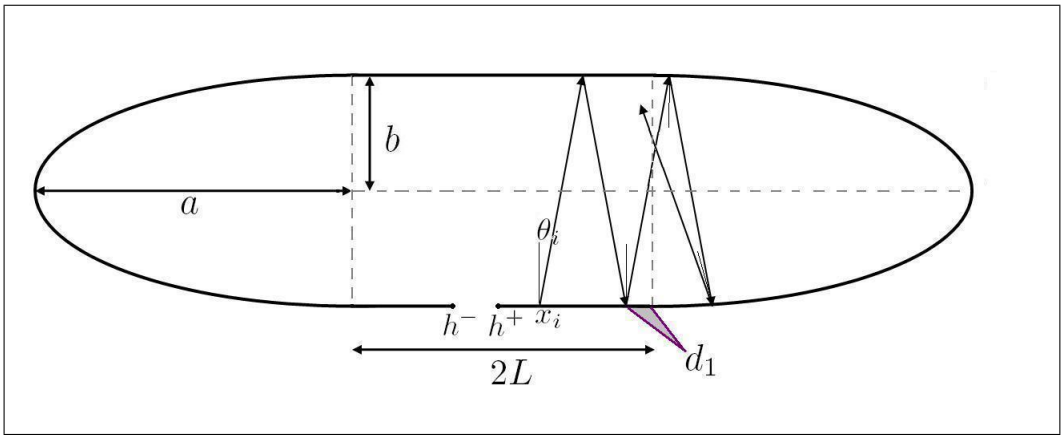

Figure A.1: The Set-Up of the open, chaotic elliptical stadium billiard.

Collisions of the particle with the parallel segments of the billiard preserve the absolute value of the incident angle $\theta \in \left(\frac{-\pi}{2}, \frac{\pi}{2}\right)$. Collisions on the curved elliptical segment cause a defocusing of the incoming wavefronts and therefore eventually give the stadium its ergodic character. Let θ_i denote the initial angle of an orbit moving away from the hole towards the right and x_i its initial position on one of the parallel segments of the billiard. We find that small angles remain small after colliding with the elliptic curved segment of the billiard. The reflected final angle $|\theta_f| = M\theta_i$, $f = 3, 4$ is given by a modified version of (3.10) and (3.11):

$$M = \begin{cases} -\frac{2bd_1}{a^2\theta_i} + \left(\frac{4b^2}{a^2} - 1\right), & \theta_i \geq \frac{\left(a^2-4b^2\right)d_1}{4(a^2b-2b^3)}, \quad \text{1 collision} \\ \left(-\frac{4bd_1}{a^2\theta_i} + \frac{8b^3d_1}{a^4\theta_i}\right) + \left(-1 + \frac{12b^2}{a^2} - \frac{16b^4}{a^4}\right), & \frac{d_1}{2b} < \theta_i < \frac{\left(a^2-4b^2\right)d_1}{4(a^2b-2b^3)}, \quad \text{2 collisions,} \end{cases} \tag{A.2}$$

and $d_1 = L-(x_i+2bn\tan\theta_i)$ is the distance from the point of the last straight wall reflection (before hitting a curved wall) to the edge of the straight at $x = L$ (see Figure A.1). The top scenario corresponds to one bounce off the curved segment while the lower to two bounces. The chaoticity requirement by [164] guarantees a maximum of 2 collisions for near bouncing ball orbits. This is confirmed by the fact that the transition from one ($f = 3$) to two ($f = 4$) bounces off the semi-

elliptical segment of the billiard is continuous. This can be seen in Figure A.2 since M is piecewise linear in $\lambda = \frac{d_1}{2a\theta_i}$ such that

$$M = \begin{cases} -\frac{4}{c}\lambda + \left(\frac{4}{c^2} - 1\right), & 0 \leq \lambda < \frac{2(c-2)}{(c^3-4c)}, \\ \left(-\frac{8}{c} + \frac{16}{c^3}\right)\lambda + \left(-1 + \frac{12}{c^2} - \frac{16}{c^4}\right), & \frac{2(c-2)}{(c^3-4c)} \leq \lambda < \frac{1}{c}, \end{cases} \tag{A.3}$$

where $c = \frac{a}{b}$. It is interesting to note that in the limit $c = 1$, M is reduced to that

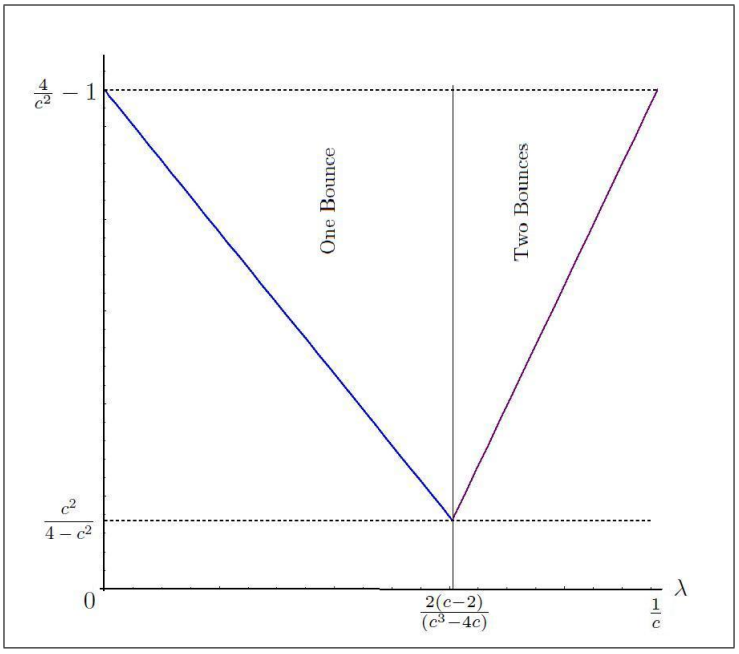

Figure A.2: The dependence of $M = \frac{\theta_f}{\theta_i}$ on λ for $\theta_i \ll 1$, where $\lambda = \frac{d_1}{2a\theta_i}$.

of the stadium with semi-circular arcs given in Ref [83, 163].

We thus formulate two equations for the time to escape given initial conditions (x_i, θ_i)

$$T(x_i, \theta_i) = \frac{2bn}{\cos\theta_i} + \frac{2bm}{\cos\theta_f} + D, \tag{A.4}$$

where n and m are the respective number of non-essential collisions (consecutive collisions with straight walls) before and after the reflection process on the semi-elliptical end. They can be described by:

$$n = \left(\frac{L - x_i}{2b\tan|\theta_i|} - \delta_i\right)$$
$$m = \left(\frac{L - h^+}{2b\tan|\theta_f|} - \delta_f\right),$$

where $0 < \delta_{i,f} < 1$. D is the time taken by the reflection process itself at the curved end, and is bounded from above. Substituting (A.2) into (A.4), we obtain two equations which are quadratic in both variables x_i and θ_i, which describe hyperbolae in the $x_i - \theta_i$ plane. The domain of each hyperbola is defined by the inequalities in (A.2). These inequalities also define straight lines in the $x_i - \theta_i$ plane, and hence together with the two hyperbolae define for each n an area within which all initial conditions survive up to time t are enclosed (see Figure A.3). The problem of calculating the measure of initial conditions that survive up to time t is now equivalent to calculating the area enclosed by each spike for all available values of n.

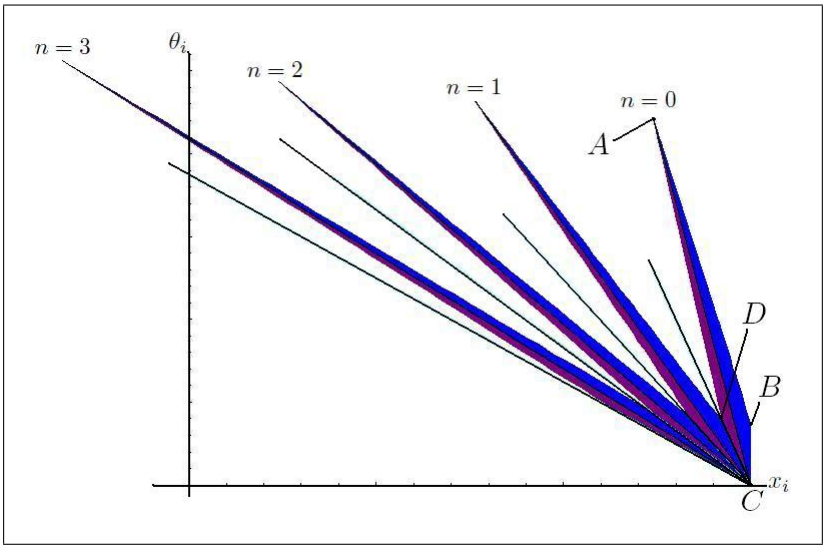

Figure A.3: Area enclosed by the hyperbolas for n = 0, 1, 2 and 3. The blue area describes the initial conditions which experience one collision off the semi-elliptical segment whilst the purple is for two bounces. The line in the middle of each spike is given by $\theta_i = (\frac{b(c^2-4)(L-x_i))}{(2c^2(2+n)-8(1+n))}$, while the line in between each spike is $\theta_i = \frac{(L-x_i)}{(2b(1+n))}$.

We now show how to calculate the area of interest. First we approximate the

hyperbolae by straight lines. The corners $A - D$ of each spike are given below

$$A_{x_i} = \frac{32b^5(h^+ - L)(1+n) + a^4(2bh2(2+n) - Lt) + 4a^2b^2(2b(L(2+n) - h2(3+2n)) + Lt)}{a^2(a^2(2b(2+n) - t) + 4b^2(t - 2b(1+n)))}, \tag{A.5}$$

$$A_{\theta_i} = \frac{(a^2 - 4b^2)^2(L - h^+)}{a^2(a^2(2b(2+n) - t) + 4b^2(t - 2b(1+n)))}, \tag{A.6}$$

$$B_{x_i} = L + \frac{2a^2b(L - h^+)n}{(a^2 - 4b^2)(t - 2bn)}, \tag{A.7}$$

$$B_{\theta_i} = -\frac{a^2(L - h^+)}{(a^2 - 4b^2)(t - 2bn)}, \tag{A.8}$$

$$C_{x_i} = L, \tag{A.9}$$

$$C_{\theta_i} = 0, \tag{A.10}$$

$$D_{x_i} = \frac{4b^2L(t - 2b(1+n)) + a^2(2bh^+(1+n) - Lt)}{(a^2 - 4b^2)(2b(1+n) - t)}, \tag{A.11}$$

$$D_{\theta_i} = \frac{a^2(-h2 + L)}{(a^2 - 4b^2)(2b(1+n) - t)}. \tag{A.12}$$

The area formed by joining these points is

$$Area_1 = \frac{b(h^+ - L)^2}{(2bn - t)(2b(1+n) - t)}. \tag{A.13}$$

We now considered how the hole truncates the spikes as they shift and tilt and eventually surpass the holes location for larger values of n. We obtain three more expressions for the area enclosed, one for every time the x_i coordinate of a corner $A - D$ overshoots the position of the hole at h^+. These expressions are then inserted in sums over the respective values of n:

$$Area_{Right} = \sum_{n=0}^{N_1} Area_1 + \sum_{n=N_1}^{N_2} Area_2 + \sum_{n=N_2}^{N_3} Area_3 + \sum_{n=N_3}^{\infty} Area_4, \tag{A.14}$$

where

$$N_1 = \left\lfloor \frac{16b(2 - c^2) + c^2(c^2 - 4)t}{8b(c^2 - 4)} \right\rfloor, \qquad N_2 = \left\lfloor \frac{t}{2b} - \frac{c^2t}{b} - 1 \right\rfloor, \qquad N_3 = \left\lfloor \frac{t}{2b} - \frac{c^2t}{b} \right\rfloor$$

and $\lfloor \cdot \rfloor$ is the floor function.

The sum approximation method is as described in section 3.5. Finally, we add the obtained result to (3.7) and divide by the total equilibrium measure of the

elliptical stadium's billiard map $2|\partial Q| = 2(4L + \mathcal{E})$, where $\mathcal{E}$ is the circumference of the ellipse with half angles a and b such that

$$\mathcal{E} = 4 \int_0^{\pi/2} \sqrt{a^2 \cos^2 t + b^2 \sin^2 t}\, \mathrm{d}t, \tag{A.15}$$

and obtain

$$P(t, L, c, h^-, h^+) = \frac{1}{2(4L + \mathcal{E})t} \left[\left(\frac{\left(\frac{4}{c^2} - 1\right) \ln\left(\frac{4}{c^2} - 1\right)}{2\left(\frac{2}{c^2} - 1\right)\frac{1}{c^2}} + 2 \right) \left((L + h^-)^2 + (L - h^+)^2 \right) \right], \tag{A.16}$$

where we have neglected terms of order $\sim t^{-2}$.

Appendix B

Product of n uniform random variables

Reproduced as in Ref [88]

Abstract: We give an alternative proof of a useful formula for calculating the probability density function of the product of n uniform, independently and identically distributed random variables. Ishihara (2002, in Japanese) [195] proves the result by induction; here we use Fourier analysis and contour integral methods which provide a more intuitive explanation of how the convolution theorem acts in this case.

To obtain the probability density function (PDF) of the product of two continuous random variables (r.v.) one can take the convolution of their logarithms. This is explained for example by Rohatgi (1976) [166]. It is possible to use this repeatedly to obtain the PDF of a product of multiple but fixed number ($n > 2$) of random variables. This is however a very lengthy process, even when dealing with uniform distributions supported on the interval $[a, b]$. We encountered the latter problem with $a = \frac{1}{3}$ and $b = 3$, in the article by Armstead *et al.* (2004) [83] on the approximation for the open-ended stadium billiard dynamical system; there are undoubtedly other applications in a variety of fields. A formula for calculating

the PDF of the product of n uniform independently and identically distributed random variables on the interval $[0, 1]$ first appeared in Springer's book (1979) [196] on "The algebra of random variables". This was then generalized (see Ishihara 2002 (in Japanese)) to accommodate for independent but not identically (i.e. $\{[a_i, b_i], i = 1, 2, \ldots n\}$) distributed uniform random variables through the use of the proof by induction. In the current paper we use Fourier analysis, as suggested by Springer, to re-derive a subset of Ishihara's results: the PDF of a product of n independent and identically distributed uniform [a, b] random variables. Through this analysis one can see exactly how the n smooth components of the resulting PDF arise from contour integrals in Fourier space and thus obtain a more intuitive idea of how the convolution theorem (see Bracewell, 2000 [197]) acts. Specifically, we shall show that the convergence of the contour integrals defines the supports of the components of the PDF.

Theorem 1. *Let X_i be independent random variables with PDF $f_{X_i}(x) = \frac{1}{b-a}$ on the interval $x \in [a, b]$ and 0 otherwise, where $0 \leq a < b < \infty$ and $i = 1, 2, \ldots n$, $n \geq 2$. Then the PDF of $X = \prod_{i=1}^{n} X_i$ is given by the piecewise smooth function:*

$$f_X(x) = \begin{cases} f_X^k(x), & a^{n-k+1}b^{k-1} \leq x \leq a^{n-k}b^k, \\ & k = 1, 2, \ldots n, \\ 0, & \text{otherwise}, \end{cases}$$

where

$$f_X^k(x) = \sum_{j=0}^{n-k} \frac{(-1)^j}{(b-a)^n (n-1)!} \binom{n}{j} \left(\ln \frac{b^{n-j}a^j}{x} \right)^{n-1}.$$

Remark 1. *It is interesting to note that the components' derivatives ($\frac{\mathrm{d}^l}{\mathrm{d}x^l} f_X^k(x)$), of order $l = 1, 2, \ldots (n-2)$, are continuous at their end-points while the $(n-1)_{th}$ derivative is not (see Springer 1979).*

Remark 2. *The known result that $\ln X = \ln \prod_{i=1}^{n} X_i = \sum_{i=1}^{n} \ln X_i$ is Gamma distributed ($\sim -\Gamma(n, 1)$), as explained by Devroye, (1986) [198], is only valid for*

$a = 0$, with the natural normalization $b = 1$. Unfortunately, we cannot find a representation in terms of standard distributions if $a > 0$. We can however comment that according to the Central Limit Theorem (CLT), the distribution of $\ln X$ converges asymptotically to the Normal distribution. In fact, since the third central moment of $\ln X_i$ exists and is finite, then by the Berry-Esséen theorem (see Feller 1972 [199]), the convergence is uniform and the convergence rate is at least of the order of $1/\sqrt{n}$; this can be used to approximate $f_X(x)$ for large n where direct numerical computation is inefficient.

Proof. Let $Y_i = \ln X_i$. Then the PDF of Y_i is $f_{Y_i}(y) = \frac{1}{b-a}e^y = \kappa e^y$ supported on $y \in (\ln a, \ln b)$ and is zero otherwise. We find the characteristic function by taking the Fourier transform of $f_{Y_i}(y)$:

$$\begin{aligned}\mathcal{F}(f_{Y_i}(y))(\eta) = \mathbb{E}(e^{i\eta Y_i}) = \hat{f}_{Y_i}(\eta) &= \int_{-\infty}^{\infty} \kappa e^y e^{i\eta y} \mathrm{d}y, \\ &= \frac{\kappa}{(1+i\eta)}\left(be^{i\eta \ln b} - ae^{i\eta \ln a}\right). \end{aligned} \tag{B.1}$$

The convolution theorem (see Bracewell, 2000) states that the characteristic function (c.f.) of the sum of n random variables is given by the product of the individual c.f. of each r.v. Hence, the c.f. of $Y = \sum_{i=1}^{n} Y_i$ is given by the nth power of $\hat{f}_{Y_i}(\eta)$ which we expand here using the binomial theorem:

$$[\hat{f}_{Y_i}(\eta)]^n = \hat{f}_Y(\eta) = \sum_{j=0}^{n} \frac{\kappa^n (-1)^j}{(1+i\eta)^n} \binom{n}{j} b^{(n-j)} a^j e^{i\eta\lambda_j} \tag{B.2}$$

where $\lambda_j = (n-j)\ln b + j \ln a$. To perform the inverse Fourier transform we shall use Cauchy's residue theorem (see Knopp, 1996 [200]). Note that according to Springer (1979), we should expect n piecewise continuous components which make up a C^{n-2} curve. Also note that the inverse Fourier transform of equation (2), $\mathcal{F}^{-1}\big([\hat{f}_{Y_i}(\eta)]^n\big)(y)$, will have support only in the interval $(n \ln a, n \ln b)$.

$$\begin{aligned}\mathcal{F}^{-1}\big([\hat{f}_{Y_i}(\eta)]^n\big)(y) &= \frac{1}{2\pi}\int_{-\infty}^{\infty} \hat{f}_Y(\eta) e^{-i\eta y}\, \mathrm{d}\eta \\ &= \int_{-\infty}^{\infty} \sum_{j=0}^{n} \frac{\kappa^n (-1)^j \binom{n}{j} b^{(n-j)} a^j e^{i\eta(\lambda_j - y)}}{2\pi(\eta - i)^n (i)^n}\, \mathrm{d}\eta \\ &\equiv \int_{-\infty}^{\infty} \sum_{j=0}^{n} h_j(\eta, y)\, \mathrm{d}\eta, \end{aligned} \tag{B.3}$$

where the integral-sum order can be interchanged. We define two contours γ_m $(m = 1, 2.)$ such that γ_1 goes along the real axis from $-R$ to R and then into the upper complex plane along an anti-clockwise semicircular arc of radius $R > 1$, centered at the origin, $\gamma_{c_1} \subset \gamma_1$. Contour γ_2 is defined similarly but into the lower complex plane along a clockwise semicircular arc of radius R, $\gamma_{c_2} \subset \gamma_2$. Notice that for all j there is only one pole due to $h_j(\eta, y)$ enclosed by γ_1, that it is of order n, that it is situated at $\eta_0 = i$ and that there are no poles in γ_2. We use the residue theorem to calculate:

$$\begin{aligned}\oint_{\gamma_1} h_j(\eta, y)\ \mathrm{d}\eta &= 2\pi i \mathrm{Res}\Big(h_j(\eta, y), i\Big) \\ &= \frac{(\kappa)^n(-1)^j}{(n-1)!}\binom{n}{j}\big(\lambda_j - y\big)^{(n-1)}e^y. \end{aligned} \tag{B.4}$$

The choice of contour to be used for every $0 \leq j \leq n$ and $y \in (n \ln a, n \ln b)$ when calculating (3) depends on the sign of the exponential. In other words, m depends on both j and y. Explicitly, we write $\eta = R(\cos\phi + i \sin\phi)$ and estimate the integrals over the semicircular arcs γ_{c_1} and γ_{c_2}:

$$\int_{\gamma_{c_m}} h_j(\eta, y)\mathrm{d}\eta = \int_{\gamma_{c_m}} g(R, \phi)e^{-R\sin\phi(\lambda_j - y)}\mathrm{d}\phi, \tag{B.5}$$

where $g(R, \phi) = \mathcal{O}(R^{-n+1})$, as $R \to \infty$. For $n \geq 2$ we know that if the exponent: $-R\sin\phi(\lambda_j - y) \leq 0$, then the integrals in (5) will converge to zero. We rearrange this inequality to find that for γ_1 we need $j \leq j^*(y)$ while for γ_2 we need $j > j^*(y)$, where $j^*(y) = \left\lfloor \frac{n\ln b - y}{\ln b - \ln a} \right\rfloor$ and $\lfloor . \rfloor$ denotes the floor function. Note that when $\lambda_j = y$, both contour integrals (along γ_{c_1} and γ_{c_2}) converge and we see that (4) is identically zero. Hence we obtain the following equation:

$$\begin{aligned} f_Y(y) &= \sum_{j=0}^{n} \int_{-\infty}^{\infty} h_j(\eta, y)\ \mathrm{d}\eta \\ &= \sum_{j=0}^{j^*(y)} \Big(\oint_{\gamma_1} h_j(\eta, y)\ \mathrm{d}\eta - \int_{\gamma_{c_1}} h_j(\eta, y)\ \mathrm{d}\eta \Big) \\ &+ \sum_{j=j^*(y)+1}^{n} \Big(\oint_{\gamma_2} h_j(\eta, y)\ \mathrm{d}\eta - \int_{\gamma_{c_2}} h_j(\eta, y)\ \mathrm{d}\eta \Big) \end{aligned} \tag{B.6}$$

as $R \to \infty$, where all integrals along γ_{c_1}, γ_2 and γ_{c_2} vanish and the remaining integral is given by (4). Note that the sums in (6) only make sense if $0 \leq j^*(y) < n$;

as expected from the known support of y. We find n intervals on which $f_Y(y)$ is supported and number them by $k = 1, 2, \ldots n$, where $k = n - j^*(y)$. To obtain $f_X(x)$, as given in **Theorem 1.**, simply transform back to $X = \exp(Y)$. □

Remark 3. *It is an interesting exercise to show that* $\sum_{j=0}^{n} \Big(\oint_{\gamma_m} h_j(\eta, y)\ d\eta \Big) = 0$ *for both* $m = 1$ *and* $m = 2$ *and for any* y *as* $R \to \infty$. *To see this for* $m = 1$, *expand* $(\lambda_j - y)^{(n-1)}$ *using the binomial theorem, collect the* j*-dependent terms and interchange the sums to obtain:*

$$\sum_{j=0}^{n} \Big(\oint_{\gamma_1} h_j(\eta, y)\ d\eta \Big) = \sum_{l=0}^{n-1} \frac{(\kappa)^n \big(\ln \frac{a}{b} \big)^l e^y}{(n-1)!(i)^{n-1}} \binom{n-1}{l} \big(n \ln b - y \big)^{n-1-l} \times \sum_{j=0}^{n} (-1)^j \binom{n}{j} j^l.$$

To show that the last sum over j *is zero, we write it as:*

$$\sum_{j=0}^{n} (-1)^j \binom{n}{j} j^l e^{ls} \Big|_{s=0} = \frac{\mathrm{d}^l}{\mathrm{d}s^l} \sum_{j=0}^{n} (-1)^j \binom{n}{j} e^{ls} \Big|_{s=0} = \frac{\mathrm{d}^l}{\mathrm{d}s^l} \big(1 - e^s \big)^n \Big|_{s=0} = 0,$$

for all $0 \le l \le (n-1)$. *For* $m = 2$, *the contour integral is zero as there are no poles enclosed by the contour.*

Remark 4. *To prove Ishihara's general result (where the* X_i*'s are not identically distributed), one would have to expand the product* $\prod_{j=1}^{n} \frac{(b_j e^{i\eta \ln b_j} - a_j e^{i\eta \ln a_j})}{(b_j - a_j)}$ *and evaluate the* $(n-1)_{th}$ *derivative at* $\eta = i$, *and then look at the various contour integrals as above. While possible in principle, this would defeat the purpose of this paper, namely a simpler but more explicit and intuitive derivation of the result.*

Appendix C

C code which calculates the CDF

The following computer code is written in ANSI C and is used to calculate the cumulative distribution function $F_X(x) = \int_{a^n}^{x} f_X(x)\mathrm{d}x$ of the product of n independent and identically distributed uniform on $[a, b]$ random variables (see equation (4.2)).

```
#include <stdio.h>
#include <stdlib.h>
#include <math.h>
// define the endpoints of the supports of each function
#define alpha(k) (pow(a,(n-k+1))* pow(b,(k-1)))
#define beta(k) ( pow(a,(n-k))* pow(b,k))

int n=4;  // input here the value of n

int j, m;
double a= 0.3, b=3, tau= 0.31; // input here the values of a, b and tau
double Prob, diff, OutPut, A;

// define the factorial function
double fac( int n )
{double fact = 1.0;
while ( n > 1) {
fact = fact * n;
n = n - 1;}
return fact;}
```

```
// define the F2 function
double F2(int k)
{for(j=0,OutPut=0;j<(n-k+1);j++)
{
for(m=1,A=0;m<n;m++)
{A+= pow(log( (pow(a,j)*pow(b,n-j))/beta(k) ), m) / fac(m);}
OutPut+=beta(k)*fac(n-1)*(1+A)*n*pow((-1),j)/(fac(j)*fac(n-j)*pow((b-a),n));
}
return OutPut;}

// define the F1 function
double F1(int k)
{for(j=0,OutPut=0;j<n-k+1;j++)
{
for(m=1,A=0;m<n;m++)
{A+= pow(log( (pow(a,j)*pow(b,n-j))/alpha(k) ), m) / fac(m);}
OutPut+=alpha(k)*fac(n-1)*(1+A)*n*pow((-1),j)/(fac(j)*fac(n-j)*pow((b-a),n));
}
return OutPut;}

// define the Ftau function
double Ftau(int k)
{for(j=0,OutPut=0;j<n-k+1;j++)
{
for(m=1,A=0;m<n;m++)
{A+= pow(log( (pow(a,j)*pow(b,n-j))/tau ), m) / fac(m);}
OutPut+= tau*fac(n-1)*(1+A)*n* pow((-1),j)/(fac(j)*fac(n-j)*pow((b-a),n));
}
return OutPut;}

// the main code
int main()
{
int k=1;
Prob = 0.00;
while ( tau > beta(k)) {
diff= F2(k)-F1(k);
Prob= Prob + diff;
```

```
k=k+1;
}
Prob+= Ftau(k) - F1(k);
printf("\na= %g,\t b= %g,\t tau= %g,\n\nP(X <= tau) = %.17f \n\n",a,b,tau,Prob)
system ("PAUSE"); // remove this line according to your compiler
}

//The END
```

Appendix D

A Bound on R_2

To obtain a bound on R_2 in equation (6.8) we shall use the remainder term from Taylor's theorem several times. Taylor's theorem states that if f is a function which is n times differentiable on the closed interval $[a, x]$ and $n+1$ times differentiable on the open interval (a, x), then

$$f(x) = f(a) + \frac{f'(a)}{1!}(x-a) + \frac{f''(a)}{2!}(x-a)^2 + \ldots + \frac{f^{(n)}(a)}{n!}(x-a)^n + R_n(x),$$

where $R_n(x) = \frac{f^{(n+1)}(\xi)}{(n+1)!}(x-a)^{n+1}$ for some $a < \xi < x$.

Let $c = \cos\left(\alpha\pi\frac{p}{q}\right) \leq \cos\pi\vartheta^*$, and $\varepsilon = c\left(\frac{1}{\cos\left(\frac{\alpha\pi}{q}\right)} - 1\right)$ such that equation (6.6) corresponds to $c \leq \rho < c + \varepsilon$. We have to compute a bound for $\arccos(c+\varepsilon) = \arccos\left(\frac{\cos\left(\alpha\pi\frac{p}{q}\right)}{\cos\left(\frac{\alpha\pi}{q}\right)}\right)$. The Taylor expansion of $\arccos(c+\varepsilon)$ at $\varepsilon = 0$ is

$$\arccos(c+\varepsilon) = \arccos(c) - \frac{\varepsilon}{\sqrt{1-c^2}} + A_1, \tag{D.1}$$

with $A_1 = -\frac{c+x}{2\left(1-(c+x)^2\right)^{\frac{3}{2}}}\varepsilon^2 < 0$ and $0 \leq x \leq \varepsilon$. Now, for $q \to \infty$, we have

$$\frac{\varepsilon}{c} = \left(\frac{1}{\cos(\frac{\alpha\pi}{q})} - 1\right) = \frac{\alpha^2\pi^2}{2q^2} + B_2 = B_0, \tag{D.2}$$

with $q^3B_2 = \frac{\sin(\alpha\pi z)^3\alpha^3\pi^3}{\cos(\alpha\pi z)^4} + \frac{5\sin(\alpha\pi z)\alpha^3\pi^3}{6\cos(\alpha\pi z)^2}$ and $qB_0 = \frac{\sin(\alpha\pi w)\alpha\pi}{\cos(\alpha\pi w)^2}$ for some $0 \leq z, w \leq \frac{1}{q}$. Since for $q \geq Q$ we have $1 < \frac{1}{\cos(\alpha\pi z)} \leq \frac{1}{\cos\left(\frac{\alpha\pi}{Q}\right)}$ and $0 < \sin(\alpha\pi z) \leq \sin\left(\frac{\alpha\pi}{Q}\right)$. Hence

$$0 < q^3B_2 \leq \left(\frac{\sin(\frac{\alpha\pi}{Q})^2}{\cos(\frac{\alpha\pi}{Q})^4} + \frac{5}{6\cos(\frac{\alpha\pi}{Q})^2}\right)\alpha^3\pi^3\sin\left(\frac{\alpha\pi}{q}\right) \leq \left(\frac{\sin(\frac{\alpha\pi}{Q})^2}{\cos(\frac{\alpha\pi}{Q})^4} + \frac{5}{6\cos(\frac{\alpha\pi}{Q})^2}\right)\frac{\alpha^4\pi^4}{q},$$

and similarly $0 < qB_0 \leq \frac{\alpha^2\pi^2}{\cos(\frac{\alpha\pi}{Q})^2 q}$. This, together with (D.1) and (D.2), gives $\arccos(c+\varepsilon) = \arccos(c) - \frac{\alpha^2 c\pi^2}{2\sqrt{1-c^2}}\frac{1}{q^2} + C_1 + A_1$, where $C_1 = -\frac{cB_2}{\sqrt{1-c^2}} < 0$ is bounded by

$$\begin{aligned}|C_1| &\leq \left(\frac{\sin(\frac{\alpha\pi}{Q})^2}{\cos(\frac{\alpha\pi}{Q})^4} + \frac{5}{6\cos(\frac{\alpha\pi}{Q})^2}\right)\frac{\alpha^4\pi^4}{q^4}\frac{c}{\sqrt{1-c^2}} \\ &\leq \left(\frac{\sin(\frac{\alpha\pi}{Q})^2}{\cos(\frac{\alpha\pi}{Q})^4} + \frac{5}{6\cos(\frac{\alpha\pi}{Q})^2}\right)\frac{\alpha^4\pi^4}{q^4}\frac{\cos\pi\vartheta^*}{\sqrt{1-(\cos\pi\vartheta^*)^2}},\end{aligned}$$

and $A_1 < 0$ by

$$\begin{aligned}|A_1| &\leq \frac{c(1+B_0)}{2\left(1-c^2(1+B_0)^2\right)^{\frac{3}{2}}}c^2B_0^2 \leq \left(1+\frac{\alpha^2\pi^2}{\cos(\frac{\alpha\pi}{Q})^2Q^2}\right)\frac{\alpha^4\pi^4c^3}{2\cos(\frac{\alpha\pi}{Q})^4\left(1-c^2(1+B_0)^2\right)^{\frac{3}{2}}q^4} \\ &\leq \left(1+\frac{\alpha^2\pi^2}{\cos(\frac{\alpha\pi}{Q})^2Q^2}\right)\frac{\alpha^4\pi^4(\cos\pi\vartheta^*)^3}{2\cos(\frac{\alpha\pi}{Q})^4\left(1-(\cos\pi\vartheta^*)^2(1+\frac{\alpha^2\pi^2}{\cos(\frac{\alpha\pi}{Q})^2q^2})^2\right)^{\frac{3}{2}}q^4},\end{aligned}$$

for $q > \frac{\alpha\pi}{\cos(\frac{\alpha\pi}{Q})}\sqrt{\frac{\cos\pi\vartheta^*}{(1-\cos\pi\vartheta^*)}}$. In the same way

$$\frac{\alpha^2 c\pi^2}{2\sqrt{1-c^2}}\frac{1}{q^2} = \frac{\alpha^2\pi^2\cos\pi\vartheta^*}{2\sqrt{1-c^2}}\frac{1}{q^2} + C_2, \tag{D.3}$$

with $C_2 < 0$ and bounded by

$$|C_2| \leq \frac{\alpha^2\pi^2\varepsilon}{2\sqrt{1-c^2}}\frac{1}{q^2} \leq \frac{\alpha^2\pi^2B_0\cos\pi\vartheta^*}{2\sqrt{1-(\cos\pi\vartheta^*)^2}}\frac{1}{q^2} \leq \frac{\alpha^4\pi^4\cos\pi\vartheta^*}{2\cos(\frac{\alpha\pi}{Q})^2\sqrt{1-(\cos\pi\vartheta^*)^2}}\frac{1}{q^4}.$$

Finally we must bound $\frac{1}{\sqrt{1-c^2}} = \frac{1}{\sqrt{1-(\cos\pi\vartheta^*)^2+((\cos\pi\vartheta^*)^2-c^2)}} = \frac{1}{\sqrt{1-(\cos\pi\vartheta^*)^2+\nu}}$, where we wrote $\nu = (\cos\pi\vartheta^*)^2 - c^2$ so that we may expand for ν small

$$\frac{1}{\sqrt{1-(\cos\pi\vartheta^*)^2+\nu}} = \frac{1}{\sqrt{1-(\cos\pi\vartheta^*)^2}} + D_0,$$

where $D_0 = -\frac{\nu}{2(1-(\cos\pi\vartheta^*)^2+y)^{\frac{3}{2}}}$, with $0 \leq y \leq \nu$ and so it is bounded by

$$|D_0| \leq \frac{\nu}{2\kappa^{\frac{3}{2}}} \leq \frac{2\varepsilon\cos\pi\vartheta^*}{2\left(1-(\cos\pi\vartheta^*)^2\right)^{\frac{3}{2}}} \leq \frac{\alpha^2\pi^2(\cos\pi\vartheta^*)^2}{\cos(\frac{\alpha\pi}{Q})^2\left(1-(\cos\pi\vartheta^*)^2\right)^{\frac{3}{2}}}\frac{1}{q^2}.$$

Therefore for (D.3) we have

$$\frac{\alpha^2\pi^2 c}{2\sqrt{1-c^2}}\frac{1}{q^2} = \frac{\alpha^2\pi^2\cos\pi\vartheta^*}{2\sqrt{1-(\cos\pi\vartheta^*)^2}}\frac{1}{q^2} + C_2 + C_3,$$

where

$$|C_3| \leq \frac{\alpha^4\pi^4(\cos\pi\vartheta^*)^3}{2\cos(\frac{\alpha\pi}{Q})^2\left(1-(\cos\pi\vartheta^*)^2\right)^{\frac{3}{2}}}\frac{1}{q^4}.$$

Putting everything together, for $q \geq \max\left(Q, \frac{\alpha\pi}{\cos(\frac{\alpha\pi}{Q})}\sqrt{\frac{\cos\pi\vartheta^*}{(1-\cos\pi\vartheta^*)}}\right)$ we have

$$\begin{aligned}\arccos(c+\varepsilon) &= \arccos(c) - \frac{\alpha^2 c\pi^2}{2\sqrt{1-c^2}}\frac{1}{q^2} + C_1 + A_1 \\ &= \arccos(c) - \frac{\alpha^2\pi^2\cot\pi\vartheta^*}{2q^2} + C_1 + A_1 + C_2 + C_3,\end{aligned}$$

where the remainders have magnitudes bounded by

$$\begin{aligned}|C_1| &\leq \left(\frac{\sin(\frac{\alpha\pi}{Q})^2}{\cos(\frac{\alpha\pi}{Q})^4} + \frac{5}{6\cos(\frac{\alpha\pi}{Q})^2}\right)\frac{\alpha^4\pi^4\cot\pi\vartheta^*}{q^4}, \\ |A_1| &\leq \left(1+\frac{\alpha^2\pi^2}{\cos(\frac{\alpha\pi}{Q})^2Q^2}\right)\frac{\alpha^4\pi^4(\cos\pi\vartheta^*)^3}{2\cos(\frac{\alpha\pi}{Q})^4\left(1-(\cos\pi\vartheta^*)^2(1+\frac{\alpha^2\pi^2}{\cos(\frac{\alpha\pi}{Q})^2q^2})^2\right)^{\frac{3}{2}}q^4}, \\ |C_2| &\leq \frac{\alpha^4\pi^4\cot\pi\vartheta^*}{2\cos(\frac{\alpha\pi}{Q})^2q^4}, \\ |C_3| &\leq \frac{\alpha^4\pi^4(\cot\pi\vartheta^*)^3}{2\cos(\frac{\alpha\pi}{Q})^2q^4},\end{aligned}$$

and are all negative.

Appendix E

Corners of the polygonal Area

The corners of the polygons (for fixed n) as shown in Figure 7.5 are found by solving for the intersections of the various curves and lines obtained from equations (7.22) and (7.23):

$$\begin{aligned} A_{x_i} = &\Big(-2(h^+\rho(1+2\rho)(1+n+\rho+2n\rho) - L(1+\rho)(1+2(2+n)\rho+(2+4n)\rho^2)) \\ &+ R(-2L\rho R - LR)t\Big) \\ &\div \Big(2+2(4+n)\rho+(6+4n)\rho^2 + R(-2\rho R - R)t\Big), \end{aligned} \tag{E.1}$$

$$A_{\theta_i} = \frac{(h^+ - L)(1+2\rho)^2}{2R(1+\rho(4+n+3\rho+2n\rho)) - t(1+2\rho)}, \tag{E.2}$$

$$\begin{aligned} B_{x_i} = &\frac{-2h^+R\rho(1+2\rho)(1+n+\rho+2n\rho) + L(-2(1+\zeta)R + t + 4(1+3\zeta+2(1+\zeta)n)R\rho^3)}{(2\zeta\rho-1)(-t(1+2\rho)+2R(1+\zeta+2\zeta\rho+\rho(4+n+3\rho+2n\rho)))} \\ &+ \frac{2\rho(t-\zeta t(1+2L\rho)+R(-3+2\zeta^2+2L(n+\zeta(4+2\zeta+n))\rho))}{(2\zeta\rho-1)(-t(1+2\rho)+2R(1+\zeta+2\zeta\rho+\rho(4+n+3\rho+2n\rho)))}, \end{aligned} \tag{E.3}$$

$$B_{\theta_i} = \frac{(h^+ - L)(2\rho+1)^2}{(2\zeta\rho-1)(-t(1+2\rho)+2R(1+\zeta+2\zeta\rho+\rho(4+n+3\rho+2n\rho)))}, \tag{E.4}$$

$$C_{x_i} = L - \frac{2(h^+ - L)R\rho(2\zeta\rho-1)(\zeta\rho+n(2\zeta\rho-1))}{(1+2\rho)(t-2\zeta t\rho+2R(-1-\zeta+(-1+2\zeta(1+\zeta)-n)\rho+\zeta(3+2n)\rho^2))}, \tag{E.5}$$

$$C_{\theta_i} = \frac{(h^+ - L)(1-2\zeta\rho)^2}{(1+2\rho)(t-2\zeta t\rho+2R(-1-\zeta+(-1+2\zeta(1+\zeta)-n)\rho+\zeta(3+2n)\rho^2))}, \tag{E.6}$$

$$D_{x_i} = \Big(2(L + h^+ n)R\rho - Lt + 4\zeta^2 R\rho((h^+ - L)(1 + 2n)\rho^2 - L) \tag{E.7}$$

$$+ 2\zeta(LR + Lt\rho - (h^+ - 2L(n-1) + 4h^+ n)R\rho^2)\Big) \tag{E.8}$$

$$\div \left(-t - 4\zeta^2 R\rho + 2(1+n)R\rho + 2\zeta(R + t\rho - (3+2n)R\rho^2)\right), \tag{E.9}$$

$$D_{\theta_i} = \frac{(h^+ - L)(1 - 2\zeta\rho)^2}{-2\zeta R + t - 2((1 - 2\zeta^2 + n)R + \zeta t)\rho + 2\zeta(3+2n)R\rho^2}, \tag{E.10}$$

$$E_{x_i} = \frac{Lt + 4\zeta^2 LR\rho - 2(h^+ + L + h^+ n)R\rho + 2\zeta L(R(-1 + 2(2+n)\rho^2) - t\rho)}{(2\zeta\rho - 1)(2R(\zeta + (2+n)\rho) - t)}, \tag{E.11}$$

$$E_{\theta_i} = \frac{(h^+ - L)}{(-1 + 2\zeta\rho)(-t + 2R(\zeta + (2+n)\rho))}, \tag{E.12}$$

$$F_{x_i} = \frac{L(2R(1+\rho)(1 + 2(1+n)\rho) - t(1+2\rho)) - 2h^+ nR\rho}{(1+2\rho)(2R(1 + \rho + n\rho) - t)}, \tag{E.13}$$

$$F_{\theta_i} = \frac{(h^+ - L)}{(1+2\rho)(-t + 2R(1 + \rho + n\rho))}, \tag{E.14}$$

$$G_{x_i} = L, \tag{E.15}$$

$$G_{\theta_i} = 0, \tag{E.16}$$

where $\zeta = \left\lceil \frac{R}{r} \right\rceil$ and $\rho = \frac{r}{R}$.

Appendix F

Values of n when corners hit the hole

The upper and lower limits of the sums in expressions (7.24) and (7.23) are the solutions for n when the x_i coordinate of the corners $A - F$ exceeds h^+:

$$n_B = \left\lfloor \frac{(2+\zeta-\frac{t}{R}) + \left(6-4\zeta^2+\frac{t}{R}(2\zeta-2)\right)\rho + (-16\zeta-8\zeta^2+4\zeta\frac{t}{R})\rho^2 + (-4-12\zeta)\rho^3}{4(1+\zeta)(2\rho+1)\rho^2} \right\rfloor, \tag{F.1}$$

$$n_C = \left\lfloor \frac{(2+\zeta-\frac{t}{R}) + \left(6-4\zeta^2+\frac{t}{R}(2\zeta-2)\right)\rho + (4-12\zeta-8\zeta^2+4\zeta\frac{t}{R})\rho^2 + (-12\zeta-4\zeta^2)\rho^3}{4(1+\zeta)(2\zeta\rho-1)\rho^2} \right\rfloor, \tag{F.2}$$

$$n_D = \left\lfloor \frac{2\zeta-\frac{t}{R}+(2-4\zeta^2+2\zeta\frac{t}{R})\rho-4\zeta\rho^2-4\zeta^2\rho^3}{4\zeta(2\zeta\rho-1)\rho^2} \right\rfloor, \tag{F.3}$$

$$n_E = \left\lfloor \frac{2\zeta-\frac{t}{R}+(2-4\zeta^2+2\zeta\frac{t}{R})\rho-8\zeta\rho^2}{4\zeta\rho^2} \right\rfloor, \tag{F.4}$$

$$n_F = \left\lfloor \frac{-2+\frac{t}{R}+(-6+\frac{t}{R})\rho-4\rho^2}{4\rho(\rho+1)} \right\rfloor, \tag{F.5}$$

where $\zeta = \left\lceil \frac{R}{r} \right\rceil$ and $\rho = \frac{r}{R}$.

Appendix G

Approximating Sums (7.24) and (7.25)

The leading order approximations to sums (7.24) and (7.25) are:

$$\sum_{n=n_A+1}^{n_B} \hat{P}_2 = \frac{(h^+ - L)^2}{4\rho t}\left[\frac{(4+2\zeta)\rho + (-8\zeta - 2\zeta^2)\rho^2 + 4\zeta^2\rho^3}{(2\zeta\rho - 1)(2\rho + 1)} + \ln(2\zeta\rho - 1)\right], \tag{G.1}$$

$$\sum_{n=n_B+1}^{n_D} \hat{P}_3 = \frac{(h^+ - L)^2}{4(1+\zeta)t\rho}\Big[\frac{2\rho(-1+2\zeta(\zeta\rho)-1)(2\rho+\zeta(-1+\rho+2\zeta\rho-2\rho^2))}{(1+2\rho)(1-2\zeta\rho)^2} + (2+\zeta)\ln\left(\frac{2\rho+1}{(2\zeta\rho-1)^2}\right)\Big], \tag{G.2}$$

$$\sum_{n=n_D+1}^{n_E} \hat{P}_4 = \frac{(h^+ - L)^2}{4\zeta(1+\zeta)t\rho}\Big[\frac{-2\rho(1+\zeta-\zeta^2+2\zeta^3\rho)(1+\rho(1+2\zeta(-1+\zeta\rho)))}{(1+2\rho)(1-2\zeta\rho)^2} + (1+3\zeta+\zeta^2)\ln(2\rho-1)\Big], \tag{G.3}$$

$$\sum_{n=n_E+1}^{n_C} \hat{P}_5 = \frac{(h^+ - L)^2}{4(1+\zeta)t\rho}\Big[\frac{2\rho(-1+2\zeta(-1+\zeta\rho))(2\rho+\zeta(-1+\rho+2\zeta\rho-2\rho^2))}{(1+2\rho)(1-2\zeta\rho)^2} + (2+\zeta)\ln\left(\frac{2\rho+1}{(2\zeta\rho-1)^2}\right)\Big], \tag{G.4}$$

$$\sum_{n=n_C+1}^{n_F} \hat{P}_6 = \frac{(h^+ - L)^2}{4\rho t}\left[\frac{2\rho(\zeta\rho-1)(\zeta(2\rho-1)-2)}{(1+2\rho)(2\zeta\rho-1)} + \ln(2\zeta\rho-1)\right], \tag{G.5}$$

$$\sum_{n=n_F+1}^{\infty} \hat{P}_7 = \frac{(h^+ - L)^2(\rho+1)}{(2\rho+1)t}, \tag{G.6}$$

$$\sum_{n=n_A+1}^{n_D} \tilde{P}_2 = \frac{(h^+ - L)^2}{4\rho t}\left[\frac{(2-2\zeta)\rho + (2-4\zeta+2\zeta^2)\rho^2}{(2\zeta\rho-1)(2\rho+1)} + \ln\left(\frac{2\rho+1}{2\zeta\rho-1}\right)\right], \tag{G.7}$$

$$\sum_{n=n_D+1}^{n_B} \tilde{P}_3 = \frac{(h^+ - L)^2}{4\zeta t\rho}\Big[\frac{2\rho(1+\rho+2\zeta^2\rho-\zeta(1+\rho))(1-2\zeta(\zeta\rho-1))}{(1+2\rho)(1-2\zeta\rho)^2} + (1+\zeta)\ln\left(\frac{(2\zeta\rho-1)^2}{(2\rho+1)}\right)\Big], \tag{G.8}$$

$$\sum_{n=n_B+1}^{n_C} \tilde{P}_4 = \frac{(h^+ - L)^2}{4\zeta(1+\zeta)t\rho}\Big[\frac{4(1+\zeta)\rho(1-(\zeta-1)\rho)(1+\zeta-\zeta^2+2\zeta^3\rho)}{(1+2\rho)(1-2\zeta\rho)^2} + (1+3\zeta+\zeta^2)\ln\left(\frac{(2\zeta\rho-1)^2}{(2\rho+1)^2}\right)\Big], \tag{G.9}$$

$$\sum_{n=n_C+1}^{n_E} \tilde{P}_5 = \frac{(h^+ - L)^2}{4\zeta t\rho}\Big[\frac{2\rho(1+\rho+2\zeta^2\rho-\zeta(1+\rho))(1-2\zeta(\zeta\rho-1))}{(1+2\rho)(1-2\zeta\rho)^2} + (1+\zeta)\ln\left(\frac{(2\zeta\rho-1)^2}{2\rho+1}\right)\Big], \tag{G.10}$$

$$\sum_{n=n_E+1}^{n_F} \tilde{P}_6 = \frac{(h^+ - L)^2}{4\rho t}\left[\frac{(2-2\zeta)\rho + (2-4\zeta+2\zeta^2)\rho^2}{(1+2\rho)(2\zeta\rho-1)} + \ln\left(\frac{2\rho+1}{2\zeta\rho-1}\right)\right], \tag{G.11}$$

$$\sum_{n=n_F+1}^{\infty} \tilde{P}_7 = \frac{(h^+ - L)^2(\rho+1)}{(2\rho+1)t}, \tag{G.12}$$

where $\zeta = \left\lceil \frac{R}{r} \right\rceil$ and $\rho = \frac{r}{R}$.

Appendix H

Coefficients of eq (7.27)

The coefficients of equation (7.27) for the two different orderings $\hat{\cdot}$ and $\tilde{\cdot}$ of $n_A - n_F$ are

$$\hat{\varepsilon}_1 = -2 - 4\zeta + 4\zeta^3 \qquad \tilde{\varepsilon}_1 = 8 + 18\zeta + 2\zeta^2 - 8\zeta^3$$

$$\hat{\varepsilon}_2 = -2(1 + \zeta + \zeta^2 + 2\zeta^3 + 6\zeta^4) \qquad \tilde{\varepsilon}_2 = 8 + 12\zeta - 20\zeta^2 + 24\zeta^4$$

$$\hat{\varepsilon}_3 = -12\zeta^2 - 8\zeta^3 - 4\zeta^4 + 8\zeta^5 \qquad \tilde{\varepsilon}_3 = -16\zeta^2 + 8\zeta^3 + 8\zeta^4 - 16\zeta^5$$

$$\hat{\varepsilon}_4 = 16\zeta^3 + 16\zeta^4 + 8\zeta^5 \qquad \tilde{\varepsilon}_4 = 16(\zeta^3 + \zeta^4)$$

$$\hat{\jmath}_1 = 1 + 7\zeta + 3\zeta^2 \qquad \tilde{\jmath}_1 = -4 - 8\zeta - 2\zeta^2$$

$$\hat{\jmath}_2 = -6\zeta - 2\zeta^2 \qquad \tilde{\jmath}_2 = 6 + 12\zeta + 4\zeta^2$$

where $\zeta = \left\lceil \frac{R}{r} \right\rceil$.

Publication List

1. "Survival probability for the stadium billiard", C. P. Dettmann and O. Georgiou, Physica **D**, **238**, 2395-2403 (2009)

2. "Product of n independent uniform random variables", C. P. Dettmann and O. Georgiou, Statistics & Probability Letters, **79**, 2501-2503, (2009)

3. "Transmission and Reflection in the Stadium Billiard: Time-dependent asymmetric transport", C. P. Dettmann and O. Georgiou, Physical Review E, **83**, 036212 (2011)

4. "Open Mushrooms: Stickiness revisited", C. P. Dettmann and O. Georgiou, Journal of Physics A: Mathematical and Theoretical, **44**, 195102, (2011)

Bibliography

Bibliography

[1] L.A. Bunimovich and A. Yurchenko. Where to place a hole to achieve a maximal escape rate. *Israel J. Math. (to appear)*, page arXiv:0811.4438, 2008.

[2] M. Kac. Can one hear the shape of a drum? *Eur.J.Phys*, 73:1, 1966.

[3] S. Wiggins. *Chaotic Transport in Dynamical Systems*. Interdisciplinary Applied Mathematics. Springer - Verlag, New York, 2010.

[4] Ya.G. Sinai. "WHAT IS... a billiard". *Not. Am. Math. Soc.*, 51:412, 2004.

[5] S. Tabachnikov. *Geometry and billiards*. Mathematics Advanced Study Semesters. Amer. Math. Soc., 2005.

[6] N.I. Chernov and R. Markarian. *Chaotic* B*illiards*, volume 127 of *Math. Surveys*. American. Math. Soc., 2006.

[7] Ya. G. Sinai. Dynamical systems with elastic reflections. *Ergodic properties of dispersing billiards Math. Surv.*, 25:137, 1970.

[8] L.A. Bunimovich, R.L. Dobrushin S.G. Dani, M.V. Jakobson, I.P. Kornfeld, N.B. Maslova, Ya.B. Pesin, Ya.G. Sinai, J. Smillie, Yu.M. Sukhov, and A.M. Vershik. *Dynamical systems, ergodic theory and applications*, volume 100 of *Encyclopedia of Mathematical Sciences*. Springer, New York, 2000.

[9] A. Katok and B. Hasselblatt. *Introduction to the Modern Theory of Dynamical Systems*. Cambridge University Press, Cambridge, 1995.

[10] H.J. Stöckmann. *Quantum Chaos: An Introduction*. Cambridge University Press, Cambridge, 1999.

[11] A. Rockett and P. Szüsz. *Continued Fractions*. World Scientific Publishing, Singapore, 1994.

[12] S. Koyanagi, T. Nakano, and T. Kawabe. Application of Hamiltonian of ray motion to room acoustics. *J. Acoust. Soc. Am.*, 124:719, 2008.

[13] S. Montangero, D. Frustaglia, T. Calarco, and R. Fazio. Quantum billiards in optical lattices. *Europhys. Lett.*, 88:30006, 2009.

[14] A.I. Nosich, E.I. Smotrova, S.V. Boriskina, T.M. Benson, and P. Sewell. Trends in microdisk laser research and linear optical modelling. *Opt. Quant. Electron.*, 39:1253, 2007.

[15] H.A. Oliveira, C. Manchein, and M.W. Beims. Soft wall effects on interacting particles in billiards. *Phys. Rev. E*, 78:046208, 2008.

[16] S. Lansel, M.A. Porter, and L.A. Bunimovich. One-particle and few-particle billiards. *Chaos*, 16:013129, 2006.

[17] F. Cecconi, M. Cencini, and A. Vulpiani. Transport properties of chaotic and non-chaotic many particle systems. *J. Stat. Mech.:Theory Exp.*, page 12001, 2007.

[18] B. Gutkin, E. Gutkin, and U. Smilansky. Hyperbolic billiards on surfaces of constant curvature. *Commun. Math. Phys.*, 208:65, 1999.

[19] M. Robnik. Regular and chaotic billiard dynamics in magnetic fields. In *Nonlinear Phenomena and Chaos*. ed. S. Sarkar, Adam-Hilger, Bristol, page 303, 1986.

[20] N. Chernov and J. Lebowitz. Stationary shear flow in boundary driven Hamiltonian systems. *Phys. Rev. Lett.*, 75:2831, 1995.

[21] A. Arroyo, R. Markarian, and D.P. Sanders. Bifurcations of periodic and chaotic attractors in pinball billiards with focusing boundaries. *Nonlinearity*, 22:1499, 2009.

[22] F. Lenz, F.K. Diakonos, and P. Schmelcher. Classical dynamics of the time-dependent elliptical billiard. *Phys. Rev. E*, 76:066213, 2007.

[23] M. Sieber, N. Pavloff, and C. Schmit. Uniform approximation for diffractive contributions to the trace formula in billiard systems. *Phys. Rev. E*, 55:2279, 1997.

[24] F. Goos and H. Hänchen. Ein neuer und fundamentaler versuch zur total-reflexion. *Ann. Phys.*, 436:333, 1947.

[25] J.H. Jeans. *An Introduction to the Kinetic Theory of Gases*. Cambridge University Press, Cambridge, 1940.

[26] A. Rapoport and V. Rom-Kedar. Chaotic scattering by steep repelling potentials. *Phys. Rev. E*, 77:016207, 2008.

[27] T. Gilbert and D.P. Sanders. Stable and unstable regimes in higher - dimensional convex billiards with cylindrical shape. *New Journal of Physics*, 13:023040, 2011.

[28] H.A Lorentz. The motion of electron in metallic bodies. *Proceedings of Amsterdam Akademie*, 7:438, 1905.

[29] L.A. Bunimovich and Y.G. Sinai. Statistical properties of Lorentz gas with periodic configuration of scatterers. *Comm. Math. Phys.*, 78:479, 1981.

[30] L.A. Bunimovich and D. Szász. *Hard Ball Systems and the* L*orentz Gas*. Springer, New York, 2000.

[31] L.A. Bunimovich. Kinematics, equilibrium, and shape in Hamiltonian systems: The "LAB" effect. *Chaos*, 13:903, 2003.

[32] L.A. Bunimovich. Relative volume of KolmogorovArnoldMoser tori and uniform distribution, stickiness and nonstickiness in hamiltonian systems. *Nonlinearity*, 21:T13, 2008.

[33] L.A. Bunimovich and C.P. Dettmann. Peeping at chaos: Nondestructive monitoring of chaotic systems by measuring long-time escape rates. *Europhys. Lett.*, 80:40001, 2007.

[34] M.F Demers and L.S. Young. Escape rates and conditionally invariant measures. *Nonlinearity*, 19:377, 2006.

[35] E.G. Altmann and T. Tél. Poincare recurrences and transient chaos in systems with leaks. *Phys. Rev. E*, 79:016204, 2009.

[36] C.P. Dettmann. *Recent advances in open billiards with some open problems.* In: Frontiers in the study of chaotic dynamical systems with open problems. World Scientific, Singapore, 2011.

[37] G. Pianigiani and J. A. Yorke. Expanding maps on sets which are almost invariant: decay and chaos. *Trans. American. Math. Soc.*, 252:351, 1979.

[38] J. Schneider, T. Tél, and Z. Neufeld. Dynamics of "leaking" Hamiltonian systems. *Phys. Rev. E*, 66:066218, 2002.

[39] F. Mortessagne, O. Legrand, and D. Sornette. Transient chaos in room acoustics. *Chaos*, 3:529, 1993.

[40] E. Doron and U. Smilansky. Chaotic spectroscopy. *Phys Rev. Lett.*, 68:1255, 1992.

[41] E. Doron and U. Smilansky. Chaotic spectroscopy. *Chaos*, 2:117, 1992.

[42] V. Paar and N. Pavin. Bursts in average lifetime of transients for chaotic logistic map with a hole. *Phys. Rev. E*, 55:4112, 1997.

[43] H. Buljan and V. Paar. Many-hole interactions and the average lifetimes of chaotic transients that precede controlled periodic motion. *Phys. Rev. E*, 63:066205, 2001.

[44] V. Milner, J. L. Hanssen, W. C. Campbell, and M. G. Raizen. Optical billiards for atoms. *Phys. Rev. Lett.*, 86:1514, 2001.

[45] N. Friedman, A. Kaplan, D. Carasso, and N. Davidson. Observation of chaotic and regular dynamics in atom-optics billiards. *Phys. Rev. Lett.*, 86:1518, 2001.

[46] R. T. Pierrehumbert. On tracer microstructure in the large-eddy dominated regime. *Chaos Sol. Fractals*, 4:1091, 1994.

[47] Z. Neufeld, P. Haynes, and G. Picard. The effect of forcing on the spatial structure and spectra of chaotically advected passive scalars. *Phys. Fluids*, 12:2506, 2000.

[48] J. Schneider, T. Tél, and Z. Neufeld. Dynamics of "leaking" Hamiltonian systems. *Phys. Rev. E*, 66:066218, 2002.

[49] J. Nagler. Crash test for the Copenhagen problem. *Phys. Rev. E*, 69:066218, 2004.

[50] A. E. Motter and P. S. Letelier. Mixmaster chaos. *Phys. Lett. A*, 285:127, 2001.

[51] K. Nakamura and T. Harayama. *Quantum chaos and quantum dots*. Oxford University Press, New York, 2004.

[52] H. Schomerus and P. Jacquod. Quantum-to-classical correspondence in open chaotic systems. *J. Phys. A: Math. Gen.*, 38:10663, 2005.

[53] H. Ishio and J.P. Keating. Semiclassical wavefunctions in chaotic scattering systems. *J. Phys. A*, 37:L217, 2004.

[54] J.B. Keller. Geometrical theory of diffraction. *J. Opt. Soc. Am.*, 52:116, 1962.

[55] M. Sieber. Geometrical theory of diffraction and spectral statistics. *J. Phys. A*, 32:7679, 1999.

[56] J.U. Nöckel and A.D.Stone. Ray and wave chaos in asymmetric resonant cavities. *Nature*, 385:45, 1997.

[57] C.W.J. Beenakker and H. van Houten. Quantum transport in semiconductor nanostructures. *Solid State Physics*, 44:1, 2004.

[58] W. Arendt, R. Nittka, W. Peter, and F. Steiner. W*eyls Law: Spectral Properties of the* L*aplacian in Mathematics and Physics*. WILEY-VCH Verlag GmbH & Co. KGaA, Weinhei, 2009.

[59] M.V. Berry. Semiclassical theory of spectral rigidity. *Proc. R. Soc. A*, 400:229, 1985.

[60] J.W.S. Rayleigh. *The Theory of Sound*. Dover, New York, 1894.

[61] H. Weyl. Über die asymptotische verteilung der eigenwerte. *Nachr. Akad. Wiss. Göttingen*, page 110, 1911.

[62] M.C. Gutzwiller. *Chaos in classical and quantum mechanics*. Springer, New York, 1990.

[63] R. Aurich, A. Bäcker, R. Schubert, and M. Taglieber. Maximum norms of chaotic quantum eigenstates and random waves. *Physica D*, pages 1–14, 1999.

[64] W.T. Lu, S. Sridhar, and M. Zworski. Fractal Weyl laws for chaotic open systems. *Phys. Rev. Lett.*, 91:154101, 2003.

[65] S. Nonnenmacher. Some open questions in 'wave chaos'. *Nonlinearity*, 21:T113, 2008.

[66] C. M. Marcus, A. J. Rimberg, R. M. Westervelt, P. F. Hopkins, and A. C. Gossard. Conductance fluctuations and chaotic scattering in ballistic microstructures. *Phys. Rev. Lett.*, 69:506, 1992.

[67] R.A. Jalabert, H.U. Baranger, and A.D. Stone. Conductance fluctuations in the ballistic regime: A probe of quantum chaos? *Phys. Rev. Lett.*, 65:26442, 1990.

[68] K. Richter and M. Sieber. Semiclassical theory of chaotic quantum transport. *Phys. Rev. Lett.*, 89:206801, 2002.

[69] H.D. Cornean, A. Jensen, and V. Moldoveanu. A rigorous proof of the Landauer - Büttiker formula. *J. Math. Phys.*, 46:1, 2005.

[70] C.P. Dettmann, G.V. Morozov, M. Sieber, and H. Waalkens. Unidirectional emission from circular dielectric microresonators with a point scatterer. *Phys. Rev. A*, 80:063813, 2009.

[71] A. Burbanks H. Waalkens and S. Wiggins. Escape from planetary neighbourhoods. *Mon. Not. R. Astron. Soc.*, 361:763, 2005.

[72] J. Schneider, J. Schmalzl, and T.Tél. Lagrangian avenues of transport in the earth's mantle. *Chaos*, 17:033115, 2007.

[73] I. Tuval, J. Schneider, O. Piro, and T. Tél. Opening up fractal structures of three-dimensional flows via leaking. *Europhys. Lett.*, 65:633, 2004.

[74] P. Gaspard and T. Gilbert. Heat conduction and Fourier's law by consecutive local mixing and thermalization. *Phys. Rev. Lett.*, 101:020601, 2008.

[75] E.D. Leonel and L.A. Bunimovich. Suppressing Fermi acceleration in a driven elliptical billiard. *Phys. Rev. Lett.*, 104:224101, 2010.

[76] H. Waalkens, A. Burbanks, and S. Wiggins. Efficient procedure to compute the microcanonical volume of initial conditions that lead to escape trajectories from a multidimensional potential well. *J. Phys. A*, 37:L257, 2004.

[77] G.S. Ezra, H. Waalkens, and S. Wiggins. Microcanonical rates, gap times, and phase space dividing surfaces. *J. Chem. Phys.*, 130:164118, 2009.

[78] O.G. Jepps, C. Bianca, and L. Rondoni. Onset of diffusive behavior in confined transport systems. *Chaos*, 18:013127, 2008.

[79] C.P. Dettmann and O. Georgiou. Transmission and reflection in the stadium billiard: Time-dependent asymmetric transport. *Phys. Rev. E.*, 83:036212, 2011.

[80] L.A. Bunimovich and C.P. Dettmann. Open circular billiards and the Riemann hypothesis. *Phys. Rev. Lett.*, 94:100201, 2005.

[81] C.P. Dettmann. New horizons in multidimensional diffusion: The Lorentz gas and the Riemann hypothesis. *arXiv:1103.1225*, 2011.

[82] E.G. Altmann, A.E. Motter, and H. Kantz. Stickiness in Hamiltonian systems: From sharply divided to hierarchical phase space. *Phys. Rev. E*, 73:026207, 2006.

[83] D. N. Armstead, B. R. Hunt, and E. Ott. Power-law decay and self-similar distributions in stadium-type billiards. *Physica D*, 193:96, 2004.

[84] E. Falcon, S.G. Roux, and C. Laroche. On the origin of intermittency in wave turbulence. *Europhys. Lett.*, 90:34005, 2010.

[85] L. Debnath. *Wavelets and signal processing.* Birkhäuser, Boston, 2003.

[86] F. Vivaldi, G. Casati, and I. Guarneri. Origin of long-time tails in strongly chaotic systems. *Phys. Rev. Lett.*, 51:727, 1983.

[87] C.P. Dettmann and O. Georgiou. Survival probability for the stadium billiard. *Physica D*, 238:2395, 2009.

[88] C.P. Dettmann and O. Georgiou. Product of n independent uniform random variables. *Stat. Prob. Lett.*, 79:2501, 2009.

[89] A.S. Pikovsky. Escape exponent for transient chaos and chaotic scattering in non-hyperbolic Hamiltonian systems. *J. Phys. A: Math. Gen.*, 25:477, 1992.

[90] C.P. Dettmann and E.D. Leonel. Asymmetric transport in the bouncer model: mixed, time dependent, noncompact dynamics. *arXiv:1010.2228*, 2010.

[91] C.P. Dettmann and O. Georgiou. Open mushrooms: Stickiness revisited. *J. Phys. A.*, 44:195102, 2011.

[92] J.R. Nielsen, editor. *Niels Bohr Collected Works, Vol. 3: The Correspondence Principle (1918 - 1923).* Elsevier, Amsterdam, 1976.

[93] P. Cvitanović, R. Artuso, P. Dahlqvist, R. Mainieri, G. Tanner, G. Vattay, N. Whelan, and A. Wirzba. *Chaos: Classical and Quantum.* www.nbi.dk/ChaosBook/, 2004.

[94] E. Ott. *Chaos in Dynamical Systems.* Cambridge University Press, Cambridge, 2002.

[95] H. Poincaré. *Les méthodes nouvelles de la méchanique céleste*, volume 2. Dover, New York, 1957.

[96] V.I. Oseledet. A multiplicative ergodic theorem. *Trans. Moskow Math. Soc.*, 19:197, 1968.

[97] J.R Dorfman. *An Introduction to Chaos in Nonequilibrium Statistical Mechanics.* Cambridge University Press, Cambridge, 1999.

[98] Y-C. Lai and T. Tél. *Transient Chaos.* Applied Mathematical Sciences. Springer, New York, 2011.

[99] G. Keller and C. Liverani. Rare events, escape rates and quasistationarity: Some exact formulae. *J. Stat. Phys.*, 135:519, 2008.

[100] P. Manneville and Y. Pomeau. Intermittency and the Lorenz model. *Phys. Lett. A*, 75:1, 1979.

[101] P. Manneville and Y. Pomeau. Intermittent transition to turbulence in dissipative dynamical systems. *Commun. Math. Phys.*, 74:189, 1980.

[102] D. Ruelle. *Thermodynamic Formalism: The Mathematical Structures of Classical Equilibrium Statistical Mechanics*. Cambridge University Press, Cambridge, 2004.

[103] P. Dahlqvist. Escape from intermittent repellers: periodic orbit theory for crossover from exponential to algebraic decay. *Phys. Rev. E*, 60:6639, 1999.

[104] B.V. Chirikov. Research concerning the theory of nonlinear resonance and stochasticity, engl. trans., cern trans. 71-40 (1971). *Institute of Nuclear Physics, Novosibirsk*, page 267, 1969.

[105] S. Smale. Differentiable dynamical systems. *Bulletin of the Amer. Math. Soc.*, 73:747, 1967.

[106] R.S. MacKay and I.C. Percival. Converse KAM: Theory and practice. *Comm. Math. Phys.*, 98:469, 1985.

[107] B.V. Chirikov and D.I. Shepelyansky. Correlation properties of dynamical chaos in hamiltonian systems. *Physica D*, 13:395, 1984.

[108] M. Kac. On the notion of recurrence in discrete stochastic processes. *Bulletin of the Amer. Math. Soc.*, 53:1002, 1947.

[109] J. D. Meiss. Average exit time for volume-preserving maps. *Chaos*, 7:139, 1997.

[110] G. Cristadoro and R. Ketzmerick. On universality of algebraic decays in Hamiltonian systems. *Phys. Rev. Lett.*, 100:184101, 2008.

[111] E.G. Altmann. *Intermittent chaos in* H*amiltonian systems*. PhD thesis, Wuppertal University, 2007.

[112] E.G. Altmann, T. Friedrich, A.E. Motter, H. Kantz, and A. Richter. Prevalence of marginally unstable periodic orbits in chaotic billiards. *Phys. Rev. E*, 77:016205, 2008.

[113] S. Lansel and M.A. Porter. Billiard simulator for MATLAB (software), 2004.

[114] N.I. Chernov and H.K. Zhang. On statistical properties of hyperbolic systems with singularities. *J. Stat. Phys.*, 136:615, 2009.

[115] M.V Berry and M. Tabor. Level clustering in the regular spectrum. *Proc. R. Soc. A*, 356:375, 1977.

[116] R.D. Connors and J.P. Keating. Degeneracy moments for the square billiard. *J. Phys. G: Nucl. Part. Phys.*, 25:555, 1999.

[117] E. Gutkin. Billiards in polygons: Survey of recent results. *J. Stat. Phys.*, 83:7, 1996.

[118] E. Gutkin and C. Judge. Affine mappings of translation surfaces: geometry and arithmetic. *Duke Math. J. V.*, 103:191, 2000.

[119] F. Valdez. Infinite genus surfaces and irrational polygonal billiards. *Geom. Dedicata*, 143:143, 2009.

[120] D.A. Poet and R.R.W. Poet. Confocal conic billiards. *Physics Letters A*, 271:277, 2000.

[121] F.S. Henyey and N. Pomphrey. The autocorrelation function of a pseudointegrable system. *Physica D*, 6:78, 1982.

[122] J.H. Hannay and R.J. McCraw. Barrier billiards a simple pseudo integrable system. *J. Phys. A*, 23:887, 1990.

[123] J. L. Vega, T. Uzer, F. Borondo, and J. Ford. Deterministic diffusion in almost integrable systems. *Chaos*, 6:519, 1996.

[124] L.A. Bunimovich. Absolute focusing and ergodicity of billiards. *Regul. Chaotic Dyn.*, 8:15, 2003.

[125] L.A. Bunimovich, Y.G Sinai, and N.I. Chernov. Markov partitions for two-dimensional hyperbolic billiards. *Russ. Math. Surv.*, 45:105, 1990.

[126] P. Bálint and I. Melbourne. Decay of correlations and invariance principles for dispersing billiards with cusps, and related planar billiard flows. *J. Stat. Phys.*, 133:435, 2008.

[127] V.F. Lazutkin. Existence of a continuum of closed invariant curves for a convex billiard. *Uspehi Mat. Nauk*, 27:201, 1972.

[128] V.F. Lazutkin. Existence of caustics for the billiard problem in a convex domain. *Izv. Akad. Nauk SSSR Ser. Mat.*, 37:186, 1973.

[129] L.A. Bunimovich. The ergodic properties of certain billiards. *Funct. Anal. Appl.*, 8:73, 1974.

[130] L.A. Bunimovich. On ergodic properties of nowhere dispersing billiards. *Commun. Math. Phys.*, 65:295, 1979.

[131] H.W. Broer. Kam theory: the legacy of Kolmogorov's 1954 paper. *Bull. Amer. Math. Soc. (New Series)*, 41:507, 2004.

[132] V. Lopac, I. Mrkonjic, and D. Radic. Chaotic behavior in lemon-shaped billiards with elliptical and hyperbolic boundary arcs. *Phys. Rev. E*, 64:016214, 2001.

[133] M.V. Berry. Regularity and chaos in classical mechanics, illustrated by three deformations of a circular billiard. *Eur.J.Phys*, 2:91, 1981.

[134] W. Bauer and G.F. Bertsch. Decay of ordered and chaotic systems. *Phys. Rev. Lett.*, 65:2213, 1990.

[135] J.B. Conrey. The Riemann Hypothesis. *Not. Amer. Math. Soc.*, 50:341, 2003.

[136] C.P. Dettmann and E.G.D. Cohen. Microscopic chaos and diffusion. *J. Stat. Phys.*, 101:775, 2000.

[137] G.M. Zaslavsky. Chaos, fractional kinetics, and anomalous transport. *Phys. Rep.*, 371:461, 2002.

[138] N.I. Chernov and H. K. Zhang. Billiards with polynomial mixing rates. *Nonlinearity*, 18:1527, 2005.

[139] G. Carlo, E. Vergini, and P. Lustemberg. Scar functions in the Bunimovich stadium billiard. *J. Phys. A: Math. Gen.*, 35:7965, 2002.

[140] A. Hassell and L. Hillairet. Ergodic billiards that are not quantum unique ergodic. *Ann. Math.*, 171:605, 2010.

[141] G. Tanner. How chaotic is the stadium billiard? a semi-classical analysis. *J. Phys. A: Math. Gen.*, 30:2863, 1997.

[142] M. Sieber, U. Smilansky, S.C. Creagh, and R.G. Littlejohn. Non-generic spectral statistics in the quantized stadium billiard. *J. Phys. A. Math. Gen.*, 26:6217, 1993.

[143] H.-D. Gräf, H.L. Harney, H. Lengeler, C.H. Lewenkopf, C. Rangacharyulu, A. Richter, P. Schardt, and H.A. Weidenmüller. Distribution of eigenmodes in a superconducting stadium billiard with chaotic dynamics. *Phys. Rev. Lett.*, 69:1296, 1992.

[144] P. Gaspard and J.R. Dorfman. Chaotic scattering theory, thermodynamic formalism, and transport coefficients. *Phys. Rev. E*, 52:3525, 1995.

[145] N.I. Chernov and C. Haskell. Nonuniformly hyperbolic K-systems are Bernoulli. *Ergodic Theory and Dynamical Systems*, 16:19, 1996.

[146] S. Bleher, E. Ott, and C. Grebogi. Routes to chaotic scattering. *Phys. Rev. Lett.*, 63:919, 1989.

[147] G. Benettin and J. M. Strelcyn. Numerical experiments on the free motion of a point mass moving in a plane convex region: Stochastic transition and entropy. *Phys. Rev. A*, 17:773, 1978.

[148] P. V. Elyutin. Kolmogorov entropy of billiard "stadiums". *Dokl. Akad. Nauk SSSR*, 291:595, 1986.

[149] L. A. Bunimovich. Mushrooms and other billiards with divided phase space. *Chaos*, 11:802, 2001.

[150] L. A. Bunimovich. Conditions of stochasticity of two dimensional billiards. *Chaos*, 1:187, 1991.

[151] M. Wojtkowski. Principles for the design of billiards with nonvanishing Lyapunov exponents. *Commun. Math. Phys*, 105:391, 1986.

[152] A. Bäcker and F. Steiner. Quantum chaos and quantum ergodicity, in "Ergodic theory, analysis and efficient simulation of dynamical systems, B. Fiedler (Ed.). *Springer-Verlag Berlin/Heidelberg*, page 717, 2001.

[153] L. S. Young. Statistical properties of dynamical systems with some hyperbolicity. *Ann. Math.*, 147:585, 1998.

[154] L. S. Young. Recurrence times and rates of mixing. *Israel J. Math.*, 110:153, 1999.

[155] R. Markarian. Billiards with polynomial decay of correlations. *Ergodic Theory Dynam. Systems*, 24:177, 2004.

[156] P. Bálint and S. Gouëzel. Limit theorems in the stadium billiard. *Commun. Math. Phys.*, 263:461, 2006.

[157] N.I. Chernov and H. K. Zhang. Improved estimates for correlations in billiards. *Commun. Math. Phys*, 277:305, 2008.

[158] M. Courbage, M. Edelman, S. M. Saberi Fathi, and G. M. Zaslavsky. Problem of transport in billiards with infinite horizon. *Phys. Rev. E.*, 77:036203, 2008.

[159] R. S. Dumont and P. Brumer. Decay of a chaotic dynamical system. *Chem. Phy. Lett*, 188:565, 1992.

[160] M. V. Berry. 'Regular and irregular motion' in topics in nonlinear mechanics. *Am. Inst. Ph. Conf. Proc*, 46:16, 1978.

[161] H. Alt, H.D. Graf, H.L. Harney, R. Hofferbert, H. Rehfeld, A. Richter, and P. Schardt. Decay of classical chaotic systems: The case of the Bunimovich stadium. *Phys. Rev. E*, 53:2217, 1996.

[162] H. G. Schuster and W. Just. *Deterministic Chaos: An Introduction*. Wiley John and Sons, Weinheim, 2005.

[163] K.C. Lee. Long-time tails in a chaotic system. *Phys. Rev. Lett.*, 60:1991, 1988.

[164] R. Markarian, S. Kamphorst, and S. P. Carvalho. Chaotic properties of the elliptical stadium. *Commun. Math. Phys.*, 174:661, 1996.

[165] L. A. Bunimovich and G. Del Magno. Semi-focusing billiards: ergodicity. *Ergodic Theory and Dynamical Systems*, 28:1377, 2008.

[166] V.K. Rohatgi. *An Introduction to Probability Theory and Mathematical Statistics*. John Wiley and Sons Inc, New York, 1976.

[167] H.J. Stöckmann and J. Stein. "quantum" chaos in billiards studied by microwave absorption. *Phys. Rev. Lett.*, 64:2215, 1990.

[168] B. Dietz, T. Friedrich, H.L. Harney, M. Miski-Oglu, A. Richter, F. Schäfer, and H.A. Weidenmüller. Quantum chaotic scattering in microwave resonators. *Phys. Rev. E.*, 81:036205, 2010.

[169] E. Persson, I. Rotter, H.-J. Stöckmann, and M. Barth. Observation of resonance trapping in an open microwave cavity. *Phys. Rev. Lett.*, 85:2478, 2000.

[170] C.W.J. Beenakker. Random-matrix theory of quantum transport. *Rev. Mod. Phys*, 69:731, 1997.

[171] M. Kopp and H. Schomerus. Staggered repulsion of transmission eigenvalues in symmetric open mesoscopic systems. *Phys. Rev. B*, 78:075312, 2008.

[172] I.L. Aleiner and A.I. Larkin. Divergence of classical trajectories and weak localization. *Phys. Rev. B.*, 54:14423, 1996.

[173] G. Casati, C. Tsallis, and F. Baldovi. Linear instability and statistical laws of physics. *Europhys. Lett.*, 72:355, 2005.

[174] S. Fishman, D. R. Grempel, and R. E. Prange. Temporal crossover from classical to quantal behavior near dynamical critical points. *Phys. Rev. A*, 36:289, 1987.

[175] L.A. Bunimovich. Chaotic and nonchaotic mushrooms. *Discrete Contin. Dyn. Syst.*, 22:63, 2008.

[176] W.P.K. Zapfe, F. Leyvraz, and T.H. Seligman. About imperfect mushroom billiards. *arXiv:0805.3727*, 2008.

[177] A.H. Barnett and T. Betcke. Quantum mushroom billiards. *Chaos*, 17:043125, 2007.

[178] I.C. Percival. Regular and irregular spectra. *J. Phys. B: Atom. Molec. Phys.*, 6:L229, 1973.

[179] A. Bäcker, R. Ketzmerick, S. Löck, and H. Schanz. How long is the chaotic boundary of a billiard? *arXiv:1010.5093v1*, 2010.

[180] A. Bäcker, R. Ketzmerick, and S. Löck. Dynamical tunneling in mushroom billiards. *Phys. Rev. Lett.*, 100:174103, 2008.

[181] B. Dietz, T. Friedrich, M. Miski-Oglu, A. Richter, and F. Schäfer. Spectral properties of Bunimovich mushroom billiards. *Phys. Rev. E*, 75:035203, 2007.

[182] E.G. Altmann, A.E. Motter, and H. Kantz. Stickiness in mushroom billiards. *Chaos*, 15:033105, 2005.

[183] J. Andreasen, H. Cao, J. Wiersig, and A.E. Motter. Marginally unstable periodic orbits in semiclassical mushroom billiards. *Phys. Rev. Lett.*, 103:154101, 2009.

[184] E.G. Altmann. Emission from dielectric cavities in terms of invariant sets of the chaotic ray dynamics. *Phys. Rev. A*, 79:013830, 2009.

[185] B. Dietz, T. Friedrich, M. Miski-Oglu, A. Richter, T.H. Seligman, and K. Zapfe. Nonperiodic echoes from mushroom billiard hats. *Phys. Rev. E*, 74:056207, 2006.

[186] A.Ya. Khinchin. *Continued Fractions*. Dover, New York, 1997.

[187] D. Hensley. Continued fraction cantor sets, Hausdorff dimension, and functional analysis. *J. Number Theory*, 40:336, 1992.

[188] N.I. Chernov. Entropy, Lyapunov exponents and mean-free path for billiards. *J. Stat. Phys*, 88:19, 1997.

[189] P. Bálint, M. Halász, J.H. Tahuilán, and D.P. Sanders. Chaos and stability in a two-parameter family of convex billiard tables. *Nonlinearity*, 24, 2011.

[190] H.M. Ammari and S.K. Das. Critical density for coverage and connectivity in three-dimensional wireless sensor networks using continuum percolation. *IEEE Ttrans. Par. & Distr. Sys.*, 20:872, 2009.

[191] G. Stell. Continuum theory of percolation. *J. Phys.: Condens. Matter*, 8:A1, 1996.

[192] L.A. Bunimovich and G. Del Magno. Track billiards. *Commun. Math. Phys.*, 288:699, 2009.

[193] J. Feist, A. Bäcker, R. Ketzmerick, J. Burgdörfer, and S. Rotter. Nano-wires with surface disorder: Giant localization lengths and dynamical tunneling in the presence of directed chaos. *Phys. Rev. B*, 80:245322, 2009.

[194] E. Canale, R. Markarian, S.O. Kamphorst, and S.P. Carvalho. A lower bound for chaos on the elliptical stadium. *Physica D*, 115:189, 2001.

[195] T. Ishihara. The distribution of the sum and the product of independent uniform random variables distributed at different intervals (in japanese). *Transactions of the Japan Society for Industrial and Applied Mathematics*, 12:197, 2002.

[196] M.D. Springer. *The Algebra of Random Variables*. John Wiley and Sons Inc.

[197] R.N Bracewell. *The Fourier Transform and Its Applications*. McGraw-Hill, Boston, 2000.

[198] L. Devroye. *Non-Uniform Random Variate Generation*. Springer-Verlag, New York.

[199] W. Feller. *An Introduction to Probability Theory and Its Applications*. John Wiley and Sons Inc, New York, 1972.

[200] K. Knopp. *Theory of Functions*. Dover, New York, 1996.